eman ta zabal zazu

Universidad del País Vasco

Euskal Herriko Unibertsitatea

CHARACTERIZATION OF VERTICAL CRACKS USING LOCK-IN VIBROTHERMOGRAPHY

by

Alazne Castelo Varela

Thesis presented in partial fulfilment of the requirements for the degree of

Doctor of Philosophy

at the Department of Applied Physics I, Faculty of Engineering, UPV/EHU

2017

Agradecimientos

Mediante estas líneas, me gustaría expresar mi más sincero agradecimiento a todas las personas que han contribuido, de una manera u otra, a que esta tesis llegue a buen puerto.

En primer lugar a mis directores, Dra. Arantza Mendioroz y Dr. Ricardo Celorrio de Pablo, por su esfuerzo, dedicación y paciencia, así como también a Dr. Agustín Salazar. Este trabajo me ha permitido aprovechar su competencia y experiencia y les agradezco la confianza depositada en mí desde el principio. Su inestimable ayuda y el ánimo infundido han supuesto una constante fuente de motivación para abordar este proyecto. En especial a Arantza, por explicar, corregir, animar, volver a explicar y volver a corregir…

A la UPV/EHU, por el contrato de Personal Investigador concedido. No me gustaría olvidarme del servicio recibido por parte de IZO-SGI SGIker y European funding (ERDF and ESF), sin el cual los cálculos realizados no habrían podido llevarse a cabo. En especial a Dr. Txema Mercero y Dr. Edu Ogando, por su inmejorable atención y por hacer que trabajar con Arina me haya resultado tan cómodo. También a IK4-Lortek, por la muestra con grietas reales prestada y el trabajo realizado en conjunto.

A la gente del departamento de Física Aplicada I, por hacerme los días en el laboratorio mucho más agradables con sus visitas y animarme, otros días, desde la distancia.

A los amigos y amigas que me han acompañado durante todo el camino. A las de la uni, por seguir siendo tan especiales y permanecer siempre a mi lado tras tantos años. A los del máster, por hacerme pasar un año inolvidable dentro y fuera del Aula Espazio y darme los mejores recuerdos de mi paso por la UPV/EHU y, por último, a las de la cuadrilla, por endulzar mis sábados con Sugus y hacerme saber que, tanto en los momentos felices como en los de agobio, están ahí para escucharme :)

Y sobre todo a mis padres, también a Cristina, José Mari y Esti y a Iñaki, por aguantarme, preocuparse, llenar mi mesa de fruta y chocolate y demostrar que tienen muchas otras maneras de ayudarme día a día. Esto es por y para vosotros.

Contents

1 Introduction

After a brief introduction to infrared thermography, this chapter presents the principles of vibrothermography as a technique in the field of non-destructive testing. Then, key aspects regarding vibrothermography are addressed along with an outline of research activities. Finally, the concept of characterization of vertical cracks is introduced, leading to the objectives of this thesis.

The sensations of hot and cold are fundamental to the human experience, yet finding ways to measure temperature has challenged many great minds. Over history, most methods of measuring temperature have been indirect, observing the effect it has on something's properties and deducing temperature from it.

Galileo Galilei built a device that showed changes in temperature around 1592, called *thermoscope*, but it lacked a scale and was affected by changes in atmospheric pressure. In 1714, Daniel Gabriel Fahrenheit, the inventor of the *mercury thermometer* as we know it, realised that he needed a temperature scale. Anders Celsius proposed the 0 to 100 scale, whereas William Thomson, later Lord Kelvin, proposed using the absolute zero as starting point.

Being Isaac Newton, in 1666, the first scientist introducing the term *spectrum* as he realized that white light could be split into colours using a glass prism, it was William Herschel, in 1800, who first discovered the infrared region upon which thermography is based, when he was measuring the "temperature of each colour" and he found the highest temperature to fall beyond the red end. In 1840, his son, John Herschel, who was more into photography, was the first one who managed to capture a thermal image on paper, by

creating an evaporograph image using carbon suspension in alcohol. He called it a *thermogram*.

Thermography is, thus, the detection of radiation in the infrared range and formation of a thermal image, which is related to the object temperature, but also to the surface nature of the measured object.

By the time of World War I, scientists had begun to discover the military and aeronautic uses for infrared detection and thermography. In 1935, night vision was invented. It had obvious military applications and it was not until the mid-sixties when civilian and engineering applications came up. Advances in infrared detectors and semiconductors along with the invention of the CCD in the seventies promoted the development of the infrared focal plane array (IRFPA) which, in turn, made a variety of technologies on the thermography field emerge, such as *non-destructive testing (NTD)*.

At this point it is meaningful to distinguish between the two main divisions of infrared thermography: passive and active. In *passive infrared thermography*, the thermal radiation of an object is observed without interfering with its natural conditions regarding heating or cooling and the involved heat transfer mechanisms. Here, the temperature itself is the magnitude of interest. For simplicity reasons, passive thermography was the first to arise, with a wide range of applications such as inspection of buildings in engineering, night vision in the military field or body temperature mapping in medicine.

Active infrared thermography, in contrast, implies an artificial change of the object's energetic equilibrium. Some energy is deposited on the object and it diffuses along the sample, as well as to the surroundings. Thus, in active infrared thermography, temperature changes, which are obtained from changes in the recorded infrared emission from the sample surface, are used to retrieve information. The absolute value of the temperature, on the contrary, is of minor importance. This considered, active infrared thermography reveals a deviated thermal response produced at the position of the defects compared to that in sound regions, in order to detect and characterize such defects.

1.1 Vibrothermography as a non-destructive technique

Ultrasound excited thermography, also known as vibrothermography, thermosonics or sonic infrared, was first proposed as a thermographic non-destructive evaluation (NDE) technique in the late seventies [1, 2]. In this technique, the part or structure under study is

excited by high amplitude ultrasounds. At the defects, part of this mechanical energy is dissipated as heat, due to rubbing of the defect's faces or, in the case of cracks, to plastic deformation at the surrounding area [3]. The thermal energy produced at the defects diffuses in the material, producing a temperature rise at the surface that can be measured with an IR videocamera. If the material is not viscoelastic, the bulk attenuation of the ultrasounds is small, so the defect turns into a heat source on a cold environment, which makes the technique defect selective. Given that the detection is based on heat diffusion, vibrothermography is used to detect surface breaking or shallow subsurface defects.

The development of ultrasound excited thermography has been linked to the availability of modern IR cameras. In order for vibrothermography to reveal the presence of a defect in a live image sequence, surface temperature rises need to be above the temperature resolution of the camera. Pioneering works by Henneke [1, 2], Pye [4, 5] and Mignona [6] lacked continuity until the late nineties due to the low temperature resolution (about 0.2 K) of the IR cameras available at that time.

The development of affordable IR cameras in the last decade of the twentieth century, with temperature resolutions in the 20 to 30 mK range, boosted vibrothermography, both in the lock-in [7] and burst [8] regimes. Since then, the application range of vibrothermography has spread out over different types of materials such as polymers, fibre reinforced polymers, metals, ceramics or timber. Regarding polymers and carbon fibre reinforced plastic laminates, vibrothermography has been used to detect cracks and impact damage [1-5, 7-11], delaminations, disbonds [12] and heat damage [13], as well as to assess the overall damage in composites after mechanical loading [14, 15].

Other fields of application are the detection of corrosion [16] and cracks [6, 17-20] in metallic plates and timber [21], the identification of microcracks in plasma sprayed coatings [22] (being the only non-destructive technique capable of identifying such flaws), or the assessment of defective adhesion in bondlines [13]. The technique has also been successfully applied to large aerospace structures such as cracked fuselage panels and to locate loose rivets and cracks in aluminium assemblies [23]. In addition to laminates, large massive structures have been inspected with vibrothermography. Favro et al. [9] found surface breaking and subsurface fatigue cracks in an aluminium cylinder head that had been subjected to severe thermal cyclic stressing, Guo et al. identified surface breaking cracks in aluminium aircraft structures [20] and Montanini and coworkers [19] detected buried flaws in cast iron turbocharger housings without any surface preparation, showing the potential applicability of the technique in a production line.

The variety of applications enumerated above is a manifestation of the simplicity of application of the technique together with its ability to test large parts in a single inspection. The ultrasounds injected at a certain position of the structure propagate in the material and can induce heat production at defects located at virtually any positions in the structure. This ability of producing an overall excitation of the part from a single excitation is adequately complemented by the large inspection field provided by IR cameras. However, as will be discussed later on, the actual level of excitation reached at a certain location of the test piece might be greatly affected by the geometry of the part, the coupling between sample and exciter, the clamping conditions and the excitation of mechanical resonances. Furthermore, the need for a contact between the ultrasound exciter and the sample has restrained a wide development of the technique.

As a NDE technique, vibrothermography competes mainly with classical non-destructive testing methods aimed at the detection of surface breaking or slightly subsurface flaws, namely, penetrants testing (PT), magnetic particle testing (MT) and Eddy current testing (ET). PT and MT produce indications that are easy to interpret, but the manual operation is time consuming and PT is limited to non-porous materials and surface breaking defects, which prevents it from being used with composites [24]. ET is very sensitive but is a non-imaging technique that requires highly qualified personnel. As opposed to MT and ET, in which the part needs to be made of a ferromagnetic or electrically conductive material respectively, there is no material restriction to the application of vibrothermography other than the part not being brittle. These advantages put vibrothermography in a good position for composites testing [25], for which ultrasonic testing is the current “gold standard”. Regarding the inspection of metallic parts, vibrothermography has shown better inspection accuracy than PT in Titanium 6-4 and Inconel 718 bars [26]. Actually, it has been recognized as a promising alternative to fluorescent PT in turbine blades [27].

In addition to the mechanical excitation used in vibrothermography, both electromagnetically (inductive) [28-33] and optically [34-39] activated IR thermography are also addressed to detect surface breaking and shallow subsurface defects. The mechanical excitation used in vibrothermography has some advantages and drawbacks with respect to electromagnetic and optical excitations, the choice depending on the application and the inspection circumstances.

In inductive infrared thermography, a coil induces Eddy currents in a skin of material whose depth depends on the current frequency and the electrical and magnetic properties of the material. The Eddy currents, in turn, produce heat. The presence of a flaw disturbs the electric currents in the part: they become denser at the crack boundaries, where heat

dissipation is enhanced with respect to sound areas, and thus affect the surface temperature distribution, which is monitored with an IR camera, with hot spots appearing at the crack tips. The presence of cracks can also affect the heat flow. The technique has been implemented using both, Eddy current bursts [28] and amplitude modulated inductive heating [29].

In principle, inductive thermography needs the material to be electrically conductive so that Eddy currents can be actually established. However, it can also be applied to identify flaws like impact damage in carbon fibre reinforced polymers (CFRP). In this application, the detection relies more on local variation of electric characteristics due to carbon fibre breaking than to mechanical delamination effects [30]. Anyway, a certain degree of electrical conductivity is needed, which prevents the technique from being used with pure electrical insulators. On the other hand, when the test piece is small, it can be surrounded by the induction coil, which induces Eddy currents along the whole lateral surface, allowing a fast evaluation. However, in the inspection of large parts that cannot be placed inside a coil, evaluation of flaws requires scanning the exciting coil along the sample surface, which is time consuming or even unpractical in certain circumstances. This is a significant disadvantage with respect to ultrasound excited thermography, although the contact free character of inductive thermography makes it very attractive for the detection of small surface breaking cracks, especially in ferromagnetic steels [39], where a high current density is confined in a thin skin depth, very close to the surface.

In optically excited infrared thermography [40, 41], a heat flow is established in the sample by illuminating the surface of a (typically) opaque material. The energy absorbed at the surface diffuses inside the sample and is eventually dispersed by defects. This interaction disturbs the surface temperature distribution and its time evolution with respect to a sound material, which enables the detection of defects. The perturbation of the heat diffusion by the defect is stronger the larger both the defect thickness and the effusivity mismatch between the material and the defect [42]. Hence, air filled cracks and delaminations produce larger surface temperature signatures in good thermal conductors than in thermal insulators. Additionally, the wider the air gap the larger the effect on the surface temperature distribution. In this sense, optically excited thermography is complementary to vibrothermography [43]: the signal generation in vibrothermography requires contact between the defect faces so that friction produces heat, so it is better suited to identify kissing cracks or tight delaminations.

The different spatial illumination schemes for optically excited infrared thermography that can be found in the literature are intended to maximize the “heat-defect” interaction, in

order to enhance the surface temperature fingerprint of the defect. Typically, homogeneous illumination is applied to detect planar defects parallel to the surface, such as delaminations, disbonds or impact damage in layered composite structures [35, 44-46], because thermal energy travelling perpendicularly to the sample surface is very efficiently dispersed by this kind of defects. This homogeneous illumination scheme has been implemented by modulating the light intensity (lock-in thermography) [42, 46], using a short light pulse (pulsed thermography) [35, 44-45], or a step function [47] and, more recently, implementing the photothermal imaging radar [48], which allows for the identification of deep structures.

As vibrothermography, optically excited thermography provides large inspection areas, with the advantage of being contactless. However, an intrinsic advantage associated to vibrothermography is a higher penetration potential than thermographic techniques based on optical excitation. The reason for this is that in optically excited thermography the detection of a buried defect involves thermal waves travelling from the specimen surface inwards and outwards: the energy absorbed at the surface penetrates in the material, the propagation is perturbed by the defect and this perturbation reaches the sample surface back. Accordingly, the effects of the presence of the defect are observed at the surface after a “round trip” thermal propagation. In vibrothermography, however, heat is generated at the defect and the observed temperature rise is the result of a “one-way trip”. Therefore, given the diffusive character of heat propagation, vibrothermography enables detection of deeper defects.

The homogeneous illumination scheme described above is quite inefficient to detect vertical cracks, i.e., cracks contained in a plane that is perpendicular to the measuring surface, since these barely perturb heat propagation perpendicular to the sample surface. In such situations, point or line focusing of the excitation beam is much more appropriate: when the laser beam illuminates the sample surface on one side of a vertical crack, the crack acts as a thermal resistance that hinders heat propagation, producing an asymmetry in the surface temperature distribution. The flying spot technique introduced in the nineties exploited this idea by scanning a continuous laser beam onto the sample surface and registering the surface temperature with an infrared camera [49-51]. Further developments were implemented using modulated [52] and pulsed [53-55] illumination. Once the presence of a crack has been identified, the characterization can be performed by illuminating one side of the crack with a static beam and analysing the asymmetry of the surface temperature distribution across the crack [56-60]. Using this approach, the width of artificial infinite cracks has been characterized in AISI 304 stainless steel down to 1 μm

using both modulated [58] and pulsed [60] excitations. However, this approach has only been applied to date to detect and characterize surface breaking cracks, whereas vibrothermography is able to detect buried vertical cracks as long as the surface temperature rise is above the noise level of the experiment.

As mentioned above, a further advantage of vibrothermography over other thermographic techniques, especially in metals, is that under ultrasonic excitation the defect turns into a heat source on a cold environment, whereas in optically and electromagnetically excited thermography the defect just represents a perturbation on an existing temperature field, generated by the absorbed light and the Eddy currents, respectively.

1.2 Principles of ultrasound excited thermography

1.2.1 Equipment

The experimental setup typically used in a vibrothermography experiment is depicted in Figure 1.1. The main components are an ultrasound system to excite the sample and an IR camera to register the evolution of the surface temperature distribution of the sample surface. A clamping system and control electronics complete the set-up.

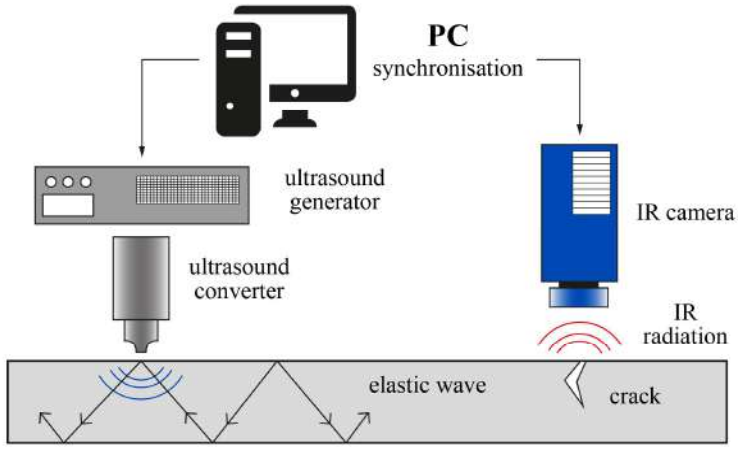

Figure 1.1. Diagram of a typical experimental setup for vibrothermography experiments.

As for the ultrasound system, the vibrations are typically generated by means of an ultrasonic welder, consisting of a high power ultrasound generator that creates high frequency electrical oscillations that are transformed into mechanical oscillations by an ultrasound stack converter. This is made up of a piezoelectric transducer, an optional vibration booster and a horn or sonotrode that is brought into mechanical contact with the test piece in order to induce elastic waves that propagate inside its structure. The three elements in the converter are designed to have the same ultrasonic resonance frequency, typically, 20 or 40 kHz. The ultrasound generator, usually in the 2-4 kW range, delivers an AC signal matching the resonance frequency of the stack and the system works at a fixed or slightly tuneable frequency.

Tuneable ultrasound generators are nowadays used in vibrothermography experiments, which provide a range of ultrasound frequencies typically between 15-25 kHz but with an efficiency curve that decays away from the resonance of the converter. Alternatively, a piezoelectric stack driven by a power amplifier fed by a waveform generator can be used to produce reasonable broad band output [61]. In standard setups, the converter is pressed against the part with a static force, so that the ultrasonic vibration is efficiently transmitted to the test piece. This is usually achieved either with a pneumatic system [62], spring loading [63], or pressing the horn against the part with a screw [20]. In portable systems, the horn is hand-held and manually pressed against the structure [25].

In order for the excitation to be fruitful, the vibration produced at the converter needs to be efficiently injected into the part. Since the incident ultrasonic wave is split at the boundary into a reflected and a transmitted wave, the mechanical impedance mismatch between the sonotrode and the test piece that hinders acoustic energy coupling can be reduced by placing in between a thin layer of a coupling material with an intermediate impedance, in order to improve ultrasound transmission. The optimum choice is the material whose impedance matches the geometric mean $Z = \sqrt{Z_1 Z_2}$, being Z_1 and Z_2 the mechanical impedance of the sonotrode and the part to be inspected, respectively. The effect of the coupling material has been proven to be very significant in the achieved vibrothermographic signal [65]. Another purpose of the coupling material is to prevent damage of the sonotrode on the sample surface, especially in polymers and composites. Typical coupling materials are duct tape [65], aluminium film [66], paper and plastic [3], or Cu sheets [7]. Whereas the excited sample tends to vibrate at the transducer's frequency, the oscillations of its internal structure are permanently damped. Attenuation is mainly caused by friction at every support and contact interface such as screw connections, in addition to inherent material damping.

With regard to the other main component of the experimental setup for vibrothermography experiments, the IR camera, nowadays, full-field temperature measurements are mostly based on two types of infrared cameras, both equipped with focal plane array detectors: the microbolometer cameras and the quantum detector cameras. On the one hand, quantum detector cameras are generally faster and provide a higher thermal sensitivity as well as a greater array size, but on the other hand, are much more expensive and they need from detector cooling, which involves maintenance of the coolant system after a certain number of operating hours.

In most laboratory tests, cooled semiconductor focal plane array cameras are used to follow the evolution of the surface temperature, with *noise equivalent temperature differences (NETD)* of around 20 mK. However, with the aim of extending the technique to out of laboratory industrial environments, portable systems have been designed that work with smaller and lighter uncooled microbolometer focal plane array cameras. The lower performance of these cameras (NETD of 80 mK in ref. [25]) can be compensated for by applying further image processing in addition to the standard background subtraction, such as low pass and salt and pepper noise filtering, clipping, i.e. setting to zero all pixels whose signal is below a certain value related to the standard deviation of the noise level, and integrating images obtained during the excitation [25].

Finally, by means of a computer, the ultrasound generator can be controlled and vibrothermography data are recorded. Besides, synchronisation between ultrasound generation and camera operation is performed in order to allow for reproducible test procedures.

In addition to the standard equipment described above, in many laboratory studies and in some new portable systems, vibrothermography experiments are complemented with measurements of the vibration of certain points of the specimen surface [18, 67], or of the relative motion of the crack lips [68]. In some cases even the whole specimen surface vibration is monitored to check vibration coverage [69]. These measurements are driven by means of laser vibrometres [18, 67-69] that measure the part surface velocity parallel to the laser beam, with strain gauges [17], or with microphones [25].

1.2.2 Excitation regimes

Coming to the excitation temporal regimes, vibrothermography has been implemented in basically two schemes: burst and amplitude modulated or lock-in.

In burst vibrothermography, a short ultrasound pulse (typically from some tens of milliseconds to some seconds) of constant amplitude is applied to the specimen and the evolution of the surface temperature distribution of the sample surface is registered with an infrared camera during and after the excitation. The main advantage of the burst approach is that the experiment is very fast, as the data acquisition takes at most a few seconds. The presence of the defect can be evaluated in the raw image sequence or, alternatively, a pulsed phase thermography analysis [35] can be conducted, in which the signal at each pixel is transformed from time domain to frequency domain via the one-dimensional Discrete Fourier Transform (DFT) to extract amplitude and phase at any of the frequencies contained in the burst, which de-noises the data. Phase images are especially interesting as they are less affected than amplitude by emissivity variations, surface orientation and environmental reflections.

In lock-in vibrothermography, the amplitude of the ultrasounds is modulated at a frequency $f_{lock\text{-}in}$ (much lower than the ultrasound frequency, f_{US}) typically from some mHz to a few Hz. This gives rise to a periodic heat deposition at the defect and thus to the production of thermal waves. The oscillating component (at frequency $f_{lock\text{-}in}$) of the surface temperature at each pixel is evaluated and averaged over a certain number of periods and amplitude and phase lag images are generated. The key advantage of the lock-in approach is that due to this averaging nature, it provides a very efficient filtering of the signal at $f_{lock\text{-}in}$ that can reduce the average noise in amplitude images, $\langle T_{noise} \rangle$, well below the noise equivalent temperature difference (NETD) of the camera, depending on the number of images analysed [41]

$$\langle T_{noise} \rangle = \frac{2}{\sqrt{N_{images}}} \mathrm{NETD} \tag{1.1}$$

The lock-in technique, thus, can extract signals that are embedded in noise being orders of magnitude above the signal level as long as they are periodic, by analysing a high number of images. For instance, using an IR camera with a NETD = 20 mK, the average noise level in amplitude is reduced below 1 mK by analysing 2,000 images.

The drawback is that data acquisition takes longer than in the burst regime, as several periods need to be analysed and only one modulation frequency is proved at a time. In order to gain some insight on the depth of the defect, several measurements at different modulation frequencies are usually conducted, which further prolong the experiments. However, noise reduction allows using relatively low ultrasound powers, which is beneficial for the reproducibility of the experiments and also to avoid damaging the sample [70].

In Figure 1.2 (a), the waveforms for ultrasound excitation in both burst and lock-in regimes are represented. However, in both regimes, the ultrasound frequency can be fixed or it can be modulated within the tuning range of the equipment, which is sometimes called *wobbulation* (see Figure 1.2 (b)). Given that it is not possible to know beforehand the right ultrasound frequency that will excite each defect in the specimen, in this way, the excitation covers a certain range of frequencies in order to maximize the probability of detecting defects in the test part. However, care has to be taken not to perform the frequency sweep too fast, so that a too low energy is deposited at the appropriate frequency to excite the defects.

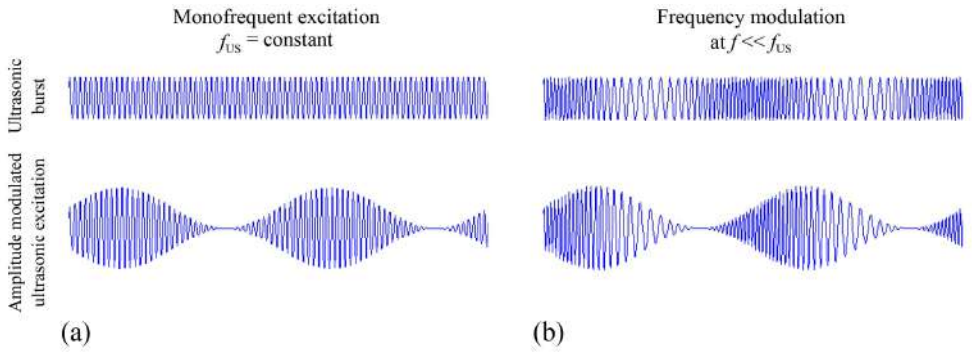

Figure 1.2. Monofrequent (a) and frequency modulated (b) excitation in burst (top) and lock-in (bottom) regimes.

A further usefulness of wobbulation is the suppression of standing waves in the specimen, since resonant excitation forms stationary vibration nodes and antinodes that in turn enhance or hinder the detection of defects in the material, respectively. This issue will be discussed later on.

1.2.3 Mechanisms of heat generation

Ultrasound excited thermography relies on the principle that defected areas are sources of mechanical damping, generating heat. If the material damping is low, as in the case of metals, heat production occurs primarily at defects, so vibrothermography provides a defect selective dark field method for flaw detection. In addition to defective areas, bulk heating can also be produced in lossy media such as viscoelastic polymers and composites, in which case, the technique is not background free. Thermoelastic effects due to sinusoidally stress-induced heating and cooling cycles occur in vibrothermography experiments in the kHz range, and are averaged out by the integration time of the IR camera typically covering several vibration periods, so in this technique they cannot be resolved.

The determination of the mechanisms that produce heat in the specimen in a vibrothermography experiment is a primary question that has been matter of intensive research [3, 70-76]. Although the most extended idea is that friction is mainly responsible for crack heating in metals, some authors have argued that the elastoplasticity in the vicinity of the crack tip is the cause for heat generation in cracks [75]. Nowadays, three physical phenomena are acknowledged to be responsible for the heat production [3]: friction between the defect faces, material damping and, in the case of cracks, plastic deformation at the crack tips.

The contribution of rubbing or clapping friction to vibrothermographic signals has been demonstrated in several studies on cracked metallic beams, showing that heat production at a given crack can be modified by applying opening and closure stresses. Lu et al. showed that heat production at the crack can be almost terminated by locking crack asperities under an external compression stress [73]. Renshaw et al. [74] and Weekes et al. [43] applied opening stresses to surface breaking cracks in Titanium and austenitic Nickel super-alloy beams, respectively, and showed that regions of heat production moved towards the crack tips as the opening stress was increased, eventually terminating heat production when the crack was completely open [74]. This provides evidence of heat production at the crack due to rubbing of contacting crack asperities under low stress. A further evidence of frictional heating is the appearance of crack surface alterations, such as micromachining and fretting damage due to friction between crack faces [3, 70].

When a purely elastic material is subjected to a cyclic uniaxial stress, time varying stress and strain are in phase and the stress-strain curve is a straight line enclosing a zero area (see Figure 1.3 (a)). At small strain levels, the behaviour of metals does not deviate much from linear elasticity. As mentioned above, thermoelasticity of the material produces cyclic

temperature oscillations that are averaged out in vibrothermography experiments by the integration time of the camera.

In a more realistic case, the viscoelasticity of the material gives rise to a phase shift between oscillating stress and strain (loss angle). In this case, the stress-strain diagram shows the elliptical shape depicted in Figure 1.3 (b), featuring hysteresis. The thermal energy released per loading cycle is represented by the area enclosed in the ellipse and is proportional to the squared strain [71]. This viscoelastic behaviour is usually referred to as material damping and produces a bulk heating in the part. The heating increases with ultrasound frequency, since more cycles take place per unit time.

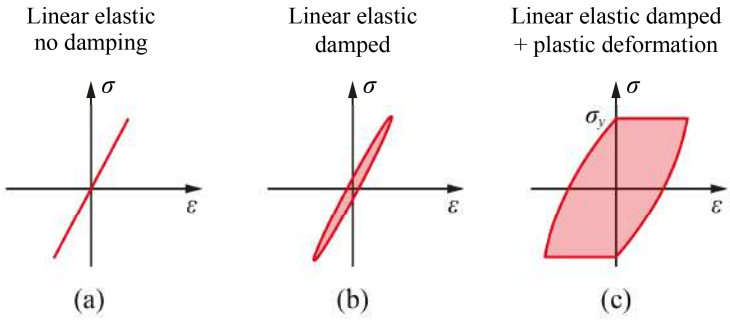

Figure 1.3. Schematic stress-strain diagrams for different material behaviours.

Examples of bulk heating caused by material damping are usually given in polymers [71] or composites [64], as viscoelastic effects are stronger than in metals. Material damping produces additional localized heating in regions of stress concentration [71].

Bulk heating due to viscoelasticity of polymers and composites can produce a deleterious effect, reducing the contrast of the signal generated at the defect. The signals generated by typical composite flaws such as delamination created by impact damage are believed to be due to frictional rubbing or clapping of delamination surfaces [11]. Besides, if the part is excited at a single ultrasound frequency that matches a resonance frequency of the structure in the clamping conditions, a standing wave pattern arises. Due to viscoelasticity, the standing wave gives rise to a temperature pattern (that is superimposed to the signal coming from the defect), in which a hot anti-node can be mistaken with a defect. On the other hand, defects located at nodes of the standing wave pattern do not vibrate and thus do not produce heat, being likely to be missed [62]. Close to nodal points, the vibration amplitude may not be high enough to activate the defect. As mentioned before, this effect can be overcome by performing frequency sweeps or by modulating the ultrasound

frequency during both lock-in or burst excitations [13]. The generation of standing waves, however, has been exploited to measure the thermal diffusivity of sound viscoelastic materials [77].

Back to the different material behaviours, if higher stresses are applied on the material reaching the yield stress, plastic deformation can occur. The stress-strain curve exhibits then the aspect shown in Figure 1.3 (c), with an enclosed area that grows linearly with the strain, as the stress is limited to the yield stress. Such large stresses are likely to be present at crack tips rather than in sound areas and, since no stress higher than the yield stress can occur in the material, a plastic zone appears beyond the crack tips [71]. The heating due to plasticity can be distinguished from viscoelasticity since for the generation of the former, a stress threshold needs to be exceeded. This takes place at specific locations of the specimen, as opposed to the bulk heating occurring everywhere in the sample due to viscoelasticity. Renshaw et al. [3] also showed evidence of heat production beyond the crack tips of a growing crack excited by high vibrational stress in an aluminium specimen. The heat production was attributed to plastic deformation in the plastic zone of the propagating crack. Other works by Mabrouki et al. [78, 79] presented coupled thermomechanical analyses of heat generation at cracks on steel and aluminium bars considering frictional heating of the crack surfaces [78] and dissipation due to plasticity on the crack faces [79].

In summary, under moderate vibration stresses, frictional heating of defect faces seems to be the dominant mechanism of heat generation in cracked metals. In polymers and composites, frictional heating of impact damaged delamination-type defects coexists with bulk viscoelastic heating due to material damping.

1.2.4 Enhancement of the vibrothermographic signal

Defect heating is known to be strongly dependent on ultrasound frequency in metallic parts. When a frequency sweep is performed in a cracked metallic specimen the surface temperature rise on top of a crack (vibrothermography spectrum) shows sharp peaks, which leads to the assumption that resonant excitation is required in the inspection of metallic parts. Resonant excitation produces standing waves also in metals, but is generally not accompanied by a measurable thermal pattern like in polymer based materials, because the material damping is very low. The excitation at one of these structural resonances produces large vibration amplitudes in the structure that can be used to excite defects.

In laboratory studies, standing waves are actually used to efficiently excite cracks generated on purpose at specific locations and selecting the ultrasound frequencies for which the crack location corresponds (or is close) to an anti-nodal point of the structure in the clamping conditions [80]. However, Renshaw and coworkers demonstrated, using viscous material (honey) filled holes in a Titanium beam that, if the filled hole is located at a nodal position, no heating of the viscous material is produced [81]. The low acoustic damping in metals is also advantageous, as the induced vibration keeps significant amplitude along large distances from the excitation point [82].

Plum and Ummenhofer further showed that the ultrasound frequencies at which vibrothermography peaks appear in metals and their corresponding intensities significantly depend on the particular location of the exciter on the sample [82]. The authors argued that a different configuration results in different natural frequencies and therefore different mode shapes. Accordingly, if a single frequency propagates in the metal, the defect will not be activated unless it matches one of the peaks. In composites and polymers, the peaks are broader due to a lower acoustic quality [62], which is beneficial because the particular ultrasound frequency is not so decisive to find or miss the defect.

There is little work published on the frequency dependence of the vibrothermographic signal in metals. Rothenfusser and Homma used laser vibrometry to analyse the behaviour of various cracks [83] and they identified three principal crack modes leading to heat production, sketched in Figure 1.4: mode I describes the tensile opening (clapping) and modes II and III represent the in-plane (sliding) and out-of-plane shear (tearing). If both crack faces move in unison, there is very little relative motion and heat production is very low.

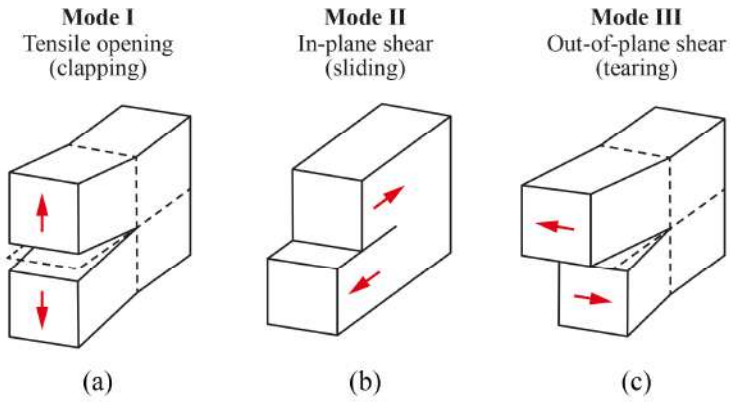

Figure 1.4. Vibration modes considered for crack heating.

Plum and coworkers [82] performed a modal finite element analysis of the cracked test piece (a 10 mm thick low carbon steel plate) and showed that all three crack modes were excited in their experiment. Performing measurements of the vibration amplitude of mode III at both sides of the crack during a frequency sweep, they could identify some of the crack heating peaks as frequencies that gave maximum mode III relative velocity between the two crack faces and thus producing maximum frictional heat. In a later work [84], the same authors presented a finite element analysis that takes into account crack surface asperities and that is able to account for experimentally observed frequency dependent and non-uniform crack heating. Further work is needed to fully understand the frequency dependence of crack heating in metals.

1.2.4.1 Generation of *acoustic chaos*

Despite the evidences of the ultrasound frequency dependence of the vibrothermographic signal in metallic parts mentioned above, soon after the renaissance of vibrothermography in the late nineties, it was acknowledged that, when exciting the specimen at a fixed ultrasound frequency typically generated with a non-tuneable ultrasonic welder vibrating at 20 or 40 kHz (beyond hearing capability), a significant enhancement of the vibrothermographic signal could be achieved under certain experimental circumstances [67, 85]. The enhancement of the IR signal was related to the presence of an audible "screech", attributed by the authors to nonlinearities in the coupling between the excitation source and the sample.

The experimental results of the first analysis of this evidence, conducted by Han et al. [67], showed an evolution in the frequency content of the sample (a Titanium specimen excited with a 500 ms burst at 40 kHz) during the excitation, that can be summarized as the random appearance of a large number of discrete frequency components (both multiples and fractions (plus harmonics) of the fundamental frequency), coinciding with the beginning of the audible "screech" and a significant enhancement of the IR signal produced at the cracks. This behaviour was described as a quasi-chaotic excitation, whose origin was attributed to the recoil of the excitation gun, which resulted in a series of impulses, rather than in a harmonic excitation of the sample.

In further work, Han et al. [86] introduced an analytical mechanical model that was able to explain this so-called acoustic chaos in the vibration of the gun in contact with a rigid wall representing an uncracked specimen. The generation of fractional subharmonics is explained by the gun bouncing on the specimen, with different heights in subsequent

rebounds, which produce random fluctuations in the frequency of the bounces. In a subsequent study [87], a finite element model of an uncracked sample bouncing between the gun and a rigid substrate on one end and clamped at the other end, seemed to confirm bouncing as the primary mechanism for generating vibration subharmonics and the corresponding family of harmonics, even in the absence of flaws in the sample. The model also describes the spontaneous switching between subharmonics (and the corresponding ultrasubharmonics) during excitation, characterizing the acoustic chaos.

The same group showed, using a finite element modeling of a cracked sample [88], that chaotic vibrations in the sample can explain the enhanced defect heating (if compared to non-chaotic excitation at similar excitation powers) due to a greater differential motion of the crack surfaces, which was attributed to the shorter wavelength of high frequency components and to the presence of a large density of such high frequencies in the chaotic regime. The generation of chaotic sound has been shown to be quite unpredictable and extremely sensitive to the engaging force applied on the specimen [89, 90] and the coupling material [91, 92].

The presence of subharmonics and ultrasubharmonics has also been observed by Solodov and coworkers, both in the MHz range in surface acoustic waves [93] and in the kHz range [94], which were attributed by the authors to nonlinear effects (contact acoustic nonlinearity [95]) associated to the presence of a crack. Furthermore, the same authors [96] argued that both subharmonics oscillations and self-modulation (wave interaction) are produced locally in the damaged area, due to the nonlinear acoustic response of the flaws. They modelled the defected area as a nonlinear oscillator exhibiting both resonance (the so-called *local defect resonance*) and nonlinear properties, and showed that when the driving frequency corresponds to the sum of two normal mode frequencies of the defected area, the pair of resonance frequencies grows in amplitude. According to their analysis, the nonlinear forces provide frequency mixing, leading to new frequency components. Further analysis of the nonlinear contribution of local defect resonances can be found in [97].

1.2.4.2 Local defect resonance and nonlinear effects at the defects

The existence of acoustic resonances that activate defects in vibrothermography experiments has been the subject of recent research. Solodov et al. [98] provided a physical interpretation of the local defect resonance (LDR). According to their description, the presence of a defect results in a reduced stiffness for a certain mass of material around the

defect, which is characterized by a resonance frequency. When the sample is vibrated at the resonance frequency of the defect, the resonance provides an efficient energy transfer mechanism from the wave to the defect. These local resonances are different from structural resonances mentioned at the beginning of section 1.2.4.

Experimental evidences of defect resonances have been given mainly in polymers and composites, such as a glass fibre-reinforced composite plate containing a horizontal delamination [99]. When exciting the sample at the defect resonance, a strong enhancement of the out-of-plane vibration amplitude is locally observed at the defect area, together with an enhancement of the vibrothermographic signal, if compared with excitation at a resonance frequency of the specimen. According to the authors, his enhancement of the thermographic signal is related to a combination of a higher amplitude of vibration and a clapping mechanism in the delamination that produce a significantly larger amount of heat than the surrounding sound areas. This efficient resonant excitation of the defect provides the opportunity of using much lower excitation powers than those usually applied with ultrasound welders, just exciting the sample with conventional piezoceramic transducers [100, 101]. LDR has been further exploited by implementing remote ultrasound excited thermography using *Air Coupled Ultrasound (ACU)* excitation [100]: flat-bottomed holes in a PMMA plate and also impact damage in a multi-ply CFRP have been detected with the transducer located in front of the defect area, just a few centimetres away from it. In both cases, the fundamental frequencies of the ACU transducers, about 50 and 70 kHz, respectively, matched the LDR frequencies of the defects.

In a further attempt to optimize the excitation of defects, Rahammer and coworkers [102] have recently proposed a system to achieve directional guiding of plate waves by placing two wires between the excitation source and the specimen. The constructive interference of the plate waves generated by each source resulted in an enhancement of the total plate wave amplitude perpendicular to the lines and in a plane wave pattern. Vibrothermography signals reported using guided waves show an enhancement of the signal similar to an increase of 25% of the input power.

In parallel to these developments, non-contact vibrothermography has been explored by other groups without making use of LDR. Zalameda and coworkers [103] presented a system in which acoustic waves in the 800 to 2000 Hz range were injected in the test specimen by means of loudspeakers located about 11 cm away from the sample. Authors were able to identify ballistic and fabricated damage on a sandwich honeycomb structure. More recently, Sathish and coworkers [104] used a conventional high amplitude ultrasound generator at 20 kHz with a maximum output power of 1 kW located at a distance of 200-

300 μm from the sample surface to assess heat damage in carbon fibre reinforced epoxy and to detect cracks in an aluminium wheel component.

Although extremely attractive due to the possibility of using low power and/or contact free excitation, LDR excitation of the defects requires previous knowledge of the defect resonance frequency, which is unlike to be known beforehand. Furthermore, in the studies published so far for air coupled ultrasounds, knowledge of the location of the defect is also required as the transducer needs to be located close to it. Besides, little experimental evidence and analysis of LDR has been given in cracked metals [105]. Further work is needed to investigate eventual relationships between LDR in metals and the sharp peaks appearing in vibrothermography spectra typical of cracked metallic samples.

1.3 Detectability of cracks and reproducibility of experiments

The detectability of a crack in a vibrothermography experiment is a complex function of many parameters. It depends on the amount of heat released at the crack, its depth and the thermal properties of the material. The heat released at the defect depends on the defect size and on the crack lips relative motion, which, in turn, is dependent on the crack closure state and vibration pattern induced in the specimen, and increases with both vibration amplitude and frequency. The vibration pattern depends on the exciter location, clamping conditions, coupling material, geometry of the part, etc. These complex interdependences make it difficult to determine a probability of detection of cracks only based on the crack size.

One of the key points for vibrothermography to become a fully accepted technique for non-destructive evaluation is the determination of the minimum strain needed to detect a crack and the identification of the minimum detectable crack size. Experimental data provided by Barden et al. [106] on the relationship between temperature rise and strain amplitude on a cracked nickel superalloy showed an offset, indicating the existence of a strain threshold that needs to be exceeded for the crack to heat up. Rothenfusser and Homma [83] gave further evidence of the existence of a threshold by measuring the relationship between temperature rise and velocity amplitude at the same location. They argued that either the crack asperities were locked, in which case an activation energy was necessary, or the

crack width was similar to the oscillation amplitude and thus a certain amplitude needed to be reached to get the crack faces into contact.

The study of the relationship between crack heating, vibration and crack size has been addressed by several groups. Holland et al. [18] published an experimental study in which a breathing mode in surface breaking half-penny cracks was produced and the longitudinal stress amplitude normal to the crack surface was derived from the velocities measured with a laser vibrometre. The displayed data on crack heating for different crack sizes and dynamic stresses are in agreement with the proposed model, in which they consider friction between crack asperities as the main mechanism to produce heat in the opening/closing mode of the crack. Morbidini et al. [17] tried to establish a relationship between the vibration strain and the temperature rise at the crack mouth. In a further work [63], authors evaluated the strain required at a single ultrasound frequency (40 kHz) to produce a temperature rise close to the resolution limit of the IR camera, under a constant excitation power for a given excitation time in mild steel beams containing cracks between 1 and 5 mm long. The results showed that strains between 85 με (for 1 mm long cracks) and 375 με (for 5 mm long cracks) were needed to produce temperature rises of 0.1 K at the crack mouth. However, when exciting at these estimated strain levels, the temperature rises where higher than expected, which was attributed to the presence of more frequency components due to nonlinear excitation.

With the aim of improving the reliability of vibrothermography, in 2009, Morbidini and Cawley proposed a calibration method for vibrothermography experiments [107]. They introduced the so-called *heating index*, that is a measure of the ability of the vibration field to generate heat at defects. Authors presented results of the maximum temperature rise versus maximum value of the heating index, that show a consistent linear behaviour with no apparent threshold other than the one imposed by the sensitivity of the camera. The slopes of these straight lines represent a *sonic IR efficiency*. In the calibration procedure, tests are conducted in different specimens containing cracks of different sizes. The sonic IR efficiency is then computed for each crack size and the resulting quadratic curve is fitted to a 2^{nd} order polynomial that is used as the main calibration curve, as it represents the temperature rise per heating index that can be expected for each crack size in a real experiment. In a real test, the maximum heating index has to be measured and compared to the threshold heating index: if this threshold is exceeded, the test is considered valid and if no temperature rises are observed in the post-processing, the specimen is classified as uncracked.

It is evident, from the analyses described above, that an evaluation of the vibration induced in the specimen is essential to determine whether a defect at a given position will be exposed to a high enough vibrational strain to be activated in a vibrothermography experiment. Holland and co-workers [69] introduced a methodology to evaluate internal dynamic stresses-strain state of a vibrating solid. The authors applied the method to measure internal stresses in a metallic beam oscillating in a flexural mode and the results agreed with predictions given by flexural wave theory. In a recent work, researchers of the same group [108] proposed the use of a viscoelastic coating on a metallic part to evaluate the vibration strain distribution from the temperature rise map of the polymer adhesive. The method provides full vibration coverage in a vibrothermography test. The proposed method is more efficient than laser velocimetry used in reference [69] by the same authors, as the later requires scanning the entire specimen surface with three laser vibrometres in order to get the full 3D vibration field. Also, high frequency microphones have also been used to measure the vibration strain field [25].

The improvement of crack detectability has also been addressed by several groups, mainly using post-processing techniques, such as the matched filter technique that Li and coworkers [109] proposed to improve the signal-to-noise ratio and thus enhance the probability of detection. In a subsequent work [110], Holland introduced a rather sophisticated algorithm in which the image sequence was reduced to a single static plot with improved sensitivity, that helps identifying the presence of flaws. Other efforts have been made to optimize experimental parameters in turbine disks inspections [111, 112] and to estimate a probability of detection in particular types of specimens such as aircraft engine turbine blades [113].

The vibration coverage data presented in several works [69, 81, 108] indicate that at the specimen resonances usually used in vibrothermography experiments, the vibration strain is uneven, maximum at antinodes and minimum at nodes, as mentioned in section 1.2.3. This indicates that, in order to determine a probability of detection, not only the crack size, but also the crack position and orientation should be taken into account, together with the crack closure state. Despite the difficulty of this ultimate goal, some efforts have been devoted to achieving full description of vibrothermography experiments and prediction of vibrothermographic signals. Guo [114] presented a combined mechanical and thermal analytical model to predict the surface temperature evolution during the excitation of the crack. Recently, Holland and co-workers [115] presented a model that combines a computational vibration modelling, an empirical crack heating model and a computational heat flow model to predict surface temperature rise of cracks in a given specimen. The

specimen geometry, mounting and excitation parameters are fed into the vibration model stage. The resulting vibrations enter the empirical crack heating model that, in turn, predicts heat generation taking into account the vibrations, the relative mobility of crack surfaces and the crack closure state. Finally, a computational heat propagation model is used to predict surface temperature.

Regarding the reproducibility of experiments, there is not much research published on the effect of repeated ultrasound excitation on crack heating. Homma et al. [71] and Renshaw et al. [70] performed repeated vibrothermography experiments on turbine blades and titanium bars, respectively. Homma et al. found a signal decrease in subsequent excitations, and Renshaw et al. concluded that the application of large stresses to fracture surfaces can alter the crack surface as plastic deformation, fretting, adhesive wear oxidation, phase transformation and melting were observed, which can lead to reduced heat production in subsequent experiments. Evidences of crack growing in vibrothermography experiments under high vibrational stresses [3] together with the evidence of crack surface damage mentioned above, suggests that moderate vibrational stresses, below 20% of the materials endurance limit [70], should be used in vibrothermography experiments to guarantee the nondestructive character and the repeatability of the technique.

1.4 Characterization of vertical cracks and objectives of this thesis

The preceding sections summarize the efforts made by researchers to gain knowledge of the heating mechanisms in ultrasound excited thermography and to improve flaw detectability and experiments reliability that are necessary to expand the use of this technology in real nondestructive testing applications.

The step beyond detection is characterization, i.e., the determination of geometrical parameters of the defect such as size, shape and depth from vibrothermography experiments. The characterization of delaminations typically resulting from impact damage in polymer based composites has been addressed using both in lock-in [116] and burst [117] vibrothermography with the aim of identifying the depth of delaminations. Optically excited thermography is quite efficient to detect this kind of defects and several processing techniques such as thermographic signal reconstruction [118] or pulsed phase thermography [35] can be efficiently applied to characterize delaminations.

On the contrary, kissing vertical cracks, which are quite elusive to other nondestructive testing methods, are target flaws for vibrothermography and crack characterization has been the subject of recent research [119-124]. *This thesis is aimed at exploiting the ability of lock-in vibrothermography to characterize buried vertical cracks.*

The "cause-to-consequence" relationship, i.e., the calculation of the surface temperature distribution caused by a certain crack, is the so-called *direct problem*. The *inverse problem* consists in retrieving the cause (the crack geometry). However, since the measured magnitude is surface temperature, what is physically accessible from vibrothermography data is the heat source distribution responsible for it, rather than the crack geometry itself. The region that contains the heat sources and the crack geometry may coincide in the case of kissing cracks for vibrational stresses that induce heat production all along the crack surface [83], but in open cracks heat is more likely to be produced only in part of crack [74,83]. Given a certain level of crack heating, the surface temperature rise that is measured in vibrothermography experiments is governed by heat diffusion. The diffusive nature of heat propagation and the fact that temperature data can only be measured at the surface and are not available at heat production sites (buried below the surface), makes the general problem of retrieving the geometry of the heat source distribution an ill-posed inverse problem, which results in arbitrarily small errors in the data yielding arbitrarily large differences in the solution.

In this kind of problems, regular least-square minimization does not give satisfactory results because the minimization does not converge. The ill-posedness of the inverse problem can be addressed using more sophisticated inversion procedures that involve regularization of the inversion. These minimization techniques can be classified into two groups: global methods and local methods.

Global methods such as neural networks [125], genetic algorithms [126] or particle swarm optimization [127], require many evaluations of the objective function, which is time consuming, but are efficient at identifying the global minimum. Local methods [128, 129] such as the conjugate gradient method, on the contrary, start from one set of parameter values and modify them to look for the minimum residue. This is computationally cheaper and allows a more accurate estimation of the parameters, but local methods risk getting trapped in local (instead of global) minima.

On the other hand, the degree of ill-posedness of the inverse problem increases with the number of unknowns. Accordingly, instead of tackling a general inverse problem, a possible strategy consists in reducing the number of unknowns (for instance, by assuming a

certain shape of the heat source [123]) to diminish or even remove the ill-posedness of the inverse problem. Of course, this approach lacks generality as only heat sources of a given shape can be characterized accurately.

The first objective of this thesis is to implement a robust inversion algorithm, based on stabilized least squares minimization, in order to retrieve vertical buried heat source distributions of any geometry from lock-in vibrothermography data. Thus, our approach to characterize inner heat source distributions from vibrothermography data involves the fitting of the data to the result of a semi-analytical model that describes the propagation of the thermal waves generated at the defects. The treatment is purely thermal, as we leave aside the heat generation mechanisms at the defects.

An analysis of the implemented inversion algorithm will be carried out as well inverting synthetic data, aimed at optimizing the inversion algorithm so as to expand its application to the widest range of heat source geometries and gain accuracy in the reconstructions providing quantitative information of the buried defects.

Experimental verification is necessary in order to prove the potential of the inversion algorithm to characterize vertical heat sources from real experimental data, with the ultimate goal of implementing it in the characterization of cracks in real applications. Thus, *the second objective of this thesis is to verify the results of the inversion algorithm with experimental instead of synthetic data, obtained from vibrothermography experiments performed in the lock-in regime, using both samples with calibrated heat sources and real samples with inner defects.*

This thesis is composed of nine sections, including this introductory section, and it is organised as follows:

Section 2 provides theoretical background regarding thermal radiation and heat conduction, as they represent the basis of the direct problem of this thesis, and also about inverse problems, focusing on the key aspects that will be needed further on for the statement, resolution and analysis of our inverse problem. The treatment of ill-posed inverse problems is addressed.

Section 3 states and solves the direct problem of this thesis. The solution is then analysed by performing simulations for homogeneous square heat sources, with the aim of observing the impact of varying the geometrical parameters of the heat sources on the surface temperature distribution. The frequency dependence of the surface temperature amplitude and phase is checked and, lastly, other geometries are also considered to check the ability

of vibrothermography to distinguish between the particular features of heat sources of different geometry.

Section 4 describes the experimental setup for the performance of vibrothermography experiments in the lock-in regime using samples containing vertical calibrated heat sources, focusing on the equipment used and the construction of the samples. For the verification of the direct problem, experimental data are analysed, the frequency response of the equipment is characterized and different methods for the elimination of the contribution of the transient temperature rise of the sample on surface temperature data are proposed. Finally, the optimum experimental conditions for data acquisition are settled.

Section 5 addresses the inverse problem of this thesis. First, the inverse problem is stated and its ill-posed nature is analysed. Then, regularization procedures together with a minimization process based on a local method are proposed in order to implement a robust inversion algorithm, capable of retrieving heat source distributions from vibrothermography data. Lastly, the inversion algorithm is described in detail.

Section 6 analyses the ability of the inversion algorithm to retrieve heat source distributions by inverting synthetic data generated for heat sources representing homogeneous vertical kissing cracks of square/rectangular geometry. After describing the generation of synthetic data, the effects of various aspects regarding both the inversion algorithm and the data entering it on the reconstructions are analysed. The optimum inversion protocol is then defined, the convergence property of the inversion algorithm is shown and the use of multi-frequency data, as well as the experimental design, are verified. In order to evaluate quantitatively the quality of the retrieved heat source distributions, an “accurate reconstruction criterion” is defined and, in addition, the spatial resolution of the inversion algorithm is tested and the situations where the shadowing effect arises in the reconstructions are identified.

In section 7 we present assessment of the behaviour of the inversion algorithm when retrieving heat source distributions of geometries other than square/rectangular. The performance of the inversion algorithm to recover the particular features of the different geometries for kissing heat sources is checked, the robustness of the algorithm against noise is shown and, in order to approach situations arising in experiments with real cracks, open heat sources representing surface breaking open cracks of different geometries are also considered. In addition, we tackle the qualitative recovery of inhomogeneous heat fluxes, for both kissing and open heat sources.

Section 8 verifies experimentally the potential of the inversion algorithm to characterize vertical heat sources. To this purpose, we check the predictions from synthetic data by inverting data obtained in vibrothermography experiments using samples with calibrated heat sources representing both homogeneous vertical kissing and open cracks of different geometries. Heat sources of arbitrary orientation and shape are considered in order to prove that any geometry can be accurately retrieved with the inversion algorithm. In addition, for semicircular and triangular open heat sources, inhomogeneous fluxes are produced in the experiments. Finally, in order to prove that the inversion algorithm can be extended to real applications, vibrothermography experiments are performed using a welded Inconel 718 sample with real instead of calibrated defects, and the defects found are characterized.

Section 9 summarizes the conclusions drawn from this thesis and points out future research.

Finally, a list of publications resulting from this thesis is presented.

2 Theoretical background

This section provides theoretical background regarding thermal emission and heat conduction, which is fundamental for the comprehension of the direct problem in this thesis. Similarly, inverse problems are introduced in a general and theoretical way, addressing the key points that play a role for the further statement, resolution and analysis of the inverse problem in this thesis and focusing on the treatment of ill-posed inverse problems.

2.1 Thermal radiation and heat conduction

The term radiation refers to the continuous energy emission from any body's surface. All bodies with a temperature over 0 K emit radiation, as it corresponds to the fact that particles are in motion. This motion is constrained by interactions with other atoms or molecules, e.g., collisions and bonds, so the elementary charges within these atoms are subjected to accelerations, and accelerating charges radiate electromagnetically.

Radiant energy is carried by electromagnetic waves, which, in turn, travel through a vacuum at a speed of $3 \cdot 10^8$ ms^{-1}. Radio waves, microwaves, IR, visible and ultra-violet radiation, X-rays and gamma rays form the different regions of the electromagnetic spectrum (see Figure 2.1).

Infrared radiation is the electromagnetic radiation with wavelengths lying from 0.75 to 1000 µm. In turn, it can be divided into three regions: first, closest to the visible, the near infrared, with wavelengths between 0.75 and 1.5 µm; then, the middle infrared ranges from

1.5 to 30 µm, being the thermal imaging region and last, the far infrared, with wavelengths ranging from 30 to 1000 µm.

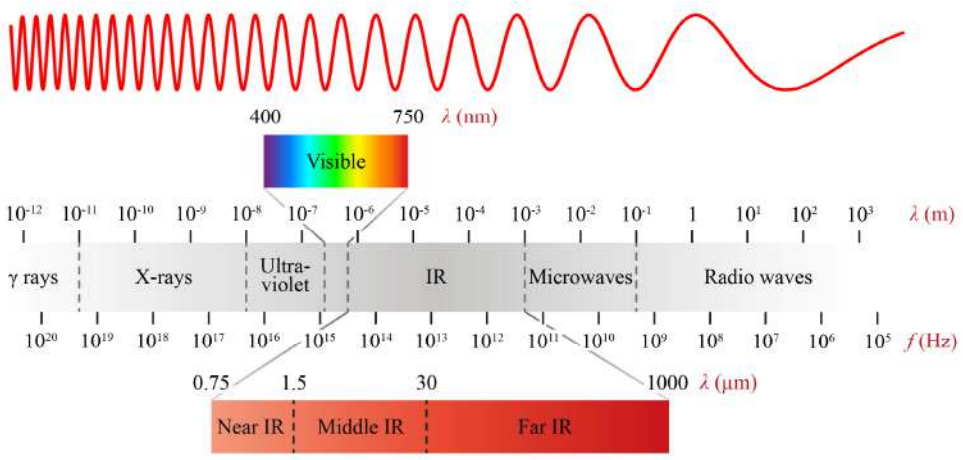

Figure 2.1. Electromagnetic spectrum showing the IR regions.

Back to the fact that all bodies emit electromagnetic radiation, this emission depends on various factors: the surface nature, the body temperature, the wavelength and the direction. A body that is a perfect emitter is called a *blackbody*, and is able to absorb radiation from any direction or wavelength and emit it in the same way until it reaches the thermodynamic equilibrium. A blackbody follows *Planck's law*, which takes into account that electromagnetic emission is not uniformly distributed over the wavelength spectrum

$$M_b(\lambda,T)=\frac{2\pi hc^2}{\lambda^5\left[e^{\frac{hc}{\lambda kT}}-1\right]} \tag{2.1}$$

Equation (2.1) is the *spectral radiance* for a blackbody ($Wm^{-2}\mu m^{-1}$), where λ is the emitted wavelength in µm, T is the absolute temperature in K, $h = 6.63\cdot10^{-34}$ Ws^2 is the Planck's constant, $c = 3\cdot10^8$ ms^{-1} is the speed of light and $k = 1.38\cdot10^{-23}$ WsK^{-1} is the Boltzmann's constant.

As mentioned before, the spectral radiance is not uniformly distributed over the spectrum, but it has a maximum at a certain wavelength and then is reduced at both sides of the spectrum. To illustrate this, Figure 2.2 shows the spectral radiance for a blackbody at

different temperatures, highlighting those corresponding to room temperature and to the temperature of the Sun, in green and orange, respectively.

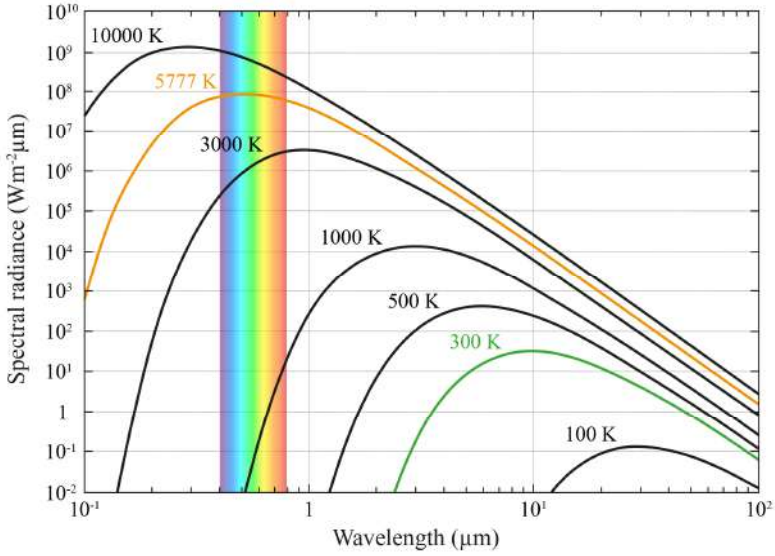

Figure 2.2. Spectral radiance for a blackbody with different temperatures.

As for the maximum spectral radiance at a certain blackbody temperature, the *Wien's displacement law* gives the relation between temperature and the peak wavelength of Planck's function, which is obtained by setting the wavelength derivative of equation (2.1) to zero

$$\frac{\partial M_b(\lambda,T)}{\partial \lambda}=0 \tag{2.2}$$

and solving for the value of λT that maximizes $M_b(\lambda,T)$

$$\lambda_{\max} T = 2898\ \mu\mathrm{m\,K} \tag{2.3}$$

Using equation (2.3) we can check that the peak wavelength at room temperature is 9.6 µm, located in the middle infrared region, whereas at the temperature of the Sun it is $\lambda_{\max}$ = 502 nm, lying on the visible region.

On the other hand, if the total emission in all wavelengths is of interest, equation (2.1) then needs to be integrated from $\lambda = 0$ to ∞, and the resulting expression is known as the *Stefan-Boltzmann law*

$$M_b(T) = \int_0^\infty M_b(\lambda, T)\, d\lambda = \sigma_b T^4 \tag{2.4}$$

where $\sigma_b = 5.67 \cdot 10^{-12}$ is the Stefan-Boltzmann constant.

Concerning the fact mentioned above that infrared emission depends on the body's surface nature, we may note that all laws above do not include any parameter regarding it, since the blackbody represents the ideal surface in which the emitted energy equals the absorbed energy. However, so as to account for real surfaces, we need to introduce a parameter called *emissivity*, which represents the ratio of the spectral radiance of a body to the spectral radiance of a blackbody at the same temperature

$$\varepsilon(\lambda) = \frac{M(\lambda, T)}{M_b(\lambda, T)} \tag{2.5}$$

Emissivity depends on the wavelength, temperature and direction of the emitted radiation, and it varies from $\varepsilon(\lambda) = 0$ to 1. This considered, the emissivity should be included in laws of electromagnetic emission explained above. Therefore, the Planck's law for real surfaces can be now written as

$$M(\lambda, T) = \varepsilon(\lambda, T) \frac{2\pi hc^2}{\lambda^5 \left[e^{\frac{hc}{\lambda k T}} - 1 \right]} \tag{2.6}$$

and the Stefan-Boltzmann law results

$$M(T) = \varepsilon(T) \sigma_b T^4 \tag{2.7}$$

As *Kirchhoff's law for electromagnetic radiation* states, the amount of energy absorbed must equal the amount of energy emitted, not only for a blackbody but for all surfaces, as long as the thermodynamic equilibrium is reached

$$\alpha(\lambda) = \varepsilon(\lambda) \tag{2.8}$$

where α (λ) is the *absorptance*, the fraction of incident electromagnetic power absorbed at an interface. This is illustrated in Figure 2.3 (a), from which it can concluded that a poor absorber is also a poor emitter. Of course, a good absorber is also a good emitter, and in the case of a blackbody (see Figure 2.3 (b)), $\varepsilon_b(\lambda) = \alpha_b(\lambda) = 1$.

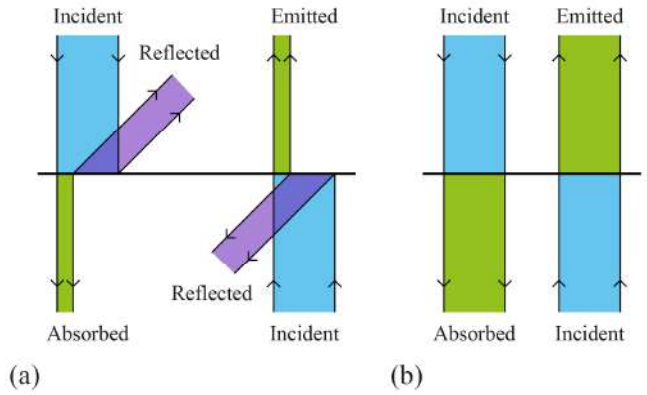

Figure 2.3. Representation of energy absorbed and emitted for (a) a real surface and (b) a blackbody.

At this point, it is worth mentioning that there are only three possible components to the behaviour of radiation incident on a surface

$$\alpha + \rho + \tau = 1 \tag{2.9}$$

where ρ is the *reflectance*, i.e., the portion of incident power that is reflected, and τ is the *transmittance* or the fraction of incident power that emerges from the other side of the surface. As only metallic samples are inspected within this work, there is no radiation from beyond the sample that can pass through the sample.

Thus, the radiated energy in vibrothermography experiments depends only on the sample surface temperature and on the emissivity. For this reason, the uncertainty about the emissivity of the sample surface would become a major problem, if absolute temperatures were to be measured. However, only relative temperatures are evaluated in this work and, moreover, for small changes of temperature, just what we often need in lock-in vibrothermography, the emissivity can be considered constant.

Infrared radiation emitted from the sample surface must travel to the detector through the atmosphere. Figure 2.4 shows a diagram of the atmospheric absorption bands. As can be observed, there are three main areas where low atmospheric absorption occurs, the so-called *atmospheric windows* (from 1 to 2.5 µm, from 3 to 5 µm and from 8 to 12 µm) and IR cameras are equipped with detector materials coincident with these atmospheric windows.

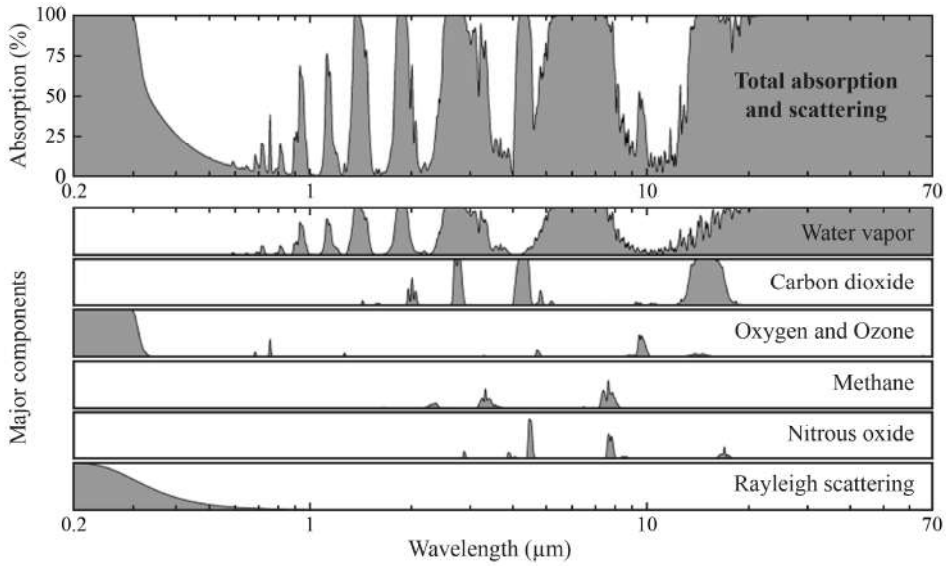

Figure 2.4. Absorption spectrum of the atmosphere and its major absorption components.

Another issue worth mentioning is that thermal radiation from objects in the room could contribute to the radiation reaching the detector, causing it to observe an apparent temperature of the sample surface different from the real one. However, the fact that the room emits infrared radiation reaching the detector is not a problem since, as it is not amplitude modulated, it will not affect lock-in experiments.

Once reviewed the basics of infrared radiation, we cannot forget that in lock-in vibrothermography experiments, the IR emission from the sample surface is a product of mechanical energy absorption, production of thermal energy, diffusion through the material, and lastly emission as IR radiation. Therefore, it is useful to review heat conduction through solids.

The *heat conduction equation* for homogeneous and isotropic materials writes [130]

$$\nabla^2 T(\boldsymbol{r},t) - \frac{1}{D}\frac{\partial T(\boldsymbol{r},t)}{\partial t} = -\frac{Q(\boldsymbol{r},t)}{K} \tag{2.10}$$

where $Q(\boldsymbol{r},t)$ is the energy generated per unit time and unit volume, D is the *thermal diffusivity* and K is the *thermal conductivity* of the material. As the deposited energy is periodic in the lock-in regime, $Q(\boldsymbol{r},t)$ can be expressed as

$$Q(\boldsymbol{r},t) = Q_0(\boldsymbol{r})\left(1 + e^{i\omega t}\right) \tag{2.11}$$

This periodic heat deposition produces a DC temperature rise above the ambient temperature plus an oscillating (AC) temperature component. In consequence, in steady state, the temperature field will be of the form

$$T(\boldsymbol{r},t) = T_{amb} + T_{DC}(\boldsymbol{r}) + T_{AC}(\boldsymbol{r},t) \tag{2.12}$$

where the AC temperature component shows the same harmonic dependence as the energy source

$$T_{AC}(\boldsymbol{r},t) = T_{AC}(\boldsymbol{r})e^{i\omega t} \tag{2.13}$$

Since lock-in thermography is based on the detection of the AC component of the temperature, by substituting $T(\boldsymbol{r},t)$, given by equation (2.12), into the heat conduction equation (2.10), we obtain the differential equation for the oscillating component of the temperature

$$\nabla^2 T_{AC}(\boldsymbol{r},t) - \frac{1}{D}\frac{\partial T_{AC}(\boldsymbol{r},t)}{\partial t} = -\frac{Q_0(\boldsymbol{r})e^{i\omega t}}{K} \tag{2.14}$$

If we now use expression (2.13) for $T_{AC}(\boldsymbol{r},t)$, we obtain the equation governing the spatial dependence of the AC temperature

$$\nabla^2 T_{AC}(\boldsymbol{r}) - q^2 T_{AC}(\boldsymbol{r}) = -\frac{Q_0(\boldsymbol{r})}{K} \tag{2.15}$$

where $q = \sqrt{i\omega / D}$ is the *thermal wave vector*. Thus, the oscillating temperature field depends on the excitation and the thermal properties of the material. Equation (2.15), which describes the AC temperature field in the material, is the *Helmholtz equation* with heat source term. Its solution represents the AC temperature distribution, which leads us to the direct problem of this thesis.

2.2 Inverse problems

As mentioned in section 1.4, whereas the calculation of the surface temperature distribution caused by a certain heat source distribution is the direct problem, the inverse problem consists in retrieving the cause (the heat source distribution) that produces the observed surface temperature rise, which is severely ill-posed due to the diffusive nature of heat propagation.

Apart from introducing inverse problems in a general and theoretical way, this section addresses the main aspects that will arise in the inverse problem considered in this thesis, such as the discretization of integral equations, the least square solution, the singular value decomposition for the analysis and resolution of ill-posed inverse problems, the generalized inverse and the regularization of the generalized inverse using Tikhonov penalization.

2.2.1 Introduction to inverse problems

With the aim of solving a physical problem, we often wish to relate physical parameters characterizing a model, *m*, to collected observations making up some set of data, *d*. To do so, we can define a function, *A*, such that

$$A(m) = d \tag{2.16}$$

Equation (2.16) is called *mathematical model*. An important issue is that actual observations always contain some amount of noise, frequently due to instrument readings and numerical round-off, so we can divide data into noiseless observations from a "perfect" experiment, d_{true}, and a noise component, η

$$d = d_{true} + \eta \tag{2.17}$$

$$d = A\left(m_{true}\right) + \eta \tag{2.18}$$

where d_{true} satisfies equation (2.16) for m equal to the true model, m_{true}, in which case, we assume that the forward modelling is exact. However, as data always contain noise, it is often the case that a solution for m that is influenced by even a small noise level η may have little or no correspondence to m_{true}. As for A, we typically refer to it as an *operator*, when d and m are functions.

The inverse problem is defined as finding m given d. When we want to determine a finite number of parameters, n, to define a model, we can express the model parameters as an n element vector **m**. Similarly, when there are a finite number of data points, we can express data as an m element vector **d**. Such problems are called *discrete inverse problems* or *parameter estimation problems*. A general parameter estimation problem can be written as a system of equations

$$A\left(\mathbf{m}\right) = \mathbf{d} \tag{2.19}$$

On the other hand, when the model and data are functions of continuous variables, the task of estimating m from d is called a *continuous inverse problem*, yet continuous inverse problems can often be well-approximated by discrete inverse problems.

A type of mathematical model for which many useful results exist is the class of linear operators, which obey superposition (2.20) and scaling (2.21)

$$A\left(m_1 + m_2\right) = A\left(m_1\right) + A\left(m_2\right) \tag{2.20}$$

$$A\left(\alpha m\right) = \alpha A\left(m\right) \tag{2.21}$$

In the case of a discrete linear inverse problem, equation (2.19) can always be written in the form of a linear system of algebraic equations

$$A\left(\mathbf{m}\right) = \mathbf{A}\mathbf{m} = \mathbf{d} \tag{2.22}$$

and in the case of a continuous linear inverse problem, A can often be expressed as a linear integral operator, where (2.16) has the form

$$\int_a^b g(x,y)m(y)\,\mathrm{d}y = d(x) \tag{2.23}$$

where the data, $d(x)$, is a function of x and, hence, so is the function $g(x,y)$, the so-called *kernel*. Equations of the form of (2.23) where $m(y)$ is the unknown are called *Fredholm's integral equations of the first kind (IFK)*. IFKs arise in a large number of inverse problems, including the one in this thesis, and they have the inconvenience of making the inverse problem ill-posed when the kernel is a smooth function.

2.2.2 Discretization of integral equations

In problems of the form of equation (2.23), the kernel, $g(x,y)$, which encodes the physics relating the unknown model, $m(y)$, to the observed data, $d(x)$, is considered to be given. For the sake of simplicity, we consider that $g:\mathbb{R}\times[a,b]\rightarrow\mathbb{R}$ and, also, that $d(x)$ refers to measurements at a finite set of points, even though it might be known over an entire interval. Assuming that $d(x)$ is known at a finite number of points x_1, x_2, ..., x_m, we can rewrite equation (2.23) as

$$\begin{aligned} d_i = d(x_i) &= \int_a^b g(x_i,y)m(y)\,\mathrm{d}y \\ &= \int_a^b g_i(y)m(y)\,\mathrm{d}y \qquad i = 1, 2, ..., m \end{aligned} \tag{2.24}$$

where the functions $g(x_i,y) = g_i(y)$ are the *data kernels*. For the discretization of equation (2.24) we apply a quadrature rule. The simplest quadrature approach is the *midpoint rule*, in which we divide the interval [a, b] into n subintervals and pick points y_1, y_2, ..., y_n in the middle of each subinterval (see Figure 2.5), being Δy the length of each subinterval

$$\Delta y = \frac{b-a}{n} \tag{2.25}$$

The points in the middle of each subinterval, y_j, are then

$$y_j = a + \frac{\Delta y}{2} + (j-1)\Delta y \tag{2.26}$$

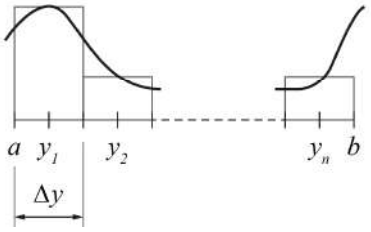

Figure 2.5. Grid for the midpoint rule.

The integral equation (2.24) is then approximated by

$$d_i = \int_a^b g_i(y)\, m(y)\, \mathrm{d}y \approx \sum_{j=1}^{n} g_i(y_j)\, m(y_j)\, \Delta y \qquad i = 1, 2, \ldots, m \tag{2.27}$$

Finally, if we define

$$A_{i,j} = g_i(y_j)\, \Delta y \qquad \begin{pmatrix} i = 1, 2, \ldots, m \\ j = 1, 2, \ldots, n \end{pmatrix} \tag{2.28}$$

and

$$m_j = m(y_j) \qquad j = 1, 2, \ldots, n \tag{2.29}$$

then we obtain a linear system of equations **Am** = **d**. We have used the midpoint rule to approximate the Fredholm's integral equation of the first kind. This procedure is known as *simple collocation* and lets us with an *m* by *n* linear system of equations.

2.2.3 Least squares solution, SVD and the generalized inverse

From the linear system of equations **Am** = **d** obtained from the discretization of the Fredholm's integral equation of the first kind, the unknown model is solved as

$$\mathbf{m} = \mathbf{A}^{-1}\mathbf{d} \tag{2.30}$$

However, **m** may not always be obtained directly from equation (2.30): if there are more data points than model parameters ($m > n$) and data are affected by noise, it is impossible to find a solution **m** that satisfies every equation exactly, because the dimension of the range of **A** is smaller than m, meaning that no solution exists.

Nevertheless, useful solutions may be found by solving for model parameters that fit the data in an approximate or "best-fit" sense. In order to get the best approximate solution to an overdetermined system of linear equations, i.e., with more data points than unknowns, we need to find an **m** that minimizes some misfit measure, calculated from the differences between the observations and the theoretical predictions, commonly called *residuals*. The residual vector is

$$\mathbf{r} = \mathbf{d} - \mathbf{Am} \tag{2.31}$$

A very commonly used measure of the misfit is the 2-norm (euclidean length) of the residual vector

$$\|\mathbf{d} - \mathbf{Am}\|_2 = \sqrt{\sum_{i=1}^{m} \left(d_i - (\mathbf{Am})_i\right)^2} \tag{2.32}$$

and a model that minimizes this 2-norm is called a least squares solution. To obtain the least squares solution of (2.31), we solve its normal equations

$$\mathbf{A}^T\mathbf{Am} = \mathbf{A}^T\mathbf{d} \tag{2.33}$$

The least squares solution is then

$$\mathbf{m} = \left(\mathbf{A}^T\mathbf{A}\right)^{-1}\mathbf{A}^T\mathbf{d} \tag{2.34}$$

If **A** has full column rank, then $(\mathbf{A}^T\mathbf{A})^{-1}$ exists. However, if **A** is rank deficient, $(\mathbf{A}^T\mathbf{A})^{-1}$ does not exist and equation (2.34) cannot be applied in order to obtain **m**.

Singular Value Decomposition (SVD) is a method to analyse and solve equation (2.33) in a more sophisticated way than using (2.34), even for rank deficient matrices. In the SVD, the *m* by *n* matrix **A** is factored into 3 matrices

$$\mathbf{A} = \mathbf{U}\mathbf{S}\mathbf{V}^T \tag{2.35}$$

where **U** is an *m* by *m* matrix whose columns are orthogonal vectors spanning the data space, **V** is an *n* by *n* matrix whose columns are orthogonal vectors spanning the model space and **S** is an *m* by *n* diagonal matrix with diagonal elements called *singular values*. Recall that orthogonal matrices meet $\mathbf{U}^{-1} = \mathbf{U}^T$.

The singular values along the diagonal of **S** are arranged in decreasing size, $s_1 \geq s_2 \geq \ldots \geq s_{\min(m,n)} \geq 0$. If only the first *p* singular values are nonzero ($p < m$), we can write **S** as

$$\mathbf{S} = \begin{bmatrix} \mathbf{S}_p & \mathbf{0} \\ \mathbf{0} & \mathbf{0} \end{bmatrix} \tag{2.36}$$

where **S** is a *p* by *p* diagonal matrix composed of the positive singular values. Expanding equation (2.35) in terms of **U** and **V** gives

$$\begin{aligned} \mathbf{A} &= \begin{bmatrix} \mathbf{U}_{.,1}, \mathbf{U}_{.,2}, \ldots, \mathbf{U}_{.,m} \end{bmatrix} \begin{bmatrix} \mathbf{S}_p & \mathbf{0} \\ \mathbf{0} & \mathbf{0} \end{bmatrix} \begin{bmatrix} \mathbf{V}_{.,1}, \mathbf{V}_{.,2}, \ldots, \mathbf{V}_{.,n} \end{bmatrix}^T \\ &= \begin{bmatrix} \mathbf{U}_p, \mathbf{U}_0 \end{bmatrix} \begin{bmatrix} \mathbf{S}_p & \mathbf{0} \\ \mathbf{0} & \mathbf{0} \end{bmatrix} \begin{bmatrix} \mathbf{V}_p, \mathbf{V}_0 \end{bmatrix}^T \end{aligned} \tag{2.37}$$

where $\mathbf{U}_p$ refers to the first *p* columns of **U**, $\mathbf{U}_0$ refers to the last $(m - p)$ columns of **U**, $\mathbf{V}_p$ refers to the first *p* columns of **V** and $\mathbf{V}_0$ refers to the last $(n - p)$ columns of **V**. As the last $(m - p)$ columns of **U** and the last $(n - p)$ columns of **V** are multiplied by zeros in **S**, we can simplify equation (2.37) into its compact form

$$\mathbf{A} = \mathbf{U}_p \mathbf{S}_p \mathbf{V}_p^T \tag{2.38}$$

The SVD can be used to compute a generalized inverse of **A**, the so-called Moore-Penrose pseudoinverse, $\mathbf{A}^{\dagger}$, because it has desirable inverse properties originally identified by Moore and Penrose [131, 132]

$$\mathbf{A}^{\dagger} = \left(\mathbf{A}^T\mathbf{A}\right)^{-1}\mathbf{A}^T \tag{2.39}$$

According to (2.39), in order to obtain the Moore-Penrose pseudoinverse, we need to calculate the transposed of **A** and then the inverse of the product $\mathbf{A}^T\mathbf{A}$. Since $\mathbf{S}_p$ is a diagonal matrix, $\mathbf{S}_p^T = \mathbf{S}_p$ and the transposed of **A** is

$$\begin{aligned}\mathbf{A}^T &= \left(\mathbf{V}_p^T\right)^T \mathbf{S}_p^T \mathbf{U}_p^T \\ &= \mathbf{V}_p \mathbf{S}_p^T \mathbf{U}_p^T \\ &= \mathbf{V}_p \mathbf{S}_p \mathbf{U}_p^T\end{aligned} \tag{2.40}$$

Thus, the product $\mathbf{A}^T\mathbf{A}$ is

$$\begin{aligned}\mathbf{A}^T\mathbf{A} &= \mathbf{V}_p \mathbf{S}_p \mathbf{U}_p^T \mathbf{U}_p \mathbf{S}_p \mathbf{V}_p^T \\ &= \mathbf{V}_p \mathbf{S}_p^2 \mathbf{V}_p^T\end{aligned} \tag{2.41}$$

and its inverse gives

$$\begin{aligned}\left(\mathbf{A}^T\mathbf{A}\right)^{-1} &= \left(\mathbf{V}_p^T\right)^{-1}\left(\mathbf{S}_p^2\right)^{-1}\left(\mathbf{V}_p\right)^{-1} \\ &= \mathbf{V}_p\left(\mathbf{S}_p^2\right)^{-1}\mathbf{V}_p^T\end{aligned} \tag{2.42}$$

At last, the Moore-Penrose pseudoinverse is, introducing (2.42) and (2.40) into (2.39)

$$\begin{aligned}\mathbf{A}^{\dagger} &= \mathbf{V}_p\left(\mathbf{S}_p^2\right)^{-1}\mathbf{V}_p^T\mathbf{V}_p\mathbf{S}_p\mathbf{U}_p^T \\ &= \mathbf{V}_p\left(\mathbf{S}_p^2\right)^{-1}\mathbf{S}_p\mathbf{U}_p^T \\ &= \mathbf{V}_p\mathbf{S}_p^{-1}\mathbf{U}_p^T\end{aligned} \tag{2.43}$$

Using equation (2.43), we define the pseudoinverse solution to be

$$\mathbf{m}^{\dagger} = \mathbf{A}^{\dagger}\mathbf{d} = \mathbf{V}_p\mathbf{S}_p^{-1}\mathbf{U}_p^T\mathbf{d} \tag{2.44}$$

The most important property of equation (2.44) is that $\mathbf{A}^{\dagger}$ (given in (2.43)), and hence $\mathbf{m}^{\dagger}$, always exist, unlike $(\mathbf{A}^T\mathbf{A})^{-1}$ in equation (2.34). In the inverse problem of this thesis, we will normally have that $n = p$, being the number of unknown model parameters who determines the number of nonzero singular values, and also $p < m$, so we have more data points than unknown model parameters to solve. Under these conditions, the solution cannot fit noisy data exactly.

In order to get a more explicit expression of $\mathbf{m}^{\dagger}$ than equation (2.44), we follow the steps below: first, the elements of the vector $\mathbf{U}_p^T\mathbf{d}$ are the dot products of the first p columns of $\mathbf{U}_p$ with $\mathbf{d}$

$$\mathbf{U}_p^T\mathbf{d} = \begin{bmatrix} \mathbf{U}_{.,1}^T\mathbf{d} \\ \mathbf{U}_{.,2}^T\mathbf{d} \\ \cdots \\ \mathbf{U}_{.,p}^T\mathbf{d} \end{bmatrix} \tag{2.45}$$

When we multiply equation (2.45) by $\mathbf{S}_p^{-1}$, we obtain

$$\mathbf{S}_p^{-1}\mathbf{U}_p^T\mathbf{d} = \begin{bmatrix} \dfrac{\mathbf{U}_{.,1}^T\mathbf{d}}{s_1} \\ \dfrac{\mathbf{U}_{.,2}^T\mathbf{d}}{s_2} \\ \cdots \\ \dfrac{\mathbf{U}_{.,p}^T\mathbf{d}}{s_p} \end{bmatrix} \tag{2.46}$$

And finally, when we multiply equation (2.46) by $\mathbf{V}_p$, we obtain a linear combination of the columns of $\mathbf{V}_p$ that can be written as

$$\mathbf{m}^{\dagger} = \sum_{i=1}^{p} \frac{\mathbf{U}_{.,i}^{T}\mathbf{d}}{s_i}\mathbf{V}_{.,i} \tag{2.47}$$

Equation (2.47) is the generalized inverse, which may include terms involving model space vectors in $\mathbf{V}_{.,i}$ with very small singular values. The presence of near-zero singular values in the denominator of equation (2.47) can provoke very large coefficients for their corresponding model space vectors $\mathbf{V}_{.,i}$, which can dominate the model and, in the worst case, act as a noise amplifier.

Inverse problems stated in the form of Fredholm's integral equations of the first kind with smooth kernels lead to a severe ill-posedness of the inverse problem in the presence of noise [133]. The concept of a well-posed inverse problem, originally introduced by Hadamard [134], requires that its solution should satisfy the following three conditions:

- *The solution must exist*

- *The solution must be unique*

- *The solution must be stable under small changes to the input data (stability condition)*

For the inverse problem of retrieving the heat source distribution that gives rise to a certain surface temperature distribution from vibrothermography data, in the absence of noise, a solution exists and, according to the *corollary of Holmgren's uniqueness theorem*, the solution is unique [135]. However, the third condition is not fulfilled: the Fredholm's integral equations lead to lack of stability of the inversion. Obtaining the solution to an ill-posed inverse problem can be an extremely unstable process, in that a small change in the measurement, i.e., a small η in equation (2.18), can lead to an enormous change in the estimated model. If the inverse problem is very sensitive to random errors in the input data, it needs to be stabilized by imposing additional constraints that bias the solution, which is generally called *regularization*, in order to satisfy the stability condition.

In the analysis of the generalized inverse solution, it is useful to examine the range of singular values: the more near-zero singular values, the more severely ill-posed the inverse problem can be considered to be. The shape of the curve that the singular values take on when plotted (versus the singular value number), can also be a visual indicator of the ill-posedness of the inverse problem: if the singular values s_i decay following laws such as $s_i \approx i^{-1}$ or $s_i \approx i^{-2}$, the inverse problem may be mildly ill-posed, whereas if their decay fits a

decreasing exponential function such as $s_i \approx e^{-i}$, the inverse problem can be considered to be severely ill-posed.

If we chop very small singular values and thus eliminate the model space vectors associated to them, then the solution becomes more stable. However, this stability comes at the expense of reducing the accuracy of the solution, as the fit to the data worsens. Therefore, the chopping criterion should satisfy a compromise between stability and accuracy of the solution.

For a long time it was thought that, if any of the conditions required for well-posedness were violated, the problem would be unsolvable or the results obtained from such a solution would be physically meaningless. It was more sophisticated inversion procedures such as *Tikhonov regularization* [136] that revitalized the interest in the solution for inverse problems.

A successful solution of an inverse problem generally involves its reformulation as an approximate well-posed problem. Tikhonov regularization procedure modifies the least squares equation by adding smoothing terms in order to reduce the unstable effects of errors in data.

2.2.4 Tikhonov regularization

As we have seen, the generalized inverse solution can become extremely unstable when one or more singular values, s_i, are very small. Dealing with this difficulty implies the implementation of a method for the stabilization or regularization of the solution, in the sense that the solution becomes less sensitive to noise in the data, at the expense of reducing resolution and having no longer an unbiased solution.

Tikhonov regularization is a very widely applied and easy to implement technique for regularizing ill-posed problems. The Tikhonov series solution has coefficients that are functions of a regularization parameter, α_{Tk}, controlling the degree of regularization, and which give a greater weight to model elements associated with larger singular values, in a similar way to a low-pass filter.

For a general least squares problem where data contain noise, there is no point in fitting such noise exactly, but there can be many solutions $\mathbf{m} \in \mathbb{R}^n$ that can adequately fit the data so that $\|\mathbf{Am} - \mathbf{d}\|_2$ is small enough. In zero-order Tikhonov regularization, we consider all

solutions that meet $\|\mathbf{Am} - \mathbf{d}\|_2 \leq \delta$, being δ a particular residual misfit tolerance value, and select the one that minimizes the 2-norm of **m**

$$\min \left\|\mathbf{m}\right\|_2 , \text{ subject to } \left\|\mathbf{Am} - \mathbf{d}\right\|_2 \leq \delta \tag{2.48}$$

Implementing Tikhonov regularization including Lagrange multipliers, the minimization problem now is

$$\mathbf{m}_\alpha = \arg\min_{\mathbf{m}\in\mathbb{R}^n} \left[\left\|\mathbf{Am} - \mathbf{d}\right\|_2^2 + \alpha_{Tk} \left\|\mathbf{m}\right\|_2^2 \right] \tag{2.49}$$

We refer to the first and second terms in equation (2.49) as *discrepancy term* and *regularization term*, respectively. The larger α_{Tk}, the more powerful the regularization term so as to damp model elements associated with small singular values, as we will see later on.

This solution is equivalent to an ordinary least squares problem augmenting it in the following manner

$$\mathbf{m}_\alpha = \arg\min_{\mathbf{m}\in\mathbb{R}^n} \left\| \begin{bmatrix} \mathbf{A} \\ \sqrt{\alpha_{Tk}}\mathbf{I} \end{bmatrix} \mathbf{m} - \begin{bmatrix} \mathbf{d} \\ \mathbf{0} \end{bmatrix} \right\|_2^2 \tag{2.50}$$

For the sake of clarity, we will refer to the new augmented matrix **A** as matrix $\mathbf{A}_{aug}$. Following the same procedure as the steps followed above for the obtention of the generalized inverse with no regularization, $\mathbf{A}_{aug}$ and its transposed are

$$\mathbf{A}_{aug} = \begin{bmatrix} \mathbf{A} \\ \sqrt{\alpha_{Tk}}\mathbf{I} \end{bmatrix} \tag{2.51}$$

$$\mathbf{A}_{aug}^T = \begin{bmatrix} \mathbf{A}^T & \sqrt{\alpha_{Tk}}\mathbf{I} \end{bmatrix} \tag{2.52}$$

where the size of **A** remains *m* by *n* and **I** is the *n* by *n* identity matrix. As long as α_{Tk} is nonzero, the last *n* rows of matrix $\mathbf{A}_{aug}$ are linearly independent, so equation (2.50) is thus a full rank least squares problem that can be solved by its normal equations

$$\mathbf{A}_{aug}^T \mathbf{A}_{aug} \mathbf{m}_\alpha = \mathbf{A}_{aug}^T \mathbf{d} \tag{2.53}$$

Expanding equation (2.53), we have

$$\begin{aligned}\begin{bmatrix}\mathbf{A}^T & \sqrt{\alpha_{Tk}}\mathbf{I}\end{bmatrix}\begin{bmatrix}\mathbf{A}\\ \sqrt{\alpha_{Tk}}\mathbf{I}\end{bmatrix}\mathbf{m}_\alpha &= \begin{bmatrix}\mathbf{A}^T & \sqrt{\alpha_{Tk}}\mathbf{I}\end{bmatrix}\begin{bmatrix}\mathbf{d}\\ \mathbf{0}\end{bmatrix}\\ \left(\mathbf{A}^T\mathbf{A}+\alpha_{Tk}\mathbf{I}\right)\mathbf{m}_\alpha &= \mathbf{A}^T\mathbf{d}\end{aligned} \tag{2.54}$$

Employing the SVD of **A**, where $\mathbf{A} = \mathbf{USV}^T$ and $\mathbf{A}^T = \mathbf{VS}^T\mathbf{U}^T$, equation (2.54) can be written as

$$\begin{aligned}\left(\mathbf{VS}^T\mathbf{U}^T\mathbf{USV}^T+\alpha_{Tk}\mathbf{I}\right)\mathbf{m}_\alpha &= \mathbf{VS}^T\mathbf{U}^T\mathbf{d}\\ \left(\mathbf{VS}^T\mathbf{SV}^T+\alpha_{Tk}\mathbf{I}\right)\mathbf{m}_\alpha &= \mathbf{VS}^T\mathbf{U}^T\mathbf{d}\end{aligned} \tag{2.55}$$

The following simple substitutions diagonalize this system and make it straightforward to write out the solution: let $\mathbf{x} = \mathbf{V}^T\mathbf{m}_\alpha$ and $\mathbf{m}_\alpha = \mathbf{Vx}$. Since $\mathbf{VV}^T = \mathbf{I}$, we can write equation (2.55) as

$$\begin{aligned}\left(\mathbf{VS}^T\mathbf{SV}^T+\alpha_{Tk}\mathbf{VV}^T\right)\mathbf{m}_\alpha &= \mathbf{VS}^T\mathbf{U}^T\mathbf{d}\\ \mathbf{V}\left(\mathbf{S}^T\mathbf{S}+\alpha_{Tk}\mathbf{I}\right)\mathbf{V}^T\mathbf{m}_\alpha &= \mathbf{VS}^T\mathbf{U}^T\mathbf{d}\\ \left(\mathbf{S}^T\mathbf{S}+\alpha_{Tk}\mathbf{I}\right)\mathbf{x} &= \mathbf{S}^T\mathbf{U}^T\mathbf{d}\end{aligned} \tag{2.56}$$

Because the left-hand side of the equation (2.56) is diagonal, it is trivial to solve the system of equations

$$x_i = \frac{s_i}{s_i^{\,2}+\alpha_{Tk}}\mathbf{U}_{.,i}^T\mathbf{d} \tag{2.57}$$

and since $\mathbf{m}_\alpha = \mathbf{Vx}$, we get to the solution

$$\mathbf{m}_\alpha = \sum_{i=1}^{k}\frac{s_i}{s_i^{\,2}+\alpha_{Tk}}\mathbf{U}_{.,i}^T\mathbf{d}\mathbf{V}_{.,i} \tag{2.58}$$

where $k = \min(m,n)$, so that all the non-zero singular values and vectors are included. To relate this solution to that obtained without Tikhonov regularization (equation (2.47)) more clearly, we can rewrite equation (2.58) as

$$\begin{aligned}\mathbf{m}_\alpha &= \sum_{i=1}^{k} \frac{s_i^{\,2}}{s_i^{\,2} + \alpha_{Tk}} \frac{\mathbf{U}_{.,i}^T \mathbf{d}}{s_i} \mathbf{V}_{.,i} \\ &= \sum_{i=1}^{k} f_i \frac{\mathbf{U}_{.,i}^T \mathbf{d}}{s_i} \mathbf{V}_{.,i}\end{aligned} \tag{2.59}$$

where $f_i = s_i^{\,2} / \left(s_i^{\,2} + \alpha_{Tk} \right)$ are the so-called *filter factors*, which control the contribution of the different terms to the sum, in the same way as a low-pass filter. Thus, the penalization of the different model space vectors depends on the relation between α_{Tk} and their associated singular values. Accordingly, the degree of regularization can be varied between two extremes: for $s_i >> \alpha_{Tk}$, $f_i \approx 1$ and equation (2.59) remains exactly the same as equation (2.47), meaning that the regularization is dismissed, whereas for $s_i << \alpha_{Tk}$, $f_i \approx 0$, which is equivalent to damping the model space vectors associated with very small singular values, $\mathbf{V}_{.,i}$. Logically, for singular values ranging between these two extremes, as s_i decrease, f_i produce a monotonically decreasing contribution of their corresponding model space vectors to the solution.

This considered, the Tikhonov series produces a softer filtering of model space vectors associated to small singular values, than just chopping them as mentioned in the SVD description. Thus, this produces a smooth solution, since sharp, high frequency model space vectors are filtered out.

As for the choice of α_{Tk}, the curve of optimal values of $\|\mathbf{m}_\alpha\|_2$ versus $\|\mathbf{A}\mathbf{m}_\alpha - \mathbf{d}\|_2$ as a function of α_{Tk}, plotted on a log-log scale, often takes on a characteristic "L" shape in linear problems

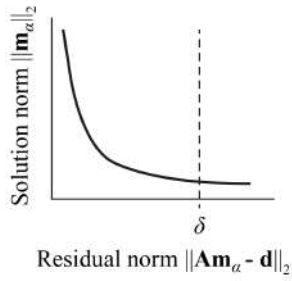

Figure 2.6. L-curve: a particular residual misfit, δ, and its position on the curve between the model norm, $\|\mathbf{m}_\alpha\|_2$, and the residual misfit, $\|\mathbf{A}\mathbf{m}_\alpha - \mathbf{d}\|_2$, as a function of α_{Tk}.

For this reason, Figure 2.6 is called *L-curve* [137], which is useful for picking the optimal value of the regularization parameter according to the *L-curve criterion*, that selects the value of α_{Tk} that gives the solution closest to the corner of the L-curve. Note that as δ increases, the set of feasible models expands and $\|\mathbf{m}\|_2$ decreases. In other words, as we allow a poorer fit to the data, a smaller norm model is sufficient to fit the data.

3 The direct problem

This section states and solves the direct problem in this thesis, consisting in the calculation of the surface temperature distribution caused by a certain heat source distribution. The solution is then analysed by performing simulations for homogeneous square heat sources, in order to observe the impact of varying the geometrical parameters of the heat sources on the surface temperature distribution. Finally, other geometries are considered too, in order to assess the ability of vibrothermography to distinguish between the particular geometries of the heat sources.

The vibrothermographic signal is a result of heat sources activated by ultrasounds at defect areas. In the case of the moderate ultrasound intensities usually used to keep the test nondestructive, heat is mainly produced by rubbing and/or clapping friction between the crack surfaces. Due to amplitude modulated activation at a frequency $f_{lock\text{-}in}$, thermal waves are generated at the defects, they propagate in the material and are the cause of the resulting surface temperature distribution, which is monitored as a function of time with an IR camera. This process is governed by heat diffusion.

Thermal waves are highly attenuated as well as dispersive. The attenuation of thermal waves is characterized by the *thermal diffusion length* [42], which represents the distance for which the temperature amplitude decreases to a value of 1/e with respect to the temperature amplitude at the location of the modulated heat source, in 1D problems

$$\mu = \sqrt{\frac{D}{\pi f_{lock-in}}} \tag{3.1}$$

According to equation (3.1), the penetration range of a thermal wave depends on the thermal diffusivity of the material and the modulation frequency, increasing with decreasing $f_{lock\text{-}in}$. However, a sample with a vertical heat source of finite size states a 3D thermal diffusion problem, in which an additional radial decay of the temperature field takes places aside from the attenuation due to its diffusive nature.

Characterization of cracks by inversions from vibrothermography data involves fitting the observed surface temperature distribution to a mathematical model. Thus, the first step is to solve the direct problem, consisting in calculating the surface temperature distribution caused by a certain heat source distribution, and analyse it with the aim of observing how the different geometries of the heat sources affect the surface temperature distribution.

In the following, the direct problem is stated and solved. Then, the solution is analysed in depth for homogeneous rectangular heat sources, by performing variations in all the geometrical parameters that come to play such as width, height and the depth at which the heat source is buried beneath the sample surface, so that the results can be extrapolated to other geometries. The amplitude and phase dependence with modulation frequency is also addressed and, finally, other geometries, namely, semicircles and triangles, are considered in order to analyse the ability of vibrothermography to distinguish between the particular features of the geometries.

3.1 Statement and solution of the direct problem

The direct problem consists in calculating the surface temperature distribution corresponding to inner heat sources covering a certain area Ω modulated at a frequency $f_{lock\text{-}in}$, contained in plane Π ($x = 0$), perpendicular to the sample surface. These heat sources represent a vertical kissing crack excited by amplitude modulated ultrasounds at $f_{lock\text{-}in}$ in vibrothermography experiments. The sample has a thickness e and it is infinite in x and y directions. Figure 3.1 shows the geometry of the problem.

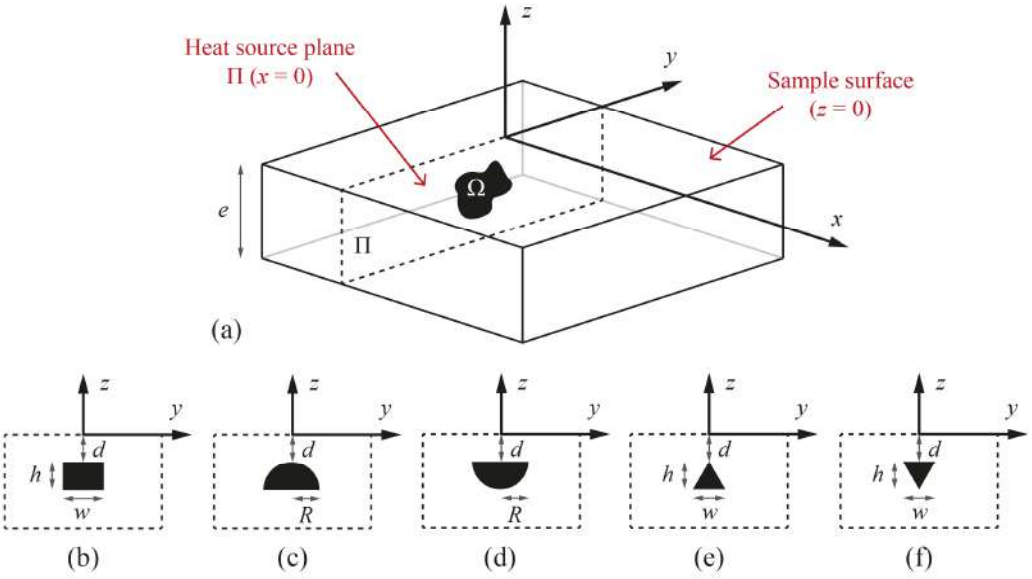

Figure 3.1. (a) Geometry of the problem: an inner heat source of area Ω and arbitrary shape contained in plane Π (x = 0), perpendicular to the measuring surface (z = 0), (b) rectangular heat source, (c) semi-circular heat source with the circular side upward and (d) downward, (e) triangular heat source with the apex on the middle upward and (f) downward.

As mentioned in section 2.1, lock-in thermography is based on the measurement of the oscillating component (AC) of the surface temperature distribution, governed by the Helmholtz equation with heat source term (equation (2.15)).

Thus, we start considering the Helmholtz equation for a point-like modulated heat source in an infinite medium located at $\boldsymbol{r'}$ (x', y', z'), whose intensity is modulated at frequency $f_{lock\text{-}in}$ ($\omega = 2\pi f_{lock\text{-}in}$)

$$\nabla^2 T_{AC}(\boldsymbol{r}) - q^2 T_{AC}(\boldsymbol{r}) = -\frac{P\delta(\boldsymbol{r'}-\boldsymbol{r})}{K} \tag{3.2}$$

where P is the maximum emitted power and $q^2 = \frac{i\omega}{D} = \left(\frac{1+i}{\mu}\right)^2$. The solution to equation (3.2) is known as the *normal solution of the Helmholtz equation*, which gives the AC temperature at any point of the sample, $\boldsymbol{r}$ (x, y, z), and writes [130]

$$T_{AC}(\boldsymbol{r}) = T_{AC}(x,y,z) = \frac{P(\boldsymbol{r}')}{8\pi K}\frac{\mathrm{e}^{-q|\boldsymbol{r}-\boldsymbol{r}'|}}{|\boldsymbol{r}-\boldsymbol{r}'|} = \frac{P(x',y',z')}{8\pi K}\frac{\mathrm{e}^{-q\sqrt{(x-x')^2+(y-y')^2+(z-z')^2}}}{\sqrt{(x-x')^2+(y-y')^2+(z-z')^2}} \tag{3.3}$$

where the square root represents the distance between heat source and the position where the temperature is calculated. Equation (3.3) represents a highly damped spherical thermal wave.

If we now consider the contributions of the point-like heat sources covering area Ω, contained in plane Π ($x = 0$), equation (3.3) writes

$$T_{AC}(\boldsymbol{r}) = T_{AC}(x,y,z) = \iint_{\Omega}\frac{Q(\boldsymbol{r}')}{8\pi K}\frac{\mathrm{e}^{-q|\boldsymbol{r}-\boldsymbol{r}'|}}{|\boldsymbol{r}-\boldsymbol{r}'|}dS' = \iint_{\Omega}\frac{Q(0,y',z')}{8\pi K}\frac{\mathrm{e}^{-q\sqrt{x^2+(y-y')^2+(z-z')^2}}}{\sqrt{x^2+(y-y')^2+(z-z')^2}}dy'dz' \tag{3.4}$$

where Q is the maximum flux (power density) emitted over area Ω.

In order to account for the thickness of the sample, we apply the images method assuming adiabatic conditions. With this method, the effect of the surface boundaries is equivalent to having successive reflected images of the heat source at the sample surfaces. In this way, the position-dependent part of the AC temperature is now given by

$$T_{AC}(\boldsymbol{r}) = T_{AC}(x,y,z) = \iint_{\Omega+\Omega'+\Omega''+\Omega'''\ldots}\frac{Q(\boldsymbol{r}')}{8\pi K}\frac{\mathrm{e}^{-q|\boldsymbol{r}-\boldsymbol{r}'|}}{|\boldsymbol{r}-\boldsymbol{r}'|}dS' = \iint_{\Omega+\Omega'+\Omega''+\Omega'''\ldots}\frac{Q(0,y',z')}{8\pi K}\frac{\mathrm{e}^{-q\sqrt{x^2+(y-y')^2+(z-z')^2}}}{\sqrt{x^2+(y-y')^2+(z-z')^2}}dy'dz' \tag{3.5}$$

where Ω’ is the reflection of Ω at the front surface of the sample, Ω’’ is the reflection of Ω at the rear surface of the sample, Ω’’’ is the reflection of Ω twice, first at the front surface and then at the rear surface, and so forth.

In the experiments performed in this thesis using samples with calibrated heat sources, the sample is made of AISI 304 stainless steel (D = 4 mm^2s^{-1} and K = 15 $Wm^{-1}K^{-1}$), its thickness is e = 15 mm and the minimum modulation frequency is 0.05 Hz. Under these conditions, we have checked that the rear surface (z = -e) does not affect the temperature distribution at the front surface (z = 0), where data are taken. Since thermal diffusion length diminishes with increasing modulation frequency, this check at the lowest modulation frequency implies making sure that the sample can be considered semi-infinite, so only Ω and Ω' are considered.

Accordingly, as we are only interested in calculating the temperature at the sample surface because of being the only information that is experimentally accessible, the result for $T_{AC}\left(\boldsymbol{r}_{z=0}\right)$ is just the first term of equation (3.5), multiplied by 2

$$\begin{aligned} T_{AC}\left(\boldsymbol{r}_{z=0}\right) = T_{AC}\left(x,y,0\right) &= \iint_{\Omega} \frac{Q\left(\boldsymbol{r}'\right)}{4\pi K} \frac{\mathrm{e}^{-q\left|\boldsymbol{r}-\boldsymbol{r}'\right|}}{\left|\boldsymbol{r}-\boldsymbol{r}'\right|} dS' \\ &= \iint_{\Omega} \frac{Q\left(0,y',z'\right)}{4\pi K} \frac{\mathrm{e}^{-q\sqrt{x^2+\left(y-y'\right)^2+z'^2}}}{\sqrt{x^2+\left(y-y'\right)^2+z'^2}} dy'dz' \end{aligned} \tag{3.6}$$

Equation (3.6) is the general form of the solution of the direct problem considered in this thesis, and it represents the complex position-dependent part of the AC temperature at any point of the surface of a semi-infinite sample, generated by inner vertical modulated heat sources of area Ω, contained in plane Π, perpendicular to the sample surface.

Note that this solution is valid either for homogeneous, i.e., with uniform Q over area Ω, or inhomogeneous heat sources of any shape Ω, which will both be considered further on.

We next analyse the influence of the geometrical parameters of the heat source on the solution, for homogeneous rectangular heat sources. This analysis is carried out by performing simulations in order to give an idea of the impact of varying geometrical parameters such as height, weight and depth of the heat sources, on the surface temperature distribution.

3.2 Rectangular heat sources: analysis of the influence of geometrical parameters

In this section we present simulations that consist in computing the phase, Ψ, and the natural logarithm of the amplitude, Ln(|*T*|), of the surface temperature distribution, generated by homogeneous rectangular heat sources, at various modulation frequencies.

All the simulations are performed for AISI 304 stainless steel. We show the results at two modulation frequencies, $f_{lock\text{-}in}$ = 0.05 Hz and 6.4 Hz, representative of the ends of the typical modulation frequency range in our vibrothermography experiments, performed in the lock-in regime.

For the sake of simplicity, instead of comparing amplitude and phase surface maps we compare two key profiles: *x*-profile, perpendicular to the heat source along *OX* axis, and *y*-profile, parallel to the heat source along *OY* axis (see Figure 3.1 (a)). In order to allow for an easier comparison between different profiles, all surface temperature amplitudes have been normalized to their value at position (0, 0, 0), and they have been shifted along the vertical axis to better distinguish between amplitudes and phases. It is worth mentioning that the representation range of both *x*- and *y*-profiles depends on the thermal diffusion length corresponding to the modulation frequency in each case.

For the particular case of a homogeneous rectangular heat source of height *h* and width *w* submerged at depth *d*, as depicted in Figure 3.1(b), equation (3.6) can be written as

$$T_{AC\_r}(x,y,0) = \int_{-w/2}^{w/2} \int_{-(d+h)}^{-d} \frac{Q}{4\pi K} \frac{e^{-q\sqrt{x^2+(y-y')^2+z'^2}}}{\sqrt{x^2+(y-y')^2+z'^2}} dy'\,dz' \tag{3.7}$$

Below, the effect of varying the size parameters (*w* and *h*) on the surface temperature distribution given by equation (3.7) is analysed. To do so, we have taken a standard square of 1 mm in side (*h* = *w* = 1 mm) reaching the sample surface (*d* = 0) and checked the influence of variations of 50% and 200% in these parameters. Similarly, as for the influence of the depth, we have buried the standard square at increasing depths: |*d*| = 0, 0.25, 0.5 and 1 mm. Finally, the influence of varying the size parameters is checked for the heat sources being buried at a depth |*d*| = 0.5 mm.

In addition, the frequency dependence of both maximum surface temperature amplitude and phase is checked for the standard square buried at increasing depths, namely, $|d|$ = 0, 0.5 and 1 mm.

3.2.1 Effect of modifying the width

Figure 3.2 shows the effect of modifying the width (w = 0.5, 1 and 2 mm) of a h = 1 mm tall heat source reaching the sample surface (d = 0) on the surface temperature.

Both x- and y-profiles are sensitive to width variations, but changes are logically most significant in y-profiles since the defect is located parallel to the y-axis. In y-profiles, the width of the flat centre in both amplitude and phase follows the width of the defect, whereas in x-profiles, width differences affect the slope of the branches of amplitude and phase.

Differences are bigger at 6.4 Hz than at 0.05 Hz, because high frequencies carry more detailed information regarding the shape of the heat sources, which gets diffuse at low frequencies.

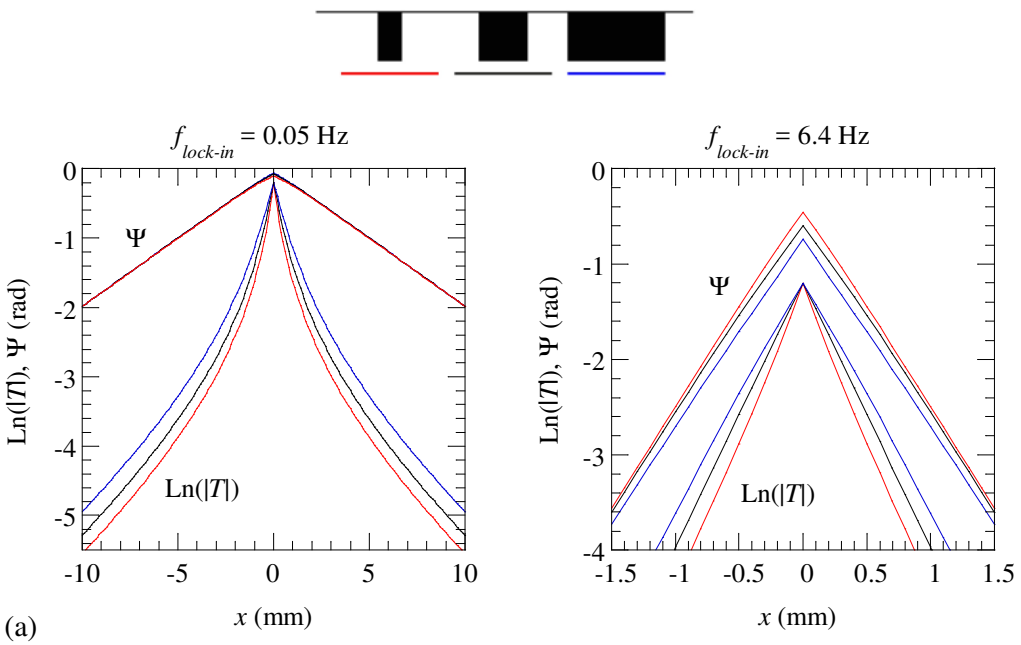

(a)

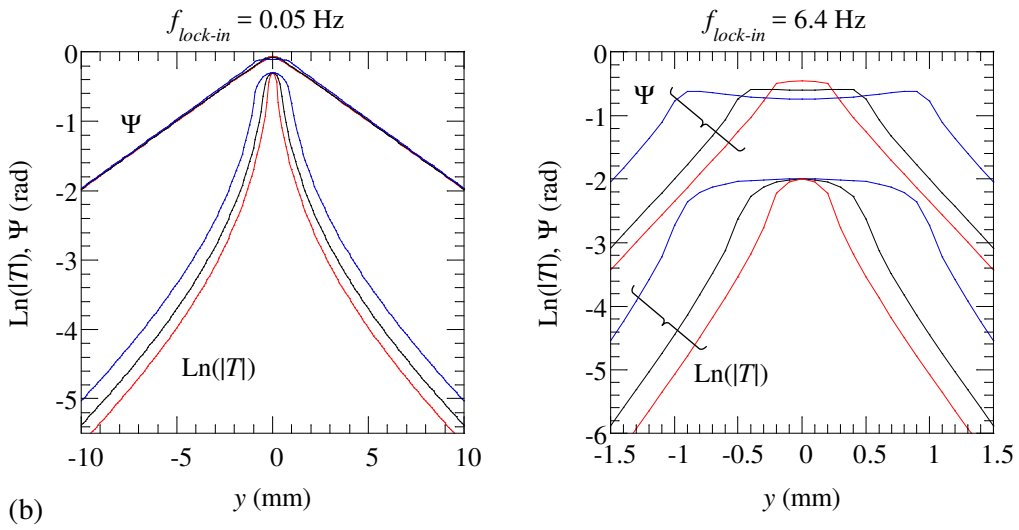

Figure 3.2. Calculated Ln(|*T*|) and Ψ of the surface temperature along (a) *x*- and (b) *y*-profiles, for heat sources reaching the surface (d = 0), all with the same height h = 1 mm and three different widths: w = 0.5 (red), 1 (black) and 2 mm (blue). Results at two modulation frequencies are shown: $f_{lock\text{-}in}$ = 0.05 Hz (left) and 6.4 Hz (right).

3.2.2 Effect of modifying the height

Figure 3.3 shows the effect on the surface temperature of modifying the height (h = 0.5, 1 and 2 mm) of a w = 1 mm wide heat source reaching the sample surface (d = 0). As can be observed, the taller the defect, the wider both *x*- and *y*-profiles. Differences are more significant in amplitude than in phase.

As for the amplitude, differences in the height of the heat source are better distinguished at 0.05 Hz than at 6.4 Hz. The reason for this is that at high frequencies, due to the damped character of thermal waves, the additional effect of heat sources located at increasingly deeper positions barely affects the surface temperature distribution. Thus, at low frequencies, which provide larger thermal diffusion lengths, the effect of having taller heat sources is better appreciated in both *x*- and *y*-profiles.

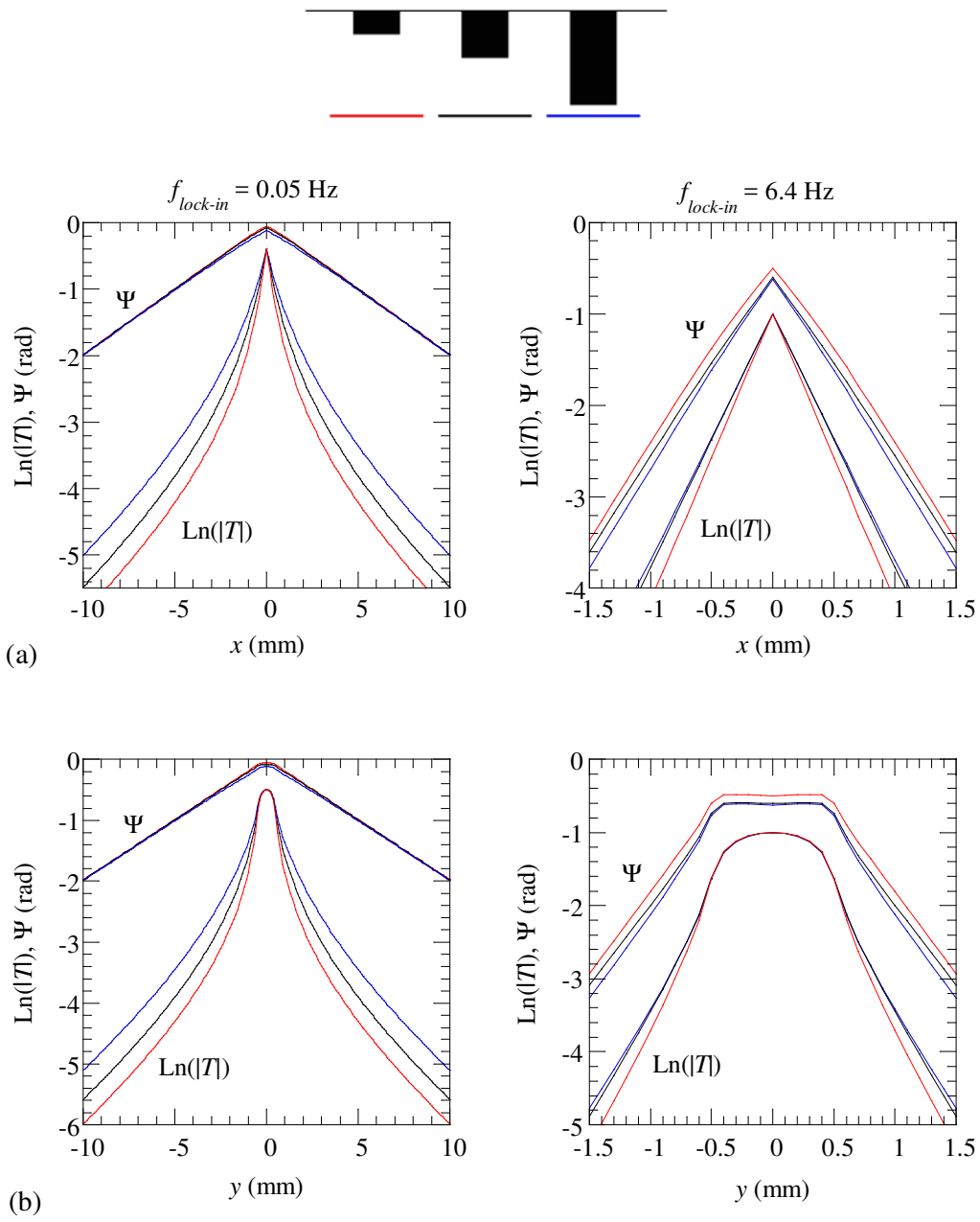

Figure 3.3. Calculated Ln(|*T*|) and Ψ of the surface temperature along (a) *x*- and (b) *y*-profiles, for heat sources reaching the surface (d = 0), all with the same width w = 1 mm and three different heights: h = 0.5 (red), 1 (black) and 2 mm (blue). Results at two modulation frequencies are shown: $f_{lock\text{-}in}$ = 0.05 Hz (left) and 6.4 Hz (right).

3.2.3 Effect of modifying the depth

The effect of burying the standard square (h = w = 1 mm) at increasing depths ($|d|$ = 0, 0.25, 0.5 and 1 mm) is shown in Figure 3.4, where it can be checked that deeper heat sources give rise to round instead of sharp profiles close to the centre. Absolute phase differences with depth are significantly larger at high modulation frequencies. However, at large distances, all phase values converge.

Differences with depth are better distinguished at 6.4 Hz than at 0.05 Hz, contrary to what happens if we increase the height (section 3.2.2). The reason for this is that we are not adding heat sources located at increasingly deeper positions to an initial heat source distribution anymore but we are calculating the surface temperature distribution corresponding to different inner heat sources, and as high frequencies provide a higher spatial resolution, differences in surface temperature with the depth are more pronounced at high frequencies.

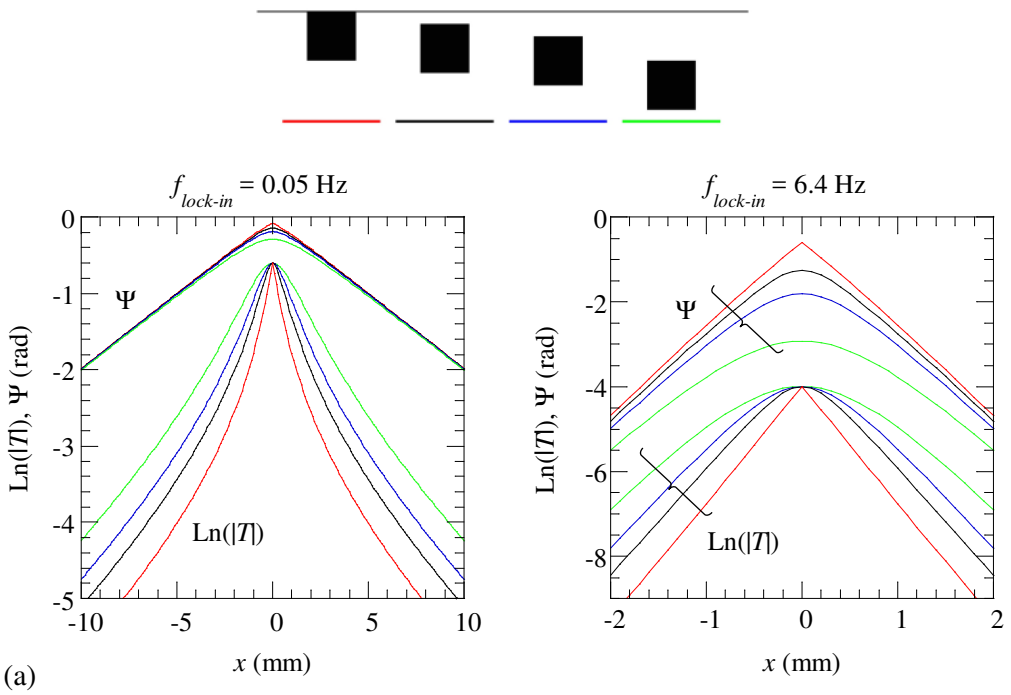

(a)

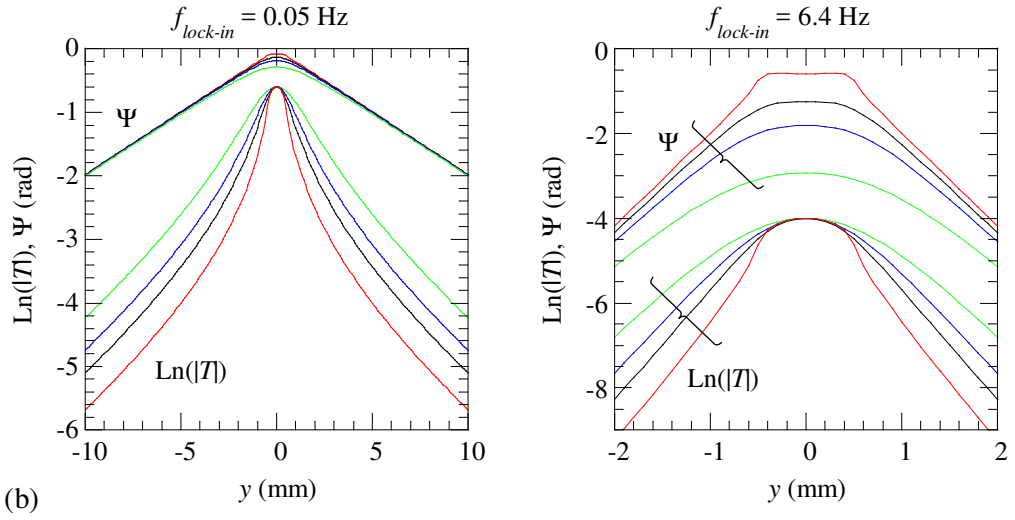

Figure 3.4. Calculated Ln(|*T*|) and Ψ of the surface temperature along (a) *x*- and (b) *y*-profiles, for a square heat source of $w = h = 1$ mm, located at increasing depths: $|d| = 0$ (black), 0.25 (red), 0.5 (blue) and 1 mm (green). Results at two modulation frequencies are shown: $f_{lock\text{-}in} = 0.05$ Hz (left) and 6.4 Hz (right).

It must be mentioned, though, that increasing the depth of a heat source of a certain size provokes a signal reduction, which is not apparent in Figure 3.4 because the amplitudes are normalized.

3.2.4 Effect of modifying the size parameters for buried heat sources

Once we have looked at the influence of modifying both the width and the height of a surface breaking square heat source, we now want to see how the observed effects are modified in the case that the square heat source is buried deeper beneath the surface.

In Figure 3.5 we modify the width ($w = 0.5$, 1 and 2 mm) and the height ($h = 0.5$, 1 and 2 mm) of a $h = 1$ mm tall and $w = 1$ mm wide heat source buried at a depth $|d| = 0.5$ mm, respectively. For the sake of simplicity, we show the results at an intermediate modulation frequency $f_{lock\text{-}in} = 0.8$ Hz, for both *x*- and *y*-profiles.

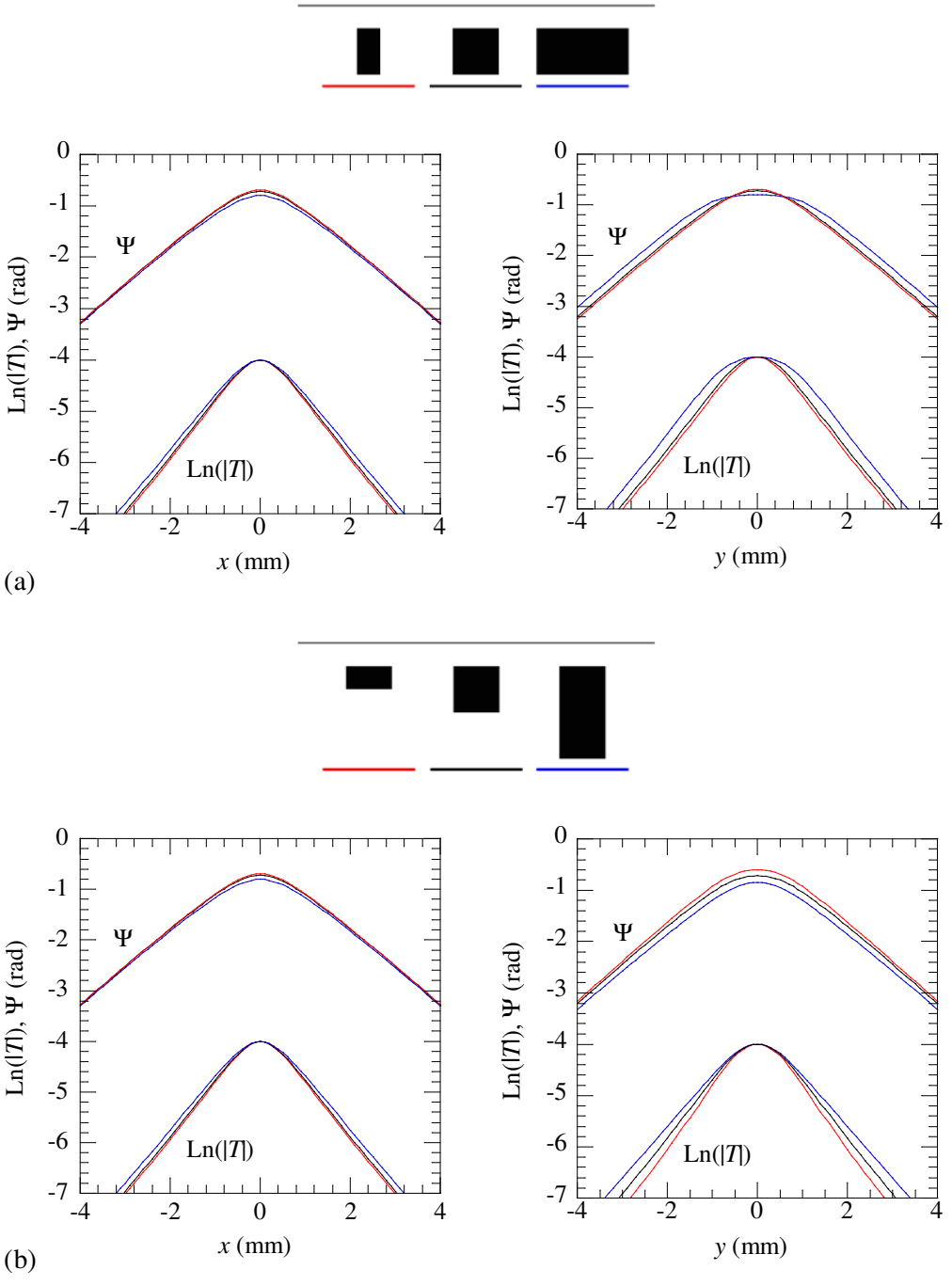

Figure 3.5. Calculated Ln(|*T*|) and Ψ of the surface temperature along *x*- (left) and *y*-profiles (right), for a heat source buried a depth |*d*| = 0.5 mm: (a) all with the same height *h* = 1 mm and three different widths, *w* = 0.5 (red), 1 (black) and 2 mm (blue) and (b) all with the same width *w* = 1 mm and three different

heights, h = 0.5 (red), 1 (black) and 2 mm (blue). All results are shown at the intermediate modulation frequency $f_{lock\text{-}in}$ = 0.8 Hz.

The results show the same features as in Figure 3.2 and Figure 3.3, but the profiles are closer to each other, meaning that the deeper the heat source, the more difficult it is to distinguish between different sizes. This evidences the ill-posed nature of the problem, since heat sources of different geometries can give rise to very similar temperature distributions. If, besides this, even a very small amount of noise is added, the surface temperature distribution corresponding to two heat sources could be undistinguishable, making the inverse problem of retrieving them very difficult to solve.

It is worth recalling that since all the surface temperatures shown in the analysis carried out above have been normalized, i.e., the maximum temperature in each case has been brought to 1 in order to make the direct comparison of the profiles possible, the decay of the signal with increasing depth is hidden, as well as the rise of the signal with increasing area of the heat source.

3.2.5 Amplitude and phase dependence with frequency

Finally, we represent the maximum values of both the phase, Ψ, and the amplitude, $|T|$, of the temperature distribution as a function of $f_{lock\text{-}in}$, in order to illustrate how they decrease with increasing modulation frequency.

In Figure 3.6 we compare the maximum values of $|T|$ (a) and Ψ (b) of the surface temperature distribution corresponding to a square heat source ($w = h$ = 1 mm) buried at increasing depths, namely, $|d|$ = 0.1, 0.5 and 1 mm, and emitting with a uniform flux Q = 1 Wm^{-2}. For a homogeneous square heat source, these maximum values logically correspond to the origin of the coordinates (0, 0, 0), just on top of the centre of the square.

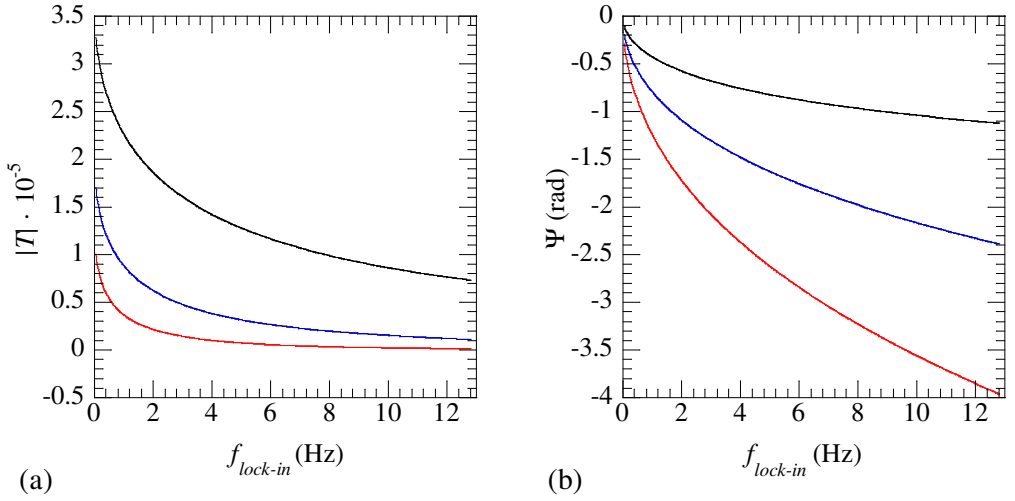

Figure 3.6. Maximum (a) $|T|$ and (b) Ψ of the surface temperature as a function of $f_{lock\text{-}in}$, for a square heat source of width w = 1 mm and height h = 1 mm, located at increasing depths: $|d|$ = 0.1 (black), 0.5 (blue) and 1 mm (red), emitting with a homogeneous flux Q = 1 Wm^{-2}.

As for the amplitudes, the signal decay can be checked when the heat source is buried gradually deeper. In all cases, both $|T|$ and Ψ decrease with increasing $f_{lock\text{-}in}$.

3.3 Other geometries

After the analysis of the solution of the direct problem performed with homogeneous rectangular heat sources, we now consider other geometries, in order to see if vibrothermography is able to distinguish between the different particular geometries of the heat sources. Two geometries different from rectangles are chosen, namely, semicircles and triangles, as representative of heat sources having smooth contours and sharp features, respectively.

To this purpose, we particularize the general form of the solution of the direct problem and we compare the surface temperature distributions calculated for these geometries with those for rectangular heat sources of similar dimensions. In this way, we can see how sensitive the solution of the direct problem is as for the particular geometries of the heat sources.

3.3.1 Semicircular heat sources

Considering a homogeneous semicircular heat source of radius R in plane Π (x = 0) submerged at a depth d (measured at the shallowest side of the semicircle), we consider two possible configurations, with the circular side upward and with the circular side downward, as depicted in Figure 3.1 (c) and (d), respectively. From now on, these two configurations for semicircular heat sources will be referred to as *sUp* and *sDown*, respectively.

For *sUp*, the position-dependent AC part of the surface temperature distribution can be written as

$$T_{AC\_sUp}(x,y,0)=\int_0^R\int_{\pi}^{2\pi}\frac{Q}{4\pi K}\frac{e^{-q\sqrt{x^2+(y-r'\cos\varphi')^2+(R+d+r'\sin\varphi')^2}}}{\sqrt{x^2+(y-r'\cos\varphi')^2+(R+d+r'\sin\varphi')^2}}r'dr'd\varphi' \tag{3.8}$$

while in the case of *sDown*, equation (3.6) reduces to

$$T_{AC\_sDown}(x,y,0)=\int_0^R\int_{0}^{\pi}\frac{Q}{4\pi K}\frac{e^{-q\sqrt{x^2+(y-r'\cos\varphi')^2+(d+r'\sin\varphi')^2}}}{\sqrt{x^2+(y-r'\cos\varphi')^2+(d+r'\sin\varphi')^2}}r'dr'd\varphi' \tag{3.9}$$

As mentioned above, we now wish to compare the surface temperature along both the x- and y-profiles for a semicircular heat source of radius R = 1 mm and a rectangular heat source of width w = 2R and height h = R, both reaching the sample surface (d = 0). Calculations are performed at an intermediate frequency $f_{lock\text{-}in}$ = 0.8 Hz.

Figure 3.7 (a) shows the comparison when the circular side of the semicircle is upward: although the different features of the upper part of the heat sources provoke little differences in x-profiles, differences in y-profiles allow us to clearly distinguish between the two shapes. However, when the circular side of the semicircle is downward (see Figure 3.7 (b)), the buried structure of the heat sources is barely distinguishable, as the signal is dominated by the shallowest contributions.

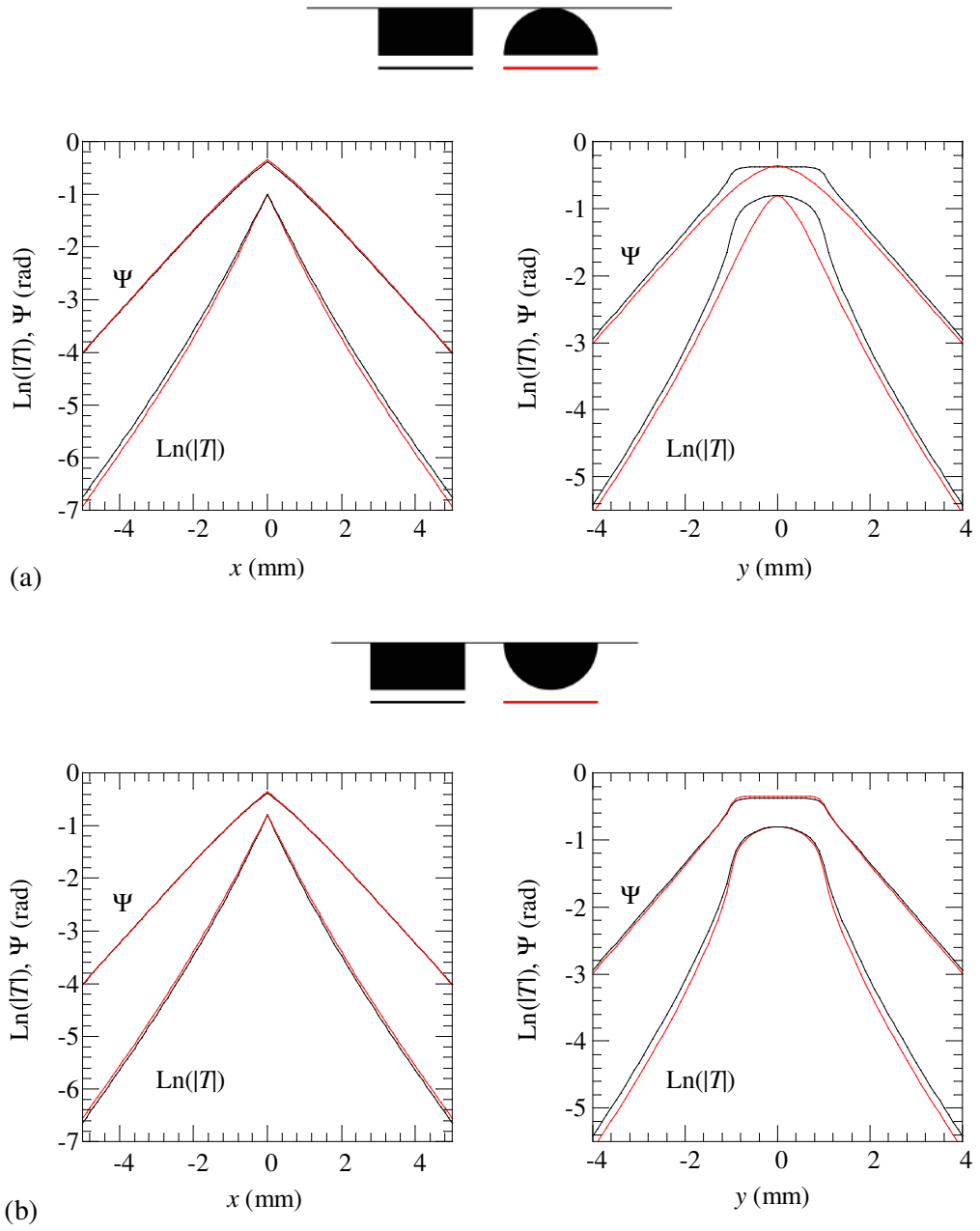

Figure 3.7. Calculated Ln(|*T*|) and Ψ of the surface temperature along *x*- (left) and *y*-profiles (right), for a rectangular heat source of width $w = 2$ mm and height $h = 1$ mm (black) and a semicircular heat source of radius $R = 1$ mm (red) with the circular side of the semicircle (a) upward and (b) downward, both reaching the sample surface ($d = 0$). Results are shown at an intermediate modulation frequency $f_{lock\text{-}in} = 0.8$ Hz.

3.3.2 Triangular heat sources

As mentioned in the introduction of this section, we want to check the ability of vibrothermography to distinguish between different shapes of heat sources of similar dimensions, this time having sharp features like corners.

We now consider a triangular homogeneous heat source of height h and width w in plane Π ($x = 0$) buried at a depth d (measured at the shallowest side of the triangle) and we also consider two possible configurations, with the apex on the middle upward and with the apex on the middle downward, as depicted in Figure 3.1 (e) and (f), respectively. Similarly as with semicircles, the two configurations for triangular heat sources will be referred to as *tUp* and *tDown* respectively, from now on.

For *tUp*, equation (3.6) can be particularized as

$$T_{AC\_tUp}(x,y,0) = \int_{-(h+d)}^{-d} \int_{(z'+d)w/(2h)}^{-(z'+d)w/(2h)} \frac{Q}{4\pi K} \frac{e^{-q\sqrt{x^2+(y-y')^2+z'^2}}}{\sqrt{x^2+(y-y')^2+z'^2}} dy'dz' \tag{3.10}$$

while in the case of *tDown*, equation (3.6) can be written as

$$T_{AC\_tDown}(x,y,0) = \int_{-(h+d)}^{-d} \int_{-(z'+d+h)w/(2h)}^{(z'+d+h)w/(2h)} \frac{Q}{4\pi K} \frac{e^{-q\sqrt{x^2+(y-y')^2+z'^2}}}{\sqrt{x^2+(y-y')^2+z'^2}} dy'dz' \tag{3.11}$$

Figure 3.8 (a) compares the surface temperature along the x- and y-profiles for a triangular heat source of width w = 1 mm and height h = 1 mm with the apex on the middle being upward and for a square heat source ($w = h$ = 1 mm), both reaching the sample surface (d = 0). Figure 3.8 (b) shows the same but with the apex on the middle of the triangle being downward. Calculations are performed at $f_{Lock\text{-}in}$ = 0.8 Hz.

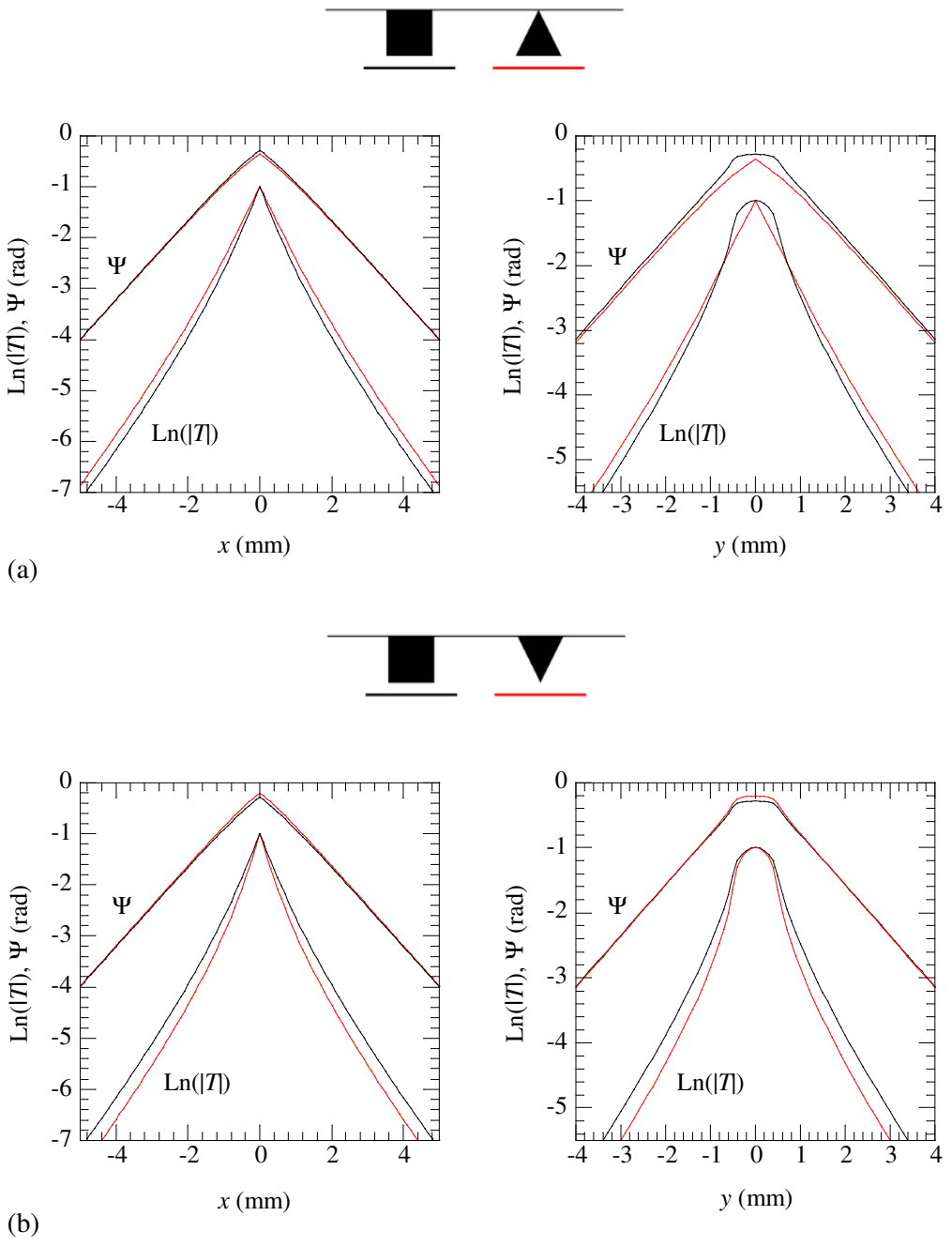

Figure 3.8. Calculated Ln(|*T*|) and Ψ of the surface temperature along *x*- (left) and *y*-profiles (right), for a square heat source of width $w = 1$ mm and height $h = 1$ mm (black) and a triangular heat source of $w = 1 = h = 1$ mm (red) with the apex on the middle (a) upward and (b) downward, both reaching the sample surface ($d = 0$). Results are shown at an intermediate modulation frequency $f_{lock\text{-}in} = 0.8$ Hz.

The conclusions of these simulations are similar to those obtained from the comparison between rectangles and semicircles, meaning that when the apex on the middle is upward, we can easily distinguish between the two shapes because of differences in *y*-profiles mainly, whereas when the apex on the middle is downward, the buried structure of the heat sources is harder to distinguish, but easier than in the case of semicircles. The reason for this is that the lack of heat sources on the upper side of the geometries is more abrupt in triangles than in semicircles, with respect to rectangular heat sources.

All the previous results indicate that the dimensions and location of the heat sources affect different aspects of the corresponding surface temperature distribution: depending on the parameter considered, high or low frequencies may be more sensitive, amplitude or phase may display more information and examining the temperature distribution closer or further away from the heat source may better reveal certain details.

Therefore, in order to characterize a certain heat source distribution, full amplitude and phase surface temperature maps need to be recorded, in the widest possible modulation frequency range, in order to gather as much information as possible.

This considered, in the vibrothermography experiments performed in this thesis, we will take data at nine modulation frequencies ranging from 0.05 to 12.8 Hz, which correspond to thermal diffusion lengths between 5 and 0.3 mm, respectively, in AISI 304 stainless steel (see Table 3.1).

Table 3.1. Modulation frequencies at which surface temperature data will be taken in vibrothermography experiments along with their corresponding thermal diffusion lengths, for AISI 304.

$f_{lock\text{-}in}$ **(Hz)**	0.05	0.1	0.2	0.4	0.8	1.6	3.2	6.4	12.8
μ **(mm)**	5.04	3.56	2.52	1.78	1.25	0.89	0.63	0.44	0.31

We have chosen 0.05 Hz as our lowest modulation frequency because, as explained in the statement of the direct problem, the rear surface of the sample does not affect the temperature distribution at the measuring surface. At lower $f_{lock\text{-}in}$, such as 0.025 Hz, surface temperature data recorded in vibrothermography experiments using our AISI 304 samples may be affected by the rear surface of the sample, which would make it necessary to consider in our model reflected images of the heat sources at the rear surface of the sample.

As for the upper limit of our set of modulation frequencies, 12.8 Hz has been chosen because it provides enough spatial resolution considering the size of the heat sources in our experiments, i.e., a thermal diffusion length of 0.3 mm provides detailed enough information in order to retrieve shallow heat sources of a similar size as the defined standard square ($w = h = 1$ mm).

4 Experimental setup and verification of the direct problem

This section describes the construction of samples containing inner calibrated heat sources, as well as the experimental equipment needed in order to perform vibrothermography experiments in the lock-in regime. After analysing experimental data and dealing with the frequency response of the equipment, the optimum experimental procedure for data acquisition is described, as well as the post-processing of the data.

With the aim of verifying the predictions of the theoretical simulations of the direct problem presented in section 3, we perform vibrothermography experiments using samples with calibrated inner heat sources.

Below, the experimental setup in our vibrothermography experiments is described, focusing on the construction of metallic samples with calibrated inner heat sources, as well as on the equipment needed for the performance of the experiments in the lock-in regime.

Experimental data are then shown and analysed. Since lock-in thermography is based on measuring the oscillating part of the surface temperature of the sample, we deal with the fact that data are affected by the transient temperature rise of the sample, proposing three different methods to remove it and reaching to conclusions regarding the optimum experimental conditions for our vibrothermography experiments.

Finally, the issue that the experimental equipment has a non-flat response with frequency that overlaps the frequency dependence of our signal is also addressed, and the data post-processing in order to remove it is described.

4.1 Experimental setup

4.1.1 Construction of samples with calibrated inner heat sources

In order to prepare metallic samples containing calibrated heat sources, we designed two AISI 304 stainless steel parts with a common flat surface, that can be joined and pressed together by means of two screws. The common flat surface is well rectified in both halves, and it is where a thin Cu foil (38 μm thick) is placed, representing a vertical homogeneous defect. The use of other materials in order to produce an inhomogeneous heat generation in vibrothermography experiments will be addressed further in the study.

Figure 4.1 shows the features of the sample and the Cu foils placed in the common surface of the two halves.

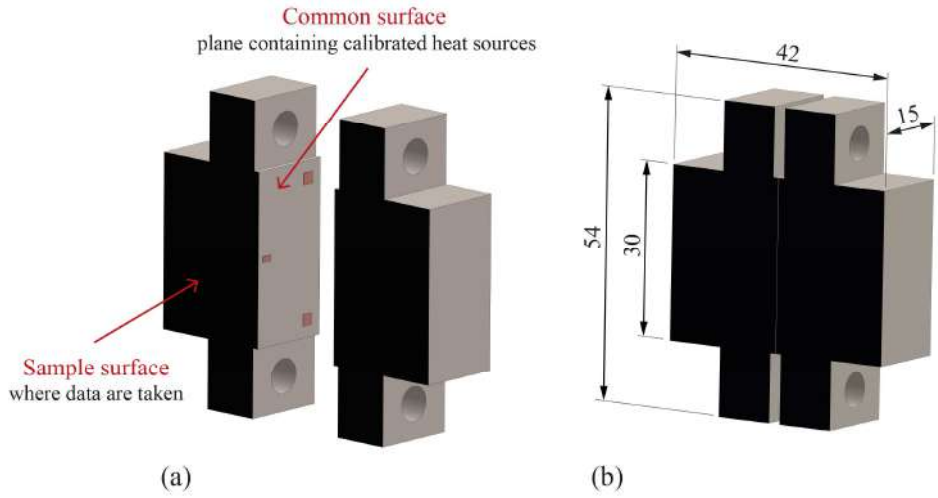

Figure 4.1. Diagram of the AISI 304 stainless steel sample (a) open with a calibrated heat source on the common surface between the two halves and (b) closed with dimensions (in mm).

When the ultrasounds are launched into the sample, friction takes place between the Cu foil and the steel surfaces and, in order to guarantee that the surface temperature that will be recorded only corresponds to friction at the location of the Cu foil and not to friction between the steel planes somewhere else on the common surface, two additional Cu foils

are placed at the back side, near the rear surface and far enough from the measuring surface so that the thermal waves generated there do not affect the data.

The dimensions of the Cu foil representing the defect and its location on the common surface with respect to the surface where data are taken, which is perpendicular to it, are measured by means of an optical stereoscope. In order to enhance the emissivity of the sample surface, black paint is applied on it with the two halves joined with the screws, without the Cu films.

It is worth mentioning that an important point when attaching the two halves of the sample is to tighten the two screws with a similar torque, so as to guarantee that the whole area of the Cu foil will rub homogeneously during the experiment. As mentioned in section 1.2.3 when explaining the mechanisms of heat generation, heat production at a real defect can be modified depending on the opening and closure stresses [73]. In the case of our samples with calibrated heat sources, care has to be taken not to over-tighten the screws, since it can reduce the relative motion between the Cu foil representing the defect and the steel planes, provoking a signal decay of even its complete disappearance. Similarly, if the two halves are attached too loosely, no friction between the Cu foil and the steel planes takes place either and the foil risks losing its position in the sample.

4.1.2 Experimental equipment

The experimental equipment typically used in vibrothermography experiments has been detailed in section 1.2.1, paying special attention to the two main elements: the ultrasound system and the IR camera.

In our vibrothermography experiments, the needed equipment elements are the following: an ultrasound system, two function generators, an IR camera and a PC with the specific IR imaging software for image acquisition and control of the lock-in process. Figure 4.2 shows all these elements.

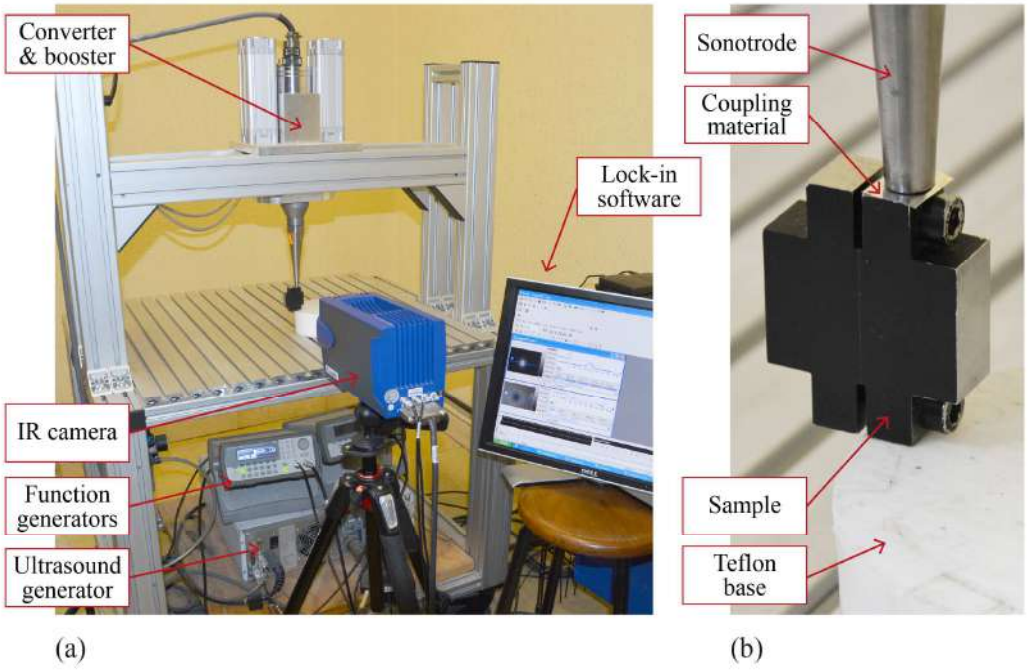

Figure 4.2. (a) Elements of the experimental equipment in our vibrothermography experiments and (b) detail of the sample being held in a vertical position by the sonotrode, with a coupling Al film in between.

Ultrasound excitation is performed with the UTvis equipment from Edevis. The US converter turns the high frequency electrical oscillations created by the ultrasound generator into mechanical oscillations. The sonotrode launches the ultrasounds into the sample, at the same time as it holds it in a vertical position.

The basis of our sample stands on a Teflon base in such a way that only one of the halves is fixed between the base and the sonotrode, so that the other half can vibrate freely. Also, a thin adhesive Al film is placed between the steel sample and the titanium sonotrode, as mechanical coupling material.

The ultrasound generator provides ultrasound frequencies ranging between 15 and 25 kHz, with a maximum power of 2 kW at 20 kHz. Excitation can be performed either at a fixed ultrasound frequency or modulating the ultrasound frequency within the range mentioned.

For the experiments in the lock-in regime, monofrequent ultrasounds are amplitude modulated at $f_{lock\text{-}in}$. The optimum ultrasound frequency is previously determined so as to get the maximum heat generation at the location of the Cu foil. In order to know the

resonant frequency of the sample, we first perform frequency sweeps (with the Cu foils inside) at constant ultrasound amplitude. The ultrasound frequency is controlled by means of a function generator, by applying voltages that range from 0 to 10 V, corresponding to 15 and 25 kHz, respectively. Similarly, the ultrasound amplitude for the frequency sweeps is chosen by means of a second function generator, by applying a constant voltage that can range from 0 to 400 mV. The frequency sweeps are performed slowly enough to appreciate temperature variations accurately: the transition between 15 and 25 kHz is performed within 20 s.

Provided that the structural resonances depend on both the sample geometry and the location of the exciter on the sample, in the case of performing experiments with different samples, either containing calibrated or real defects, a new frequency sweep is required for each sample and configuration. All the experiments with calibrated heat sources shown in this thesis are carried out using the same AISI 304 stainless steel sample previously described. Figure 4.3 shows a frequency sweep using this sample, where a main peak on the surface temperature on top of the Cu foil as a function of the ultrasound frequency can be clearly seen, indicating that the optimum ultrasound frequency is around 22,900 Hz.

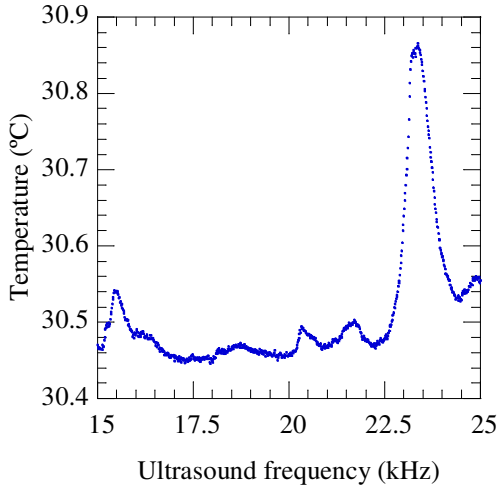

Figure 4.3. Temperature on top of a heat source during a frequency sweep using the AISI 304 sample.

Once the optimum ultrasound frequency so as to activate the defect is set, amplitude modulation of the ultrasound excitation is performed for the vibrothermography experiments: we modulate the ultrasound amplitude at the nine $f_{lock\text{-}in}$ defined in Table 3.1

by means of a function generator. The amplitude of the modulation may be increased or decreased: since the signal weakens with increasing modulation frequency, it is interesting to have the opportunity to increase the ultrasound power at high modulation frequencies in order to partially compensate for this signal reduction.

Moreover, at this point it is worth mentioning that we have considered two regimes of modulation amplitude, that can be understood as ultrasound electrical power and to which we will refer as *high US power* and *low US power*, from now on. Experiments using high US power have been performed with the intention of maximizing the vibrothermographic signal, especially when the Cu foil is very small or it is buried very deep, with values around 250-300 W. On the contrary, low US power, with values around 25-40 mW, has been used with the aim of preventing the experiments from being performed in transient state, i.e., when the DC part of the temperature of the sample is still rising due to the energy deposition, as well as to keep the non-destructive nature of vibrothermography. This issue will be addressed more in detail in section 4.2. Anyway, it is worth clarifying that despite calling it high US power (in order to distinguishing it from low US power), it is actually low in comparison with the power typically applied in the burst regime.

The thermal radiation emitted from the sample surface is captured using a JADE J550M infrared camera, from Cedip, that features a cooled 320 x 240 px (full frame) InSb focal plane array detector, which is sensitive in the wavelength range of 3.6 to 5 μm. The camera has a noise equivalent temperature difference (NETD) of 25 mK, measured at 25 ºC and over a detector integration time of 1600 μs, according to the manufacturer. Each pixel averages the temperature of a 137 μm square on the sample at the minimum working distance, which is about 25 cm. The maximum frame rate at full frame is 148 Hz, but it can be increased by working at the *subwindowing modes*, that consist in reducing the picture size so that the frame rate may be increased. This way, the frame rate can be increased up to 336 Hz by working at half frame (160 x 120 px), up to 446 Hz at quarter frame (64 x 120 px) or even up to 605 Hz by setting the custom size (64 x 8 px).

In experiments using low US power, we mostly work at half frame and capture images at a fixed frame rate of 320 Hz, taking a certain number of frames per modulation period that range from 6,400 (at 0.05 Hz) to 25 (at 12.8 Hz). We average the signal over 32,000 images regardless of the modulation frequency, which implies exciting the sample during a certain number of periods that range from 5 (at 0.05 Hz) to 1,280 (at 12.8 Hz).

Data acquisition is done using *Altair* and *Altair LI* infrared imaging software from FLIR for live registration and lock-in applications, respectively, which allow for complex capturing

procedures such as externally triggering or using varying frame rates and record durations. Also, the lock-in process can be carried out on-line on the live image sequence, as well as off-line on the recorded image sequence. Once the image capturing and the lock-in process at each $f_{lock\text{-}in}$ are carried out, the surface amplitude and phase thermograms are displayed and saved. In next section, these experimental data are shown and analysed.

4.2 Verification of the direct problem

Experimental data refer to surface amplitude and phase thermograms at each one of the nine $f_{lock\text{-}in}$ defined in our set of modulation frequencies, from vibrothermography experiments in the lock-in regime. Thus, experimental data consist of 18 images that can be easily handled as matrices for further treatment.

Figure 4.4 shows experimental amplitude and phase thermograms in grey scale for a rectangular Cu foil of width w = 1.4 mm and height h = 2.3 mm buried at a depth $|d|$ = 95 µm, obtained in an experiment using high US power at $f_{lock\text{-}in}$ = 0.1 (a), 0.8 (b) and 6.4 Hz (c), representing an intermediate modulation frequency and the ones close to the ends of our set of modulation frequencies.

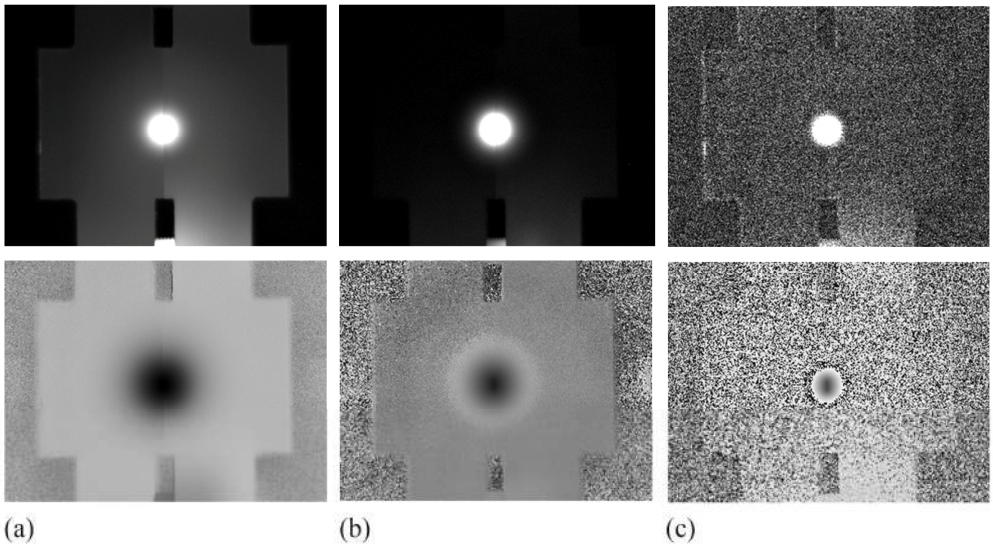

Figure 4.4. Amplitude (top) and phase (bottom) thermograms obtained at $f_{lock\text{-}in}$ = 0.1 (a), 0.8 (b) and 6.4 (c) Hz, for with a square heat source of width w = 1.4 mm and height h = 2.3 mm, buried at a depth $|d|$ = 95 µm, in an experiment using high US power. Grey scales are not comparable.

At first sight, it can be seen that both the amplitude and phase thermograms corresponding to 0.1 and 6.4 Hz have a clearly different appearance. Indeed, when analysing these thermograms obtained in an experiment using high US power, two different types of behaviour are observed depending on the modulation frequency, that become more obvious as we analyse the thermograms further away from the heat source. These results are better appreciated if we draw the *x*-profiles and compare them to the predictions of the theory (see Figure 4.5).

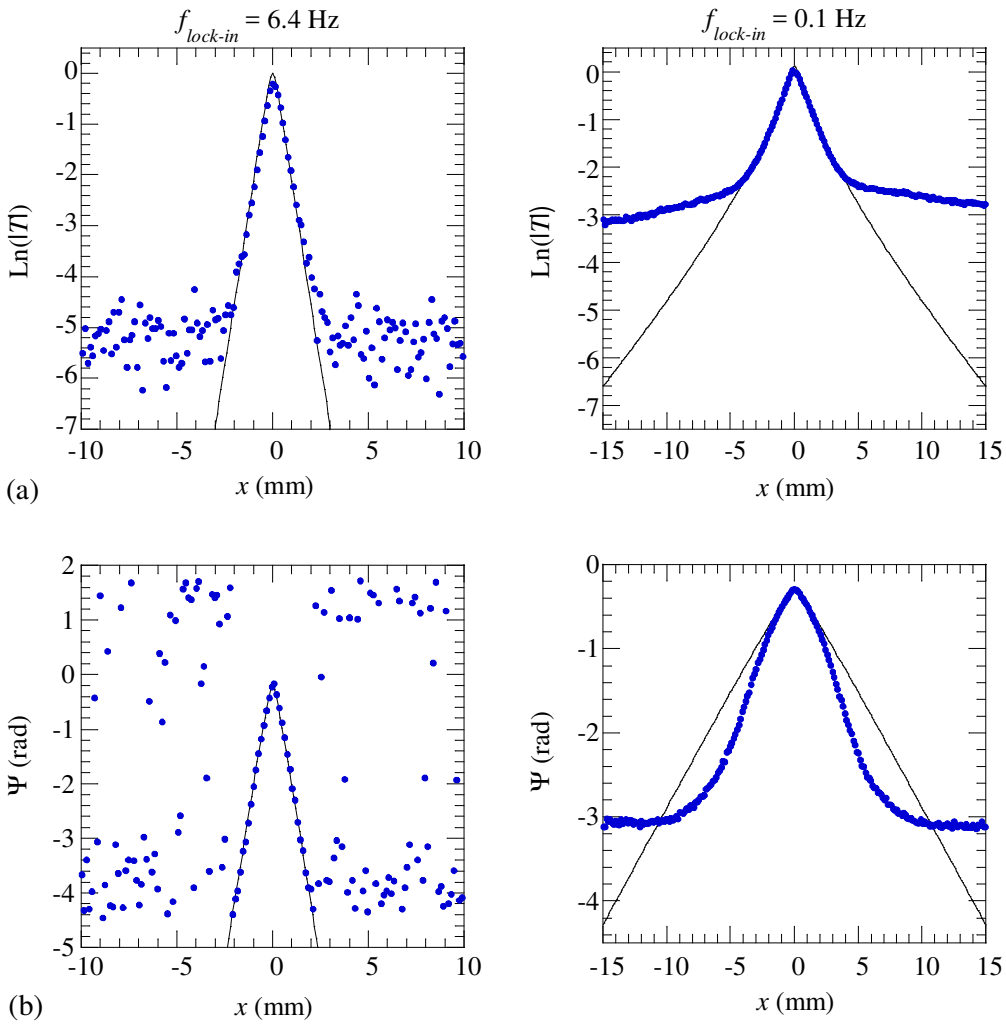

Figure 4.5. Ln(|*T*|) (a) and Ψ (b) of the surface temperature *x*-profiles obtained with a rectangular calibrated heat source of width w = 1.4 mm and height h = 2.3 mm, buried at a depth $|d|$ = 95 µm, at $f_{lock\text{-}in}$ = 6.4 Hz (left) and 0.1 Hz (right) in experiments using high US power. Blue dots stand for experimental raw data and solid lines are the predictions of the theory.

As can be observed, at 6.4 Hz both the amplitude and phase *x*-profiles match the predictions of the model: starting on top of the heat source, the signal decreases until the noise level is reached (down to -5.5 in Figure 4.5 (a)), whereas further away the amplitude is dominated by noise and, accordingly, the phase is random.

At 0.1 Hz, however, neither the amplitude nor the phase *x*-profiles match the predictions of the theory: although they coincide on top of the heat source, they soon differ from the model and the noise level cannot be reached, even though the size of the thermogram allows for a far enough measurement to reach it. Instead, far away from the heat source there is a remaining amplitude and a rather stable phase, which points out the existence of a signal in regions where the thermal wave is already faded away. This effect is related to the fact that vibrothermography data are recorded in transient state, i.e., while the temperature of the sample is still increasing all over the sample volume.

In order to give an idea of how the DC temperature of the sample rises in an experiment using high US power, Figure 4.6 (a) shows the evolution of the surface temperature as a function of time, both on top of the heat source (red line) and also far away from it along *x*-profile (blue line), recorded at $f_{lock\text{-}in}$ = 0.1 Hz. In Figure 4.6 (b), both the AC and the DC components of the surface temperature can be appreciated in detail.

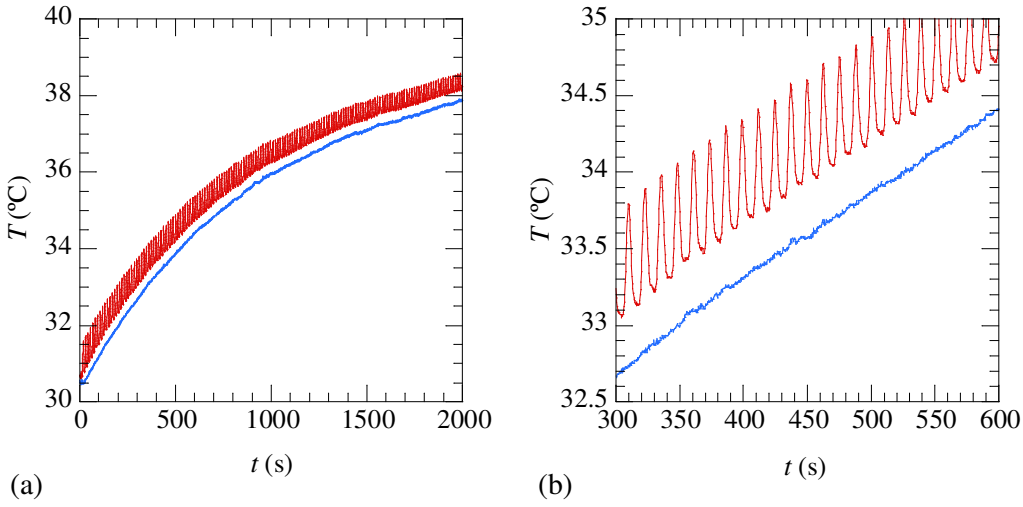

Figure 4.6. (a) Evolution of the surface temperature as a function of time in an experiment using high US power (250 W), on top of the Cu foil (red line) and far away from it along *x*-profile (blue line) recorded at $f_{lock\text{-}in}$ = 0.1 Hz and (b) detail of (a) in a shorter time interval, showing the AC and DC parts of the surface temperature.

It is worth noting that after 30 minutes, the sample has not reached the stationary state yet. The rising temperature of the sample has a certain Fourier content, which is more significant at low frequencies, as the temperature rise is slow. These Fourier components add up to the thermal signal generated at the heat source.

According to this, the recorded experimental surface temperature, $T_{exp} = |T_{exp}| e^{i\Psi_{exp}}$, is actually the sum of the AC component due to the oscillating heat source, $T_{osc} = |T_{osc}| e^{i\Psi_{osc}}$, and the Fourier component due to the transient temperature rise all over the sample volume, $T_{trans} = |T_{trans}| e^{i\Psi_{trans}}$

$$T_{exp} = T_{osc} + T_{trans} \tag{4.1}$$

As mentioned above, thermograms taken at low modulation frequencies are more strongly affected by the transient temperature rise of the sample than those taken at high frequencies, which may even not be affected at all, as can be checked in Figure 4.5 (left).

This additional signal needs to be removed from experimental data in order to obtain the pure oscillating contribution to the surface temperature, as described in the theoretical model. In the following sections we deal with this problem, proposing and analysing three methods for the elimination of the Fourier component in experimental data.

4.2.1 Subtraction of the Fourier component

This method for the elimination of the Fourier component consists in subtracting it from experimental data. To do so, we obtain the Fourier component of the transient temperature rise by evaluating the amplitude and phase signals far away from the heat source where the thermal wave is already damped in a certain profile, for instance, *x*-profile. Then, we subtract it from the experimental data all along the profile, obtaining the pure oscillating contribution to the surface temperature. With this method we are assuming that the Fourier component is the same all along the considered profile.

Figure 4.7 illustrates this method for *x*- and *y*-profiles in an amplitude thermogram obtained at $f_{lock\text{-}in}$ = 0.1 Hz.

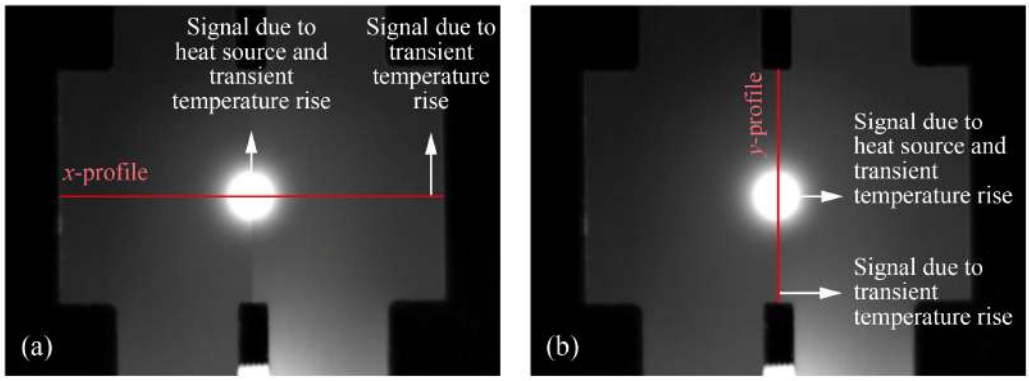

Figure 4.7. Identification of the Fourier component due to the transient temperature rise of the sample all along (a) *x*- and (b) *y*-profiles in an amplitude thermogram obtained at $f_{lock\text{-}in}$ = 0.1 Hz in an experiment using high US power.

The subtraction of the Fourier component along a profile is carried out in the complex plane according to equation (4.1)

$$\mathrm{Re}\left(T_{osc}\right) = \mathrm{Re}\left(T_{exp}\right) - \mathrm{Re}\left(T_{trans}\right) \tag{4.2}$$

$$\mathrm{Im}\left(T_{osc}\right) = \mathrm{Im}\left(T_{exp}\right) - \mathrm{Im}\left(T_{trans}\right) \tag{4.3}$$

being, for all temperature components in equation (4.1)

$$\mathrm{Re}\left(T\right) = \left|T\right|\cos\Psi \tag{4.4}$$

$$\mathrm{Im}\left(T\right) = \left|T\right|\sin\Psi \tag{4.5}$$

Once the real and imaginary parts of T_{osc} are known, we can go back to amplitude and phase using

$$\left|T_{osc}\right| = \sqrt{\mathrm{Re}\left(T_{osc}\right)^2 + \mathrm{Im}\left(T_{osc}\right)^2} \tag{4.6}$$

$$\Psi_{osc} = \tan^{-1}\left(\frac{\mathrm{Im}\left(T_{osc}\right)}{\mathrm{Re}\left(T_{osc}\right)}\right) \tag{4.7}$$

In order to correct whole thermograms, we follow this procedure for all the rows or horizontal profiles within a thermogram. The handicap of this method is that it relies on the assumption that the contribution of the transient component is uniform all along a certain profile, which is not rigorously true because the temperature rise provoked by the heat source, that acts as a continuous heat deposition on top of which modulation occurs, is a function of the distance to the heating region. But, despite this limitation, this method is fast and easy to implement and gives rather satisfactory results in terms of coincidence between experiments and simulations with slight discrepancies at low frequencies.

We have performed experiments using high US power in steady state, i.e., when the temperature of the sample has reached equilibrium, and these data are very similar to those obtained after the subtraction of the Fourier component in transient measurements, confirming that the origin of the additional signal is the increasing temperature of the sample.

Figure 4.8 compares phase thermograms at $f_{lock\text{-}in}$ = 0.1 Hz obtained in experiments carried out in both transient (a) and stationary (b) states, using high US power. As can be checked, in the phase thermogram corresponding to steady state, stable phase values are found all around the heat source and, further away, where the amplitude gets dominated by noise, the phase becomes rather random, which is an indication of the absence of any remaining signal.

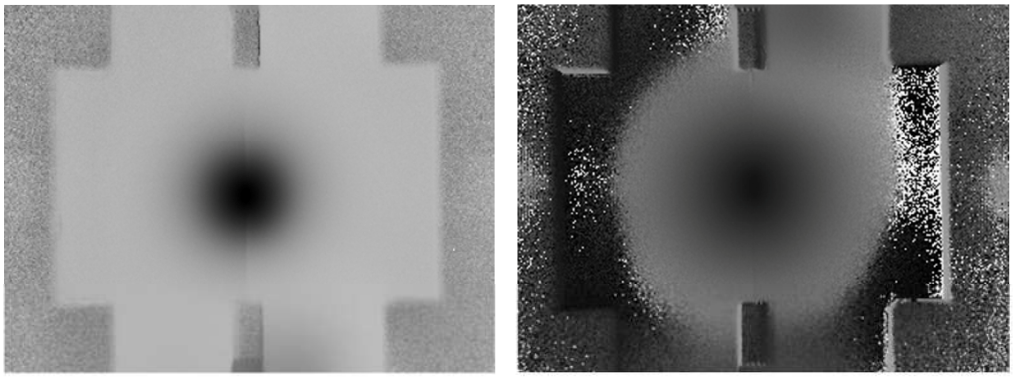

Figure 4.8. Comparison of surface temperature phase thermograms obtained at $f_{lock\text{-}in}$ = 0.1 Hz in experiments using high US power performed in transient (a) and stationary (b) state.

In order to prove that the subtraction of the Fourier component all along a certain profile corrects experimental data taken in transient state using high US power and makes them coincide with the predictions of the theory, Figure 4.9 shows the Ln(|*T*|) (a) and Ψ (b) of the surface temperature *x*-profile for a rectangular heat source of dimensions w = 1.87 mm and h = 2.77 mm, buried at a depth $|d|$ = 117 µm. Data taken in transient state, both raw (blue dots) and corrected (red dots), are compared with data taken in steady state (green dots), at $f_{lock\text{-}in}$ = 0.1 Hz.

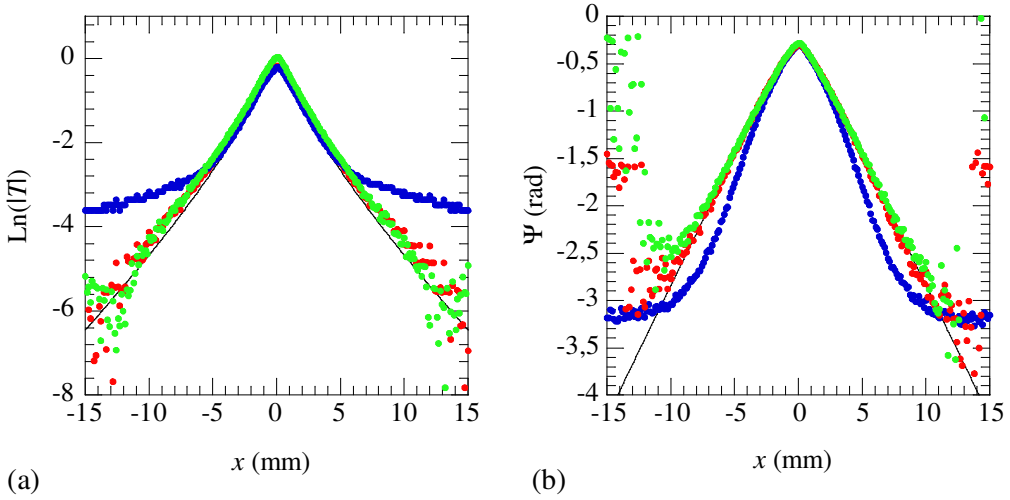

Figure 4.9. Experimental Ln(|*T*|) (a) and Ψ (b) of the surface temperature *x*-profile obtained with a rectangular calibrated heat source of width w = 1.87 mm and height h = 2.77 mm, buried at a depth $|d|$ = 117 µm, at $f_{lock\text{-}in}$ = 0.1 Hz. Blue dots stand for raw data taken in transient state, red dots correspond to processed data taken in transient state, green dots represent raw data taken in steady state and solid lines are the predictions of the theory.

Performing the experiments in steady state could be a suitable method for the elimination of the Fourier component due to the transient temperature rise of the sample, but it is time consuming and, in addition, the equilibrium of the sample temperature may be found significantly above ambient temperature: typically between 10 and 30ºC above ambient temperature, taking about 45 minutes to reach the equilibrium at 0.8 Hz in experiments using high US power.

Under these conditions, we have checked that our experiments are not completely non-destructive, since we have observed fretting damage in the Cu foil representing the defect. Logically, this makes the results after vibrothermography experiments not repeatable,

which in turn reduces the reliability of the technique. As mentioned in the introduction, researchers have concluded that, in real cracks, the application of high vibrational stresses can alter the crack surface [70] leading to plastic deformation, fretting or melting, as well as provoke crack growing [3].

Thus, mainly for time, reproducibility and reliability reasons, at this stage we decide that taking data in transient state and performing the post-processing described is more appropriate than taking data in steady state. Since the transient contribution affects low frequencies mainly, we only correct experimental data obtained at modulation frequencies $f_{lock\text{-}in} \leq 0.8$ Hz, as for higher modulation frequencies raw data agree with the predictions of the theory.

To illustrate this, Figure 4.10 shows Ln(|*T*|) (a) and Ψ (b) of the surface temperature *x*-profile for a *tUp* of width $w = 1.76$ mm and height $h = 1.72$ mm, buried at a depth $|d| = 420$ µm, obtained at $f_{lock\text{-}in} = 0.1$ Hz (processed data, in red) and 6.4 Hz (raw data, in blue), in experiments using high US power.

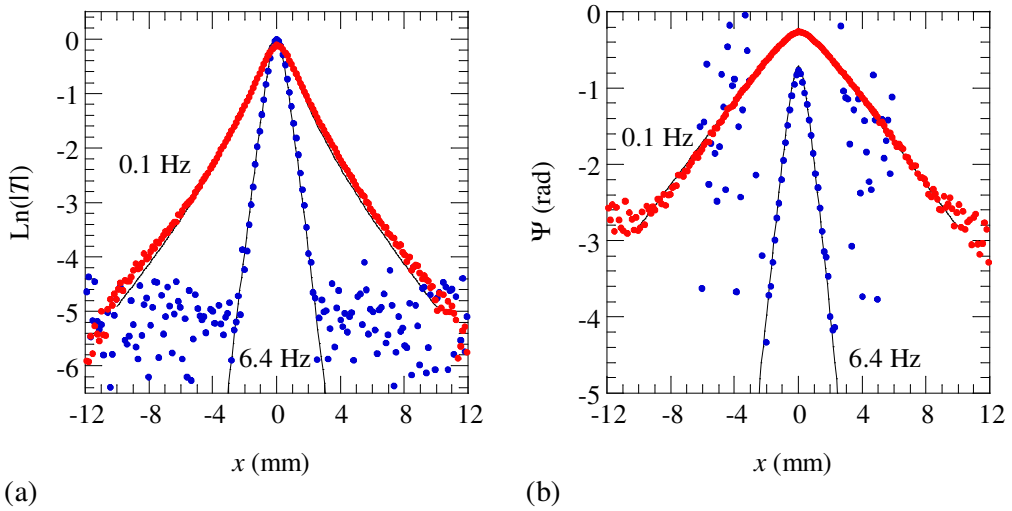

Figure 4.10. Experimental Ln(|*T*|) (a) and Ψ (b) of the surface temperature *x*-profile obtained with a *tUp* of width $w = 1.76$ mm and height $h = 1.72$ mm, buried at a depth $|d| = 420$ µm, at $f_{lock\text{-}in} = 6.4$ Hz and 0.1 Hz, in experiments using high US power. Dots represent experimental data: processed for 0.1 Hz (red) and raw for 6.4 Hz (blue). The solid lines are the predictions of the theory.

As can be seen, both processed data at 0.1 Hz and raw data at 6.4 Hz are in agreement with the predictions of the theory very satisfactorily.

4.2.2 Temperature history fitting

Another method to remove the transient component is to rewrite surface amplitude and phase thermograms in such a way that the DC temperature is not taken into account.

Whereas in the previous section each row or horizontal profile needed to be processed independently in order to correct the whole thermograms, this method generates whole amplitude and phase thermograms discarding the contribution of the transient temperature rise in each pixel. In this sense, the main handicap of the previous method is overcome, which is the assumption of uniform contribution of the transient component all along a certain profile.

This method is based on analysing the temperature history, $T = f(t)$, of all the pixels that compose the temperature maps of the sample surface. The set of data points that compose the temperature history of each pixel is then fitted to a mathematical function that includes an oscillatory function, which fits the AC part of the temperature history, and a 3rd order polynomial function, in order to fit the transient temperature rise at each pixel during the experiment, as we have checked that the 3rd order polynomial fits the DC temperature rise well enough.

Equation (4.8) expresses this mathematical function, in which the oscillatory function takes into account both the signal generated at the fundamental modulation frequency, $f_{lock\text{-}in}$, and the signal generated at twice the fundamental modulation frequency, with the aim of considering eventual excursions from perfect harmonicity

$$\begin{aligned} T_{exp}(t) = {} & \mathrm{S}_1 \sin\left(2\pi f_{lock\text{-}in} t\right) + \mathrm{C}_1 \cos\left(2\pi f_{lock\text{-}in} t\right) + \\ & \mathrm{S}_2 \sin\left(4\pi f_{lock\text{-}in} t\right) + \mathrm{C}_2 \cos\left(4\pi f_{lock\text{-}in} t\right) + \mathrm{P}_3 t^3 + \mathrm{P}_2 t^2 + \mathrm{P}_1 t + \mathrm{P}_0 \end{aligned} \tag{4.8}$$

Figure 4.11 (a) shows experimental data and fitting to equation (4.8) corresponding to a pixel located on top of the centre of the heat source and also at 1.15 and 2.30 mm from the centre of the heat source along *x*-profile, at 0.1 Hz, for a rectangular heat source of width w = 2.2 mm and height h = 0.88 mm, buried at a depth $|d|$ = 150 µm, in an experiment using high US power. Similarly, Figure 4.11 (b) shows the resultant curve fitting for a pixel located on top of the centre of the heat source and also at 1.15 and 2.30 mm along *y*-profile, at 6.4 Hz, for the same heat source.

As can be observed, although noise makes data at high modulation frequencies more challenging to fit, both the AC and DC components of the surface temperature are very

well fitted, regardless of the modulation frequency, distance and orientation with respect to the centre of the heat source.

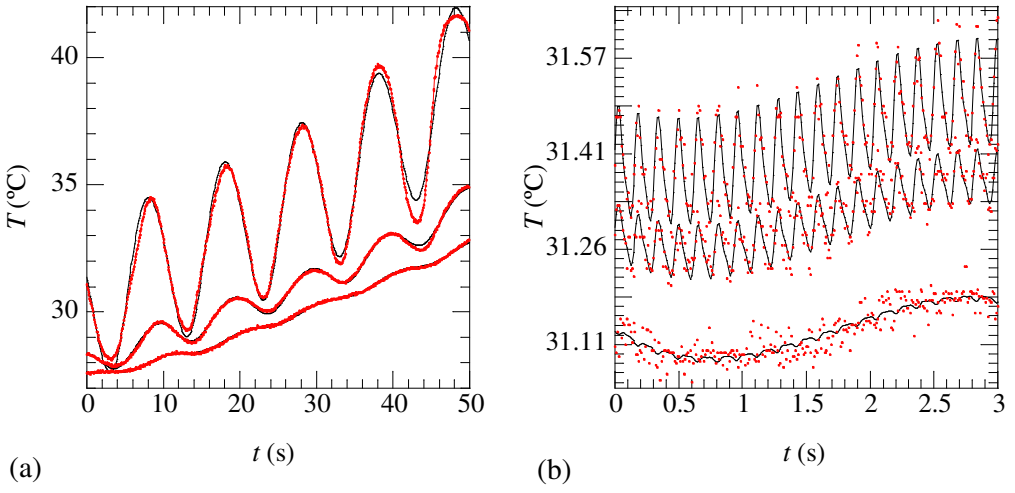

Figure 4.11. Fitting of the surface temperature history of a pixel located (a) on top of the heat source and at 1.15 and 2.30 mm from it along *x*-profile at 0.1 Hz and (b) on top of the heat source and at 1.15 and 2.30 mm from it along *y*-profile at 6.4 Hz. Red dots stand for experimental data corresponding to a rectangular heat source of width w = 2.2 mm and height h = 0.88 mm, buried at a depth $|d|$ = 150 µm in an experiment using high US power and black lines represent the fitting to equation (4.8).

After the curve fitting procedure, all the coefficients in equation (4.8) are determined for each pixel in the image, but only S_1 and C_1 account for the generation of the new amplitude $|T_{exp}|$ and phase Ψ_{exp} thermograms, according to the following expressions

$$\left|T_{exp}\right| = \sqrt{S_1^{\,2} + C_1^{\,2}} \tag{4.9}$$

$$\Psi_{exp} = \tan^{-1}\left(\frac{S_1}{C_1}\right) \tag{4.10}$$

In this way, the transient temperature rise of the sample and the second harmonic contributions are discarded and the thermograms are only composed of the AC part of the surface temperature at the fundamental modulation frequency, $f_{lock\text{-}in}$. However, a problem that may arise when generating phase thermograms with this method is that equation (4.10) can take different values depending on the instant within a modulation period in which the lock-in process has started: what we want to measure is the phase lag with respect to the

excitation at the different modulation frequencies. For this reason, it is recommended to start data acquisition at zero phase of the reference (excitation) signal. In order to visualize the differences between the processed surface amplitude and phase thermograms with this method and the original experimental ones, Figure 4.12 shows the results for two square Cu foils of $w_1 = w_2 = h_1 = h_2 = 1.2$ mm, buried at a depth $|d_1| = |d_2| = 120$ µm and with a separation distance between centres of 1.2 mm, obtained at $f_{lock\text{-}in} = 0.2$ Hz.

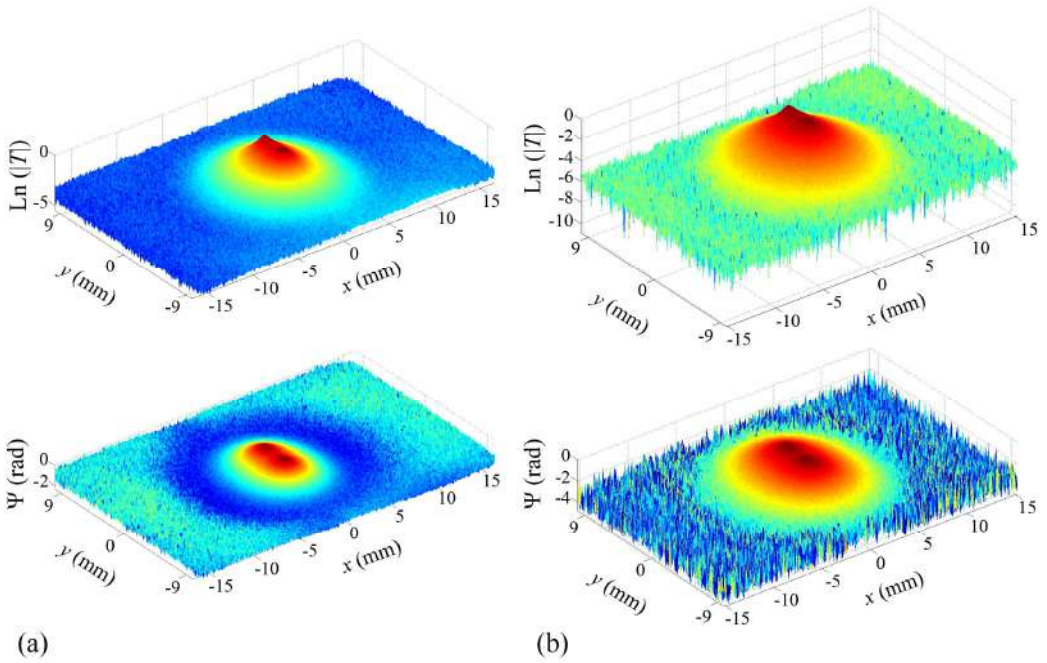

Figure 4.12. Original experimental (a) and processed by fitting of the temperature history of each pixel (b) Ln(|*T*|) (top) and Ψ (bottom) surface thermograms for two square Cu foils of $w_1 = w_2 = h_1 = h_2 = 1.2$ mm, buried at a depth $|d_1| = |d_2| = 120$ µm and with a separation distance between centres of 1.2 mm, at $f_{lock\text{-}in} = 0.2$ Hz, in an experiment using high US power.

It can be seen that processed amplitude and phase thermograms after the fitting of the temperature history of each pixel do not contain the contribution of the transient temperature rise: the phase becomes random where the thermal wave vanishes and the amplitude reaches the noise level.

As for coincidence with the predictions of the theory, Figure 4.13 compares the surface temperature *x*- and *y*-profiles generated with this method and those corrected with the Fourier component subtraction method, for two rectangular Cu foils of width $w_1 = w_2 = 0.9$

mm and height $h_1 = h_2 = 2$ mm, buried at a depth $|d_1| = |d_2| = 260$ µm and with a separation distance between centres of 1 mm, at $f_{lock\text{-}in} = 0.8$ Hz.

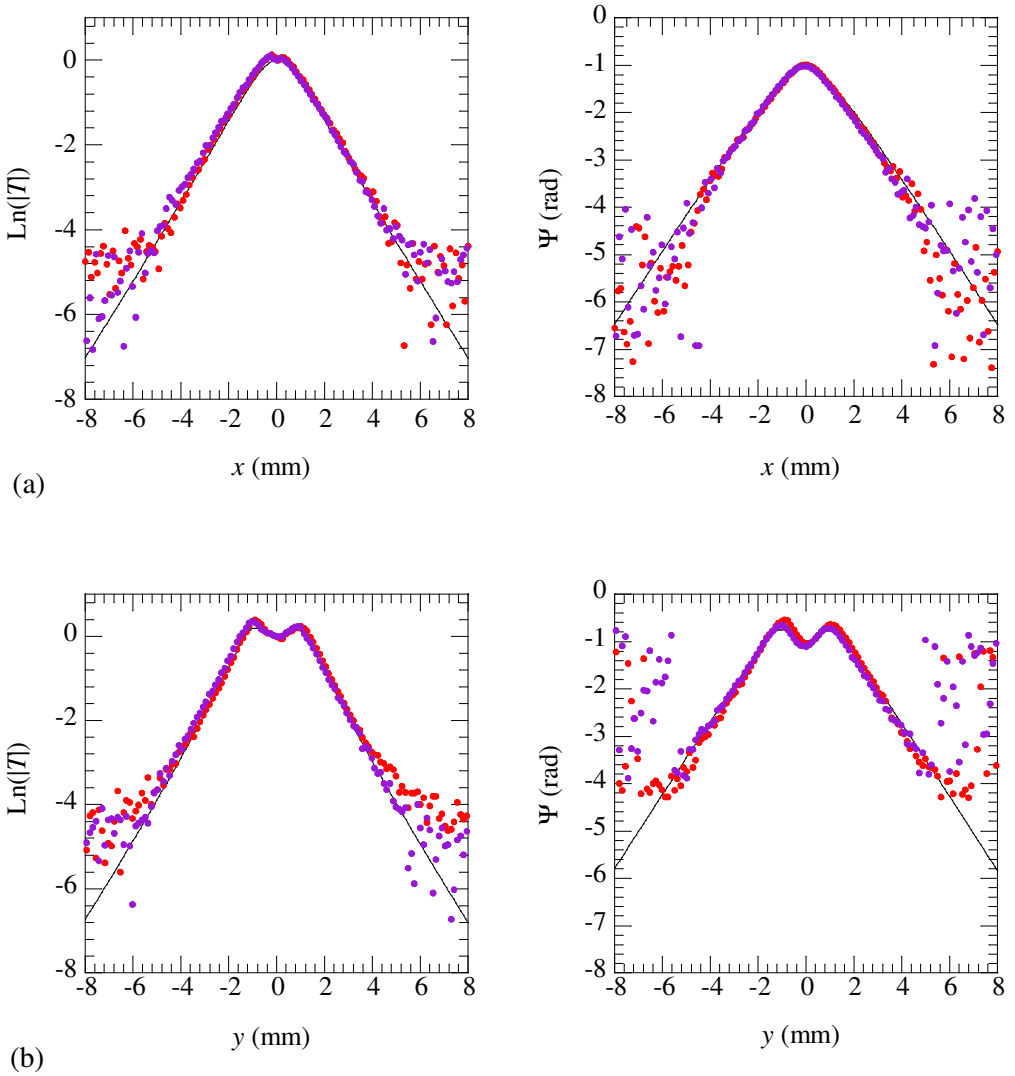

Figure 4.13. Experimental Ln(|T|) (left) and Ψ (right) of the surface temperature *x*- (a) and *y*-profiles (b) for two rectangular Cu foils of width $w_1 = w_2 = 0.9$ mm and height $h_1 = h_2 = 2$ mm, buried at a depth $|d_1| = |d_2| = 260$ µm and with a separation distance between centres of 1 mm, obtained at $f_{lock\text{-}in} = 0.8$ Hz. Red dots correspond to processed data with the Fourier component subtraction method, purple dots represent data generated with the temperature history fitting method and solid lines are the predictions of the theory.

As can be seen, both data corrected with the Fourier component subtraction method and data generated with the temperature history fitting method are very similar along both *x*- and *y*-profiles, and agree with the predictions of the theory very well.

Although the Fourier component is successfully eliminated, the main drawback of this procedure is that it does not take advantage of the key feature of the lock-in technique, which is to dig up periodic signals embedded in noise. Moreover, for the fitting of the temperature history of all pixels in an area of interest within the measuring surface, the whole surface temperature evolution at all modulation frequencies needs to be recorded and processed by computer, which is time consuming and demands a high computer capacity. Actually, the capacity of the computer may limit the number of temperature maps from which the temperature history of each pixel is analysed, in which case, reducing the sampling frequency may be preferable in order to ensure that a certain amount of complete periods are used for the temperature history fitting, especially at low modulation frequencies.

For these reasons, we have decided not to use this method and take advantage of the lock-in technique instead, as it allows analysing as many frames as needed with no further computing work.

In next section we suggest an experimental procedure that minimizes the DC temperature rise so that no further post-processing of the data is needed.

4.2.3 Low ultrasound electrical power excitation

As mentioned in the previous section, the use of high US power in lock-in experiments induces a DC surface temperature rise of 10-30ºC, together with a temperature oscillation of several degrees in amplitude. These conditions allow having AC components with high amplitudes, i.e., good signal-to-noise ratios, but they also imply having a very long transient regime coinciding with data acquisition, which in turn introduces a distortion in both amplitude and phase thermograms at low modulation frequencies. This distortion needs to be removed by post-processing and, in addition, the Cu foil representing the vertical crack shows fretting damage under high ultrasound electrical power.

For this reason, at this point we decide to reduce the ultrasound power in order to perform the experiments in steady state, which is reached in a few minutes in experiments using low US power. Moreover, the Cu foils remain unaltered, which makes the experiments more repeatable and reliable, but the price to be paid is a significant reduction of the amplitude of the oscillating component of the surface temperature. For instance, in experiments using low US power the amplitude of the oscillating component at an intermediate modulation frequency $f_{lock\text{-}in}$ = 0.8 Hz is about 0.2 K.

With this limitation, obtaining exploitable data requires reducing the noise level significantly and, in order to do that, we take advantage of the lock-in ability to reduce the noise by increasing the number of images analysed. As introduced in section 4.1.2, low US power refers to ultrasound electrical power values around 25-40 W. The fact that in real cracks friction damage has also been observed [3, 70] further supports the idea of using low US power.

To illustrate this, we have compared three lock-in analyses performed with a different number of images in experiments using low US power: 4,000, 41,000 and 200,000. This comparison is made at $f_{lock\text{-}in}$ = 12.8 Hz, the highest modulation frequency in our experiments, because as the signal-to-noise ratio is the lowest, the influence of the number of images on the averaged amplitude noise level may be better noticed.

In Figure 4.14 we show a side view of Ln(|T|) along y-axis, corresponding to two rectangular heat sources of width $w_1 = w_2$ = 0.8 mm and height $h_1 = h_2$ = 2 mm, with a separation distance between centres of 2.2 mm and buried at a depth $|d_1| = |d_2|$ = 0.25 mm. We also mark the theoretical natural logarithm of the average noise level in amplitude, $\mathrm{Ln}\langle T_{noise}\rangle$, with a red line in each case, according to equation (1.1).

The improvement of the signal-to-noise ratio when increasing the number of images is dramatic. As can be checked, increasing the number of analysed images from 4,000 to 200,000 allows digging up the signal from noise up to a radius of 2.5 mm with respect to the centre of the thermogram (y = 0), experimentally demonstrating that the larger the number of collected and analysed frames in the lock-in process, the larger the area of exploitable information. It is worth mentioning that, in the case of Figure 4.14 (c), data are clipped due to an insufficient number of decimals during the temperature measurements.

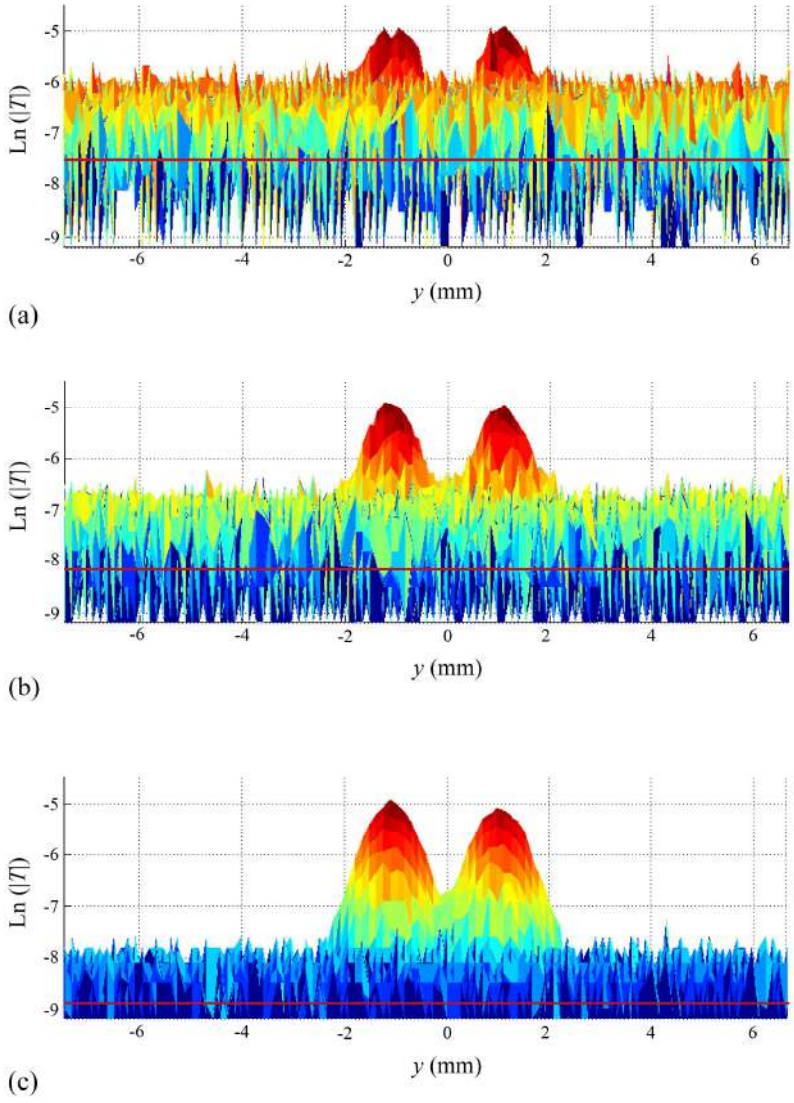

Figure 4.14. Comparison between the noise level of experimental data and the theoretical average noise level in amplitude (red line) for three different number of images analysed in experiments using low US power: (a) 4,000, with $\mathrm{Ln}\langle T_{noise}\rangle$ = -7.14, (b) 41,000, with $\mathrm{Ln}\langle T_{noise}\rangle$ = -7.83 and (c) 200,000, with $\mathrm{Ln}\langle T_{noise}\rangle$ = -9.09. Data are shown at a modulation frequency $f_{lock\text{-}in}$ = 12.8 Hz and correspond to two rectangles of width $w_1 = w_2$ = 0.8 mm and height $h_1 = h_2$ = 2 mm, with a separation distance between centres of 2.2 mm and buried at a depth $|d_1| = |d_2|$ = 0.25 mm.

Figure 4.15 compares surface temperature *x*-profiles of raw data taken using low US power and data taken using high US power and corrected by the Fourier component subtraction

method, corresponding to two square Cu foils of width $w_1 = w_2 = 1.2$ mm and height $h_1 = h_2 = 1.2$ mm, buried at a depth $|d_1| = |d_2| = 120$ µm and with a separation distance between centres of 1.15 mm, obtained at $f_{lock\text{-}in} = 0.8$ Hz.

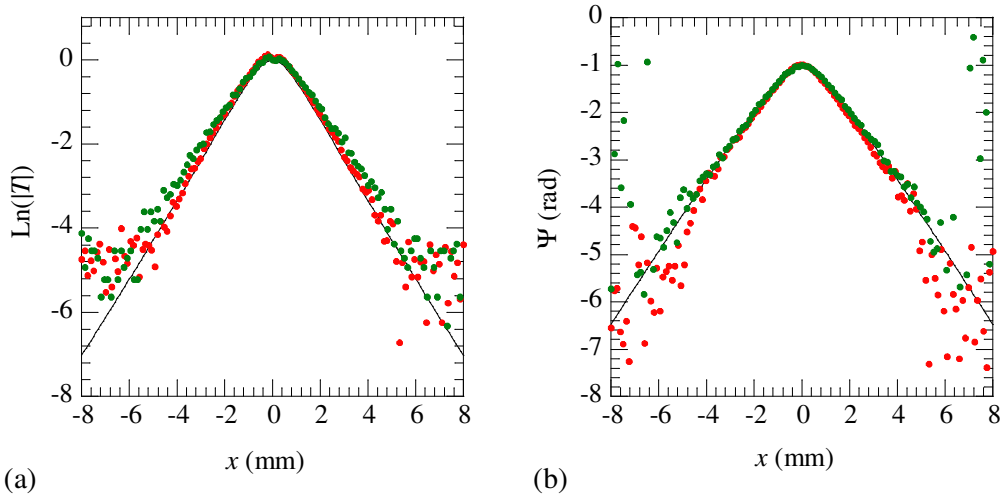

Figure 4.15. Experimental Ln(|*T*|) (a) and Ψ (b) of the surface temperature *x*-profile for two square Cu foils of width $w_1 = w_2 = 1.2$ mm and height $h_1 = h_2 = 1.2$ mm, buried at a depth $|d_1| = |d_2| = 120$ µm and with a separation distance between centres of 1.15 mm, at $f_{lock\text{-}in} = 0.8$ Hz. Red dots correspond to data obtained in transient state using high US power and processed with the Fourier component subtraction method, green dots represent raw data obtained in steady state using low US power and solid lines are the predictions of the theory.

As can be observed, both raw data taken in steady state using low US power and data taken in transient state using high US power and corrected with the Fourier component subtraction method fit the theoretical predictions, demonstrating that reducing the ultrasound electrical power allows obtaining exploitable data that are not affected by the transient DC temperature rise, as long as the noise level is reduced by analysing a larger number of images in the lock-in process enough to compensate for the signal reduction.

4.3 Frequency dependence of the equipment

Although all experimental data shown up to now correspond to certain modulation frequencies representing either the ends of our set of modulation frequencies or an intermediate one, it is worth recalling that experimental data are taken at nine $f_{lock\text{-}in}$ ranging from 0.05 to 12.8 Hz, as detailed in Table 3.1.

A problem that arises in vibrothermography experiments performed at several modulation frequencies is that, for a given heat source, the surface temperature phases at the different modulation frequencies do not follow the predictions of the theory, such as those depicted in Figure 3.6. The reason for this problem is that the experimental equipment has a non-flat response with frequency, which overlaps the frequency dependence of signal.

The frequency response of the equipment is a well-known issue in optically excited IR thermography, where several approaches have been used to overcome it: normalization of data of interest with data taken either on a reference sample [138] or on the same sample but with a different configuration (self-normalization) [139], and performing an independent evaluation of the frequency response of the equipment [140].

However, as far as we know, in vibrothermography experiments there is no way to perform normalization in order to remove the frequency dependence of the equipment and, for this reason, all the experimental phases along both *x*- and *y*-profiles presented so far have been shifted along the vertical axis, by the right amount in each case, in order to match the theoretical profiles.

In this section we deal with the fact that the acquisition system introduces an error in vibrothermographic data by measuring it experimentally, with the aim of taking into account the measured mismatch in experimental phase thermograms. To do so, we have performed 6 identical experiments using a square Cu foil of $w = h = 1$ mm buried at a depth $|d| = 230$ μm, and we have compared the values of the surface temperature phase on top of the centre of the heat source (position (0, 0, 0) in Figure 3.1) with the theoretical phase prediction (equation (3.7)), at several modulation frequencies, namely, 0.05, 0.1, 0.2, 0.4, 0.6, 0.8, 1.2, 1.6, 1.9, 3.2, 4.0, 4.8, 5.6, 6.4, 8.0, 9.6, 11.2 and 12.8 Hz. We have also made this comparison at a distance of 0.5 mm along both the *x*- and *y*-profiles with respect to the centre of the heat source.

Figure 4.16 (a) shows the experimental values of the surface temperature phase on top of the centre of the heat source obtained in the six experiments as a function of the modulation

frequency (coloured dots), along with the theoretical values (black line). As can be seen, the phases follow a similar qualitative trend with modulation frequency in all the experiments, but they do not match the theoretical values: the decay of the experimental phases with modulation frequency is more pronounced than theoretically expected.

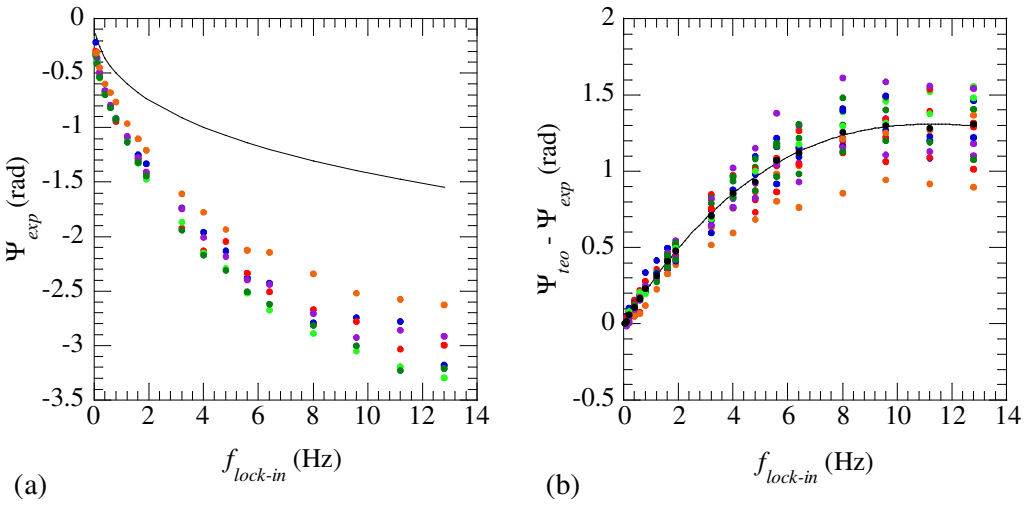

Figure 4.16. (a) Experimental (coloured dots) and theoretical (black line) values of the surface temperature phase on top of the centre of the heat source (0, 0, 0) as a function of modulation frequency, obtained with a square Cu foil of $w = h = 1$ mm buried at a depth $|d| = 230$ µm, and (b) differences between experimental and theoretical values of the surface temperature phase on top of the centre of the heat source as well as at a distance of 0.5 mm along both *x*- and *y*-profiles with respect to it (coloured dots), along with the mean values (black dots) at each modulation frequency after removing the most discordant data points, and a 3rd order polynomial (solid line) fitting the mean values.

As mentioned above, the phase shifts, i.e., the differences between experimental and theoretical phases at all modulation frequencies have been calculated also at a distance of 0.5 mm along both *x*- and *y*-profiles with respect to the centre of the heat source, in order to evaluate the frequency dependence of the equipment with data obtained at different positions along the surface. Then we fit the mean values of such phase shifts to a 3rd order polynomial function, after removing the most discordant data points (see Figure 4.16 (b)).

The experimental phase thermograms are corrected by adding the values obtained from the fitted curve to the whole thermograms, at each modulation frequency. In this way, the corrected phase thermograms take into account the shifts introduced by the acquisition system. All $f_{lock\text{-}in}$ not included in our modulation frequency set have been considered in this section only for a more accurate curve fitting.

Taking into account the frequency dependence of the equipment and according to the decisions that we have made in previous sections in relation to the experimental conditions for data acquisition in our vibrothermography experiments, we can now determine that the optimum procedure to obtain experimental data is the following: performing the experiments using low US power, in steady state, acquiring a large number of images at all modulation frequencies and, at last, removing the measured phase shifts introduced by the acquisition system from whole surface phase thermograms.

All in all, using low US power allows taking data that are not affected by the transient temperature rise of the sample and it prevents the Cu foils from being damaged due to fretting, making the experiments repeatable and more reliable. The steady state is reached within a few minutes and despite the reduction of the amplitude of the oscillating component of the surface temperature, good signal-to-noise ratios can be achieved by reducing the noise level, which in turn is achieved by taking advantage of the key feature of the lock-in technique by analysing a large number of images.

Thus, the only needed post-processing of the data is the elimination of the phase shifts introduced by the equipment from whole phase thermograms, which is a very fast operation. It is worth mentioning that the inversion algorithm, which will be described in detail in next section, is able to absorb any frequency dependence of the surface temperature amplitudes. For this reason, surface temperature amplitudes have not been considered in this section.

5 The inverse problem

This section addresses the inverse problem in this thesis, consisting in retrieving the heat source distribution giving rise to a certain surface temperature distribution and which is severely ill-posed. After analysing the ill-posedness of the inverse problem with SVD, regularization methods are proposed with the aim of implementing a robust inversion algorithm in order to characterize cracks from vibrothermography data. Finally, the inversion algorithm is described in detail.

5.1 Statement of the inverse problem

The ultimate goal of any NTD technique is the characterization of flaws. However, as mentioned before, the physical magnitude that can be retrieved from surface temperature data is the periodic heat flux responsible for it, rather than the crack geometry itself. Accordingly, the inverse problem consists in retrieving the heat source distribution giving rise to a certain surface temperature distribution. In order to tackle the inverse problem, it is worth recalling the solution of the direct problem, i.e., the calculation of the surface ($z = 0$) temperature distribution generated by a given heat source distribution covering an area Ω contained in plane Π ($x = 0$), modulated at frequency $f_{lock\text{-}in}$. As shown in section 3.1, the complex position-dependent part of the AC temperature at any point of the sample surface is given by

$$T_{AC}\left(\boldsymbol{r}_{z=0}\right) = \iint_{\Omega} \frac{Q(\boldsymbol{r}')}{4\pi K} \frac{\mathrm{e}^{-q|\boldsymbol{r}-\boldsymbol{r}'|}}{|\boldsymbol{r}-\boldsymbol{r}'|} \mathrm{d}S' \tag{5.1}$$

Note that in the direct problem, the geometry of the source, Ω, appears in the domain of integration. Since we use multi-frequency data so as to gather as much information as possible, we will refer to $f_{lock\text{-}in}$ as f_k in this section for the sake of simplicity, where $k = 1$, …, k_{max}, being $k_{max} = 9$.

From a mathematical point of view, when combining data at several modulation frequencies, the inversion of equation (5.1) consists in a system of Fredholm's integral equations of the first kind with smooth kernels, which are well known for giving severely ill-posed inverse problems [133]. The kernel in equation (5.1), $e^{-q_{f_k}|\boldsymbol{r}-\boldsymbol{r}'|}/|\boldsymbol{r}-\boldsymbol{r}'|$, is smooth except for a 1-dimensional zone corresponding to the positions of the heat sources in surface $z = 0$. The ill-posedness of the problem has been intuitively recognized in Figure 3.5, since heat sources of different geometries produce relatively small changes in the surface temperature signature, especially when buried deep inside the material.

For the inversion, no particular geometry of the heat source distribution is considered to be known and only the plane containing it (Π) is assumed as prior information. Equation (5.1) is then reformulated by introducing a function describing both position and frequency dependent heat source distributions, $Q_{f_k}(\boldsymbol{r}')$, and integrating over the whole plane Π containing the heat sources, rather than just area Ω. Therefore, $Q_{f_k}: \Pi \to \mathbb{R}$ is now defined in plane Π ($x = 0$) and not only within area Ω.

Function $Q_{f_k}(\boldsymbol{r}')$ is expressed as the product of two factors: a normalized heat source distribution, $Q(\boldsymbol{r}')$, which is common to all modulation frequencies, and a set of intensities, I_{f_k}, that only depend on the modulation frequency and that refer to the intensities the heat sources emit with, at each modulation frequency

$$Q_{f_k}(\boldsymbol{r}') = I_{f_k} Q(\boldsymbol{r}') \tag{5.2}$$

The set of intensities, I_{f_k}, is introduced in order to allow the maximum intensity of these heat sources vary from one modulation frequency to another, since in the experiments, it is interesting to increase the ultrasound amplitude at high modulation frequencies where the signal is weaker.

With this new formulation, equation (5.1) writes

$$T_{f_k}\left(\boldsymbol{r}_{z=0}\right)=\iint_{\Pi}\frac{Q_{f_k}\left(\boldsymbol{r}'\right)}{4\pi K}\frac{\mathrm{e}^{-q_{f_k}\left|\boldsymbol{r}-\boldsymbol{r}'\right|}}{\left|\boldsymbol{r}-\boldsymbol{r}'\right|}\mathrm{d}S'=\iint_{\Pi}\frac{I_{f_k}Q\left(\boldsymbol{r}'\right)}{4\pi K}\frac{\mathrm{e}^{-q_{f_k}\left|\boldsymbol{r}-\boldsymbol{r}'\right|}}{\left|\boldsymbol{r}-\boldsymbol{r}'\right|}\mathrm{d}S' \tag{5.3}$$

where we make explicit reference to the modulation frequency dependence of the surface temperature oscillation, T_{f_k}. Note that with this reformulation, the inverse problem becomes bi-linear in $Q\left(\boldsymbol{r}'\right)$ and I_{f_k}. Equation (5.3) can be written in a compact operator form

$$T_{f_k}=\mathbf{A}_{f_k}\left[Q_{f_k}\right]=I_{f_k}\mathbf{A}_{f_k}\left[Q\right] \qquad \text{for } k=1,...,k_{\max} \tag{5.4}$$

being $\mathbf{A}_{f_k}$ the operators mapping the normalized heat source distribution, $Q\left(\boldsymbol{r}'\right)$, and the set of intensities, I_{f_k}, into the complex surface temperature distribution, T_{f_k}. Equations (5.4) represent the exact relationship between the surface temperature and the heat sources.

However, in practice, all surface temperature distributions available from vibrothermography data are affected by noise, so both the normalized heat source distribution and the set of intensities can only be retrieved from noisy data, $T_{f_k}^{\delta}$. Noisy data can be considered the sum of exact data, T_{f_k}, and a certain amount of noise, being δ the noise level, defined as

$$\delta^2=\sum_{k=1}^{k_{\max}}\left\|T_{f_k}^{\delta}-T_{f_k}\right\|_2^2 \qquad \text{with } \left\|g\right\|_2^2=\iint_{z=0}\left|g\right|^2 dS \tag{5.5}$$

It is worth mentioning that δ also accounts for model errors. Due to the presence of noise, equation (5.4) does not hold anymore, it becomes an approximation and the inversion has to be understood as a minimization problem consisting in finding the normalized heat source distribution, $Q\left(\boldsymbol{r}'\right)$, and the intensities, I_{f_k}, that minimize a residual. We define such residual as the squared 2-norm (see equation (2.32)), i.e., the squared differences between exact data, T_{f_k}, calculated from equation (5.4), and actual noisy data, $T_{f_k}^{\delta}$, summed over all modulation frequencies

$$R^2 = \sum_{k=1}^{k_{\max}} \left\| I_{f_k}^{\delta} \mathbf{A}_{f_k} Q^{\delta} - T_{f_k}^{\delta} \right\|_2^2 \tag{5.6}$$

Thus, as may be noted in equation (5.6), the resulting approximated normalized heat source distribution, Q^{δ}, and the set of intensities, $I_{f_k}^{\delta}$, will be affected by the noise in the data.

As mentioned above, the fact that equations (5.4) are stated in terms of Fredholm's integral equations of the first kind with smooth kernels, leads to a severe ill-posedness of the inverse problem in the presence of noise, which is characterized by very small errors in the data giving rise to arbitrarily large errors in the solution. This, in turn, makes the minimization of the residual in equation (5.6) very unstable, which is the reason why the minimization process needs from the introduction of a regularization method.

Least squares minimization can be stabilized by introducing a regularization or penalty term in equation (5.6)

$$R_{\alpha}^2 = \sum_{k=1}^{k_{\max}} \left\| I_{f_k}^{\delta,\alpha} \mathbf{A}_{f_k} Q^{\delta,\alpha} - T_{f_k}^{\delta} \right\|_2^2 + \alpha J\left(Q^{\delta,\alpha}\right) \tag{5.7}$$

As can be seen, the penalty term is the product of a regularization parameter, α, and a functional, $J\left(Q^{\delta,\alpha}\right)$: the functional allows us make use of prior information regarding the solution of the inverse problem, whereas the regularization parameter determines the size of the penalty term with respect to the discrepancy term. Of course, the solution for $Q^{\delta,\alpha}$ and $I_{f_k}^{\delta,\alpha}$ will be affected by the value of α.

In next section, the inverse problem is analysed by means of SVD, with the aim of assessing the ill-posed character of the problem and proposing appropriate regularization methods in order to implement a robust inversion algorithm.

5.2 Analysis of the inverse problem and regularization methods

The discretization of the inverse problem is performed by meshing both planes $z = 0$ (data points) and Π ($x = 0$, unknown heat sources). As introduced in section 2.2.1, matrix $\mathbf{A}_{f_k}$ is the mathematical model that relates heat source distributions to surface temperature distributions. In order to stabilize the inverse problem with appropriate regularization methods, we first analyse the ill-posedness of the inverse problem by implementing SVD, in which $\mathbf{A}_{f_k}$ is factored into three matrices: $\mathbf{U}_{f_k}$, $\mathbf{S}_{f_k}$ and $\mathbf{V}_{f_k}$. The object of this section is to give an idea of what these matrices represent and what they look like for particular discretizations of planes $z = 0$ and Π ($x = 0$), particularizing the theory of section 2.2.3 to the inversion problem in this thesis. A representation of the discretization of the planes is shown in Figure 5.1.

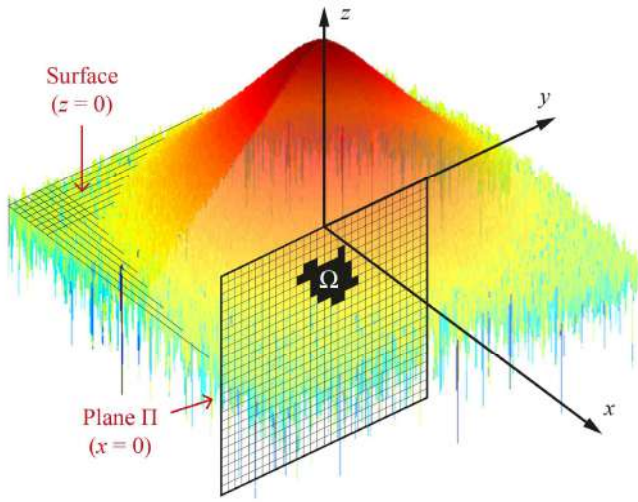

Figure 5.1. Representation of plane Π ($x = 0$) containing a heat source distribution and plane $z = 0$ with the noisy surface temperature distribution generated by modulated point-like heat sources covering area Ω. The discretization of both planes is represented by square meshes.

Starting with $\mathbf{A}_{f_k}$ and considering a single modulation frequency, each column in $\mathbf{A}_{f_k}$ contains the surface temperature distribution generated by a modulated point-like heat source located at each node of plane Π. Thus, $\mathbf{A}_{f_k}$ has as many columns as nodes in plane

Π, representing all the possible heat sources covering it. Similarly, the number of rows in $\mathbf{A}_{f_k}$ corresponds to the nodes in plane $z = 0$, the surface temperature data points. Thus, the size of $\mathbf{A}_{f_k}$ is m by n, being m the number of data points and n the number of unknowns. As we generate multi-frequency data, each modulation frequency contributes to matrix **A** following the same procedure, meaning that it gains rows while the columns remain the same, since the number of unknown model parameters does not depend on the modulation frequency

$$\mathbf{A} = \begin{bmatrix} \mathbf{A}_{f_1} \\ \mathbf{A}_{f_2} \\ \cdots \\ \mathbf{A}_{f_{k_{\max}}} \end{bmatrix} \tag{5.8}$$

Similarly, **U**, **S** and **V** refer to $\mathbf{U}_{f_k}$, $\mathbf{S}_{f_k}$ and $\mathbf{V}_{f_k}$ when combining all modulation frequencies. In order to illustrate what the diagonal of matrix **S**, i.e., the singular values look like, we next perform the SVD of **A** corresponding to a square search area in plane Π of 1 mm along both *y*- and *z*-axis with nodes separated by 100 μm, buried at a depth $|d|$ = 0.2 mm. Thus, the number of unknown model parameters, n, is 100, and since the number of data points, m, is much larger, n determines the number of singular values in this inverse problem, as in all cases in this thesis.

The diagonal values of matrix **S** are represented by a thick black line on a log scale in Figure 5.2 (a). The curve shows two main linear regions joined together by a "corner": the first region contains singular values ranging from 10^2 to 10^{-6} approximately, whereas the second region contains singular values that can be considered to be the near-zero singular values. The diagonal values of matrix $\mathbf{S}_{f_k}$ are also represented by thinner coloured lines, as would be the case if data at a single modulation frequency was used for the inversion: the blue line represent the singular values at 0.05 Hz, the maroon line stands for those at 12.8 Hz and the rest of the coloured lines correspond to those at the rest of the modulation frequencies in between. Figure 5.2 (b) shows the same but with the square search area buried at a depth $|d|$ = 3.2 mm. A linear decay of the singular values on a log scale corresponds to an exponential decay on a linear scale, meaning that our inverse problem can be considered severely ill-posed.

It can be observed that the corner that joins the singular values that carry information and the near-zero singular values becomes less obvious and moves to the right with increasing modulation frequency, and also that the curves start at a gradually lower position along the ordinate, meaning that higher modulation frequencies contribute gradually less to the solution. In other words, the area under the curve corresponding to each individual modulation frequency gives an idea of how relevant the contribution of the information at that modulation frequency is to the solution. This could be quantitatively checked if we summed all the singular values in each curve: the greater the sum of all singular values within a modulation frequency, the more relevant its contribution to the solution when combining all modulation frequencies. According to this, we can say that for a search area buried at a depth $|d|$ = 0.2 mm, information at all modulation frequencies contribute similarly to the solution with differences only in the smallest singular values, whereas at a depth $|d|$ = 3.2 mm, information at 0.05 Hz is much more relevant than at 12.8 Hz.

If we now compare the singular values of $\mathbf{S}$ and $\mathbf{S}_{f_k}$, we can easily see that the area under the thick black line is greater than under any other curves, which means that using multi-frequency data provides more information and thus helps reducing the ill-posedness of the inverse problem, if compared to inversions from data at any single modulation frequency.

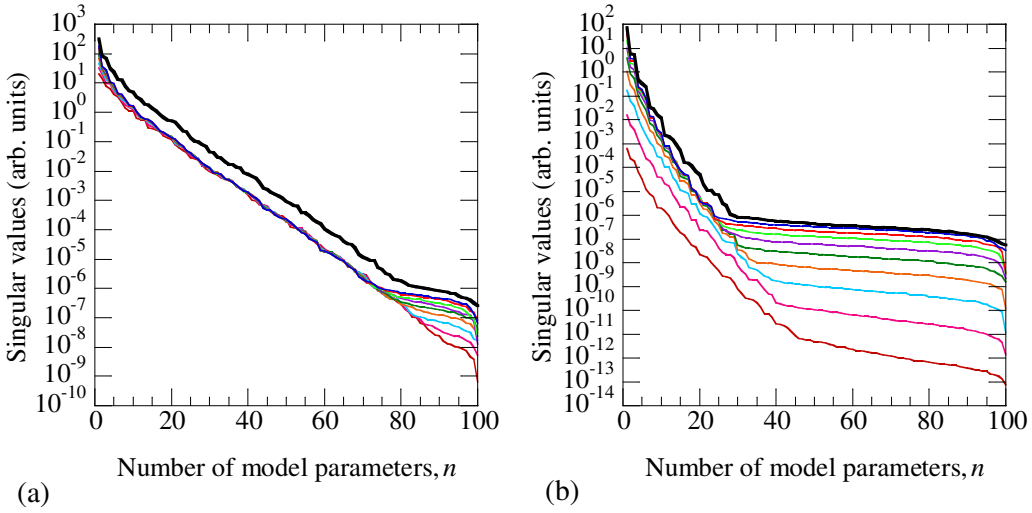

Figure 5.2. Singular values obtained from SVD of matrices $\mathbf{A}$ (black lines) and $\mathbf{A}_{f_k}$ (coloured lines) for a search area in plane Π corresponding to a square of 1 mm along both *y*- and *z*-axis with nodes separated by 100 µm, buried at a depth $|d|$ = 0.2 (a) and 3.2 mm (b). Colours stand for each modulation frequency, namely, f_1 = 0.05 (blue), f_2 = 0.1 (red), f_3 = 0.2 (green), f_4 = 0.4 (purple), f_5 = 0.8 (dark green), f_6 = 1.6 (orange), f_7 = 3.2 (light blue), f_8 = 6.4 (pink) and f_9 = 12.8 Hz (maroon).

Since we do not retrieve heat sources from data at a single modulation frequency but we introduce multi-frequency data in the algorithm, the qualitative interpretation of the singular values is useful in inversions where the high frequency content is reduced.

Figure 5.3 (a) shows the singular values for a search area of 1 mm along both *y*- and *z*-axes with nodes separated by 100 µm, buried at a depth $|d|$ = 0.2 mm, with a gradually narrower set of low frequency information: from 0.05 to 12.8 Hz, from 0.05 to 1.6 Hz and from 0.05 to 0.2 Hz, indicating that the narrower the set of low frequency information, the more severely ill-posed the inverse problem, since the singular values containing information decay faster.

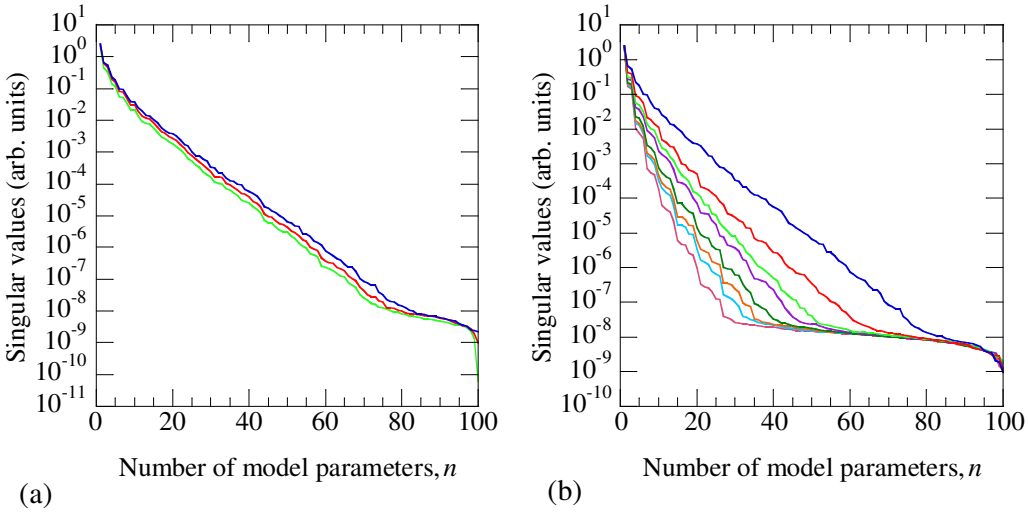

Figure 5.3. (a) Singular values obtained from SVD of matrix **A** corresponding to a square search area of 1 mm along both *y*- and *z*-axes with nodes separated by 100 µm, buried at a depth $|d|$ = 0.2 mm, with a gradually narrower set of low frequency information: from 0.05 to 12.8 Hz (blue), from 0.05 to 1.6 Hz (red) and from 0.05 to 0.2 Hz (green), and (b) singular values obtained from SVD of matrix **A** corresponding to a square search area of 1 mm along both *y*- and *z*-axes with nodes separated by 100 µm buried at increasing depths. Coloured lines represent each depth: $|d|$ = 0.2 (blue), 0.6 (red), 1.2 (green), 1.6 (purple), 2.6 (dark green), 3.2 (orange), 4.0 (light blue) and 5.0 mm (pink).

The decay of high frequency information becomes gradually more significant as heat sources are buried deeper beneath the surface. Figure 5.3 (b) shows the singular values of matrix **A** corresponding to search areas of 1 mm along both *y*- and *z*-axes with nodes separated by 100 µm, buried at increasing depths, namely, $|d|$ = 0.2, 0.6, 1.2, 1.6, 2.6, 3.2, 4.0 and 5.0 mm. As can be observed, each curve starts at a gradually lower position along the ordinate with increasing depth, but for the sake of clarity all curves have been

normalized at the first singular value of the curve corresponding to the shallowest case. Normalizing these curves, i.e., making their first singular values coincide, is representative of having the same information (signal-to-noise ratio) at all modulation frequencies, which is not realistic. Despite these favourable conditions, the singular values shown in Figure 5.3 (b) clearly indicate that the ill-posed nature of the inverse problem becomes more severe as the depth of the heat sources increases.

As for the design of experiments, i.e., the way the modulation frequencies are picked within the ends of our modulation frequency set (from 0.05 to 12.8 Hz), we have represented the singular values for two $f_{lock\text{-}in}$ distributions (see Table 5.1): doubling the modulation frequencies as considered so far, and distributing them uniformly. The results are shown in Figure 5.4 (a).

Table 5.1. Design of experiments: two different $f_{lock\text{-}in}$ distributions.

doubling $f_{lock\text{-}in}$ (Hz)	0.05	0.1	0.2	0.4	0.8	1.6	3.2	6.4	12.8
unif. distr. $f_{lock\text{-}in}$ (Hz)	0.05	1.64	3.2	4.84	6.44	8.0	9.64	11.8	12.8

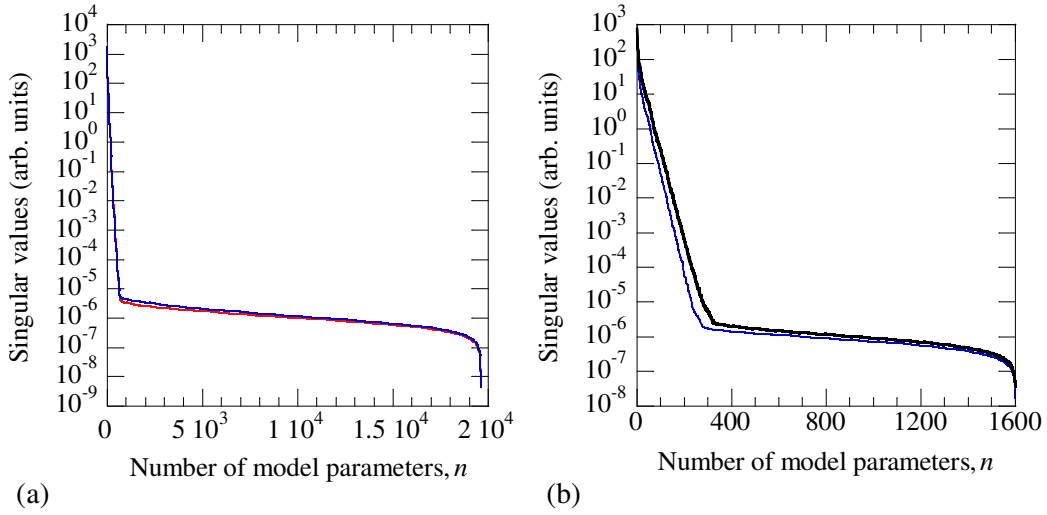

Figure 5.4. Singular values obtained from SVD of (a) matrix **A** for a search area in plane Π of 7 mm along both *y*- and *z*-axes reaching the surface with nodes separated by 50 µm, considering two $f_{lock\text{-}in}$ distributions: doubling modulation frequencies (blue) and uniformly distributed within the ends of our set of modulation frequencies (red), and of (b) matrices **A** (blue) and $\mathbf{A}_{0.05}$ (black) for a search area in plane Π of 4 mm along both *y*- and *z*-axis reaching the surface with nodes separated by 100 µm and doubling modulation frequencies.

As may be observed, doubling the modulation frequencies (blue line) provides slightly more information in relation to distributing them uniformly (red line). Anyway, the differences between either $f_{lock\text{-}in}$ distributions are very small. In this case, a search area of 7 mm along both *y*- and *z*-axes reaching the surface has been considered, with nodes separated by 50 µm and, as can be noted, the shape of the singular values is very different to those shown in previous figures: the corner is much more pronounced and the region that contains the near-zero singular values is longer and straight, which is related to the fact that the mesh in plane Π is much finer. The same effect can be observed in Figure 5.4 (b), where the singular values of matrices **A** (black thick line) and $\mathbf{A}_{0.05}$ (blue line) for a search area of 4 mm along both *y*- and *z*-axes reaching the surface with nodes separated by 100 µm is shown. Thus, the shape of the singular values strongly depends on the size and mesh of plane Π. As for matrices $\mathbf{U}_{f_k}$ and $\mathbf{V}_{f_k}$ in the SVD of matrix $\mathbf{A}_{f_k}$, Figure 5.5 (a) and (b) show the data and model space vectors, $\mathbf{U}_{0.05.,i}$ and $\mathbf{V}_{0.05.,i}$, respectively, corresponding to the first, second and last singular values represented by a blue line in Figure 5.4 (b).

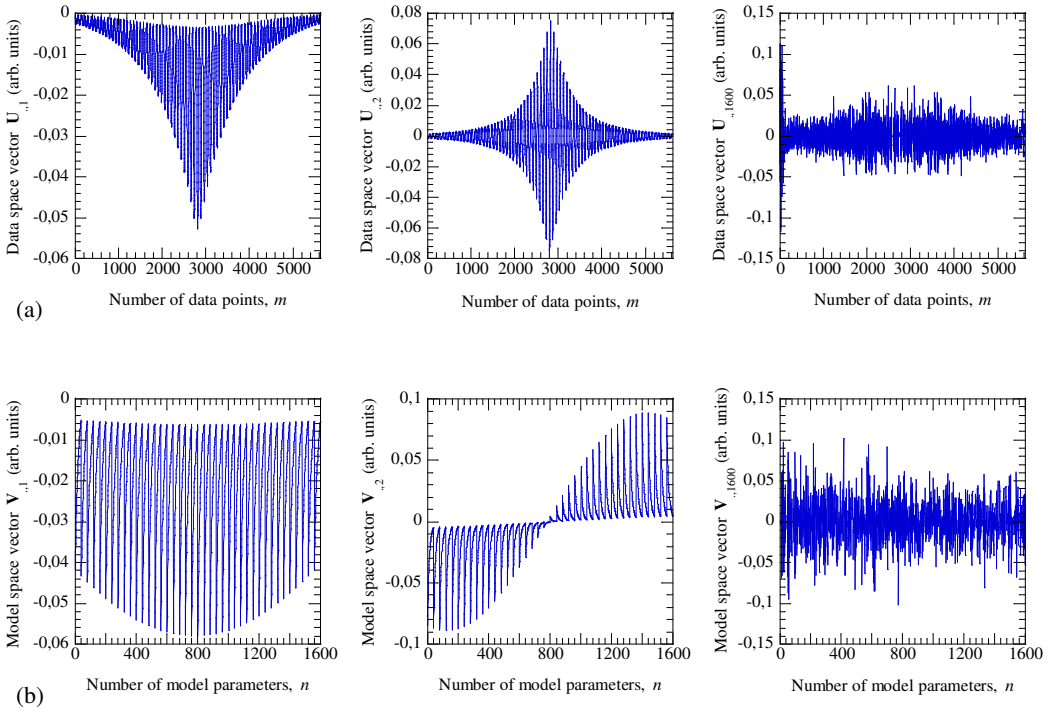

Figure 5.5. (a) Data space vectors $\mathbf{U}_{0.05.,1}$, $\mathbf{U}_{0.05.,2}$ and $\mathbf{U}_{0.05.,1600}$ as a function of the number of data points, *m*, and (b) model space vectors $\mathbf{V}_{0.05.,1}$, $\mathbf{V}_{0.05.,2}$ and $\mathbf{V}_{0.05.,1600}$ as a function of the number of model

parameters, n, obtained by performing the SVD of matrix $\mathbf{A}_{0.05}$ corresponding to a square search area in plane Π of 4 mm along both y- and z-axes reaching the surface with nodes separated by 100 μm.

As may be observed, the first model space vector acts as a low frequency component in the series whereas the last one acts as a high frequency component, which can be considered noise in the model. All the model space vectors between these two extremes contribute to the sum in the series that generate the solution of the inverse problem.

In order to see how harmful model space vectors associated to near-zero singular values are for the generalized inverse solution and how they can be damped by regularizing the inverse problem with the Tikhonov series (see section 2.2.4), we next make a comparison between equations (2.47) and (2.59), using the numerical values of Figure 5.4 (b) and those corresponding to Figure 5.5 combining all modulation frequencies (black thick line). The generalized solution with no regularization writes

$$\begin{aligned}\mathbf{m}^{\dagger} &= \sum_{i=1}^{p} \frac{\mathbf{U}_{.,i}^{T}\mathbf{d}}{s_i}\mathbf{V}_{.,i} \\ &= \frac{\mathbf{U}_{.,1}^{T}\mathbf{d}}{s_1}\mathbf{V}_{.,1} + \frac{\mathbf{U}_{.,2}^{T}\mathbf{d}}{s_2}\mathbf{V}_{.,2} + \ldots + \frac{\mathbf{U}_{.,1600}^{T}\mathbf{d}}{s_{1600}}\mathbf{V}_{.,1600} \\ &= \left(-1.46\cdot 10^{-2}\right)\mathbf{V}_{.,1} + \left(4.45\cdot 10^{-6}\right)\mathbf{V}_{.,2} + \ldots + \left(2.70\cdot 10^{13}\right)\mathbf{V}_{.,1600}\end{aligned} \tag{5.9}$$

Comparing the first and the last terms in (5.9), it can be seen that the smallest singular value provokes a very large coefficient for the last model space vector. Taking into account that about three quarters of the singular values shown in Figure 5.4 (b) are near-zero, the model may be completely dominated by noise.

Employing Tikhonov regularization, however, the regularization parameter α_{Tk} gives a lower weight to the model elements associated with smaller singular values. Setting, for instance, $\alpha_{Tk} = 10^4$, the solution now becomes

$$\begin{aligned}\mathbf{m}_{\alpha} &= \sum_{i=1}^{k} \frac{s_i^{\,2}}{s_i^{\,2} + \alpha_{Tk}} \frac{\mathbf{U}_{.,i}^{T}\mathbf{d}}{s_i}\mathbf{V}_{.,i} \\ &= \frac{s_1^{\,2}}{s_1^{\,2} + \alpha_{Tk}} \frac{\mathbf{U}_{.,1}^{T}\mathbf{d}}{s_1}\mathbf{V}_{.,1} + \frac{s_2^{\,2}}{s_2^{\,2} + \alpha_{Tk}} \frac{\mathbf{U}_{.,2}^{T}\mathbf{d}}{s_2}\mathbf{V}_{.,2} + \ldots + \frac{s_{1600}^{\,2}}{s_{1600}^{\,2} + \alpha_{Tk}} \frac{\mathbf{U}_{.,1600}^{T}\mathbf{d}}{s_{1600}}\mathbf{V}_{.,1600} \\ &= 0.98\left(-1.46\cdot 10^{-2}\right)\mathbf{V}_{.,1} + 0.89\left(4.45\cdot 10^{-6}\right)\mathbf{V}_{.,2} + \ldots + 1.15\cdot 10^{-37}\left(2.70\cdot 10^{13}\right)\mathbf{V}_{.,1600}\end{aligned} \tag{5.10}$$

As we may check in equation (5.10), we have completely discarded the contribution of the last model space vector, associated to the smallest singular value, while we have barely modified the contributions of model space vectors associated to larger singular values. In this way, the model space vectors associated to decreasing singular values are progressively filtered.

As introduced in the statement of the inverse problem, the solution is sought in the least square sense by introducing a penalty term

$$R_\alpha^2 = \sum_{k=1}^{k_{\max}} \left\| I_{f_k}^{\delta,\alpha} \mathbf{A}_{f_k} Q^{\delta,\alpha} - T_{f_k}^{\delta} \right\|_2^2 + \alpha J\left(Q^{\delta,\alpha}\right) \tag{5.11}$$

where α and J are generalized for any regularization method. In this example, in which the generalized inverse solution has been evaluated numerically without and with Tikhonov regularization, the notation corresponding to the theory in section 2.2.4 has been used. In order to relate it to our particular inverse problem, it must be clarified that $\mathbf{m}^\dagger$ and $\mathbf{m}_\alpha$ refer to the normalized heat source distribution ($Q^{\delta,\alpha}$ in equation (5.11)).

According to our notation, the Tikhonov regularization functional is defined as [141]

$$Tk(Q) = \iint_{\Pi} |Q|^2 dS \approx \sum_{i=1}^{n} |Q_i|^2 \Delta S \tag{5.12}$$

Therefore, equation (5.11) now is

$$R_{\boldsymbol{\alpha}}^2 = \sum_{k=1}^{k_{\max}} \left\| I_{f_k}^{\delta,\boldsymbol{\alpha}} \mathbf{A}_{f_k} Q^{\delta,\boldsymbol{\alpha}} - T_{f_k}^{\delta} \right\|_2^2 + \alpha_{Tk} Tk\left(Q^{\delta,\boldsymbol{\alpha}}\right) \qquad \text{with } \boldsymbol{\alpha} = \left(\alpha_{Tk}\right) \tag{5.13}$$

As mentioned at the end of section 2, the damping of model space vectors associated to very small singular values produces smoothly varying solutions, as sharp model space vectors are filtered out. These smooth solutions are not adequate for our inverse problem, as we search for heat source distributions with a well defined area.

Tikhonov regularization penalizes all nodes in plane Π equally because of applying the same regularization parameter value to each one, with no further information regarding the location of the possible heat sources. However, in order to optimize the degree of regularization in our inverse problem, other non-linear regularization procedures based on

local information can be implemented in order to perform a position-dependent penalization, besides implementing Tikhonov.

L_1 and Total Variation (TV) regularization methods allow performing a position-dependent penalization by assigning a different regularization parameter value to each node in plane Π, which, in turn, is possible if we get information about the retrieved normalized heat source distribution at each node in a previous iteration. In this way, we can guess which nodes need to be penalized most or least in a following iteration, in order to force some nodes to remain damped as well as keep other nodes dominating the solution.

Let us consider a penalty term based on Tikhonov, but with a regularization parameter that takes into account the solution in a previous iteration in order to penalize nodes differently in each iteration

$$\alpha_{Tk_{i,j}} = \alpha_{L_1} \frac{1}{\left|Q_{i,j-1}^{\delta,\boldsymbol{\alpha}}\right|} \tag{5.14}$$

where $i = 1, \ldots, n$, refers to the nodes in plane Π and j is the iteration. Expanding this new discretized penalty term for all nodes

$$\begin{gathered}\sum_{i=1}^{n} \alpha_{Tk_{i,j}} \left|Q_{i,j}^{\delta,\boldsymbol{\alpha}}\right|^2 \Delta S = \\ \alpha_{L_1} \frac{\Delta S}{\left|Q_{1,j-1}^{\delta,\boldsymbol{\alpha}}\right|} \left|Q_{1,j}^{\delta,\boldsymbol{\alpha}}\right|^2 + \alpha_{L_1} \frac{\Delta S}{\left|Q_{2,j-1}^{\delta,\boldsymbol{\alpha}}\right|} \left|Q_{2,j}^{\delta,\boldsymbol{\alpha}}\right|^2 + \ldots + \alpha_{L_1} \frac{\Delta S}{\left|Q_{n,j-1}^{\delta,\boldsymbol{\alpha}}\right|} \left|Q_{n,j}^{\delta,\boldsymbol{\alpha}}\right|^2 = \\ \alpha_{L_1} \left(\frac{1}{\left|Q_{1,j-1}^{\delta,\boldsymbol{\alpha}}\right|} \left|Q_{1,j}^{\delta,\boldsymbol{\alpha}}\right|^2 + \frac{1}{\left|Q_{2,j-1}^{\delta,\boldsymbol{\alpha}}\right|} \left|Q_{2,j}^{\delta,\boldsymbol{\alpha}}\right|^2 + \ldots + \frac{1}{\left|Q_{n,j-1}^{\delta,\boldsymbol{\alpha}}\right|} \left|Q_{n,j}^{\delta,\boldsymbol{\alpha}}\right|^2 \right) \Delta S \end{gathered} \tag{5.15}$$

As can be seen, despite being α_{L_1} common for all terms in the sum of equation (5.15), each term is affected by a different penalization, because $Q^{\delta,\boldsymbol{\alpha}}$ is divided by its value in a previous iteration. In this way, if $\left|Q_{i,j-1}^{\delta,\boldsymbol{\alpha}}\right|$ is small and thus $1/\left|Q_{i,j-1}^{\delta,\boldsymbol{\alpha}}\right|$ is large (in iteration j-1), $\left|Q_{i,j}^{\delta,\boldsymbol{\alpha}}\right|$ is forced to remain small (in iteration j). Similarly, if $\left|Q_{i,j-1}^{\delta,\boldsymbol{\alpha}}\right|$ is large, $1/\left|Q_{i,j-1}^{\delta,\boldsymbol{\alpha}}\right|$ is small and $\left|Q_{i,j}^{\delta,\boldsymbol{\alpha}}\right|$ is then free to increase or vary.

Over iterations, eventually $\left|Q_{i,j-1}^{\delta,\boldsymbol{\alpha}}\right| \approx \left|Q_{i,j}^{\delta,\boldsymbol{\alpha}}\right|$ and equation (5.15) then becomes

$$\alpha_{L_1}\left(\frac{1}{\left|Q_{1,j}^{\delta,\alpha}\right|}\left|Q_{1,j}^{\delta,\alpha}\right|^2+\frac{1}{\left|Q_{2,j}^{\delta,\alpha}\right|}\left|Q_{2,j}^{\delta,\alpha}\right|^2+\ldots+\frac{1}{\left|Q_{n,j}^{\delta,\alpha}\right|}\left|Q_{n,j}^{\delta,\alpha}\right|^2\right)\Delta S= \alpha_{L_1}\left(\left|Q_{1,j}^{\delta,\alpha}\right|+\left|Q_{2,j}^{\delta,\alpha}\right|+\ldots+\left|Q_{n,j}^{\delta,\alpha}\right|\right)\Delta S \tag{5.16}$$

that is the L_1-norm of $Q^{\delta,\alpha}$ multiplied by the regularization parameter α_{L_1}. Thus, the L_1 functional to implement in our inverse problem is

$$L_1(Q)=\iint_{\Pi}|Q|\,dS \tag{5.17}$$

Regularization with Total Variation is based on the same principle as L_1, but acting over the gradient of $Q^{\delta,\alpha}$. In practice, the main difference between L_1 and TV on the solution of the inverse problem is that L_1 favours null areas in plane Π, whereas TV favours areas with null derivatives of $Q^{\delta,\alpha}$, which provokes flat sections with sharp edges, i.e., blocky solutions, that are appropriate to characterize the confined heat sources we are seeking.

Next section describes the inversion algorithm in detail, implementing the described regularization procedures.

5.3 The inversion algorithm

Our approach to stabilize the inversion consists in implementing both L_1 and Total Variation functionals, aside from Tikhonov. L_1 and TV optimize the regularization in inversions regularized with Tikhonov, since they allow performing a position-dependent regularization in plane Π. The implementation of L_1 and Total Variation is aimed at retrieving heat sources contained in a well-defined area, i.e., featuring sharp edges, as a first step to characterization of heat source distributions.

As mentioned above, Total Variation searches for blocky functions, i.e., functions with flat sections and sharp edges, whereas L_1 tends to minimize the area where the function has non-zero values (compressive sensing effect) [144], which enhances contrast. Thus, L_1 and TV give advantage to homogeneous heat source distributions and are appropriate for the reconstruction of heat sources with well-defined geometries and sharp borders.

The function to minimize has then, with respect to that in equation (5.13), two new terms

$$R_{\boldsymbol{\alpha}}^2 = \sum_{k=1}^{k_{\max}} \left\| I_{f_k}^{\delta,\boldsymbol{\alpha}} \mathbf{A}_{f_k} Q^{\delta,\boldsymbol{\alpha}} - T_{f_k}^{\delta} \right\|_2^2 + \alpha_{Tk} Tk\left(Q^{\delta,\boldsymbol{\alpha}}\right) + \alpha_{L_1} L_1\left(Q^{\delta,\boldsymbol{\alpha}}\right) + \alpha_{TV} TV\left(Q^{\delta,\boldsymbol{\alpha}}\right) \quad \text{with } \boldsymbol{\alpha} = \left(\alpha_{Tk}, \alpha_{L_1}, \alpha_{TV}\right) \tag{5.18}$$

where each penalty functional is multiplied by a regularization parameter: α_{Tk}, α_{L_1} and α_{TV} are the regularization parameters corresponding to stabilizations with Tikhonov, L_1 and Total Variation, respectively.

In turn, we have implemented two versions of the TV functional, to which we refer as *isotropic* [142] and *anisotropic* [143], and that are defined as

$$TV_{Isot}(Q) = \iint_{\Pi} |\nabla Q| \, dS \tag{5.19}$$

$$TV_{Anisot}(Q) = \iint_{\Pi} \left(|\partial_y Q| + |\partial_z Q| \right) dS \tag{5.20}$$

The drawback of these functionals is that they are neither quadratic nor even differentiable operators, so we approximate them using lagged fix-points iterations [141]

$$\begin{aligned} TV_{Isot}(Q) = \iint_{\Pi} |\nabla Q| \, dS &\approx \lim_{j\to\infty} \iint_{\Pi} \frac{\left|\nabla Q_{(j)}\right|^2}{\sqrt{\varepsilon + \left|\nabla Q_{(j-1)}\right|^2}} dS \\ &= \lim_{j\to\infty} \iint_{\Pi} \frac{\left(\partial_y Q_{(j)}\right)^2 + \left(\partial_z Q_{(j)}\right)^2}{\sqrt{\varepsilon + \left(\partial_y Q_{(j-1)}\right)^2 + \left(\partial_z Q_{(j-1)}\right)^2}} dS \end{aligned} \tag{5.21}$$

$$\begin{aligned} TV_{Anisot}(Q) &= \iint_{\Pi} \left(|\partial_y Q| + |\partial_z Q| \right) dS \\ &\approx \lim_{j\to\infty} \iint_{\Pi} \frac{\left(\partial_y Q_{(j)}\right)^2}{\sqrt{\varepsilon + \left(\partial_y Q_{(j-1)}\right)^2}} dS + \lim_{j\to\infty} \iint_{\Pi} \frac{\left(\partial_z Q_{(j)}\right)^2}{\sqrt{\varepsilon + \left(\partial_z Q_{(j-1)}\right)^2}} dS \end{aligned} \tag{5.22}$$

As presented in equation (5.16), L_1 is approximated in a similar way

$$L_1(Q) = \iint_{\Pi} |Q| dS \approx \lim_{j\to\infty} \iint_{\Pi} \frac{\left|Q_{(j)}\right|^2}{\sqrt{\varepsilon + \left|Q_{(j-1)}\right|^2}} dS \tag{5.23}$$

where ε is a small parameter that is introduced in order to avoid dividing by zero and the parentheses stand for the iteration.

Since the regularization parameters, $\boldsymbol{\alpha} = \left(\alpha_{Tk}, \alpha_{L_1}, \alpha_{TV}\right)$, determine the size of the different regularization terms with respect to the discrepancy term, the degree of regularization can be varied by modifying the values of the regularization parameters: large values of the regularization parameters increase the stability of the inversion process in the sense that the solution becomes less sensitive to noise in the data, but, on the other hand, this stability comes at the expense of introducing an error in the solution and having no longer an unbiased solution.

In order to find the optimum regularization parameters, our choice is to start iterations with a rather high initial value of the regularization parameters, α_{Tk_0}, $\alpha_{L_{1_0}}$ and α_{TV_0}, and reduce them in each iteration with different decay factors, γ_{Tk}, γ_{L_1} and γ_{TV}, respectively

$$\alpha_{Tk_j} = \alpha_{Tk_0}\ \gamma_{Tk}^{j} = 1{,}000 \cdot 0.3^{j} \tag{5.24}$$

$$\alpha_{L_{1_j}} = \alpha_{L_{1_0}}\ \gamma_{L_1}^{j} = 100 \cdot 0.75^{j} \tag{5.25}$$

$$\alpha_{TV_j} = \alpha_{TV_0}\ \gamma_{TV}^{j} = 100 \cdot 0.75^{j} \tag{5.26}$$

It can be observed that α_{Tk_0} decays much faster than $\alpha_{L_{1_0}}$ and α_{TV_0}, so that the effect of Tikhonov regularization is only significant during the first iterations.

As mentioned in section 5.2, Tikhonov damps the model vectors associated with small singular values and provides very smooth and rounded solutions, which is beneficial in the beginning of the inversion so as to make sure that the solution does not get dominated by noise, but then, sharper solutions are sought. Moreover, L_1 and Total Variation cannot be implemented in the first iteration because they need the solution in a previous iteration.

The initial values of the regularization parameters as well as their decay factors have been chosen by performing inversions repeatedly until achieving solutions in a reasonable number of iterations, about 20.

Next, the iterative process carried out by the inversion algorithm is described.

In order to describe the iterative process for the minimization of the residual shown in (5.18), it is convenient to use the operator form (matrices and vectors in discrete version), as in equation (5.4)

$$T_{f_k}^{\delta,\boldsymbol{\alpha}} \approx \mathbf{A}_{f_k}\left[Q_{f_k}^{\delta,\boldsymbol{\alpha}}\right] = I_{f_k}^{\delta,\boldsymbol{\alpha}}\mathbf{A}_{f_k}\left[Q^{\delta,\boldsymbol{\alpha}}\right] \qquad \text{for } k = 1,...,k_{\max} \tag{5.27}$$

As mentioned above, $\mathbf{A}_{f_k}$ is the integral operator, representing the kernel in equation (5.3).

For the inversion procedure, we use domain decomposition iterations to retrieve the normalized heat source distribution, $Q^{\delta,\boldsymbol{\alpha}}$, and the set of intensities, $I_{f_k}^{\delta,\boldsymbol{\alpha}}$, in successive iterations. The process of obtaining intensities and domains in two different steps is known as *non-linear Gauss-Seidel iterations by blocks* and it is a local minimization method used in bi-linear problems like this one.

We start with *iteration zero*, in which we solve the approximated equations (5.27) by its normal equations, for each modulation frequency separately

$$Q_{f_k,0}^{\delta,\boldsymbol{\alpha}} = \left(\mathbf{A}_{f_k}^{*}\mathbf{A}_{f_k} + \alpha_{Tk}\mathbf{I}\right)^{-1}\mathbf{A}_{f_k}^{*}T_{f_k}^{\delta} \tag{5.28}$$

where $\mathbf{A}_{f_k}^{*}$ stands for the complex conjugate of $\mathbf{A}_{f_k}$. However, as the right side of equation (5.28) is complex and we assume that the heat source distribution is real, we obtain $Q_{f_k,0}^{\delta,\boldsymbol{\alpha}}$ as follows

$$Q_{f_k,0}^{\delta,\boldsymbol{\alpha}} = \left(\mathrm{Re}\left(\mathbf{A}_{f_k}^{*}\mathbf{A}_{f_k}\right) + \alpha_{Tk}\mathbf{I}\right)^{-1}\mathrm{Re}\left(\mathbf{A}_{f_k}^{*}T_{f_k}^{\delta}\right) \tag{5.29}$$

to get a first approximation of the separate intensities as

$$I_{f_k,0}^{\delta,\boldsymbol{\alpha}} = \max\left(Q_{f_k,0}^{\delta,\boldsymbol{\alpha}}\right) \tag{5.30}$$

being $Q_{f_k,0}^{\delta,\boldsymbol{\alpha}}$ and $I_{f_k,0}^{\delta,\boldsymbol{\alpha}}$ the normalized heat source distribution and the set of intensities in iteration zero, respectively. The intensities obtained are now introduced as an initial guess in equation (5.27) combining all modulation frequencies together and being regularized only with Tikhonov, using the initial value of the regularization parameter α_{Tk}

$$\begin{bmatrix} I_{f_1,0}^{\delta,\boldsymbol{\alpha}}\,\mathbf{A}_{f_1} \\ I_{f_2,0}^{\delta,\boldsymbol{\alpha}}\,\mathbf{A}_{f_2} \\ \cdots \\ I_{f_{k_{\max}},0}^{\delta,\boldsymbol{\alpha}}\,\mathbf{A}_{f_{k_{\max}}} \end{bmatrix} Q_{(1)}^{\delta,\boldsymbol{\alpha}} \approx \begin{bmatrix} T_{f_1}^{\delta} \\ T_{f_2}^{\delta} \\ \cdots \\ T_{f_{k_{\max}}}^{\delta} \end{bmatrix} \tag{5.31}$$

to get a first approximation of the reconstructed normalized heat source distribution, $Q_{(1)}^{\delta,\boldsymbol{\alpha}}$. Iteration zero then gives way to iteration one, in which the Tikhonov regularization parameter α_{Tk} is reduced for the first time, whereas the regularization parameters corresponding to L_1 and Total Variation, α_{L_1} and α_{TV}, are used for the first time with their initial values.

The retrieved normalized heat source distribution $Q_{(1)}^{\delta,\boldsymbol{\alpha}}$ is introduced in equation (5.27) for each modulation frequency separately so that a new set of intensities $I_{f_k,1}^{\delta,\boldsymbol{\alpha}}$ is obtained as follows

$$I_{f_k,1}^{\delta,\boldsymbol{\alpha}} = \frac{\left\| T_{f_k}^{\delta} \right\|}{\left\| \mathbf{A}_{f_k} \left[Q_{(1)}^{\delta,\boldsymbol{\alpha}} \right] \right\|} \tag{5.32}$$

Now, the set of intensities $I_{f_k,1}^{\delta,\boldsymbol{\alpha}}$ is introduced into the equation combining all frequencies together, similarly as in equation (5.31) but now employing L_1 and Total Variation besides Tikhonov, to get a second approximation of the reconstructed normalized heat source distribution, $Q_{(2)}^{\delta,\boldsymbol{\alpha}}$.

With the second approximation of $Q_{(2)}^{\delta,\boldsymbol{\alpha}}$ iteration two begins, in which α_{Tk} is reduced for the second time, whereas α_{L_1} and α_{TV} are reduced for the first time. The same steps as in

iteration one are followed in order to get a new set of intensities, $I_{f_k,2}^{\delta,\boldsymbol{\alpha}}$, along with a third approximation of the normalized heat source distribution, $Q_{(3)}^{\delta,\boldsymbol{\alpha}}$, and so forth.

In order to automatize recovered solutions and retrieve the different cases equally, we stop iterations when the minimum discrepancy term is found. This is a heuristic stopping criterion, which works in this kind of overdetermined problem and gives best results of the retrieved normalized heat source distribution, $Q^{\delta,\boldsymbol{\alpha}}$. An important aspect that is worth mentioning about the chosen stopping criterion is that there is no over-fitting of the data, i.e., fitting the noise rather than the underlying function. Further support for this stopping criterion will be given in section 6.4.2.

6 Analysis of the inversion algorithm

In this section we analyse the ability of the implemented inversion algorithm to retrieve heat source distributions from synthetic data representing vertical homogeneous kissing rectangular cracks, by observing the effects of various aspects regarding both the algorithm and the data entering it on the quality of the reconstructions. The object of this analysis is to optimize the inversion protocol in order to expand the use of the inversion algorithm for the characterization of the widest range of geometries of heat sources accurately and to verify key aspects concerning the inversions such as the stopping criterion and the design of experiments.

In this section, the ability of the implemented inversion algorithm to reconstruct vertical heat source distributions is analysed. The whole analysis of the inversion algorithm is performed using synthetic data corresponding to heat sources representing the simplest case, homogeneous rectangular kissing cracks, and it consists in looking at the effects on the reconstructions of aspects regarding both the algorithm and the surface temperature data entering it.

With regard to the algorithm, the effect on the reconstructions of implementing either the isotropic or the anisotropic versions of the TV functional is checked, as well as the effect of altering the values of the regularization parameters corresponding to the stabilization procedures. As for the data, the effects of the noise level and noise distribution are evaluated, as well as the effect of data normalization.

The convergence property of the implemented inversion algorithm is proved, the chosen criterion to stop iterations is verified by making use of the retrieved set of intensities, $\boldsymbol{I}_{f_k}^{\delta,\boldsymbol{\alpha}}$,

and the effect of the $f_{lock\text{-}in}$ in multi-frequency data is checked on the retrieved areas so as to verify the selected design of experiments. In addition, the shadowing effect is tackled and the spatial resolution of the inversion algorithm is tested by retrieving multiple heat sources.

The general objective of analysing the inversion algorithm is to optimize it in order to expand its use for the characterization of the widest range of geometries of vertical heat source distributions. Provided that an intrinsic advantage of ultrasound excited thermography with respect to inductive and optical excitations is that it enables the detection of defects buried deeper beneath the sample surface, we also exploit this penetration potential when retrieving the heat source distributions by checking how deep we can obtain accurate reconstructions.

6.1 Generation of synthetic data

Generation of synthetic data involves discretizing both plane Π ($x = 0$), where heat sources are located, and the sample surface ($z = 0$), where surface temperature data are calculated.

The discretization of the planes is carried out over a certain area that can be varied depending on the dimensions of the heat source distribution and de depth at which it is buried. As a rule of thumb we consider a square in plane Π ($x = 0$) that is 6 mm along both y- and z- axis for the heat source distribution and we generate surface temperature data in a rectangle at the surface ($z = 0$) that is 20 mm long along x-axis (perpendicular to plane Π) and 28 mm long along y-axis (parallel to plane Π) (see Figure 5.1 (a)).

A square mesh is used for the discretization of both planes. Again, the size of the meshes can vary depending on the geometry and size of the heat sources and the desired accuracy in the surface temperature calculation. In our standard meshes, nodes in plane Π are separated by 20 µm and we calculate the surface temperature at nodes separated by 50 µm, which provides considerably finer surface temperature data than that obtained in our vibrothermography experiments, where each pixel in the detector of the IR camera averages the temperature of a 137 µm square on the sample surface. The reason for this is that we want the analysis of the inversion algorithm to be accurate enough for experimental setups using IR cameras with a higher spatial resolution.

Surface temperature data are calculated using equation (3.6), with the same maximum homogeneous flux emitted over the heat source area for all modulation frequencies and using the thermal properties corresponding to AISI 304. Then, we generate uniform noise whose norm represents the desired percentage of the total norm of the data and we distribute it uniformly over the whole frequency range. In this way, noisy amplitude and phase surface temperature data are obtained.

This procedure represents the experimental case in which data are taken with the same ultrasound power for all modulation frequencies and the same number of images is used for each lock-in process. Finally, if it was the case, all amplitude data are normalized.

It is worth mentioning that for very low noise percentages (δ < 0.5%), the size of the rectangle at z = 0 at which surface temperature data are generated defined above may not be sufficiently large, so the considered area in plane z = 0 depends on the noise level of the data as well, apart from depending on the dimensions and depth of the heat sources.

In order to illustrate what synthetic data look like, Figure 6.1 shows synthetic Ln(|T|) (left) and Ψ (right) with 5% added uniform noise corresponding to a square heat source (w = h = 1 mm) buried at a depth |d| = 0.2 mm, at $f_{lock\text{-}in}$ = 0.1 (a) and 3.2 Hz (b).

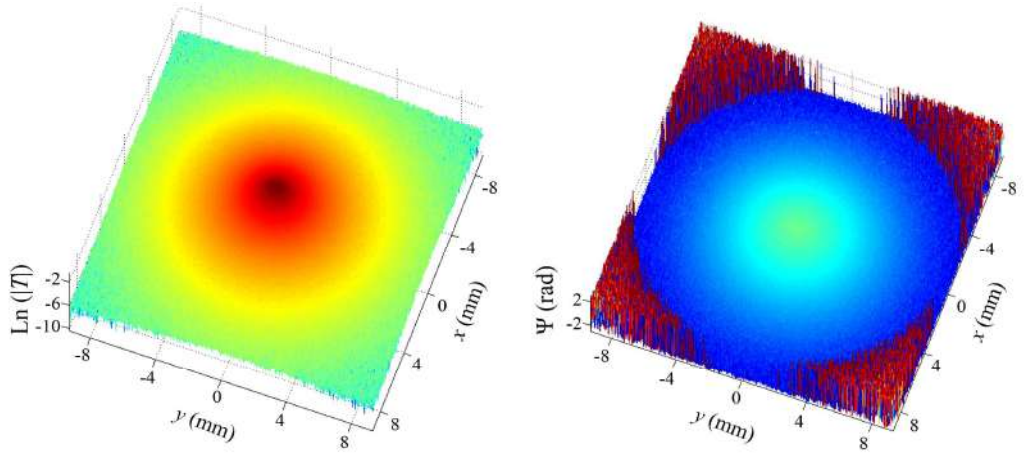

(a)

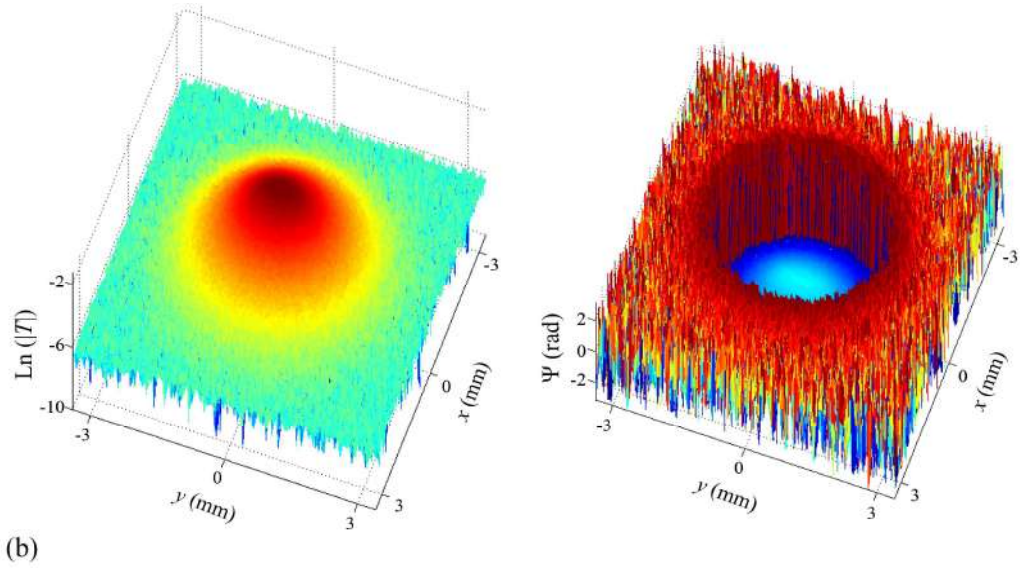

Figure 6.1. Synthetic noisy Ln(|*T*|) (left) and Ψ (right) thermograms generated at $f_{lock\text{-}in}$ = 0.1 (a) and 3.2 Hz (b), corresponding to a homogeneous square heat source (w = h = 1 mm) buried at a depth |d| = 0.2 mm. Data are affected by 5% uniform noise.

For a more detailed visualization, both Ln(|*T*|) and Ψ thermograms shown in Figure 6.1 have been cropped. For the inversion, surface temperature data may be cropped in order to demand a lower computer capacity and thus reduce the inversion time, as long as the amplitude has reached the noise level and the phase has become random, i.e., as long as the removed areas are basically noise.

6.2 Effect of the TV functional model: TV_{Isot} vs. TV_{Anisot}

We now focus on assessing the effect on the reconstructions of implementing Total Variation regularization in its two versions: TV_{Isot} and TV_{Anisot}. The definitions and the expressions of the quadratic approximations of both versions of the Total Variation functional are shown in equations (5.21) and (5.22), respectively.

We start by inverting synthetic data with 5% added uniform noise corresponding to a standard square heat source (w = h = 1 mm) located at increasing depths, namely, |d| = 0.2, 0.6, 1.2, 1.6, 2.6 and 3.2 mm. In these inversions, the amplitudes of the surface temperatures are normalized: we divide the whole amplitude thermograms by their

maximum value, at each modulation frequency, which brings all maximum amplitudes to 1. As an example, Figure 6.2 (a) shows synthetic normalized Ln(|*T*|) (left) and Ψ (right) thermograms corresponding to a square heat source ($w = h = 1$ mm) buried at a depth $|d| = 0.2$ mm, at $f_{lock\text{-}in} = 0.8$ Hz. The fitted thermograms are shown in Figure 6.2 (b).

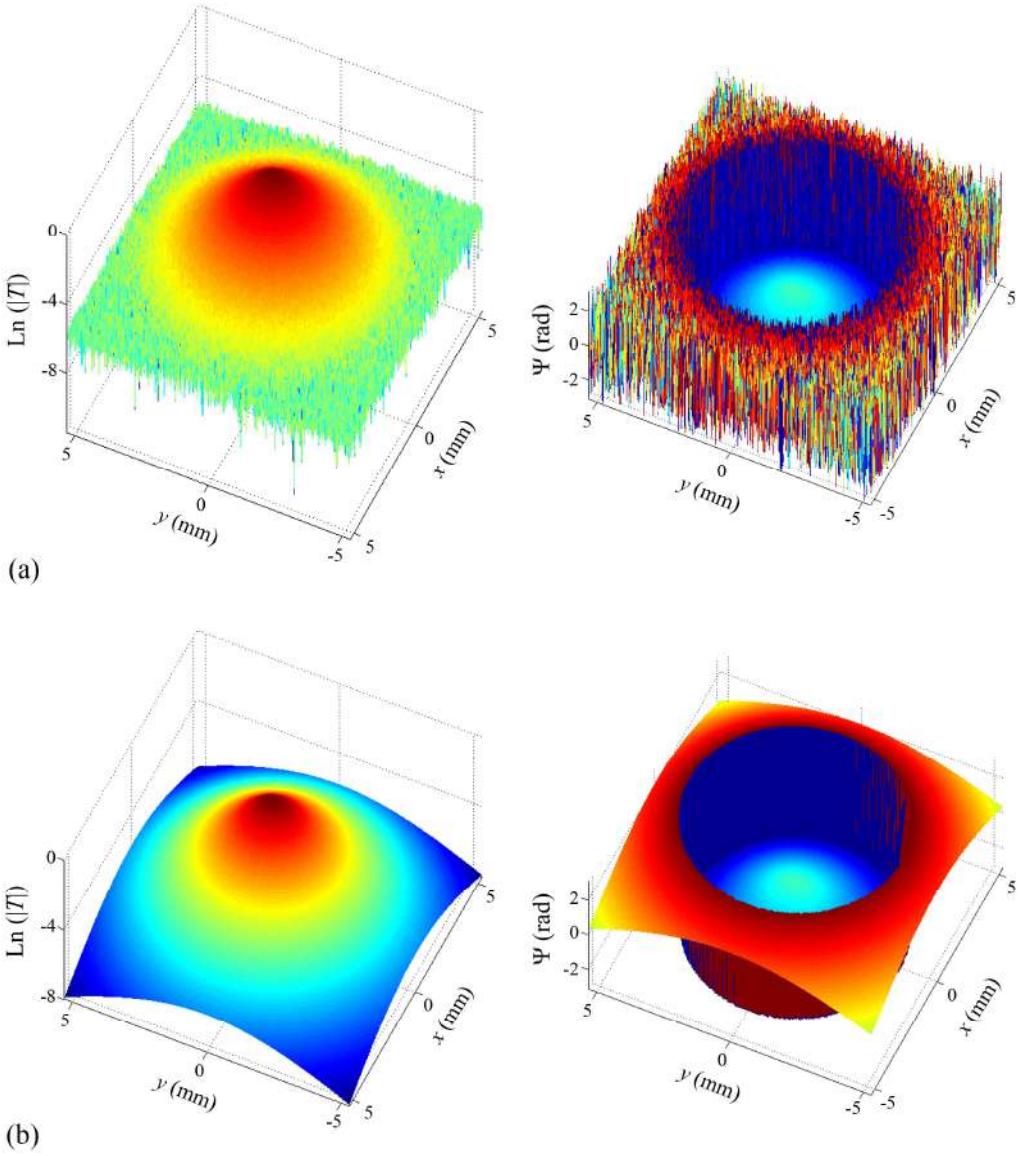

Figure 6.2. (a) Synthetic data affected by 5% uniform noise, normalized Ln(|*T*|) (left) and Ψ (right) thermograms at $f_{lock\text{-}in} = 0.8$ Hz and (b) fitted thermograms, corresponding to a homogeneous square heat source ($w = h = 1$ mm) buried at a depth $|d| = 0.2$ mm.

The results of inversions implementing TV_{Isot} and TV_{Anisot} are depicted in Figure 6.3 (a) and (b), respectively: we represent a grey level diagram of the normalized heat source distribution, $Q^{\delta,\alpha}$, retrieved in plane Π, where white corresponds to the maximum value (1) and black (0) to the absence of heat sources. The real geometry of the heat sources is represented by a red contour and, for the sake of clarity, the depth (in mm) at which the heat sources are buried is indicated on top of each reconstruction.

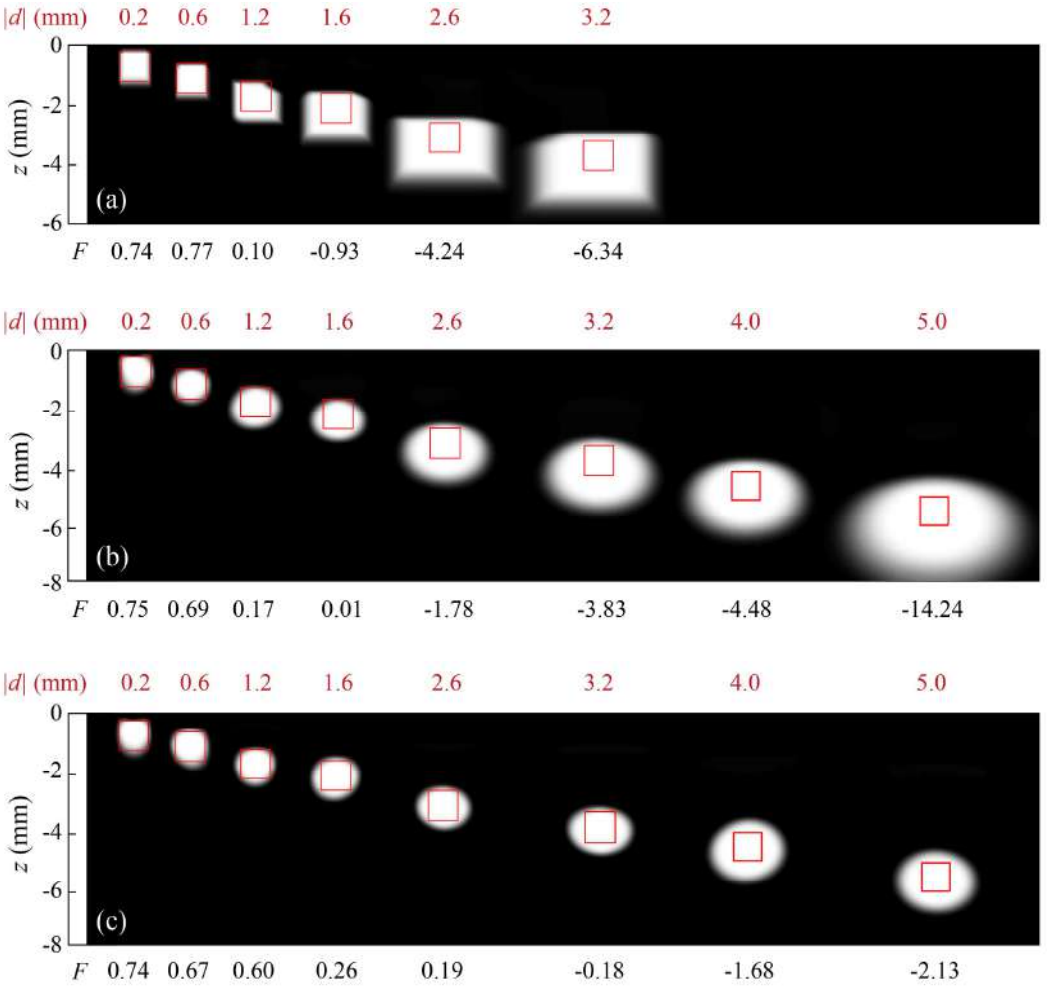

Figure 6.3. Grey level representation of the normalized heat source distribution, $Q^{\delta,\alpha}$, corresponding to synthetic data affected by 5% added uniform noise generated for square heat sources (w = h = 1 mm) buried at increasing depths, retrieved by using: (a) TV_{Anisot} and entering normalized amplitudes, (b) TV_{Isot} and entering normalized amplitudes and (c) TV_{Isot} and entering raw amplitudes. The depths of the squares in (a) are: $|d|$ = 0.2, 0.6, 1.2, 1.6, 2.6 and 3.2 mm. In (b) and (c), also $|d|$ = 4.0 and 5.0 mm. Real contours depicted in red and values of the depth of the heat sources and quality factor F, on top of and under each reconstruction, respectively.

As a general overview, it can be seen that as the depth increases the reconstructions become wider than the real squares. However, the depths of all heat sources are well recovered.

When stabilizing the inversion with either model of Total Variation, the search is performed among blocky functions, i.e., functions with flat sections and sharp edges. In the anisotropic model, the partial derivatives along the different directions of the search plane (y and z) are separated in different terms, which provokes the minimization process reduce the projection of the contour of the heat source distribution along these axes. Figure 6.3 (a) shows that the effect of separating the derivatives in the two directions of the search plane in different terms is to favour jumps along the directions of the axes (y and z), which helps defining very well the corners of the squares. TV_{Anisot}, thus, gives advantage to the reconstruction of shapes having edges that coincide with the directions of the axes, such as in square or rectangular geometries.

In the isotropic model, on the contrary, the partial derivatives along the different directions are mixed together, which makes the minimization process tend to reduce the contour of the area where the heat source distribution has non-zero values. For this reason, provided that the circle is the shape with minimum perimeter for a given area, rounded reconstructed areas are obtained when using TV_{Isot}. Despite this, for the shallowest case (see Figure 6.3 (b)), TV_{Isot} reproduces quite nicely the upper contour of the square. Given that in a real problem the geometry of the heat source distribution is unknown, it is advisable to stabilize the algorithm with TV_{Isot} so that the results are of more general applications, since heat sources are equitably retrieved regardless of their particular geometry.

In order to quantify the accuracy of the reconstructions, we have introduced a *quality factor* F. This quality factor takes into account the values of the retrieved $Q^{\delta,\alpha}$ within and outside the real contour of the heat source distribution and it is defined as

$$F = \frac{\sum_{i=1}^{M} Q_i^{\delta,\alpha} - \sum_{j=1}^{P} Q_j^{\delta,\alpha}}{M} \tag{6.1}$$

where M is the number of nodes within the real geometry and P is the number of nodes in plane Π outside the real geometry. According to this definition, $F = 1$ corresponds to a perfect reconstruction. The value of F progressively decreases as the quality of the reconstruction worsens and F can reach negative values.

In order to define what a sufficiently accurate reconstruction should look like, we have also introduced an *accurate reconstruction* criterion based on the value of the quality factor: a reconstruction can be considered to be accurate as long as $F > -1$. The values of F are displayed under each reconstruction.

Provided that TV_{Isot} improves significantly the accuracy of the reconstructions obtained with TV_{Anisot}, two deeper squares have been added in Figure 6.3 (b), at depths $|d| = 4.0$ and 5.0 mm.

6.3 Effect of data normalization: normalized vs. raw amplitudes

As mentioned above, normalized amplitudes have been introduced in the algorithm in order to obtain the reconstructions shown in Figure 6.3 (a) and (b), as a method to standardize data input in the inversion algorithm. As the amplitude decreases with increasing modulation frequency, bringing all maximum amplitudes to 1 can be understood experimentally as increasing the ultrasound intensity with modulation frequency.

However, Figure 6.3 (c) shows the reconstructions of the same heat sources in inversions entering raw amplitudes (and stabilizing the inversions with TV_{Isot}) and, as can be observed, the quality of the reconstructions improves dramatically, especially from $|d| > 2.6$ mm on: the reconstructions are sharper and the enlargement of the retrieved areas with respect to the real sizes is less significant.

This difference cannot be attributed to any inadequacy of the algorithm to deal with normalized amplitudes, since the intensities, I_{f_k}, are introduced in the inversion procedure in order to absorb any flux difference at different modulation frequencies. Due to the damped nature of thermal waves, normalizing all amplitudes implies multiplying amplitude thermograms by factor that increases with modulation frequency. As a consequence, the absolute noise in the normalized thermograms increases as well, which is the reason for the degradation of the reconstructions when normalized amplitudes enter the algorithm.

Another possibility to standardize data input into the algorithm is to normalize the amplitudes at all modulation frequencies first and then add the uniform noise. However, this procedure is experimentally unfeasible and, for this reason, it has not been considered in inversions from synthetic data.

Thus, in order to determine the optimum inversion protocol, it can be concluded that raw amplitudes should enter the inversion algorithm, which, in turn, should be stabilized with the isotropic model of the Total Variation functional so that no directions within the search area are favoured and heat source distributions of any shape are equitably retrieved.

This considered, as may be checked in Figure 6.3 (c), we are able to obtain accurate reconstructions of square heat sources of 1 mm^2 buried beneath the surface of an AISI 304 sample down to a depth about $|d|$ = 3.6 mm, for synthetic data affected by 5% uniform noise. The results of this analysis are scalable to squares of different sides L and different sample properties, as long as the data used for the inversions are generated at modulation frequencies corresponding to thermal diffusion lengths that represent the same fractions of the square size: from 0.3 to 5L.

6.4 Effect of the noise and stopping criterion verification

The reconstructions shown so far have been inverted using synthetic data with uniformly distributed 5% added uniform noise. However, we now show the influence of the noise level on the quality of the reconstructions. To that purpose, we look at the behaviour of the inversion algorithm when reducing or increasing the noise level in the data, being the noise uniformly distributed among the different $f_{lock\text{-}in}$.

Due to the ill-posed character of the inverse problem in the presence of noise, more accurately retrieved normalized heat source distributions, $Q^{\delta,\boldsymbol{\alpha}}$, can be expected when decreasing noise level, which proves the convergence property of the inversion algorithm. In addition, we propose a method to verify the established minimization stopping criterion using the retrieved set of intensities, $I_{f_k}^{\delta,\boldsymbol{\alpha}}$.

Lastly, the effect of noise distribution over the modulation frequency range on the quality of the reconstructions is considered since, in practice, noise can also be distributed non-uniformly in multi-frequency data obtained in vibrothermography experiments, if a different number of images is analysed in the lock-in process at each modulation frequency.

6.4.1 Uniform noise distribution

The effect of reducing the noise level is illustrated in Figure 6.4, where we compare the reconstructions obtained from synthetic data corresponding to a standard square heat source ($w = h = 1$ mm) located at increasing depths, namely, $|d| = 1.2$, 2.0, 2.6, 3.2, 3.6, 4.0 and 5.0 mm, with uniformly distributed (a) 5% and (b) 0.5% added uniform noise and retrieved by implementing the optimum inversion protocol.

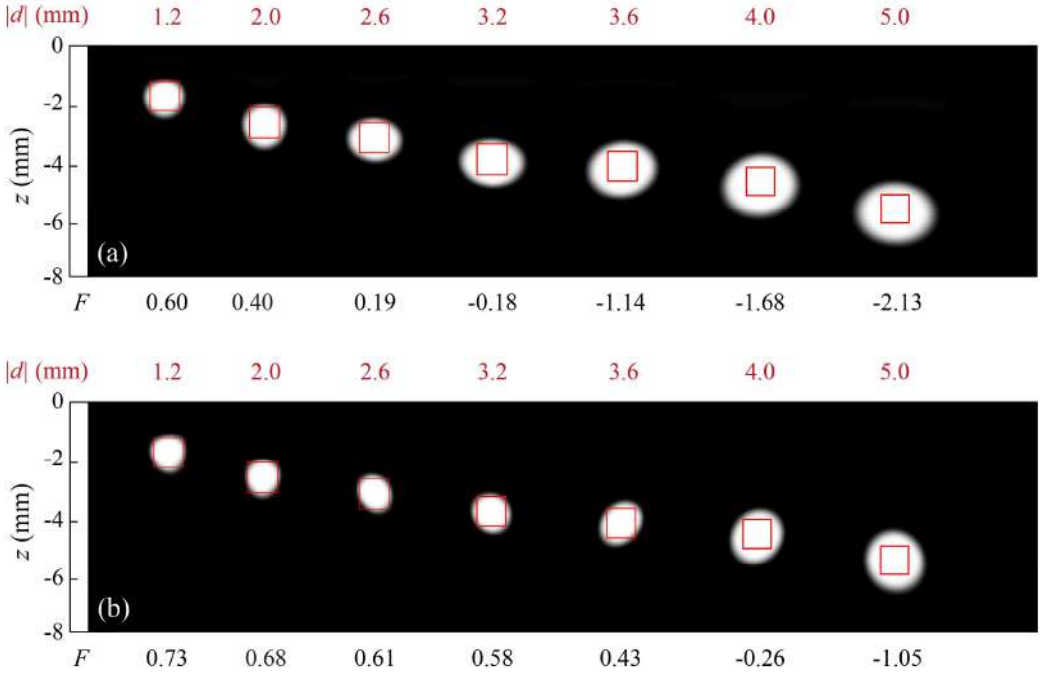

Figure 6.4. Grey level representation of the normalized heat source distribution corresponding to synthetic data generated for square heat sources ($w = h = 1$ mm) buried at increasing depths, namely, $|d| = 1.2$, 2.0, 2.6, 3.2, 3.6, 4.0 and 5.0 mm, affected by uniformly distributed (a) 5% and (b) 0.5% uniform noise. Retrieved by implementing TV_{Isot} and entering raw amplitudes. Real contours depicted in red and values of the depth of the heat sources and quality factor F, on top of and under each reconstruction, respectively.

As may be observed, improvements on the reconstructions are obvious when the noise level in the data is reduced, since noise reduction makes a noticeable difference in the contribution of high frequency information to the inversion.

This proves the convergence property of the algorithm, since the solution of the inverse problem, $Q^{\delta,\alpha}$, tends to the exact normalized heat source distribution Q, as the surface

temperature data, $T_{f_k}^{\delta}$, approach the noiseless surface temperature data, T_{f_k}, i.e., as the noise level tends to zero ($\delta \to 0$).

As mentioned above, noise reduction allows digging up information buried in noise, especially at high modulation frequencies. To illustrate how noise affects the information carried in high frequencies, in Figure 6.5 we show a side view of the surface amplitude thermogram corresponding to a square heat source buried at a depth $|d|$ = 3.2 mm with (a) 5% and (b) 0.5% added uniform noise, generated at $f_{lock\text{-}in}$ = 3.2 Hz.

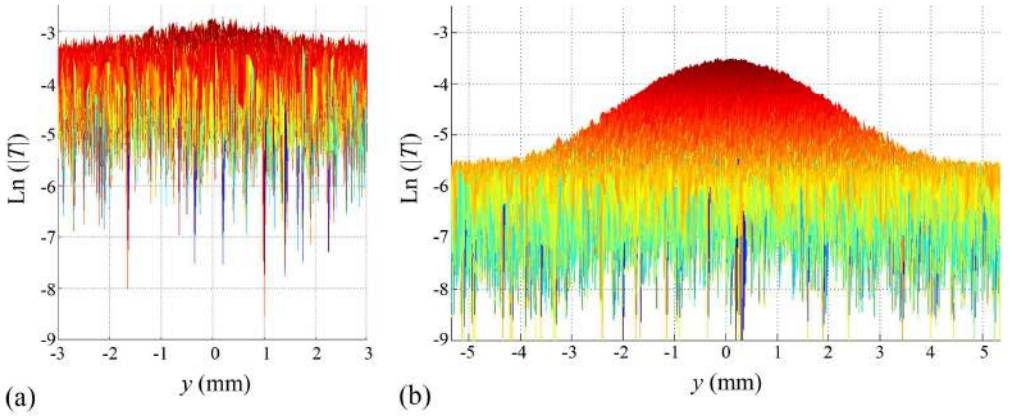

Figure 6.5. Side view of the surface amplitude thermogram corresponding to a square heat source of $w = h$ = 1 m, buried at a depth $|d|$ = 3.2 mm, with uniformly distributed (a) 5% and (b) 0.5% added uniform noise, generated at $f_{lock\text{-}in}$ = 3.2 Hz.

However, from a practical point of view, although in lock-in vibrothermography experiments the noise level can be reduced by analysing a larger number of images, the procedure takes time and the ultimate effect is a reduction of the signal-to-noise ratio with increasing depth, since the amplitude of the surface temperature diminishes as the depth of the heat source increases.

For this reason, we have also looked at the effect of increasing the noise level on the quality of the reconstructions. In Figure 6.6 we show reconstructions of the $w = h$ = 1 mm square heat source buried at a depth $|d|$ = 3.2 mm from data affected by 10% and 15% uniform noise, in addition to the result of the same heat source previously shown from data affected by 5% uniform noise. It can be checked that the quality of the reconstructions worsens as the noise level increases.

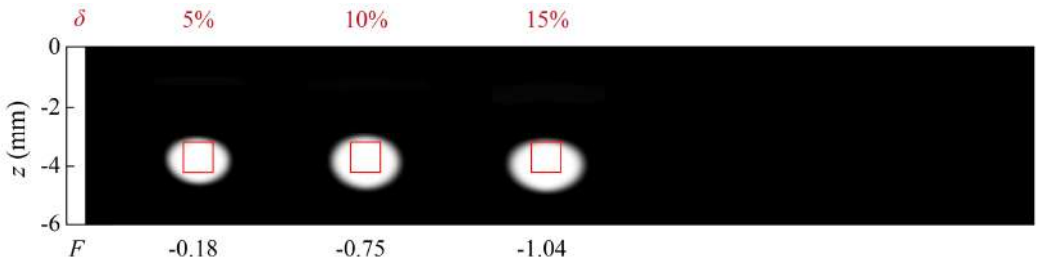

Figure 6.6. Grey level representation of the normalized heat source distribution inverted from synthetic data corresponding to a square heat source ($w = h = 1$ mm) buried at a depth $|d| = 3.2$ mm with uniformly distributed 5%, 10% and 15% added uniform noise. Retrieved by implementing the optimum inversion protocol. Real contours depicted in red and values of the noise level and quality factor F on top of and under each reconstruction, respectively.

As may be noted, the noise level in the data limits the maximum depth at which we can get accurate reconstructions in inversions implementing the optimum protocol: whereas it is about $|d| = 3.6$ mm for data affected by 5% uniform noise, it is increased to $|d| = 5.0$ mm and reduced to $|d| = 3.2$ mm for data affected by 0.5% and 15% uniform noise, respectively.

6.4.2 Stopping criterion verification

As described in section 5.3, the iterative minimization process is stopped when the minimum discrepancy term is found, obtaining the retrieved normalized heat source distribution, $Q^{\delta,\boldsymbol{\alpha}}$, and the set of intensities, $I_{f_k}^{\delta,\boldsymbol{\alpha}}$. Recall that I_{f_k} is introduced so as to allow the maximum intensity of the heat sources vary from one modulation frequency to another.

However, the values of these intensities over iterations may be used in order to verify that stopping the minimization process at the discrepancy term minimal iteration is the appropriate choice so as to obtain the optimum solution to our inverse problem.

Let's start with the illustration of the evolution of the intensities over the iterative process in such a way that the intensity at each f_k is divided by that at the next lower f_k within our modulation frequency set. We can thus define 8 relations, since we combine data at 9 modulation frequencies: relation 1 refers to $I_{f_2,j}^{\delta,\boldsymbol{\alpha}} / I_{f_1,j}^{\delta,\boldsymbol{\alpha}}$, relation 2 stands for $I_{f_3,j}^{\delta,\boldsymbol{\alpha}} / I_{f_2,j}^{\delta,\boldsymbol{\alpha}}$, and so forth, where $k = 1, \ldots, 9$, and j stands for the iteration.

Figure 6.7 (a) shows the evolution of $I^{\delta,\boldsymbol{\alpha}}_{f_{k+1},j} / I^{\delta,\boldsymbol{\alpha}}_{f_k,j}$ in an inversion from synthetic data affected by 5% uniform noise corresponding to a square heat source ($w = h = 1$ mm) buried at a depth $|d| = 1.6$ mm. In this inversion, the discrepancy term minimal iteration is the 22nd (see Figure 6.7 (b)).

If we generate surface temperature thermograms corresponding to common maximum homogeneous fluxes at all modulation frequencies and we invert raw amplitudes, an indication that the inversion algorithm is correctly fitting the data over iterations is that the defined intensity relations approach 1.

According to this, relations from 1 to 5 in Figure 6.7 indicate that the surface temperatures at the corresponding f_k (from 0.05 to 1.6 Hz) are accurately fitted. Relation 6, involving data at 1.6 and 3.2 Hz, is harder to fit but it approaches 1 and shows a smooth minimum around the minimal discrepancy term iteration. Lastly, relations 7 and 8 are not properly fitted over the whole minimization process, because data at these modulation frequencies (from 3.2 to 12.8 Hz) are dominated by noise, given the depth of the heat source.

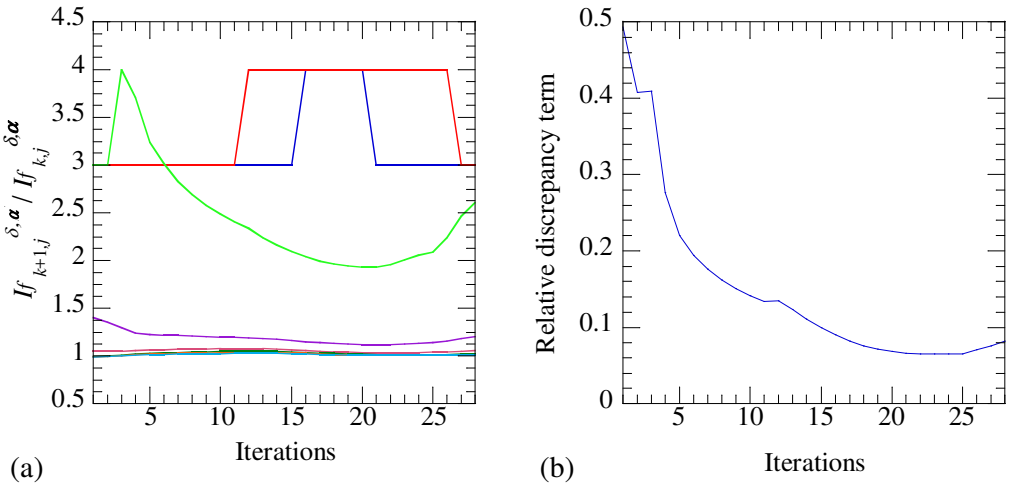

Figure 6.7. (a) Evolution of $I^{\delta,\boldsymbol{\alpha}}_{f_{k+1},j} / I^{\delta,\boldsymbol{\alpha}}_{f_k,j}$ in an inversion from synthetic data affected by 5% uniform noise corresponding to a square heat source ($w = h = 1$ mm) buried at a depth $|d| = 1.6$ mm. Coloured lines stand for the intensity relations: 1 ($I^{\delta,\boldsymbol{\alpha}}_{0.1,j} / I^{\delta,\boldsymbol{\alpha}}_{0.05,j}$) (pink), 2 ($I^{\delta,\boldsymbol{\alpha}}_{0.2,j} / I^{\delta,\boldsymbol{\alpha}}_{0.1,j}$) (light blue), 3 ($I^{\delta,\boldsymbol{\alpha}}_{0.4,j} / I^{\delta,\boldsymbol{\alpha}}_{0.2,j}$) (orange), 4 ($I^{\delta,\boldsymbol{\alpha}}_{0.8,j} / I^{\delta,\boldsymbol{\alpha}}_{0.4,j}$) (dark green), 5 ($I^{\delta,\boldsymbol{\alpha}}_{1.6,j} / I^{\delta,\boldsymbol{\alpha}}_{0.8,j}$) (purple), 6 ($I^{\delta,\boldsymbol{\alpha}}_{3.2,j} / I^{\delta,\boldsymbol{\alpha}}_{1.6,j}$) (green), 7 ($I^{\delta,\boldsymbol{\alpha}}_{6.4,j} / I^{\delta,\boldsymbol{\alpha}}_{3.2,j}$) (red) and 8 ($I^{\delta,\boldsymbol{\alpha}}_{12.8,j} / I^{\delta,\boldsymbol{\alpha}}_{6.4,j}$) (blue), and (b) discrepancy term evolution in the same inversion.

Taking the meaning of the defined intensity relations into account, we have considered a second stopping criterion, for which the following expression, based on least squares, needs to be defined

$$Int = \sum_{k=1}^{8} \left(\frac{I^{\delta,\alpha}_{f_{k+1},j}}{I^{\delta,\alpha}_{f_k,j}} - 1 \right)^2 \tag{6.2}$$

The object of this second stopping criterion is to check that the intensities are fitted in an optimum way at the iteration at which the minimization process is stopped, and it consists in verifying that *Int* shows either a local or global minimum around the discrepancy term minimal iteration.

Figure 6.8 (a) shows *Int* over iterations with all intensity relations taken into account. As can be checked, the fact that the relations that are not properly fitted over the whole minimization process (relations 8 and 7) are taken into account, is reflected on the shape of *Int*, provoking peaks in certain iterations, as it corresponds to their evolution in Figure 6.7 (a). However, by discarding the intensity relation 8, the evolution of *Int* depicted in Figure 6.8 (b) is obtained, where a local minimum can be observed around the discrepancy term minimal iteration and, preventing both relations 8 and 7 from entering equation (6.2), we get the evolution of *Int* shown in Figure 6.8 (c), where the previous minimum becomes global instead of local.

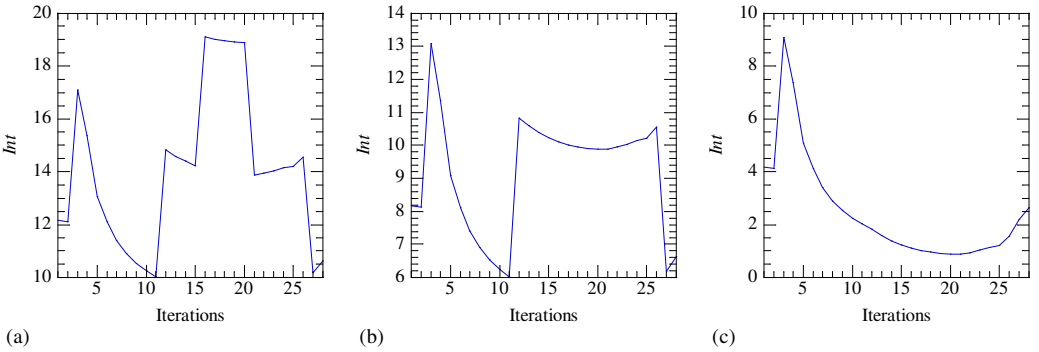

Figure 6.8. Evolution of *Int* in an inversion from synthetic data affected by 5% uniform noise corresponding to a square heat source (w = h = 1 mm) buried at a depth $|d|$ = 1.6 mm, (a) taking all intensity relations into account, (b) discarding relation 8, which relates data at the two highest modulation frequencies, and (c) discarding relations 8 and 7, which involve data at 12.8 and 6.4 Hz and data at 6.4 and 3.2 Hz, respectively.

As will be shown in section 6.5, this does not mean that entering surface temperature data in which the signal is highly affected by noise harms the retrieved normalized heat source distribution. However, for the sake of clarity in the visualization of this second stopping criterion, intensity relations fitted at no time, i.e., that do not attempt to reach 1 over the whole minimization process, can be prevented from entering equation (6.2), as they have no effect on the interpretation of the criterion.

This is a way of proving that the intensities are fitted in an optimum way when the minimization process is stopped, which supports the criterion of stopping iterations at the discrepancy term minimal iteration. In this way, optimum normalized heat source distributions are obtained, which allow for the verification of the convergence property of the algorithm, as has been shown in Figure 6.5.

6.4.3 Non-uniform noise distribution

Back to noise distribution in multi-frequency data, we now analyse the effect on the reconstructions of entering synthetic data with different noise distributions among modulation frequencies. To this purpose, we have generated synthetic noisy data with two different non-uniform noise distributions and we have compared the resulting reconstructions to the one retrieved from data with uniformly distributed noise, being the global noise level the same in the three cases.

Taking the noise level at the intermediate modulation frequency $f_{lock\text{-}in}$ = 0.8 Hz as common point, we have considered two cases: favouring higher $f_{lock\text{-}in}$, which is equivalent to analysing more images in the lock-in process at higher modulation frequencies progressively, and also the opposite case, where lower $f_{lock\text{-}in}$ are favoured.

To illustrate this, in Table 6.1 we show the ratio of the norm of the noise to the norm of the exact data at each modulation frequency, δ_{f_k}, corresponding to a square heat source ($w = h$ = 1 mm) buried at a depth $|d|$ = 2.0 mm, along with the equivalent number of images analysed, for the three cases. The signal in each case has been adjusted so that the global noise level, i.e., the ratio of the norm of the noise to the norm of the data summed all over the whole modulation frequency range, is 10% in the three cases.

$f_{lock\text{-}in}$ (Hz)	Low $f_{lock\text{-}in}$ favoured		No $f_{lock\text{-}in}$ favoured		High $f_{lock\text{-}in}$ favoured	
	N_{images}	δ_{fk} (%)	N_{images}	δ_{fk} (%)	N_{images}	δ_{fk} (%)
0.05	512,000	1.53	32,000	6.15	2,000	9.53
0.1	256,000	2.88	32,000	8.19	4,000	10.14
0.2	128,000	5.81	32,000	11.64	8,000	16.64
0.4	64,000	14.77	32,000	20.83	16,000	22.27
0.8	32,000	29.80	32,000	29.80	32,000	29.80
1.6	16,000	68.68	32,000	55.88	64,000	31.22
3.2	8,000	96.70	32,000	88.79	128,000	37.43
6.4	4,000	99.84	32,000	99.39	256,000	78.99
12.8	2,000	100.00	32,000	100.00	512,000	99.19

Table 6.1. Ratio of the norm of the noise to the norm of the exact data at each modulation frequency, δ_{f_k}, along with the equivalent number of images analysed in the lock-in process, in synthetic data corresponding to a square heat source of $w = h = 1$ mm buried at a depth $|d| = 2.0$ mm, with noise added in three different ways: uniformly distributed (centre) and non-uniformly distributed favouring both higher (right) and lower modulation frequencies (left), considering $f_{lock\text{-}in} = 0.8$ Hz as common point. The global noise level in all cases is 10%.

Figure 6.9 shows the reconstructions from synthetic data affected by 10% noise added in these three ways: uniformly distributed (centre) and non-uniformly distributed favouring low (left) and high (right) modulation frequencies. As may be noted, favouring high modulation frequencies gives the most accurate reconstruction of all. It is worth noting that as the equivalent number of images at high modulation frequencies decreases, the depth of the heat source is gradually less accurately recovered.

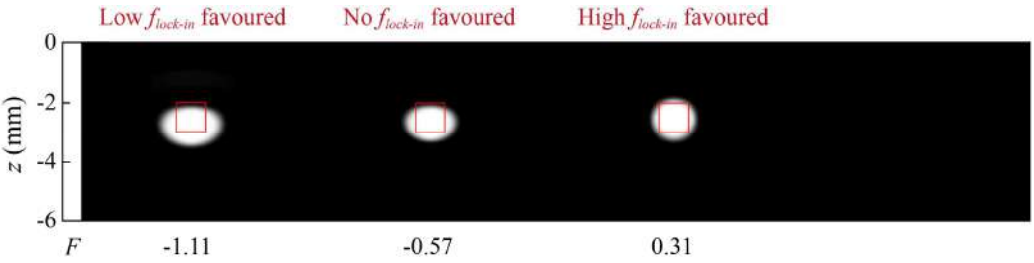

Figure 6.9. Grey level representation of the normalized heat source distribution inverted from synthetic data corresponding to a square heat source ($w = h = 1$ mm) buried at a depth (a) $|d| = 2.0$ mm with noise added in three different ways: uniformly distributed (centre) and non-uniformly distributed favouring low (left) and high (right) modulation frequencies, being the global noise level 10% in all cases. Retrieved by implementing the optimum inversion protocol. Real contours depicted in red and non-uniform noise distribution and quality factor F on top of and under each reconstruction, respectively.

All in all, at least the same number of images at all modulation frequencies should be used for the lock-in analysis in vibrothermography experiments in order to increase the accuracy of the reconstructions, as high frequency information contains higher spatial resolution.

All reconstructions shown from now on will be retrieved from synthetic data with uniformly distributed noise.

6.5 Effect of $f_{lock\text{-}in}$ in multi-frequency data and design of experiments

In the analysis of the inverse problem, we have seen that combining vibrothermography data obtained at various modulation frequencies allows us to reduce the ill-posedness of the inverse problem, since we use more information than if we performed the inversions entering data at any single modulation frequency (see Figure 5.2).

In order to check this fact and illustrate the importance of multi-frequency data on the accuracy of the retrieved normalized heat source distribution, in Figure 6.10 (a) we show reconstructions of a standard square ($w = h = 1$ mm) buried at a depth $|d| = 2.6$ mm, but inverting synthetic data at each modulation frequency separately (the corresponding f_k are displayed on top of each reconstruction). The reconstruction of the same heat source combining all modulation frequencies is also shown in Figure 6.10 (b). Data are affected by 5% added uniform noise.

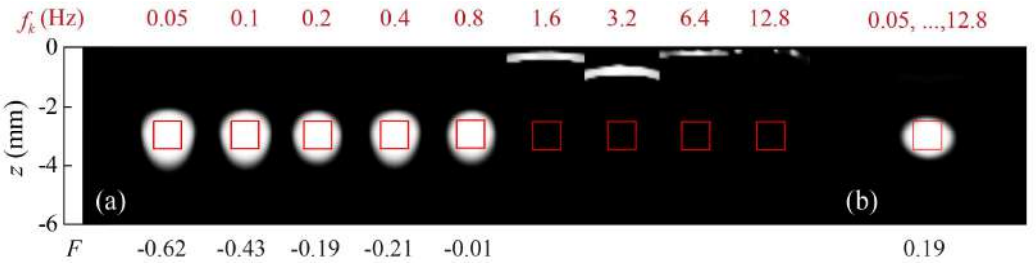

Figure 6.10. Grey level representation of the normalized heat source distribution inverted from synthetic data with 5% added uniform noise corresponding to a square heat source ($w = h = 1$ mm) buried at a depth $|d| = 2.6$ mm, retrieved by implementing the optimum inversion protocol and entering (a) data at each modulation frequency separately, namely, 0.05, 0.1, 0.2, 0.4, 0.8, 1.6, 3.2, 6.4 and 12.8 Hz, and (b) multi-frequency data. The corresponding f_k is displayed on top of each reconstruction. Real contours depicted in red and values of the quality factor F under each reconstruction.

As can be observed, the F value in the reconstruction obtained by entering multi-frequency data is higher than that in any other reconstructions retrieved from data at a single modulation frequency. Actually, the heat source cannot be retrieved from data at a single modulation frequency if this ranges from 1.6 to 12.8 Hz as the signal is highly affected by noise. Instead, some artefacts can be seen on the upper part of the search areas, which indicate that the inversion algorithm has been fitting basically noise.

Nevertheless, we have checked that, when combining all modulation frequencies, entering data at the modulation frequencies in which surface temperature information is dominated by noise does not harm the inversions. In fact, entering such thermograms improves the accuracy of the reconstructions. The reason for this is that we introduce information to the inversion algorithm (signal "almost zero"), which is better than having no thermograms at all. Of course, the further addition of thermograms at higher modulation frequencies does not improve the quality of the retrieved areas indefinitely, as improvements get saturated.

As we use multi-frequency data, the effect on the reconstructions of reducing the high frequency content is also checked here, considering a certain depth of the heat source and entering data containing a gradually narrower set of low frequency information. Figure 6.11 (a) shows reconstructions from data corresponding to a square heat source ($w = h = 1$ mm) buried at a depth $|d| = 2$ mm, at a gradually narrower set of modulation frequencies: from 0.05 to 0.2 Hz (left), from 0.05 to 1.6 Hz (centre) and from 0.05 to 12.8 Hz (right).

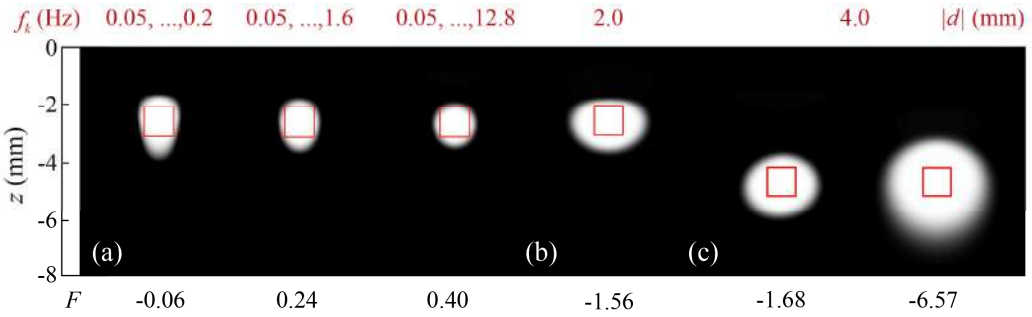

Figure 6.11. Grey level representation of the normalized heat source distribution corresponding to synthetic data affected by 5% uniform noise corresponding to a square heat source of $w = h = 1$ mm, (a) buried at a depth $|d| = 2.0$ mm and retrieved by entering data at three doubling modulation frequency sets: from 0.05 to 0.2 Hz (left), from 0.05 to 1.6 Hz (centre) and from 0.05 to 12.8 Hz (right), (b) buried at a depth $|d| = 2.0$ mm and entering data at uniformly distributed modulation frequencies and (c) buried at a depth $|d| = 4.0$ mm and entering data at both $f_{lock\text{-}in}$ distributions: doubling (left) and uniformly distributed (right) modulation frequencies. Retrieved by using the optimum inversion protocol. Real contours depicted in red and values of the quality factor F under each reconstruction.

It can be seen that the quality of the reconstructions decrease as high frequency information is lost, for a heat source at a certain depth.

As for the design of experiments, i.e., the way the different $f_{lock\text{-}in}$ are distributed within the ends of our modulation frequency set (0.05 and 12.8 Hz), we have seen in Figure 5.4 (a) that the information provided for the resolution of the inverse problem with either $f_{lock\text{-}in}$ distribution (doubling or uniformly distributing modulation frequencies, see Table 5.1) is very similar.

However, when it comes to the quality of the reconstructions, the appropriate $f_{lock\text{-}in}$ distribution becomes determinant, for synthetic data affected by the same percentage of uniform noise. In order to evince this, Figure 6.11 (b) shows the reconstruction of a square heat source ($w = h = 1$ mm) buried at $|d| = 2.0$ mm, retrieved from synthetic data with 5% added uniform noise at uniformly distributed modulation frequencies between 0.05 and 12.8 Hz. Comparing it to the reconstruction shown in Figure 6.11 (a) (right), it can be noted that the resulting reconstruction is much less accurate. The reason for this is that there are many more high modulation frequencies with very little useful information, as these frequencies have a very poor signal-to-noise ratio. This provokes no significant differences in reconstructions of shallow heat sources, but as information carried by high modulation frequencies gets lost with depth, deeper reconstructions from data at uniformly distributed modulation frequencies are obtained with less information in relation to those retrieved from data at doubling modulation frequencies.

Following this idea, in Figure 6.11 (c) we show reconstructions of a square heat source ($w = h = 1$ mm) buried at $|d| = 4.0$ mm, retrieved from synthetic data with 5% added uniform noise using both $f_{lock\text{-}in}$ distributions: doubling (left) and uniformly distributing modulation frequencies (right). At this depth, the effect of high frequency content loss becomes evident. Provided that we are interested in retrieving as deep heat sources from vibrothermography data as possible, it is clear that doubling $f_{lock\text{-}in}$ is the optimum choice for the design of experiments.

All in all, it can be concluded that doubling modulation frequencies that range from 0.05 to 12.8 Hz is the optimum design of experiments, which gives most accurate reconstructions.

6.6 Discrepancy term evolution and effect of the regularization parameters

As introduced in the description of the inversion algorithm (section 5.3), the regularization parameters corresponding to Tikhonov, L_1 and Total Variation functionals are of vital importance in the inverse problem of this thesis. The initial values and decay factors of the regularization parameters, defined in equations (5.24), (5.25) and (5.26), determine the shape of the discrepancy term evolution, i.e., the value of the discrepancy term in equation (5.18) as a function of iterations. Although the shape of the discrepancy term evolution varies in each inversion, a common behaviour can be observed regardless of the geometry of the heat sources: the minimum discrepancy term is reached in monotonically fewer iterations with increasing depth of the heat source, which is related to the fact that deeper heat sources are retrieved with a gradually narrower set of low frequency information. In other words, the less amount of information enters the algorithm, the sooner the solution is reached. To illustrate this, Figure 6.12 shows the discrepancy term evolution in inversions from synthetic data affected by 5% uniform noise corresponding to a standard square heat source of $w = h = 1$ mm buried at two different depths, namely, $|d| = 0.2$ (a) and 5.0 mm (b). The resulting reconstructions can be found in Figure 6.3 (c).

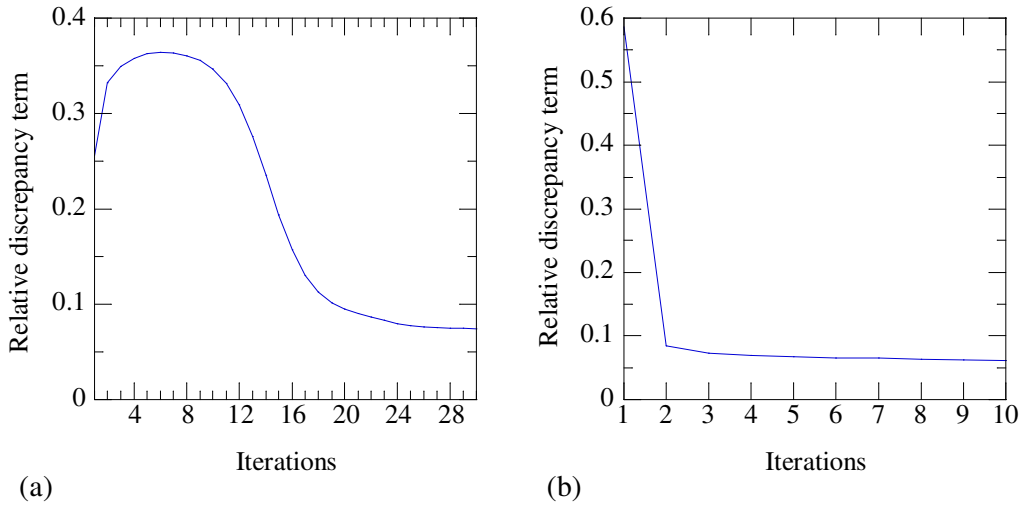

Figure 6.12. Discrepancy term evolution in inversions from synthetic data affected by 5% uniform noise corresponding to a square heat source of $w = h = 1$ mm buried at $|d| = 0.2$ (a) and 5.0 mm (b), using the values of the regularization parameters defined in equations (5.24), (5.25) and (5.26). Retrieved by implementing the optimum inversion protocol.

As can be observed, whereas for a depth $|d|$ = 0.2 mm the minimum discrepancy term is reached in 30 iterations, for a depth $|d|$ = 5.0 mm, the solution is found in only 10 iterations. By increasing the initial values of the regularization parameters, α_{Tk_0}, $\alpha_{L_{1_0}}$ and α_{TV_0}, and their decay factors, γ_{Tk}, γ_{L_1} and γ_{TV}, the minimization process may be extended. However, we have checked that performing the inversions over a higher number of iterations does not produce significant improvements on the retrieved normalized heat source distribution. In other words, the discrepancy term minimizer iteration number is independent from the accuracy of the reconstruction, as long as the minimization converges. Therefore, it can be said that all values defined in equations (5.24), (5.25) and (5.26) are optimally selected.

Only in inversions where the residual cannot be minimized, the regularization degree needs to be increased. This situation may arise when very little information regarding the heat source distribution is entered, or for surface temperature data affected by a very high noise percentage. As an example, in Figure 6.13 (a) we show the discrepancy term evolution in an inversion from synthetic data with 5% added uniform noise corresponding to a square heat source ($w = h$ = 1 mm) buried at a depth $|d|$ = 2.0 mm at uniformly distributed $f_{lock\text{-}in}$.

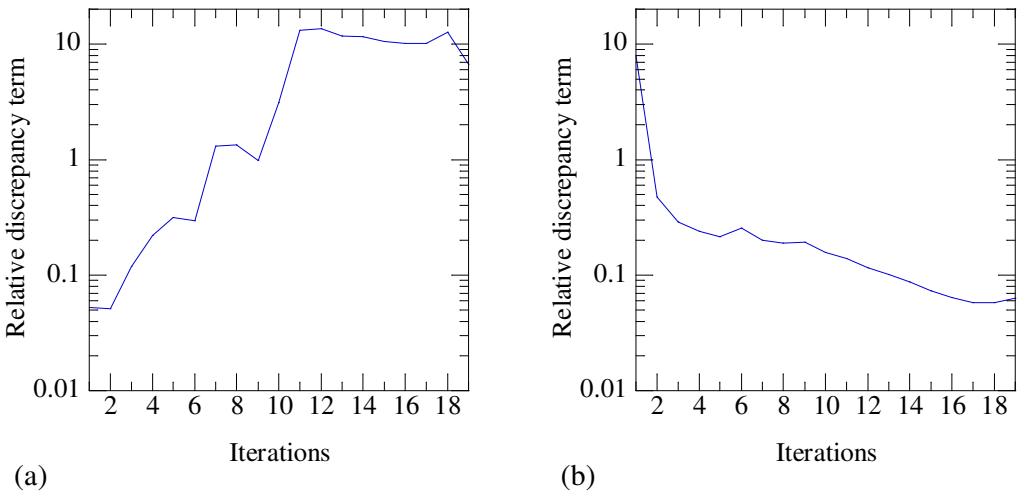

Figure 6.13. Discrepancy term evolution in inversions from synthetic data with 5% added uniform noise corresponding to a square heat source of $w = h$ = 1 mm buried at a depth $|d|$ = 2.0 mm obtained at uniformly distributed modulation frequencies with (a) values of the regularization parameters defined in equations (5.24), (5.25) and (5.26) and (b) multiplying α_{Tk_0}, $\alpha_{L_{1_0}}$ and α_{TV_0} by 10,000. Retrieved by implementing the optimum inversion protocol.

The inversion algorithm cannot minimize the residual because this $f_{lock\text{-}in}$ distribution is mainly composed of high frequency information, which at $|d|$ = 2.0 mm is basically noise. Instead, if we multiply α_{Tk_0}, $\alpha_{L_{1_0}}$ and α_{TV_0} by 10,000, the discrepancy term evolution shown in Figure 6.13 (b) is obtained, in which the minimization converges. This last inversion corresponds to the reconstruction shown in Figure 6.11 (b). Logically, the same has needed to be done to obtain the reconstruction depicted in Figure 6.11 (c) from data at uniformly distributed $f_{lock\text{-}in}$, which further proves that doubling the modulation frequencies is the optimum design of experiments if we want to see the performance of the inversion algorithm to retrieve heat sources buried gradually deeper.

6.7 Spatial resolution of the algorithm

At this point, it is worth analysing the ability of the algorithm to distinguish between multiple heat sources and reconstruct them separately, i.e., the spatial resolution. This section determines the spatial resolution of the inversion algorithm as a function of depth.

The analysis of the spatial resolution of the inversion algorithm has been carried out twice: first entering normalized amplitudes and stabilizing the inversion with TV_{Anisot} and then using the optimum inversion protocol (implementing TV_{Isot} and entering raw amplitudes). The results obtained for both cases are then shown and discussed.

6.7.1 Implementing TV_{Anisot} with normalized amplitudes

To start with, we have picked two square heat sources of the same size ($w_1 = w_2 = h_1 = h_2$ = 1 mm) buried at the same depth and emitting the same maximum homogeneous flux, and we have performed inversions by modifying the separation distance between centres, d_{cen}, with the aim of checking how well can the inversion algorithm reconstruct both heat sources separately as a function of d_{cen}. This procedure has been carried out for different depths of the two heat sources, namely, $|d_1| = |d_2|$ = 0.2, 0.6, 1.2, 1.6, 2.0, 2.6 and 3.2 mm, all with 5% added uniform noise.

As an example, Figure 6.14 shows reconstructions corresponding to the two squares buried at depths $|d_1| = |d_2|$ = 0.2 (a) and 1.6 mm (b) for different d_{cen}. The value of d_{cen} (in mm) is depicted on top of each reconstruction.

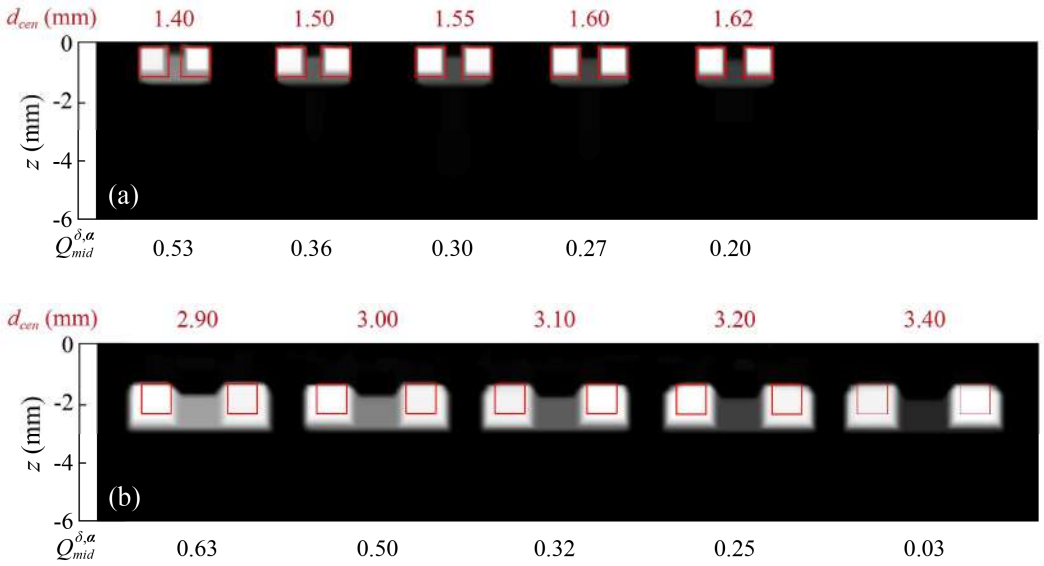

Figure 6.14. Reconstructions of two square heat sources of dimensions $w_1 = w_2 = h_1 = h_2 = 1$ mm and emitting with the same maximum homogeneous flux, for different d_{cen}, buried at depths $|d_1| = |d_2| = 0.2$ (a) and 1.6 mm (b), in inversions using TV_{Anisot} and entering normalized amplitudes. Data are affected by 5% uniform noise. The contours of the real heat sources are depicted in red and values of d_{cen} and $Q_{mid}^{\delta,\alpha}$ displayed on top of and under each reconstruction, respectively.

In order to state whether the two heat sources are resolved or not in a reconstruction, we have established a *resolution criterion*. For this purpose, for each depth of the heat sources, we have plotted the values of the retrieved normalized heat source distribution in the mid-point between the two maxima, $Q_{mid}^{\delta,\alpha}$, as a function of d_{cen} and we have selected a value of 0.3 as limiting criterion: if $Q_{mid}^{\delta,\alpha}$ is below 0.3, the two heat sources can be considered to be resolved. The values of $Q_{mid}^{\delta,\alpha}$ for the corresponding d_{cen} in Figure 6.14 are depicted under each reconstruction. We refer to the separation distance between centres for which $Q_{mid}^{\delta,\alpha} = 0.3$ as d_{cenLim}.

These curves are shown in Figure 6.15 for depths $|d_1| = |d_2| = 0.2$ (a) and 1.6 mm (b). According to our resolution criterion, the distance between centres necessary for the two heat sources to be resolved, buried at $|d_1| = |d_2| = 0.2$ mm, is 1.55 mm, whereas if they are buried at $|d_1| = |d_2| = 1.6$ mm, $d_{cenLim} = 3.1$ mm. The most relevant inversions performed as a function of d_{cen} for each depth are collected in appendix A.1.

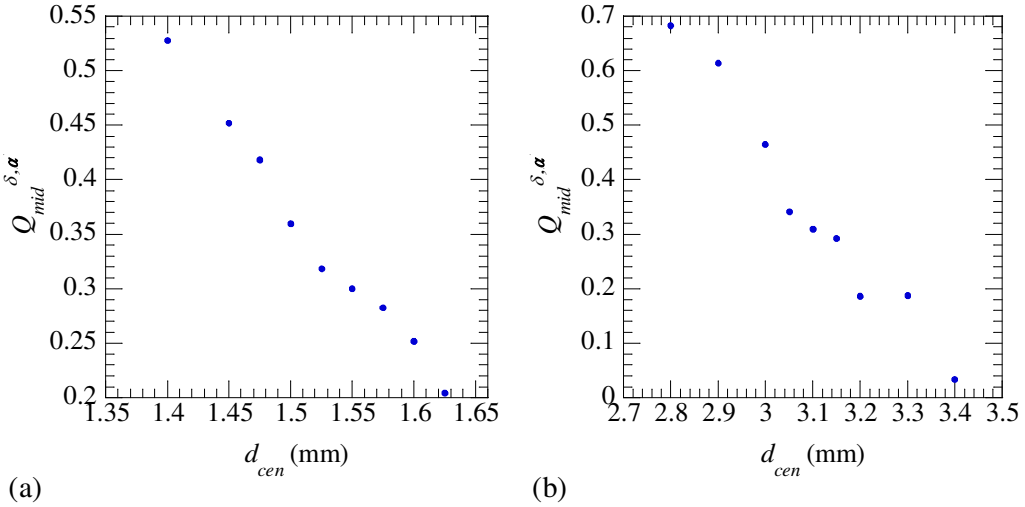

Figure 6.15. (a) Values of the retrieved $Q_{mid}^{\delta,\alpha}$ as a function of d_{cen}, for two square heat sources of dimensions $w_1 = w_2 = h_1 = h_2 = 1$ mm buried at a depth $|d_1| = |d_2| = 0.2$ (a) and 1.6 mm (b). Data are affected by 5% uniform noise.

As mentioned above, we have obtained d_{cenLim} for all the considered depths in order to determine the spatial resolution of the inversion algorithm as a function of depth. The results are depicted in Figure 6.16, where the values of d_{cenLim} at each depth have been fitted to a 3rd order polynomial in order to extrapolate d_{cenLim} at any other depth between 0.2 and 3.2 mm. The contours of the two heat sources at all the considered depths are also represented by grey squares.

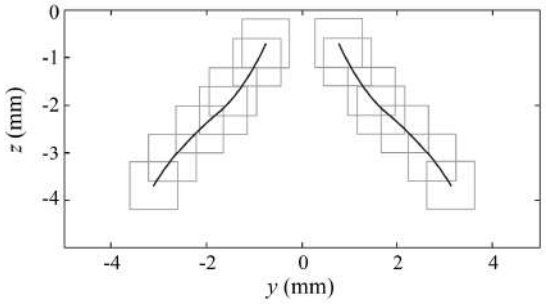

Figure 6.16. d_{cenLim} for the resolution of two square heat sources of $w_1 = w_2 = h_1 = h_2 = 1$ mm as a function of depth, in inversions from data affected by 5% uniform noise, implementing TV_{Anisot} and entering normalized amplitudes. The considered depths are: $|d_1| = |d_2| = 0.2$, 0.6, 1.2, 1.6, 2.0, 2.6 and 3.2 mm. The values of d_{cenLim} have been fitted to a 3rd order polynomial function (black lines) and the contours of the heat sources are represented by grey squares.

According to Figure 6.16, the two square heat sources buried at a certain depth and emitting with the same maximum homogeneous flux should be located in the outer regions of the fitted black curves in order to be resolved in inversions implementing TV_{Anisot} and entering normalized amplitudes, for data affected by 5% uniform noise. As expected, d_{cenLim} increases with depth, meaning that the spatial resolution of the inversion algorithm decreases as the heat sources are buried deeper inside the material.

Provided that we have obtained dramatic improvements on the reconstructions of single heat source distributions by implementing the optimum inversion protocol, we next show the same analysis using TV_{Isot} and entering raw amplitudes.

6.7.2 Implementing TV_{Isot} with raw amplitudes

In order to show what reconstructions using the optimum protocol look like when inverting multiple heat sources, Figure 6.17 shows reconstructions from synthetic data affected by 5% uniform noise corresponding to two square heat sources of $w_1 = w_2 = h_1 = h_2 = 1$ mm buried at depths $|d_1| = |d_2| = 0.2$ (a) and 1.6 mm (b) with increasing d_{cen}.

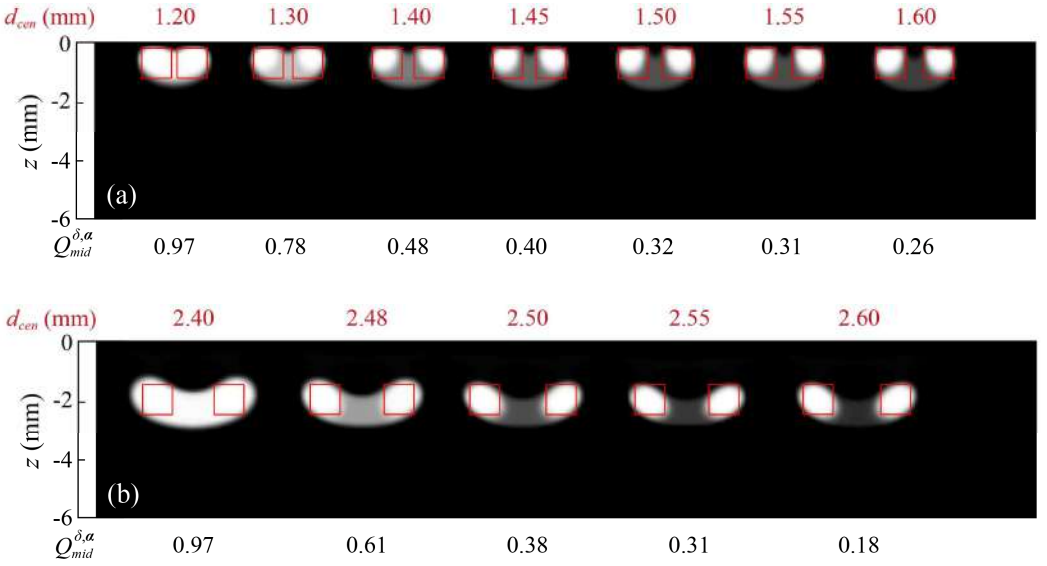

Figure 6.17. Reconstructions from synthetic data affected by 5% uniform noise corresponding to two squares of dimensions $w_1 = h_1 = w_2 = h_2 = 1$ mm buried at a depth $|d_1| = |d_2| = 0.2$ (a) and 1.6 mm (b) as a function of d_{cen}. Contours of the real heat sources depicted in red and values of d_{cen} and $Q_{mid}^{\delta,\alpha}$ displayed on top of and under each reconstruction, respectively.

Similarly, the most relevant reconstructions at the rest of the considered depths using the optimum inversion protocol can be found in appendix A.1.

We have compared the limiting distances between centres as a function of depth obtained for both inversion procedures: the comparison is shown in Figure 6.18, where maroon lines are the 3rd order polynomial fit and the red squares represent the contours of the two heat sources at all the considered depths, in inversions using the optimum protocol.

Since for the deepest heat sources ($|d_1| = |d_2| = 3.2$ mm), d_{cenLim} reduces from 6.25 to 4 mm, two more depths have been considered in inversions using the optimum protocol, namely, $|d_1| = |d_2| = 4.0$ and 5.0 mm.

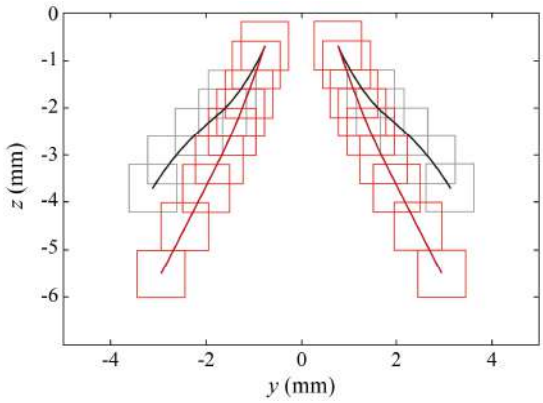

Figure 6.18. Comparison of d_{cenLim} for squares of $w_1 = h_1 = w_2 = h_2 = 1$ mm as a function of depth, using TV_{Anisot} and entering normalized amplitudes (black) and using TV_{Isot} and entering raw amplitudes (red). A 3rd order polynomial fit of d_{cenLim} at each depth (solid lines) and the contours of the heat sources (squares) are represented. The depths of the squares are $|d_1| = |d_2| = 0.2$, 0.6, 1.2, 1.6, 2.0, 2.6 and 3.2 mm. When implementing the optimum inversion protocol, also $|d_1| = |d_2| = 4.0$ and 5.0 mm.

All the limiting distances obtained for both methods, represented in Figure 6.18, are summarized in Table 6.2.

Table 6.2. Limiting separation distances for the resolution of two square heat sources of $w_1 = h_1 = w_2 = h_2 = 1$ mm, d_{cenLim}, for both inversion procedures (using TV_{Anisot} and entering normalized amplitudes and using TV_{Isot} and entering raw amplitudes) for all the considered depths.

$\|d\|$ (mm)	**0.2**	**0.6**	**1.2**	**1.6**	**2.0**	**2.6**	**3.2**	**4.0**	**5.0**
d_{cenLim} (mm) TV_{Anisot} **& norm. amplitudes**	1.55	1.92	2.90	3.10	4.32	5.47	6.25	-	-
d_{cenLim} (mm) TV_{Isot} **& raw amplitudes**	1.55	1.92	2.20	2.55	2.90	3.45	4.00	4.90	5.90

It is worth noting that d_{cenLim} for the two deepest squares ($|d_1|$ = $|d_2|$ = 5.0 mm) with the optimum inversion protocol is still shorter than for a depth $|d_1|$ = $|d_2|$ = 3.2 mm using TV_{Anisot} and entering normalized amplitudes.

6.8 The shadowing effect

In order to see how the inversion algorithm behaves if we switch from our standard square heat source to a rectangle having one side much larger than the other one, we now perform inversions of rectangular heat sources of varying width and height.

Figure 6.19 (a) shows reconstructions from synthetic data with 5% added uniform noise corresponding to a rectangle of width w = 1 mm and two different heights, namely, h = 5 and 3 mm, buried at a depth $|d|$ = 0.2 mm. As can be observed, the upper part of the rectangles is accurately reconstructed and as the height of the heat sources increases in depth, the lower parts become wider and diffuse. The reason for this is that shallower positions within the heat source distribution have a stronger contribution to the surface temperature than deeper positions, provoking the lower parts of the retrieved heat sources look poorly defined. This effect is known as *shadowing*.

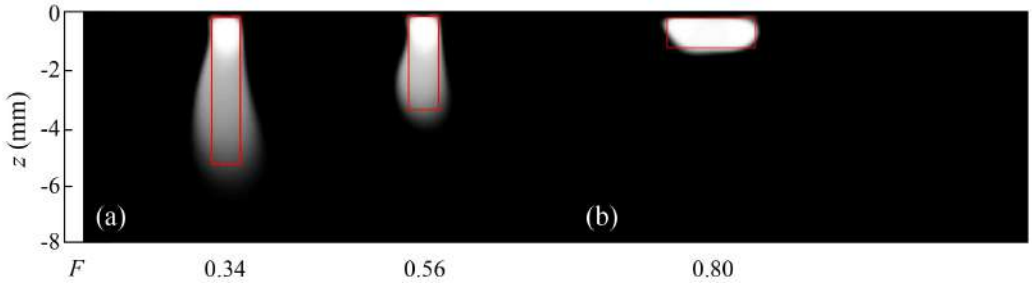

Figure 6.19. Grey level representation of the retrieved normalized heat source distribution corresponding to synthetic data with 5% added uniform noise for (a) rectangular heat sources of width w = 1 mm and two different heights, namely, h = 5 (left) and 3 mm (right), buried at a depth $|d|$ = 0.2 mm, and (b) a rectangular heat source of w = 3 mm and h = 1 mm buried at a depth $|d|$ = 0.2 mm. Retrieved by implementing TV_{Isot} and using raw amplitudes. Real contours depicted in red and quality factor F values under each reconstruction.

Also, it can be mentioned that asymmetries along the height of the retrieved heat sources, provoked by the ill-posed character of the inverse problem in the presence of noise, are

more likely to appear as the height of the rectangles increases. Nevertheless, although blurred, the overall height of the rectangles is well estimated in both reconstructions.

However, considering a rectangular heat source of w = 3 mm and h = 1 mm (see Figure 6.19 (b)) the shadowing disappears, which allows concluding that the shadowing effect weakens as the difference in depth between shallowest and deepest positions within the heat source area decreases.

Seeing that the shadowing effect appears in long and deep geometries, it is worth further studying it, since apart from arising between shallow and deep positions within a certain heat source distribution, it may also arise between different heat sources retrieved within the same inversion.

In the analysis of the spatial resolution of the algorithm carried out in section 6.7, we have considered two square heat sources of the same size, buried at the same depth and emitting with the same homogeneous flux. In this way, the resulting surface temperature distribution is symmetric and both heat sources are equally retrieved. However, if one of these three parameters is different in one of the two heat sources in such a way that its contribution to the surface temperature data is stronger than that of the other heat source, its reconstruction may be favoured. In this case, a heat source may shadow the other one.

In order to give an idea of what an asymmetric surface temperature distribution generated by two heat source distributions looks like, in Figure 6.20 (a) we show synthetic noisy Ln(|T|) and the Ψ thermograms for two square heat sources buried at the same depth $|d_1|$ = $|d_2|$ = 0.2 mm, with d_{cen} = 4 mm, both emitting with the same homogeneous flux $Q_1 = Q_2$ but having different sizes ($w_1 = h_1$ = 1 mm and $w_2 = h_2$ = 1.5 mm), generated at $f_{lock\text{-}in}$ = 0.1 Hz. The fitted thermograms are depicted in Figure 6.20 (b).

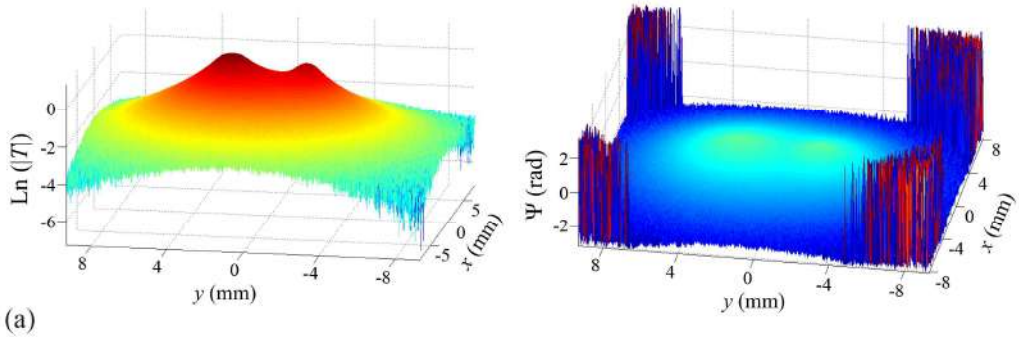

(a)

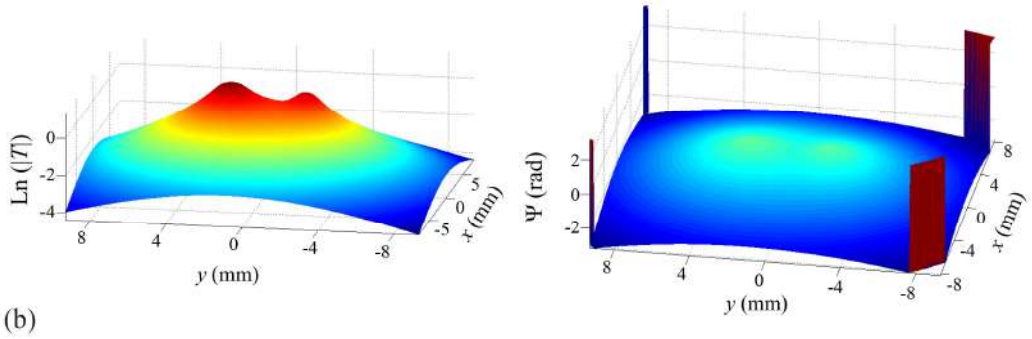

Figure 6.20. (a) Synthetic data affected by 5% uniform noise, Ln(|*T*|) (left) and Ψ (right) and (b) fitted thermograms, obtained at $f_{lock\text{-}in}$ = 0.1 Hz, for two square heat sources buried at a depth $|d_1|$ = $|d_2|$ = 0.2 mm, with a separation distance between centres d_{cen} = 4 mm, both emitting with the same flux Q_1 = Q_2 but having different sizes: w_1 = h_1 = 1 mm and w_2 = h_2 = 1.5 mm.

With the aim of analysing the ability of the algorithm to deal with shadowing arising between two heat sources, we have inverted synthetic data with 5% added uniform noise corresponding to two square heat sources with d_{cen} = 2 mm, considering three cases in which asymmetric surface temperature distributions are obtained. Note that for d_{cen} = 2 mm, two equal heat sources at a depth $|d_1|$ = $|d_2|$ = 0.2 mm are considered to be resolved, according to our resolution criterion. The heat source on the left (w_1 = h_1 = 1 mm) remains the same for the three cases, emitting with a certain flux Q_1 and buried at a depth $|d_1|$ = 0.2 mm, whereas the heat source on the right varies as follows in each case: (a) increasing the size (w_2 = h_2 = 1.5 mm), (b) decreasing the flux it emits with (Q_2 = 0.5 Q_1) and (c) increasing the depth ($|d_2|$ = 1.2 mm). The reconstructions are depicted in Figure 6.21.

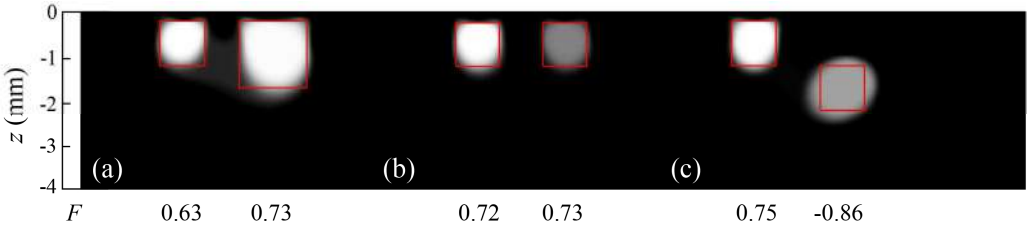

Figure 6.21. Grey level representation of the normalized heat source distribution corresponding to synthetic data with 5% added uniform noise for two square heat sources, considering three cases where the heat source on the left (w_1 = h_1 = 1 mm), buried at a depth $|d_1|$ = 0.2 mm and emitting with a flux Q_1, remains the same. The separation distance between centres is d_{cen} = 2 mm and the heat source on the right varies as follows in each case: (a) increasing the size (w_2 = h_2 = 1.5 mm), (b) decreasing the flux it emits with (Q_2 = 0.5 Q_1) and (c) increasing the depth ($|d_2|$ = 1.2 mm). Retrieved by implementing TV_{Isot} and using raw amplitudes. Real contours depicted in red and individual quality factor *F* values under each reconstruction.

As for the effects of increasing the size or decreasing the flux of the heat source on the right (see Figure 6.21 (a) and (b), respectively), the algorithm recovers both heat sources very well, obtaining very accurate individual reconstructions. We have checked that the value of the retrieved $Q^{\delta,\alpha}$ in the centre of the heat source on the right is 0.5 in Figure 6.21 (b). This proves that, in these cases, the fact that one of the two heat sources contributes more significantly to the surface temperature data entering the algorithm, does not prevent the other heat source from being recovered accurately.

However, in the case of increasing the depth of the heat source on the right (Figure 6.21 (c)), the shadowing is clearly appreciated, since its F value decreases from 0.60 (in Figure 6.3 (c) at a depth $|d|$ = 1.2 mm) to -0.84. The shadowing effect here produces an effect similar to reducing the intensity of the right heat source but with a wider reconstruction.

7 Behaviour of the inversion algorithm for different heat source distributions

This section analyses the performance of the inversion algorithm to characterize heat sources representing vertical cracks of geometries other than squares, from synthetic data. As for kissing heat sources, the ability to retrieve the particular features of the different geometries such as smooth contours or pointy ends is studied. With the aim of approaching situations arising in real experiments, open cheat sources are recovered, representing the regions within surface breaking open cracks where heat production takes place. In addition, inhomogeneous heat generation in both kissing and open heat sources is considered.

7.1 Kissing heat sources

The performance of the inversion algorithm to retrieve heat sources representing vertical homogeneous kissing cracks of other geometries than those considered in the main analysis (section 6) is analysed now, using synthetic data and implementing the optimum inversion protocol.

In addition, as a first step for the characterization of inhomogeneous heat source distributions, width- and height-dependent flux variations have been considered for square geometries.

In order to check the ability of the algorithm to reproduce the particular shapes of the different geometries, semicircular and triangular heat sources are first considered, as they feature smooth contours and pointy ends, respectively. Just as in the direct problem, *sUp* and *sDown* refer to semicircles with the curved part upward and downward, respectively, and *tUp* and *tDown* stand for triangles with the apex on the middle upward and downward, respectively. The area of all semicircular and triangular heat sources is 1 mm^2 so that the F values obtained can be compared to those obtained for square heat sources.

Figure 7.1 (a) and (b) show reconstructions obtained from synthetic data affected by 5% uniform noise corresponding to *sUp* and *sDown* of radius R = 0.8 mm buried at increasing depths, respectively, retrieved by implementing TV_{Isot} and entering raw amplitudes. The depths for all heat sources are: $|d|$ = 0.2, 0.6, 1.2, 1.6, 2.6, 3.2, 4.0 and 5.0 mm. It is worth noting that the obtained F values are similar to those for square heat sources as depth increases.

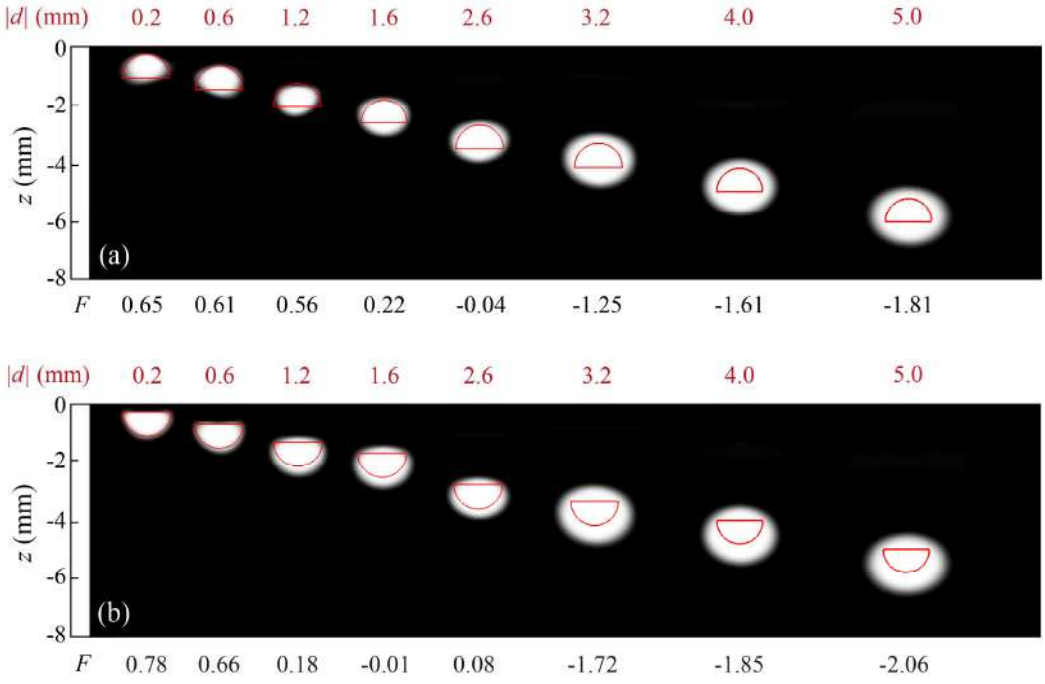

Figure 7.1. Grey level representation of the normalized heat source distribution in inversions from synthetic data affected by 5% uniform noise corresponding to (a) *sUp* and (b) *sDown* (R = 0.8 mm) buried at increasing depths, retrieved by implementing TV_{Isot} and entering raw amplitudes. The depths of the heat sources are: $|d|$ = 0.2, 0.6, 1.2, 1.6, 2.6, 3.2, 4.0 and 5.0 mm. Real contours depicted in red and values of the depth of the heat sources and quality factor F on top of and under each reconstruction, respectively.

As for the particular shapes of the semicircles, the two shallowest heat sources are very well reproduced, especially their upper part, notably in the case of *sDown*, where the straight upper contour does not coincide with the round shape favoured by TV_{Isot}.

Retrieving the lower contour of the heat sources is more challenging, unless it coincides with the round shape that TV_{Isot} delivers by default, as in the case of *sDown*. As depth increases, rounded reconstructions dominate. Anyway, all depths are well recovered.

As mentioned above, triangular heat sources have been considered in order to see the ability of the inversion algorithm to retrieve pointy features: we have inverted synthetic data affected by 5% uniform noise corresponding to *tUp* and *tDown* ($w = h = 1.4$ mm) located at increasing depths, namely, $|d| = 0.1$, 0.2, 0.4, 0.6, 1.0 and 2.0 mm. The depths for triangles start closer to the surface than for semicircles so that we can focus on the apex on the middle and distinguish it more easily, since pointy features are lost very fast with depth. The results are shown in Figure 7.2.

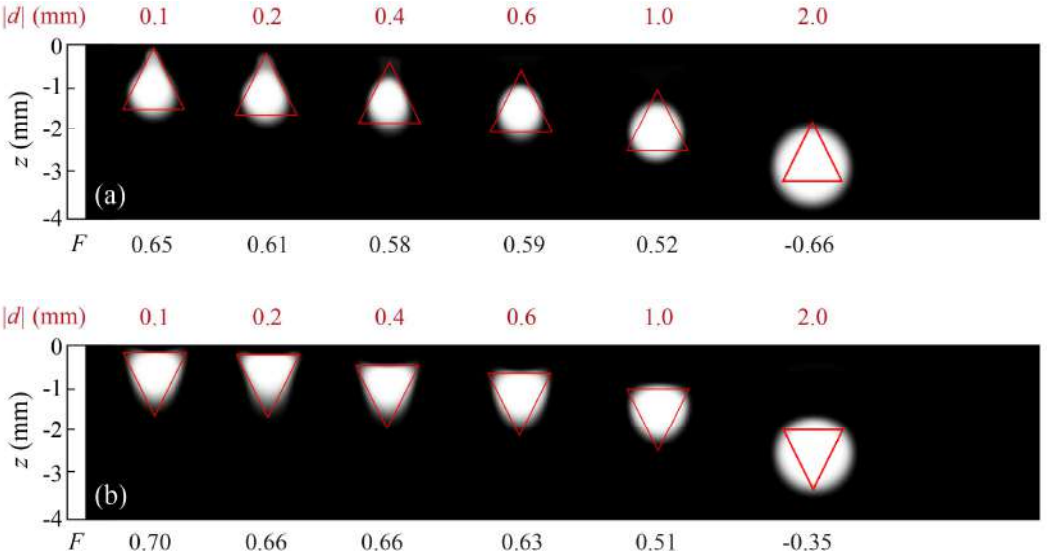

Figure 7.2. Grey level representation of the normalized heat source distribution in inversions from synthetic data affected by 5% uniform noise corresponding to (a) *tUp* and (b) *tDown*, buried at increasing depths and retrieved by implementing TV_{Isot} and entering raw amplitudes. The size of the triangles is $w = h = 1.4$ mm and the depths are: $|d| = 0.1$, 0.2, 0.4, 0.6, 1.0 and 2.0 mm. Real contours depicted in red and values of the depth of the heat sources and quality factor F on top of and under each reconstruction, respectively.

As for *tUp*, the apex on the middle is well reproduced for the shallowest case ($|d| = 0.1$ mm). At $|d| = 0.2$ mm it is still visible but fainter at the tip and it gets lost from $|d| = 0.4$

mm on, as can be seen in Figure 7.2 (a). The inversion algorithm cannot reproduce the other two apexes on the basis of the triangles at any depth.

Regarding *tDown*, the opposite happens: the two apexes on the basis of the triangles along with the straight basis are very well reproduced down to $|d| = 0.6$ mm, and the presence of the apex on the middle in the central lower side, although rounded and blurred, is pointed out by the V shape of the reconstructions, especially at $|d| = 0.1$ mm. This is the reason why *tDown* gets higher quality factor F values than *tUp*, as there is a larger area to be retrieved on the upper side of the heat sources. Anyway, from $|d| = 0.6$ mm on, all sharp corners are lost and the retrieved shapes are completely rounded for both *tUp* and *tDown*, making the F values very alike.

The fact that the particular features of the heat sources is very hard to distinguish due to the ill-posedness of the inverse problem was pointed out by the direct surface temperature distribution calculations shown in Figure 3.7 and Figure 3.8, which obviously worsens with increasing depth.

In summary, we can conclude that for 1 mm^2 heat sources in AISI 304, smoothly varying upper contours like in semicircles, can be retrieved accurately down to depths $|d| = 0.6$ mm, whereas sharp corners like in triangles are more challenging to recover and can only be retrieved accurately if they are located at the shallowest positions within the heat sources and these are buried at depths that do not exceed $|d| = 0.1$ mm.

Focusing on the shallowest positions for both semicircles and triangles where the particular features of the geometries are accurately recovered, we now want to observe if these details of the geometries can still be retrieved if we increase the noise level in the data, with the aim of checking the robustness of the inversion algorithm against noise. For this purpose, we increase the global noise level up to 10% and 15% and we retrieve *sUp* and *sDown* (R = 0.8 mm) buried at a depth $|d| = 0.2$ mm, as well as *tUp* and *tDown* ($w = h = 1.4$ mm) submerged at a depth $|d| = 0.1$ mm, and compare the resulting reconstructions to those obtained from data affected by 5% uniform noise. The results are depicted in Figure 7.3.

The most significant case is *tUp* (see Figure 7.3 (b)), where the apex on the middle is lost with increasing noise level, meaning that an accurate definition of the apex on the middle requires, in addition to shallow depths, noise levels under 5%.

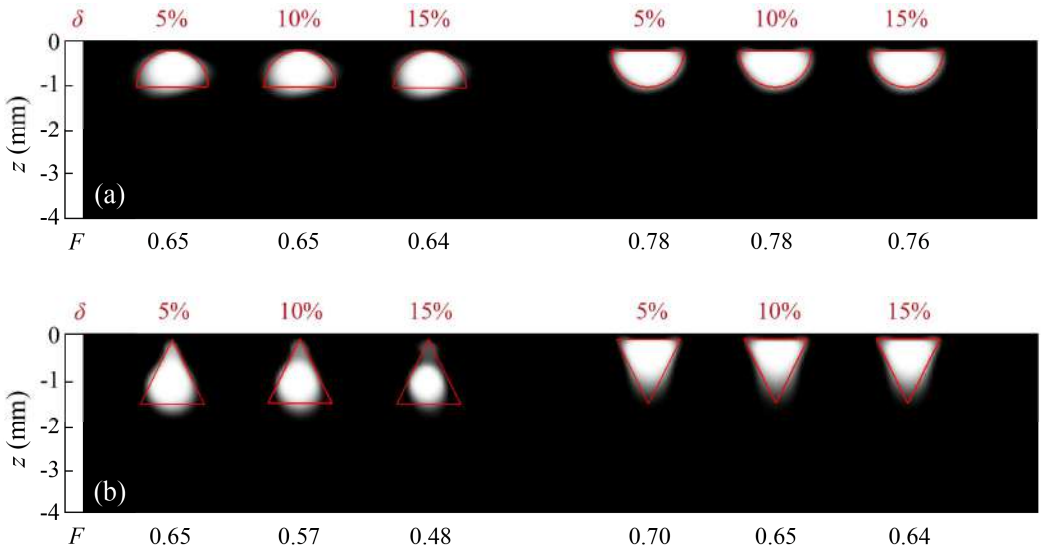

Figure 7.3. Grey level representation of the normalized heat source distribution in inversions from synthetic data affected by 5%, 10% and 15% uniform noise, corresponding to (a) *sUp* and *sDown* (R = 0.8 mm) buried at $|d|$ = 0.2 mm and (b) *tUp* and *tDown* ($w = h$ = 1.4 mm) buried at $|d|$ = 0.1 mm, retrieved by implementing the optimum inversion protocol. Real contours depicted in red and values of the noise level in the data and quality factor F on top of and under each reconstruction, respectively.

However, in the case of *tDown* and also for both semicircular heat source configurations shown in Figure 7.3 (a), the inversion algorithm is rather robust to noise, as the noise level does not significantly affect the quality of the reconstructions, just as for square heat sources (see Figure 6.6).

Thus, it can be said that the inversion algorithm is more robust with respect to noise for geometries featuring smooth contours or straight edges than for those with pointy ends.

As a first step to approach situations arising in vibrothermography experiments with real cracks, we have considered half-penny shaped heat sources, as this geometry is usually encountered in real cracks. We have considered three different cases of half-penny shaped heat source distributions, that go from deep and narrow to shallow and elongated, buried at a depth $|d|$ = 0.2 mm. The reconstructions are shown in Figure 7.4. Obviously, the shallow and elongated half-penny shaped heat source distribution is the most accurately retrieved one, even its acute corners. Anyway, all half-pennies are accurately retrieved according to our accurate reconstruction criterion.

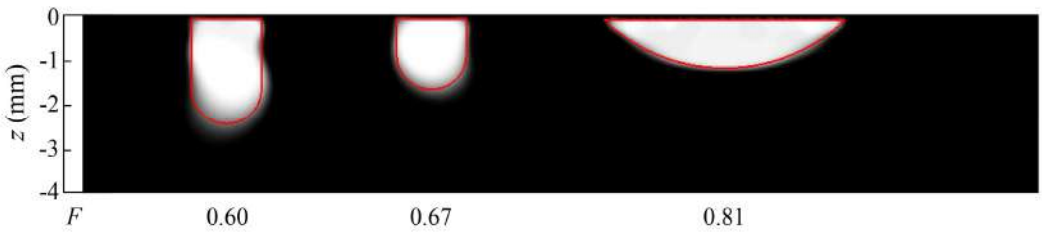

Figure 7.4. Grey level representation of the normalized heat source distribution corresponding to synthetic data with 5% added uniform noise generated for half-penny shaped heat sources that go from deep and narrow to shallow and elongated, going from left to right, buried at a depth $|d| = 0.2$ mm. Retrieved by implementing the optimum inversion protocol. Real contours depicted in red and values of the quality factor F under each reconstruction.

Homogeneous heat source distributions have been considered so far, as they represent the ideal case where the whole crack geometry emits with uniform flux. However, we now study the ability of the algorithm to retrieve inhomogeneous heat source distributions as a first step to the characterization of inhomogeneous heat generation, since in real cracks, heat may not be produced homogeneously within the whole crack geometry due to the complexity of heat generation mechanisms.

We start by a square heat source ($w = h = 2$ mm) buried at a depth $|d| = 0.2$ mm, considering two different cases of varying flux: width- and height-dependent flux. In turn, we have considered two alternatives for each case: the maximum flux being either at the centre or on the side of the square. In addition, a third case in which the flux varies with both height and width (the maximum flux being at the centre) has been considered too. The noise level is 5% in all cases. Figure 7.5 shows the reconstructions, retrieved by implementing the optimum inversion protocol. For the sake of clarity, the real heat source distributions are represented under each reconstruction.

In all cases, the region within the heat source distribution where the heat flux is maximum is well identified, but the transition from maximum to null flux is more abrupt than in the real heat source distributions. However, nice gradual flux variations are recovered at the upper part of the heat sources shown in Figure 7.5 (a) and (b), where the whole flux gradient takes place at the shallowest positions of the squares.

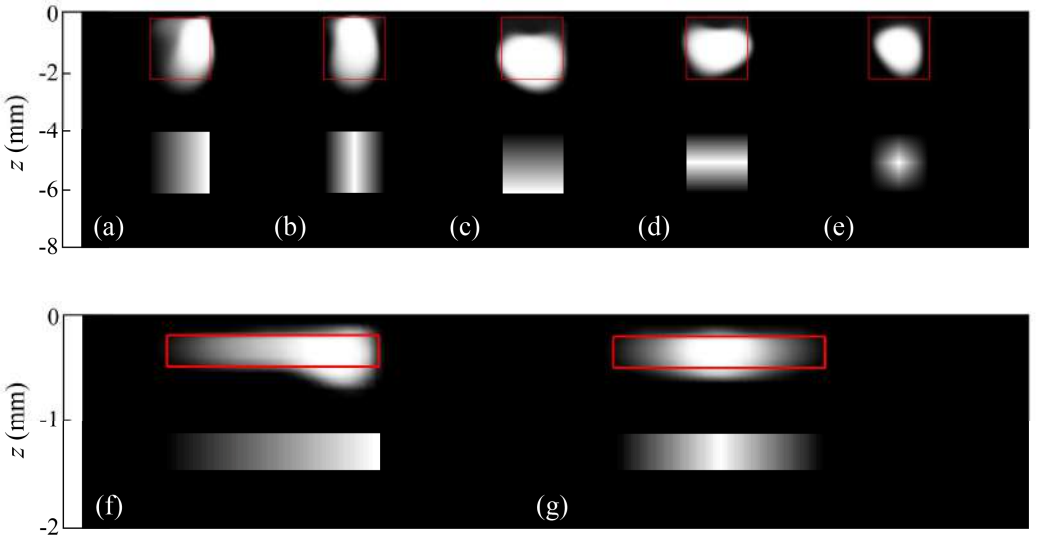

Figure 7.5. Grey level representation of the normalized heat source distribution in inversions from synthetic data affected by 5% uniform noise corresponding to an inhomogeneous square heat source (w = h = 2 mm) buried at a depth $|d|$ = 0.2 mm, considering various cases: width-dependent flux being the maximum flux (a) on the right side and (b) at the centre, height-dependent flux being the maximum flux (c) on the lower side and (d) at the centre, and (e) width- and height-dependent flux. (f) and (g) show the same as (a) and (b) but for a thread shaped heat source of w = 2 mm and h = 0.3 mm, buried at a depth $|d|$ = 0.2 mm. Retrieved by implementing the optimum inversion protocol. Real heat source distributions represented under each reconstruction.

Accordingly, two more heat sources have been considered: Figure 7.5 (f) and (g) represent the same flux variations as Figure 7.5 (a) and (b) but for a rectangular heat source of w = 2 mm and h = 0.3 mm, buried at $|d|$ = 0.2 mm, representing the geometry of a thread. The results prove that the inversion algorithm is able to retrieve width-dependent flux variations accurately, as long as the heat sources are shallow and very short in depth or, in the case of being longer, only at positions shallower than about 0.5 mm. For deeper positions, flux dependences cannot be appreciated and the reconstructions are dominated by the areas with maximum flux. Of course, a condition for the reproduction of these flux gradients is that they are performed over a long distance along y-axis in relation to the size of the mesh in plane Π.

The inability to retrieve flux variations if they are deep or exhibit large gradients is a limitation of the inversion algorithm.

7.2 Open heat sources

As a further step to approach situations arising in experiments with real cracks, it is worth tackling the case of surface breaking open cracks, to which vibrothermography is often applied, since we have proved that the inversion algorithm is able to reproduce the particular features of the different geometries for small depths.

It has been shown that, in this kind of cracks, heat is usually produced at a given portion of the crack rather than at the whole crack geometry: at regions where the crack lips do not contact there is no frictional heating and, near the crack border, heat production may be also be prevented by closure stresses that lock the crack asperities. Accordingly, heat is generally produced at a certain band where crack lips' contact and relative motion occur simultaneously.

In this section, the ability of the inversion algorithm to characterize open heat sources of different geometries is checked. In addition to semicircular and half-penny shaped heat sources, we also consider rectangular and triangular geometries emitting with a homogeneous flux.

Moreover, given that in this kind of cracks heat is most likely to be produced non-homogeneously within the stimulated region, we also tackle the recovery of inhomogeneous fluxes, which can vary in different directions, for semicircular open heat sources. The geometries for open heat source distributions considered in this section are depicted in Figure 7.6.

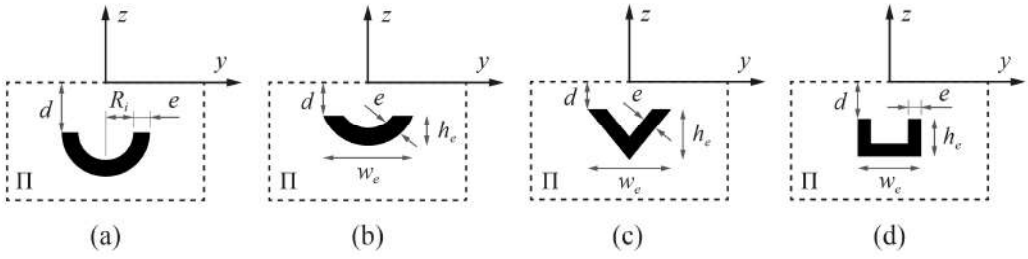

Figure 7.6. Geometries for strips representing open heat source distributions: (a) semicircle, (b) half-penny, (c) triangle and (d) rectangle.

In order to show what synthetic data affected by 5% uniform noise generated for open heat sources look like, Figure 7.7 (a) shows Ln(|T|) and Ψ thermograms for a semicircular strip of inner radius R_i = 1 mm and thickness e = 400 μm, buried at a depth |d| = 0.1 mm,

generated at $f_{lock\text{-}in}$ = 0.2 Hz. The thickness in open heat sources refers to the band within the whole open crack surface where heat production takes place. Figure 7.7 (b) shows the fitted thermograms.

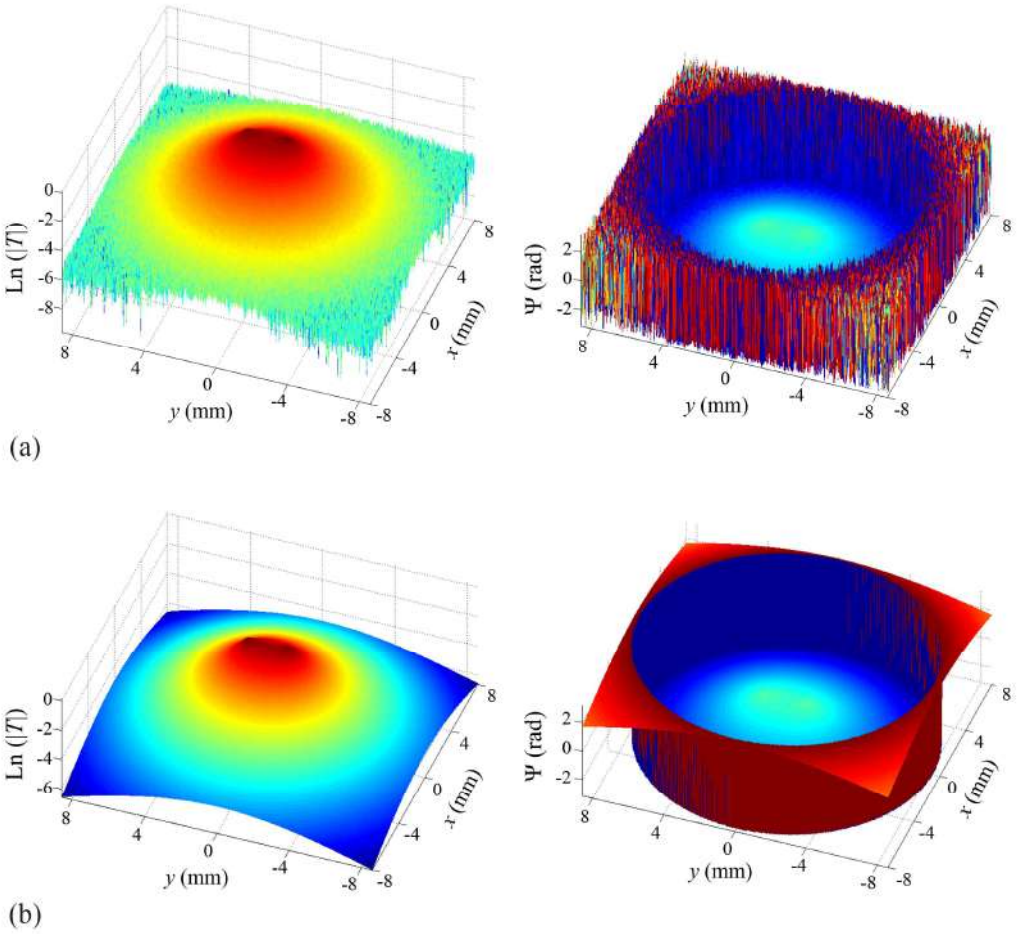

Figure 7.7. (a) Synthetic data, Ln(|*T*|) (left) and Ψ (right) thermograms with 5% added uniform noise, generated at $f_{lock\text{-}in}$ = 0.2 Hz, for a homogeneous semicircular open heat source of inner radius R_i = 1 mm and thickness e = 400 µm buried at a depth |d| = 0.1 mm, and (b) fitted thermograms.

Since heat in open cracks is produced at a certain band, we first focus on recovering strips of different thicknesses: Figure 7.8 (a) shows reconstructions from synthetic data with 5% added uniform noise corresponding to semicircular heat sources of inner radius R_i = 1 mm and increasing thickness (e = 60, 100, 160, 220, 280, 340 and 400 µm), buried at a depth |d| = 0.1 mm, retrieved by implementing the optimum protocol.

As may be noted, the shallow ends of the bands are very well reproduced in all cases and, for the thickest heat sources (e = 340 and 400 µm), the whole geometry is very accurately retrieved. However, as thickness decreases, the shadowing effect becomes gradually more significant at the lower part of the bands, as the deep central areas look larger and fainter, with clear definition loss. Actually, for the thinnest strips (e = 60 and 100 µm), the deep central area is very challenging to retrieve due to the shadowing effect. It is worth mentioning that, in these cases, the size of the mesh in plane Π may also be a limiting parameter affecting the accuracy of the reconstructions.

As an attempt to reproduce the central part of a thin band more accurately, in Figure 7.8 (b) we show the reconstruction of a larger shallow and elongated half-penny shaped open heat source of outer width w_e = 5.6 mm, outer height h_e = 1 mm and thickness e = 200 µm, buried at a depth $|d|$ = 0.1 mm. Although the deep central part remains faint, the inversion algorithm is able to show the path the band follows from one tip to the other one very well.

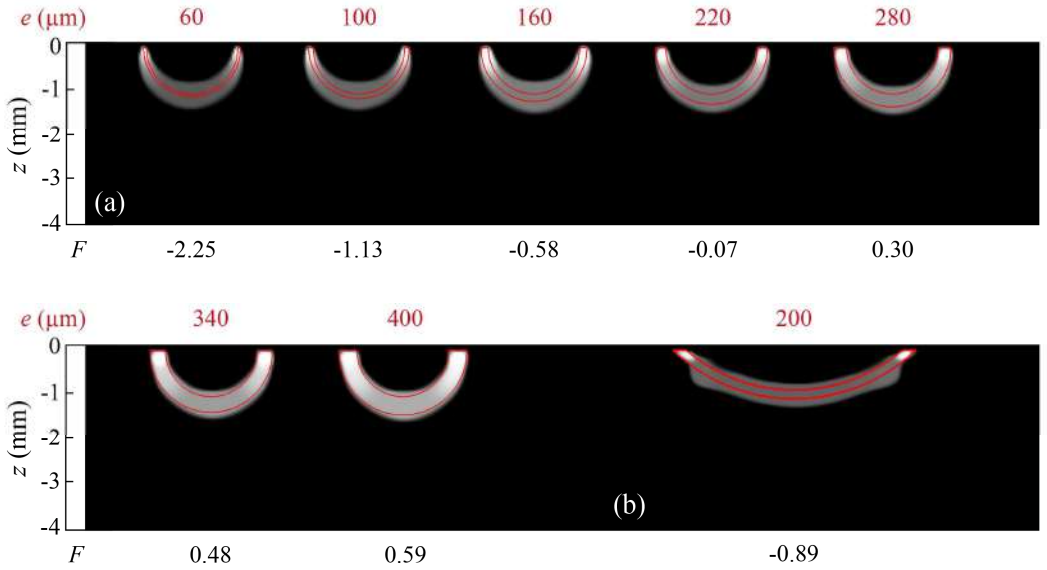

Figure 7.8. Grey level representation of the normalized heat source distribution in inversions from synthetic data with 5% added uniform noise corresponding to (a) homogeneous semicircular open heat sources of R_i = 1 mm and increasing thickness, namely, e = 60, 100, 160, 220, 280, 340 and 400 µm, buried at a depth $|d|$ = 0.1 mm and (b) a homogeneous shallow and elongated half-penny shaped open heat source of outer width w_e = 5.6 mm, outer height h_e = 1 mm and thickness e = 200 µm, buried at a depth $|d|$ = 0.1 mm. Retrieved by implementing the optimum inversion protocol. Values of the thickness (in µm) of the bands and quality factor F displayed on top of and under each reconstruction, respectively.

As for rectangular open heat sources, we have inverted synthetic data affected by 5% uniform noise representing a square crack of outer width w_e = 2.5 mm, outer height h_e = 2.5 mm and thickness e = 500 µm, buried at a depth $|d|$ = 0.2 mm, and we have looked at the effects of increasing the width (w_e = 3.75 and 5 mm) maintaining the height, as well as reducing the height (h_e = 1.8 and 1 mm) keeping the width constant. The results are shown in Figure 7.9 (a): the square open heat source is placed on the middle and the effects of increasing the width and decreasing the height are depicted on its right and left sides, respectively. As can be observed, the two tips, and therefore, the thickness of the bands, are very accurately retrieved.

Regarding the effect of increasing the width, the retrieved central areas, although rounded because of the inherent effect of TV_{Isot} and blurred due to the shadowing, show the path the bands follow and get narrower with increasing width. We can also mention that any corners on the band's path are somehow marked. As for the effect of decreasing the height, logically the "hole" in the middle is easier to retrieve the larger the width-to-depth ratio.

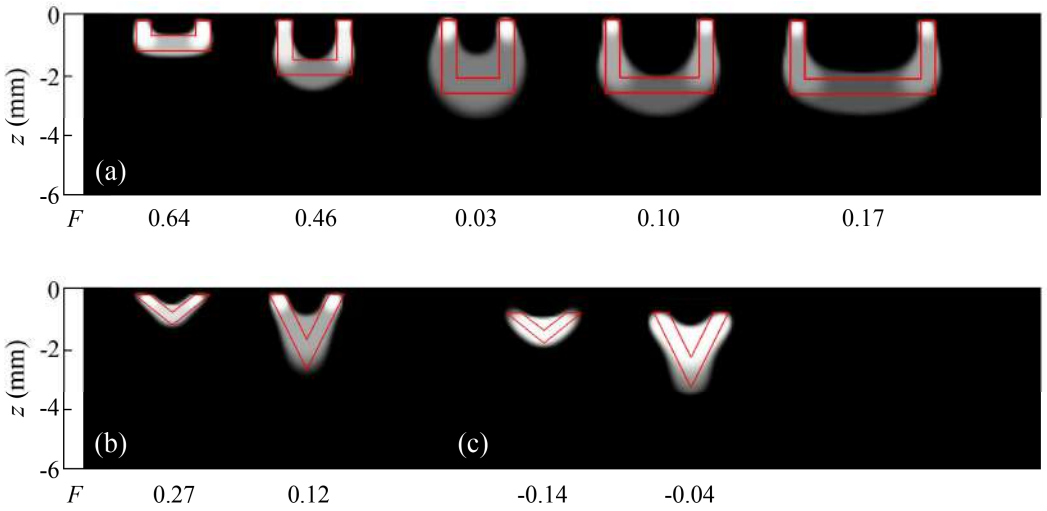

Figure 7.9. Grey level representation of the normalized heat source distribution in inversions from synthetic data with 5% added uniform noise corresponding to (a) homogeneous rectangular open heat sources buried at a depth $|d|$ = 0.2 mm: the reconstruction on the centre (outer width w_e = 2.5 mm, outer height h_e = 2.5 mm and thickness e = 500 µm) is the standard square and variations in width (w_e = 3.75 and 5 mm) as well as in height (h_e = 1.8 and 1 mm) are considered on its right and left sides, respectively, (b) triangular open heat sources of w_e = 2.5 mm and heights h_e = 1 and 2.5 mm buried at a depth $|d|$ = 0.2 mm, and (c) same as (b) but at a depth $|d|$ = 0.8 mm. Retrieved by implementing the optimum inversion protocol. Real contours depicted in red and values of the quality factor F under each reconstruction.

Reconstructions of triangular open heat sources buried at $|d|$ = 0.2 mm are shown in Figure 7.9 (b), from synthetic data affected by 5% uniform noise. The outer width of the triangles is w_e = 2.5 mm, the thickness is e = 0.5 mm and two outer heights are considered, h_e = 1 and 2.5 mm. Again, the wider the "hole" between the two tips of the strips, the easier is for the inversion algorithm to retrieve the open geometry. Figure 7.9 (c) shows reconstructions of the same triangles but buried at a depth $|d|$ = 0.8 mm. Although burying this type of heat sources makes no practical sense since open cracks are usually found reaching the surface, these reconstructions are shown in order to observe the ability of the algorithm to retrieve buried open heat sources: only the overall geometry of the heat sources can be recovered and the shadowing effect almost disappears, probably due to the reduction of spatial resolution that retrieving heat sources with less high frequency information implies.

Back to the semicircular geometry, it has been mentioned before that heat is most likely to be produced not homogeneously within the stimulated band, in experiments with real open cracks. In order to further simulate these type of cracks, three cases of varying flux have been considered: depth-, angle- and radius-dependent flux. Figure 7.10 shows the reconstructions from synthetic data affected by 5% uniform noise corresponding to semicircular strips of (a) inner radius R_i = 1 mm and thickness e = 400 µm with depth-dependent flux, (b) inner radius R_i = 1 mm and thickness e = 400 µm with angle-dependent flux and (c) inner radius R_i = 1 mm and thickness e = 800 µm with radius-dependent flux. The depth of the three heat sources is $|d|$ = 0.1 mm and the real heat source distribution from which surface temperature data are generated is represented under each reconstruction.

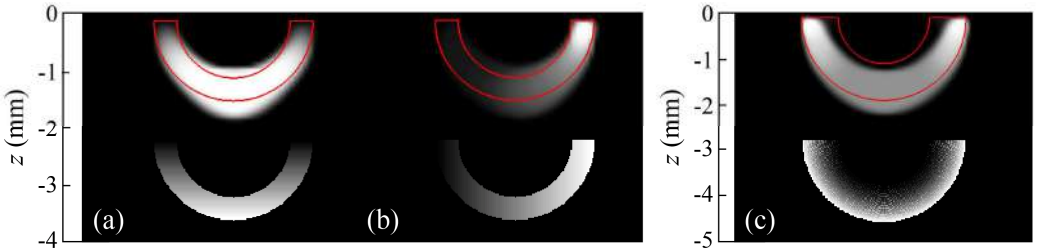

Figure 7.10. Grey level representation of the normalized heat source distribution inverted from synthetic data affected by 5% uniform noise corresponding to semicircular open heat sources, buried at a depth $|d|$ = 0.1 mm, considering three inhomogeneous flux cases: (a) flux varying with depth (R_i = 1 mm and e = 400 µm), (b) flux varying with angle (R_i = 1 mm and e = 400 µm) and (c) flux varying with radius (R_i = 1 mm and e = 800 µm). Retrieved by implementing the optimum inversion protocol. Real contours depicted in red and real heat source distributions from which surface temperature data are calculated represented under each reconstruction.

As for flux varying with depth, it is clear that the absence of heat emitted from the tips of the band allows the central deep part to dominate the reconstruction and, thus, the shadowing effect disappears. Because of this, the enlargement of the retrieved central area is more significant in comparison to that in the reconstruction of a homogeneous heat source of the same geometry and size (see Figure 7.8 (a)). Anyway, the flux dependence is well recovered.

Regarding flux varying with angle, the algorithm behaves much better: the tip on the right is accurately defined and the variation from maximum to null flux is nicely recovered, just as in the case of the thread geometry shown in Figure 7.5 (f), which further proves that width- or angle-dependent fluxes can be accurately retrieved as long as the bands are thin and the whole flux variation takes place over a long distance along *y*-axis in relation to the size of the mesh of the search area.

Lastly, the radial dependence of the flux is not identified at all. In the reconstruction corresponding to Figure 7.10 (c) the inner part of the tips of the strip are vanished, which can be easily mixed up with a thinner homogeneous open semicircle of same outer radius.

In conclusion, angle-dependent fluxes are very well recovered, even at deep positions, as long as the strips are thin in relation to the height of the heat sources, and depth-dependent fluxes can also be reproduced. However, the optimization of the recovery of some flux variations, along with the reduction of shadowing effect in the retrieved areas, will require future work.

8 Characterization of cracks from experimental data

In this section, the potential of the inversion algorithm to characterize vertical cracks is experimentally verified. To do so, the results of the inversion algorithm from synthetic data are checked using data obtained in vibrothermography experiments with samples containing calibrated heat sources. Furthermore, in order to prove that the inversion algorithm can be implemented in real applications, the defects found in a real welded sample have been characterized.

8.1 Calibrated vertical heat sources

In the following, we tackle the characterization of calibrated heat source distributions representing both kissing and open cracks in inversions from data taken in vibrothermography experiments in the lock-in regime.

All the experiments whose results are shown in this section have been performed following the defined optimum procedure for experimental data acquisition: using low US power, taking data in steady state, acquiring the same large number of images at all modulation frequencies and taking into account the phase shifts introduced by the acquisition system to whole surface phase thermograms.

As for the ultrasound electrical power, this has been selected depending on the size and depth of the heat sources: 25 W have been applied in most cases and, in samples containing

very small, thin or deep heat sources, it has been increased up to 40 W, maintaining the same US power at all modulation frequencies.

With regard to the IR camera, it has been set on half frame mode so as to capture images at a fixed frame rate of 320 Hz at all modulation frequencies, as we have checked that the picture size (21.6 x 16.5 mm) is sufficient to contain the surface temperature data for the size of heat sources considered. Similarly, 32,000 images have been analysed in the lock-in process regardless of the modulation frequency.

The construction of the samples has been described in section 4.1 and micrographs of the most significant foils used in the experiments corresponding to the reconstructions shown in this section are collected in appendix A.2, representing both kissing and open cracks of different geometries.

8.1.1 Kissing heat sources

In this section we present the results obtained with compact heat sources representing kissing cracks.

First, square heat sources are considered in order to verify that implementing the optimum inversion protocol gives best reconstructions and also to confirm the predictions from synthetic data concerning both the spatial resolution of the inversion algorithm and the shadowing effect appearing in certain cases.

Then, the performance of the inversion algorithm to retrieve the particular features of other geometries is checked and, with the aim of proving that we are able to retrieve heat sources of any geometry from experimental data, heat sources of arbitrary orientation and shape are also considered.

The experimental configuration used in this section is intended to generate a homogeneous flux over the whole heat source geometry. In order to illustrate what experimental data taken in vibrothermography experiments applying low US power look like, Figure 8.1 (a) shows Ln(|T|) (left) and Ψ (right) thermograms, obtained at $f_{lock\text{-}in}$ = 0.2 Hz, for a square Cu foil of $w = h$ = 1 mm buried at a depth |d| = 0.5 mm. The fitted thermograms are depicted in Figure 8.1 (b).

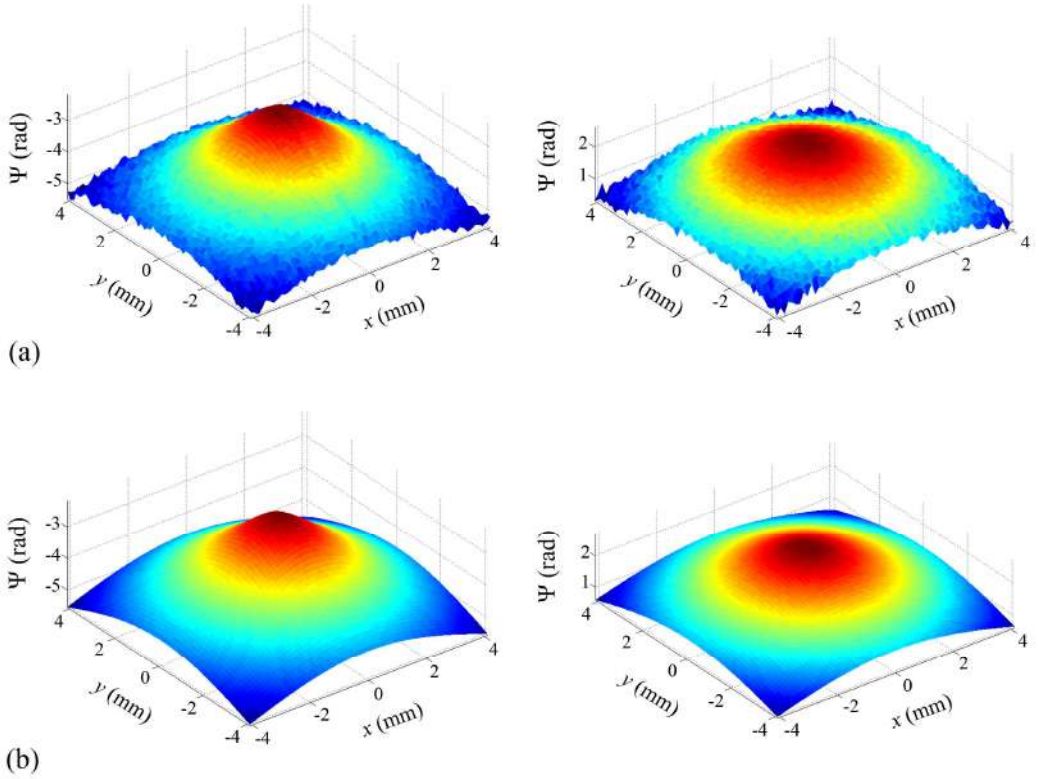

Figure 8.1. (a) Experimental Ln(|*T*|) (left) and Ψ (right) and (b) fitted thermograms, obtained at $f_{lock\text{-}in}$ = 0.2 Hz, corresponding to a square Cu foil of $w = h = 1$ mm buried at a depth $|d| = 0.5$ mm representing a homogeneous square kissing crack.

8.1.1.1 Square heat sources

In order to check that optimum retrieved areas are obtained by implementing the optimum inversion protocol, we have inverted experimental data corresponding to a standard square heat source (a Cu foil of dimensions $w = h = 1$ mm) buried at increasing depths, namely, $|d|$ = 0.1, 0.5, 1, 1.5, 2.0 and 3.0 mm, first using TV_{Anisot} and entering normalized amplitudes and then implementing TV_{Isot} and entering raw amplitudes. The results are depicted in Figure 8.2.

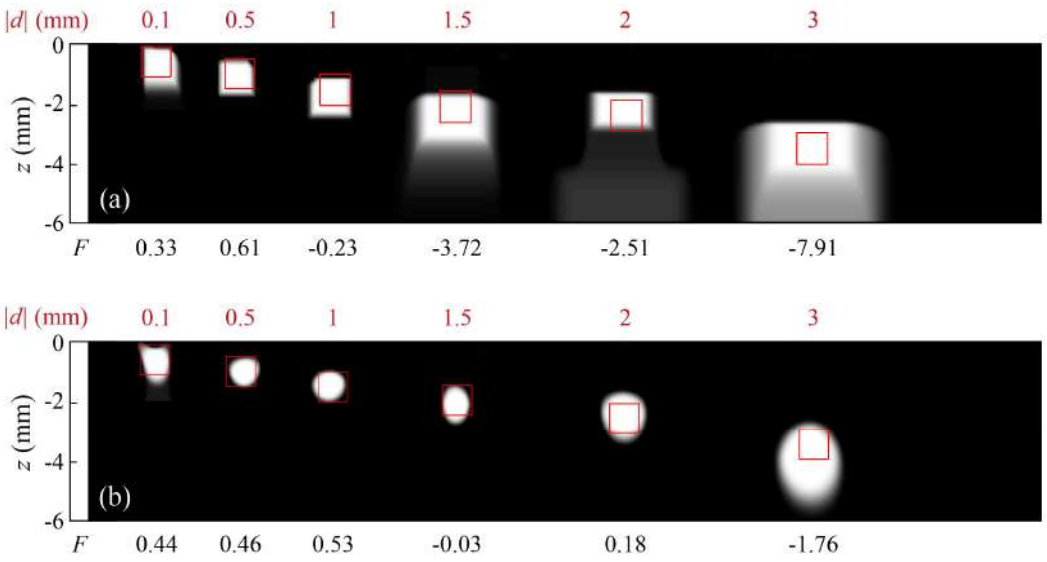

Figure 8.2. Grey level representation of the normalized heat source distribution retrieved from experimental data corresponding to a Cu foil of dimensions $w = h = 1$ mm buried at increasing depths, namely, $|d| = 0.1$, 0.5, 1, 1.5, 2.0 and 3.0 mm, in inversions implementing (a) TV_{Anisot} and entering normalized amplitudes and (b) TV_{Isot} and entering raw amplitudes. Real contours depicted in red and values of the depth of the heat sources and quality factor F on top of and under each reconstruction, respectively.

As can be observed, the quality factor F values are similar to those obtained in inversions from synthetic data affected by 5% uniform noise corresponding to square heat sources of $w = h = 1$ mm buried at similar depths, but only down to a depth about $|d| = 2.0$ mm. For deeper heat sources, the F values in reconstructions obtained from experimental data are reduced because data are affected by a significantly higher percentage of noise. Anyway, all depths at which the Cu foils are buried are very well recovered.

Although TV_{Anisot} favours the reconstruction of square and rectangular geometries, it has been determined before that the isotopic version of the Total Variation functional should be used to stabilize the inversion algorithm since, logically, the geometry of the cracks in real experiments is unknown. This considered and in order to double check that entering raw instead of normalized amplitudes provides dramatic improvements on the retrieved areas, in Figure 8.3 we show reconstructions of a standard square Cu foil ($w = h = 1$ mm) buried at other depths, namely, $|d| = 0.6$, 1.2, 2, 2.8, and 3.4 mm, inverted first entering normalized (a) and then raw amplitudes (b), in both cases using TV_{Isot}.

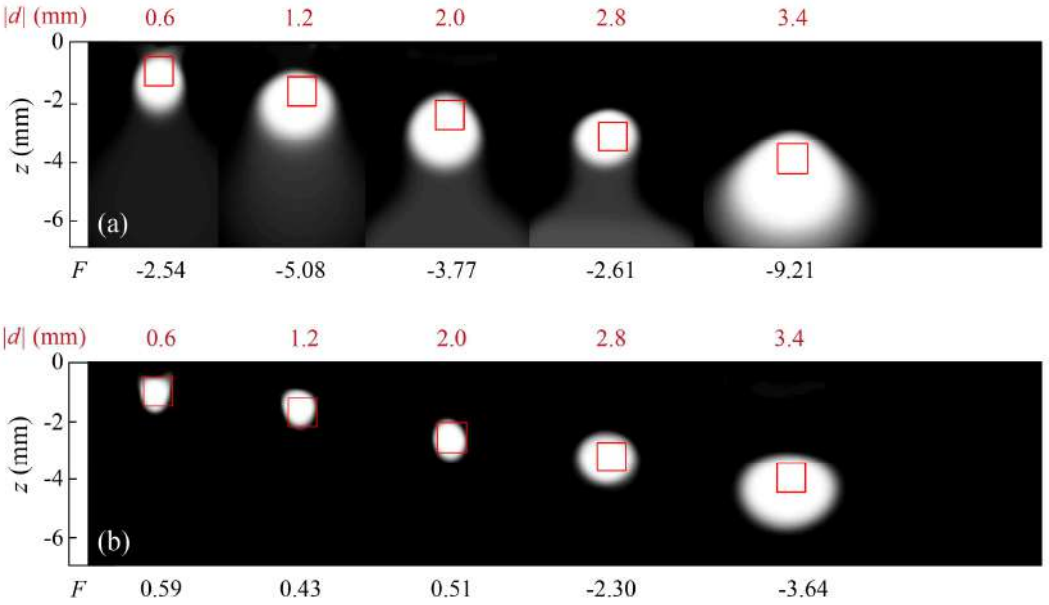

Figure 8.3. Grey level representation of the normalized heat source distribution in inversions from experimental data corresponding to a square Cu foil ($w = h = 1$ mm) buried at other depths, namely, $|d| =$ 0.6, 1.2, 2.0, 2.8 and 3.4 mm, retrieved by stabilizing the inversions with TV_{Isot} and entering: (a) normalized and (b) raw amplitudes. Real contours depicted in red and values of the depth of the heat sources and quality factor F on top of and under each reconstruction, respectively.

As for the spatial resolution of the inversion algorithm, the limiting distances between the centres of two square heat sources of $w_1 = h_1 = w_2 = h_2 = 1$ mm for their resolution, d_{cenLim}, obtained in inversions from synthetic data at increasing depths, are next verified in inversions from experimental data, using TV_{Anisot} and entering normalized amplitudes.

To that purpose, we have performed experiments using two Cu foils of $w_1 = h_1 = w_2 = h_2 =$ 1 mm buried at two different depths, namely, $|d_1| = |d_2| = 0.2$ and 1.6 mm. In turn, for each depth, we have considered two separation distances, d_{cen}, in such a way that $d_{cen} < d_{cenLim}$ in the first experiment and $d_{cen} > d_{cenLim}$ in the second one, so that the two heat sources are expected to be not resolved and resolved, respectively, according to our resolution criterion. The results are shown in Figure 8.4 (a) and (b).

The limiting distances obtained from synthetic data at depths $|d_1| = |d_2| = 0.2$ and 1.6 mm are $d_{cenLim} = 1.55$ and 3.10 mm, respectively, with TV_{Anisot} and using normalized amplitudes. The values of d_{cen} (in mm) and $Q_{mid}^{\delta,\alpha}$ are displayed on top of and under each reconstruction, respectively.

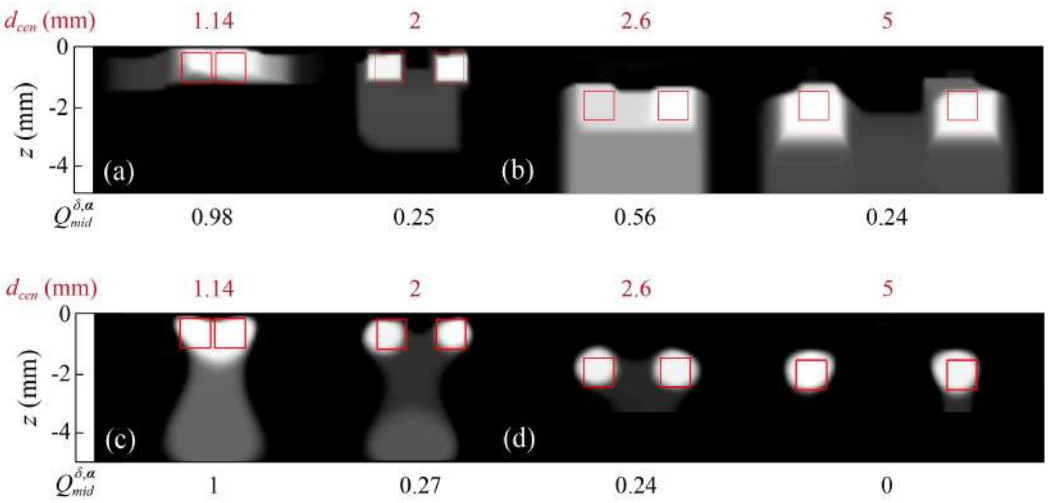

Figure 8.4. Grey level representation of the normalized heat source distribution in inversions from experimental data corresponding to two square Cu foils of dimensions $w_1 = h_1 = w_2 = h_2 = 1$ mm buried (a) at a depth $|d_1| = |d_2| = 0.2$ mm and with $d_{cen} = 1.14$ (left) and 2 mm (right) and (b) at a depth $|d_1| = |d_2| = 1.6$ mm and with $d_{cen} = 2.6$ (left) and 5 mm (right), inverted by implementing TV_{Anisot} and entering normalized amplitudes. (c) and (d) show the same as (a) and (b) but implementing TV_{Isot} and entering raw amplitudes. The values of d_{cen} (in mm) and $Q^{\delta,\alpha}_{mid}$ are displayed on top of and under each reconstruction, respectively.

As can be checked, the predictions from inversions using synthetic data are in good agreement with the results from experimental data, as the two heat sources are not resolved (left) and resolved (right), respectively, at the two considered depths.

Differences in d_{cenLim} when implementing the optimum inversion protocol are not significant when the two heat sources are shallow (see Table 6.2), but d_{cenLim} decreases significantly with depth when implementing TV_{Isot} and entering raw amplitudes (see Figure 6.18). This is experimentally confirmed in Figure 8.4 (c) and (d), where the same heat sources as in Figure 8.4 (a) and (b) are retrieved by implementing the optimum inversion protocol. Now, at a depth $|d_1| = |d_2| = 0.2$ mm, the two heat sources are not resolved (left) and resolved (right), but at $|d_1| = |d_2| = 1.6$ mm, the inversion algorithm resolves the two heat sources for the two considered d_{cen}.

Lastly, we invert experimental data corresponding to the cases where synthetic data has predicted that the shadowing effect may arise. Figure 8.5 (a) shows the reconstruction of a rectangular heat source of dimensions $w = 1$ mm and $h = 2$ mm, buried at a depth $|d| = 0.2$ mm and, as may be noted, the result is very similar to that obtained from synthetic data: the

lower half of the retrieved area is blurred due to the weaker contribution of those deep positions to surface temperature data in relation to shallower positions.

As for the shadowing effect arising between two different heat sources, we have inverted two square heat sources of $w_1 = h_1 = w_2 = h_2 = 1$ mm considering two possibilities to generate asymmetric surface temperature distributions: burying the heat source on the left deeper ($|d_1| = 0.78$ mm and ($|d_2| = 0.18$ mm) and decreasing the flux it emits with (being both buried at the same depth), for which, a stainless steel foil has been used instead of the usual Cu foil. In this last case, both the stainless steel and Cu foils are 25 µm thick and they are buried at a depth $|d_1| = |d_2| = 0.4$ mm. The results are depicted in Figure 8.5 (b) and (c), respectively.

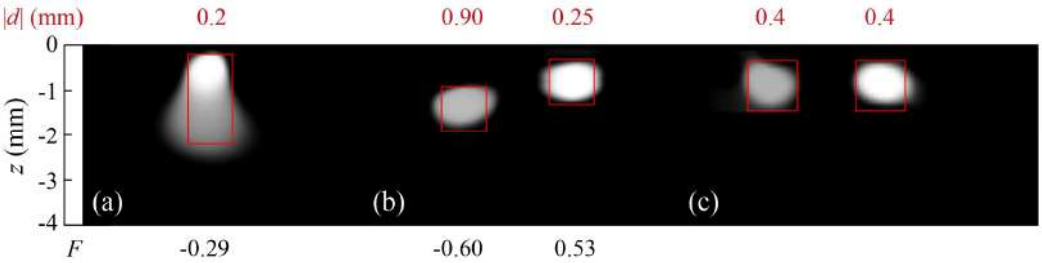

Figure 8.5. Grey level representation of the normalized heat source distribution in inversions from experimental data corresponding to (a) a rectangular Cu foil of dimensions $w = 1$ mm and $h = 2$ mm buried at a depth $|d| = 0.2$ mm, (b) two Cu foils of the same dimensions ($w_1 = h_1 = w_2 = h_2 = 1$ mm), emitting with same flux but buried at different depths ($|d_1| = 0.78$ mm and ($|d_2| = 0.18$ mm) and (c) two foils of the same dimensions ($w_1 = h_1 = w_2 = h_2 = 1$ mm) and buried at the same depth ($|d_1| = |d_2| = 0.4$ mm) but emitting with different flux (the left and right heat sources correspond to 25 µm thick stainless steel and Cu foils, respectively). Inverted by implementing the optimum protocol. Real contours depicted in red and values of the depth of the heat sources on top of each reconstruction. Values of the quality factor F under each reconstruction in (a) and (b).

As may be observed in the reconstruction shown in Figure 8.5 (b), the shallower heat source is accurately retrieved, whereas the deeper one is clearly shadowed: fainter and with a lower individual F value than if it was retrieved alone.

Finally, with regard to the two heat sources buried at the same depth but emitting with different flux (see Figure 8.5 (c)), it can be said that the differences obtained in $Q^{\delta,\alpha}$ at the centre of the heat sources are produced by the use of different materials, since the reconstruction from synthetic data in this case predicts no shadowing between the two heat sources in this case.

However, the fact that the relation of fluxes that the two different materials have produced in this experiment is unknown prevents us from calculating the quality of the

reconstruction. Thus, we cannot provide quantitative check of the quality of the reconstructions when using foils of different materials, as only qualitative evidence of different heat fluxes is obtained.

8.1.1.2 Other geometries

For the reconstruction of heat sources of geometries other than squares, only inversions implementing the optimum protocol will be shown. Semicircular and triangular heat sources are considered first.

Figure 8.6 (a) shows reconstructions from experimental data corresponding to *sUp* of R = 1.4 mm buried at increasing depths, namely, $|d|$ = 0.2, 0.75, 1.5, 2.2, 3.3 and 4.0 mm, whereas Figure 8.6 (b) shows reconstructions of *sDown* (R = 1.4 mm), buried at $|d|$ = 0.2 and 0.5 mm.

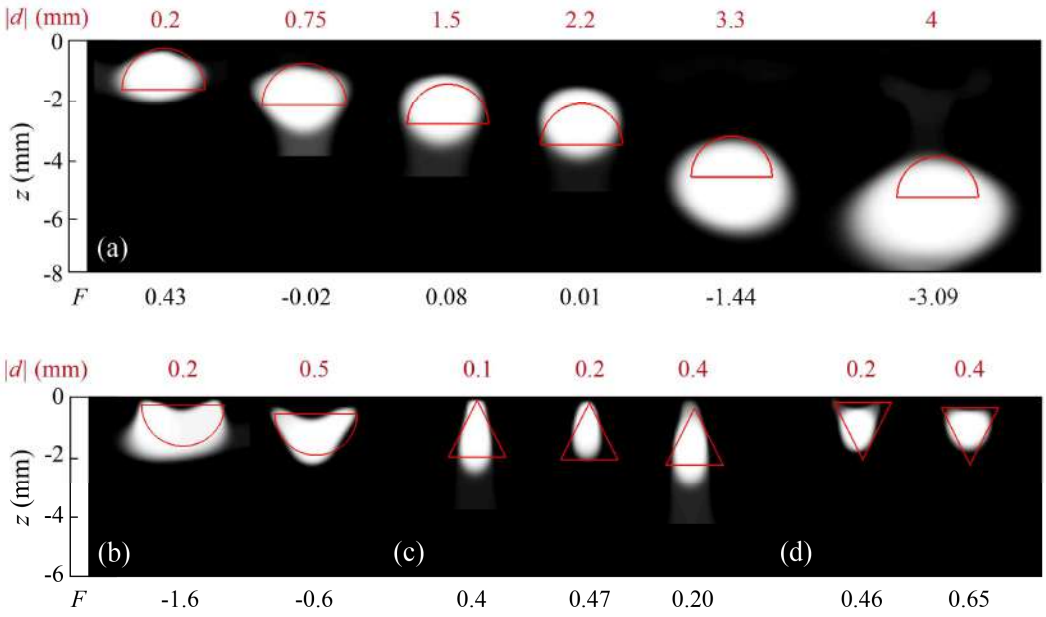

Figure 8.6. Grey level representation of the normalized heat source distribution in inversions from experimental data corresponding to (a) *sUp* of R = 1.4 mm buried at increasing depths, namely, $|d|$ = 0.2, 0.75, 1.5, 2.2, 3.3 and 4 mm, (b) *sDown* (R = 1.4 mm) buried at $|d|$ = 0.2 and 0.5 mm, (c) *tUp* of $w = h$ = 2 mm buried at $|d|$ = 0.1, 0.2 and 0.4 mm and (d) *tDown* ($w = h$ = 2 mm) buried at $|d|$ = 0.2 and 0.4 mm. Retrieved by implementing TV_{Isot} and entering raw amplitudes. Real contours depicted in red and values of the depth of the heat sources and quality factor F on top of and under each reconstruction, respectively.

As for *sUp*, the smooth contour of the semi-circles located at shallow depths are very well reproduced, but since the retrieved areas as depth increases get rounded due to stabilization with TV_{Isot}, it becomes very hard to retrieve the geometry of the heat sources, especially the lower flat side of the semicircles. With regard to *sDown*, the two corners of the upper flat side are clearly marked, which gives a correct estimate of the diameter of the semicircles.

Reconstructions of *tUp* of $w = h = 2$ mm buried at depths $|d| = 0.1$, 0.2 and 0.4 mm, as well as of *tDown* of the same size submerged at $|d| = 0.2$ and 0.4 mm, are shown in Figure 8.6 (c) and (d), respectively. Very shallow depths have been considered when placing these triangular Cu foils, since pointy ends are lost very easily with depth and reproducing them is specially challenging when data are affected by a high noise percentage (see Figure 7.3). The depth and overall height of all triangular heat sources are well retrieved and it is worth pointing out that, for *tDown*, the upper flat side of the triangles is quite well reproduced.

With the aim of proving that we are able to retrieve homogeneous heat sources of any geometry, we have performed vibrothermography experiments considering Cu foils of arbitrary orientation and shape. Figure 8.7 (a) shows the results for a rectangular ($w = 0.8$ mm and $h = 2.8$ mm) Cu foil inclined about 45º, buried at a depth $|d| = 0.4$ mm and, as can be checked, inclined heat sources can also be accurately retrieved.

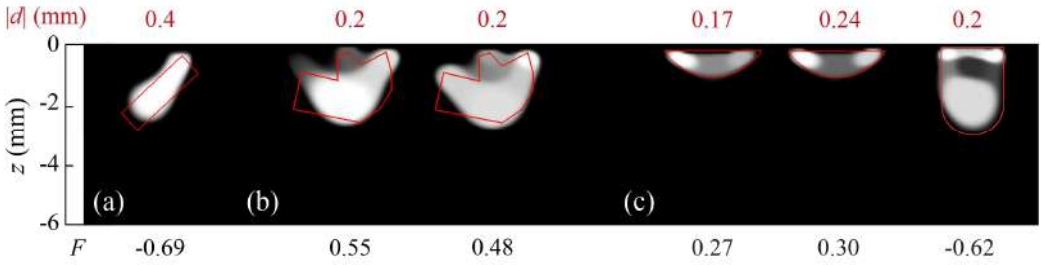

Figure 8.7. Grey level representation of the normalized heat source distribution in inversions from experimental data corresponding to (a) a rectangular Cu foil of $w = 0.8$ mm and $h = 2.8$ mm with an inclination of about 45º buried at a depth $|d| = 0.4$ mm, (b) a Cu foil of arbitrary shape in experiments applying 25 W at all modulation frequencies (left) and applying 25 W from 0.05 to 1.6 Hz and 40 W from 3.2 to 12.8 Hz (right), and (c) half-penny shaped Cu foils of different types: shallow and elongated ($w = 3.2$ mm and $h = 0.9$ mm) buried at depths $|d| = 0.17$ and 0.24 mm, and deep and narrow ($w = 2$ mm and $h = 2.8$ mm), buried at a depth $|d| = 0.2$ mm. Retrieved by implementing TV_{Isot} and entering raw amplitudes. Real contours depicted in red and values of the depth of the heat sources and quality factor F on top of and under each reconstruction, respectively.

Two reconstructions of a heat source of arbitrary shape are shown in Figure 8.7 (b). This geometry features two shallow pointy ends and a deeper rounded area: its overall size is $w = 3.5$ mm and $h = 2.5$ mm and the depth at the shallowest end is $|d| = 0.2$ mm. Low US

power has been applied in the two experiments, but whereas the experiments corresponding to the reconstruction on the left have been performed applying an ultrasound power of 25 W for all modulation frequencies, the reconstruction on the right has been obtained from data taken at 25 W for modulation frequencies ranging between 0.05 and 1.6 Hz, and at 40 W for the three highest modulation frequencies: 3.2, 6.4 and 12.8 Hz. As may be noted, increasing the ultrasound power at high modulation frequencies helps the inversion algorithm defining the contour of the heat sources.

As for geometries encountered in vibrothermography experiments with real cracks, Figure 8.7 (c) shows the reconstruction of a deep and narrow half-penny shaped heat source of width w = 2 mm and height h = 2.8 mm, buried at a depth $|d|$ = 0.2 mm, as well as the reconstructions of shallow and elongated half-penny shaped heat sources of w = 3.2 mm and h = 0.9 mm, buried at depths $|d|$ = 0.17 and 0.24 mm. In these three reconstructions, both the lower smooth contour and the upper flat side of the half-pennies are very well reproduced. Also, all corners on the upper side are clearly marked, pointing out the width of the half-pennies.

All the results shown in this section demonstrate that the inversion algorithm is able to retrieve heat sources of any geometry in inversions from data taken in vibrothermography experiments and implementing the optimum inversion protocol.

Although the particular features of the different considered geometries are very hard to recover as depth increases, both smooth contours and pointy ends, besides flat edges, can be accurately retrieved as long as the heat sources are shallow. Moreover, increasing the ultrasound power at high frequencies has shown to help the inversion algorithm defining the contours of the heat sources at shallow positions.

8.1.2 Open heat sources

In this section, we retrieve heat sources of different geometries representing surface breaking open cracks with a homogeneous heat generation from experimental data. Further in the study, our approach to produce an inhomogeneous heat generation in vibrothermography experiments is shown for open semicircular and triangular geometries, for their qualitative characterization.

Starting by heat sources representing open cracks emitting with a homogeneous flux, Figure 8.8 shows reconstructions corresponding to open (a) semicircular Cu bands of inner

radius R_i = 2.1 mm and thickness e = 0.8 mm buried at depths $|d|$ = 0.13, 0.32 and 0.71 mm, (b) a square Cu band of outer width w_e = 2.8 mm, outer height h_i = 1.7 mm and thickness e = 0.7 mm buried at a depth $|d|$ = 0.55 mm, (c) triangular Cu bands of outer width w_e = 3.6 mm, outer height h_i = 2 mm and thickness e = 0.9 mm buried at depths $|d|$ = 0.36 and 0.71 mm, and (d) shallow and elongated half-penny shaped Cu bands of outer width w_e = 4 mm, outer height h_i = 1.5 mm and thickness e = 1 mm buried at depths $|d|$ = 0.18 and 0.27 mm.

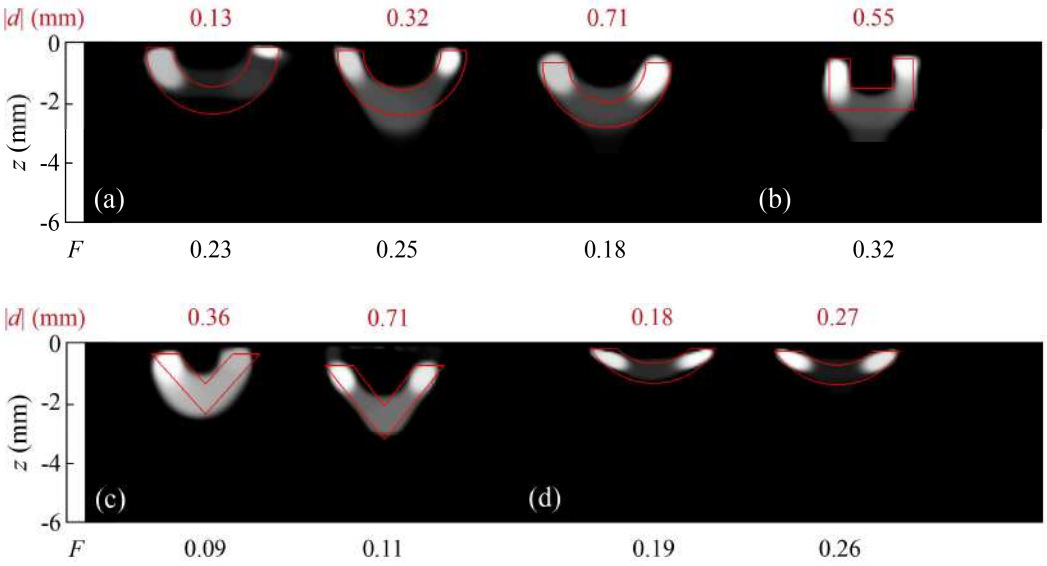

Figure 8.8. Grey level representation of the normalized heat source distribution in inversions from experimental data corresponding to (a) semicircular Cu bands of inner radius R_i = 2.1 mm and thickness e = 0.8 mm buried at depths $|d|$ = 0.13, 0.32 and 0.71 mm, (b) a square Cu band of outer width w_e = 2.8 mm, outer height h_i = 1.7 mm and thickness e = 0.7 mm buried at a depth $|d|$ = 0.55 mm, (c) triangular Cu bands of outer width w_e = 3.6 mm, outer height h_i = 2 mm and thickness e = 0.9 mm buried at depths $|d|$ = 0.36 and 0.71 mm and (d) shallow and elongated half-penny shaped Cu bands of outer width w_e = 4 mm, outer height h_i = 1.5 mm and thickness e = 1 mm buried at depths $|d|$ = 0.18 and 0.27 mm, inverted by implementing the optimum protocol. Real contours depicted in red and values of the depth of the heat sources and quality factor F on top and under of each reconstruction, respectively.

The shadowing effect, more pronounced in the recovery of open heat sources, can be appreciated in practically all cases. Nevertheless, in all geometries, the two tips of the bands are rather accurately retrieved and the deeper central areas correctly show the path the bands follow. Also, all depths are well recovered.

As an approach to simulate open cracks emitting with an inhomogeneous flux, we have taken data on semicircular and triangular strips in which an inhomogeneous heat generation

is intended to be produced, since the band that represents the open crack is now composed of two half foils of different materials (and same thicknesses).

As an example of what experimental thermograms corresponding to an inhomogeneous semicircular strip look like, Figure 8.9 (a) shows the Ln(|*T*|) (left) and Ψ (right) surface thermograms obtained at $f_{lock\text{-}in}$ = 1.6 Hz, generated by a semicircular band of inner radius R_i = 4.2 mm and thickness e = 0.9 mm, buried at depth |d| = 0.16 mm beneath the sample surface. The fitted thermograms are depicted in Figure 8.9 (b). The left and right halves of the semicircular strip correspond to 25 µm thick stainless steel and W foils.

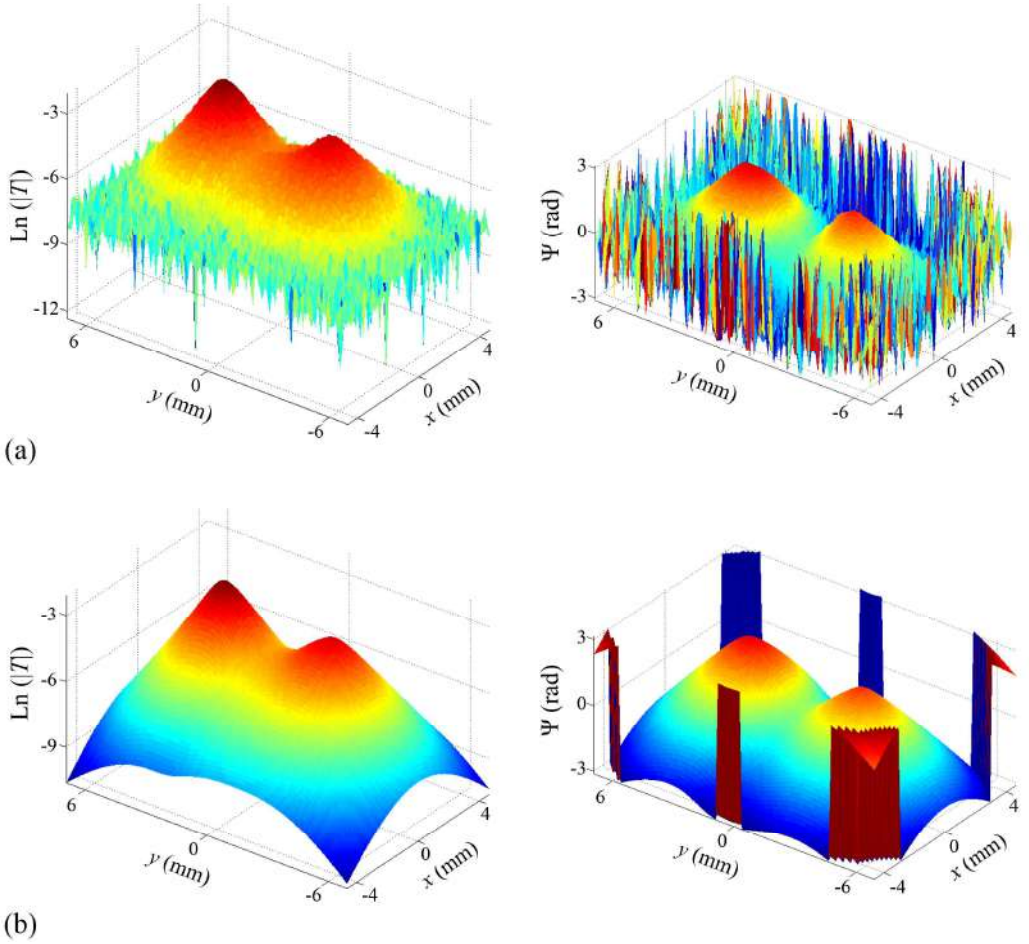

Figure 8.9. (a) Experimental Ln(|*T*|) (left) and Ψ (right) and (b) fitted thermograms, obtained at $f_{lock\text{-}in}$ = 1.6 Hz, corresponding to an inhomogeneous semicircular strip of inner radius R_i = 4.2 mm and thickness e = 0.9 mm, buried at depth |d| = 0.16 mm. The left and right halves of the strip correspond to 25 µm thick stainless steel and W foils.

Figure 8.10 (a) shows the reconstructions from experimental data corresponding to three inhomogeneous semicircular bands of inner radius R_i = 4.2 mm and thickness e = 0.9 mm, buried at depths $|d|$ = 0.2, 0.27 and 0.16 mm. In each case, the material combination for the left and right halves of the bands is different: 38 µm thick annealed and hard (usual) Cu foils (left), 25 µm thick Cu and stainless steel foils (centre) and 25 µm thick stainless steel and W foils (right). Similarly, Figure 8.10 (b) shows the results for three inhomogeneous triangular bands of outer width w_e = 5.6 mm, outer height h_e = 2.4 mm and thickness e = 0.9 mm buried at depths $|d|$ = 0.35 and 0.36 mm, using the same material combinations.

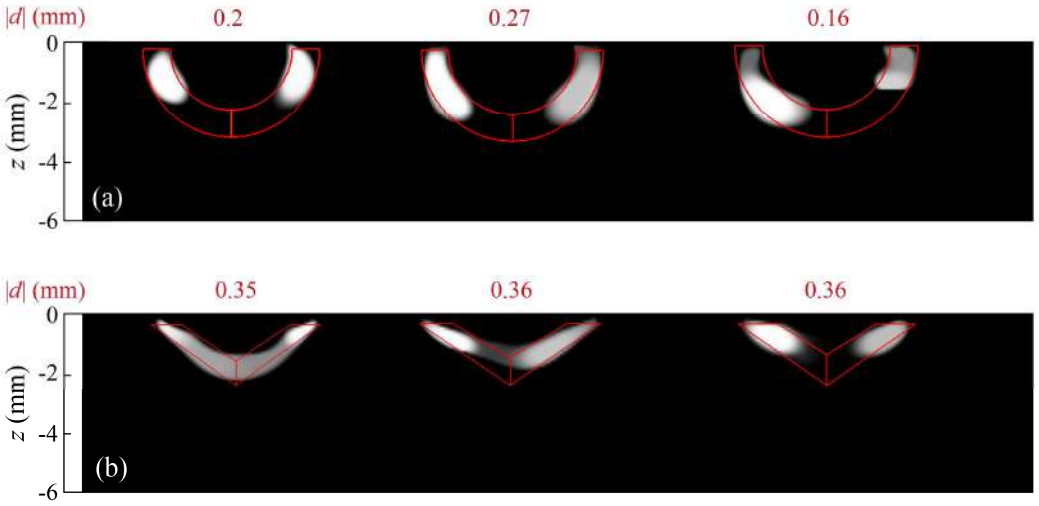

Figure 8.10. Grey level representation of the normalized heat source distribution in inversions from experimental data corresponding to (a) inhomogeneous semicircular bands of inner radius R_i = 4.2 mm and thickness e = 0.9 mm, buried at depths $|d|$ = 0.2, 0.27 and 0.16 mm and (b) inhomogeneous triangular bands of outer width w_e = 5.6 mm, outer height h_e = 2.4 mm and thickness e = 0.9 mm buried at depths $|d|$ = 0.35 and 0.36 mm. For both geometries, the material combinations for the left and right halves of the bands are the following: 38 µm thick annealed and hard (usual) Cu foils (left), 25 µm thick Cu and stainless steel foils (centre) and 25 µm thick stainless steel and W foils (right). Inverted by implementing the optimum protocol. Real contours depicted in red and values of the depth of the heat sources on top of each reconstruction.

As may be noted, for either geometry, similar results are obtained regarding the heat flux generated by each material combination: the annealed and hard Cu halves act as a homogeneous heat source, whereas differences in the retrieved $Q^{\delta,\boldsymbol{\alpha}}$ are more significant for the other two material combinations (Cu-stainless steel and stainless steel-W, respectively), meaning that using foils of different materials allows for an efficient inhomogeneous heat flux production in our vibrothermography experiments.

Although the shadowing effect makes the retrieved areas miss the contribution of the central deeper positions in most cases, the overall geometry and the depths of all heat sources are well recovered.

As mentioned before, we cannot provide quantitative check of the quality of the reconstructions because the relation of fluxes produced by the different materials is unknown. Nevertheless, these results prove that inhomogeneous heat sources can be qualitatively characterized.

8.2 Characterization of real cracks

In order to prove the potential of the inversion algorithm to retrieve and characterize defects in real applications, we have performed vibrothermography experiments in the lock-in regime using a welded Inconel 718 (D = 3.14 mm^2s^{-1} and K = 11.2 $Wm^{-1}K^{-1}$) sample containing real instead of artificial inner defects. The specimen is shown in Figure 8.11 (a).

The chosen experimental configuration is similar to that when using our AISI 304 sample: the specimen stands on the Teflon base and the sonotrode fixes it vertically, with an Al film placed in between as mechanical coupling material. Numbers from one to seven can be read on the sample, indicating the positions where the sonotrode has been placed in order to perform frequency sweeps so as to find the ultrasound frequency that excites the existing defects all along the welding bead. We have checked that a horizontal configuration for this specimen prevents the defects from giving any signal.

Thus, the IR camera records the surface temperature distribution of a welding bead (and surroundings) area that is located just under the sonotrode. As when using samples with calibrated heat sources, we run the camera at half frame, taking images at the fixed frame rate of 320 Hz and averaging the signal over 32,000 images, regardless of the modulation frequency. Also, we apply low US power (25 W), in order to prevent the crack surfaces from being altered or damaged.

Due to owner requirements, this specimen could not be coated with high emissivity paint, so data have been taken on the bare sample surface, making the test more challenging. The experimental setup for the welded Inconel 718 sample is shown in Figure 8.11 (b).

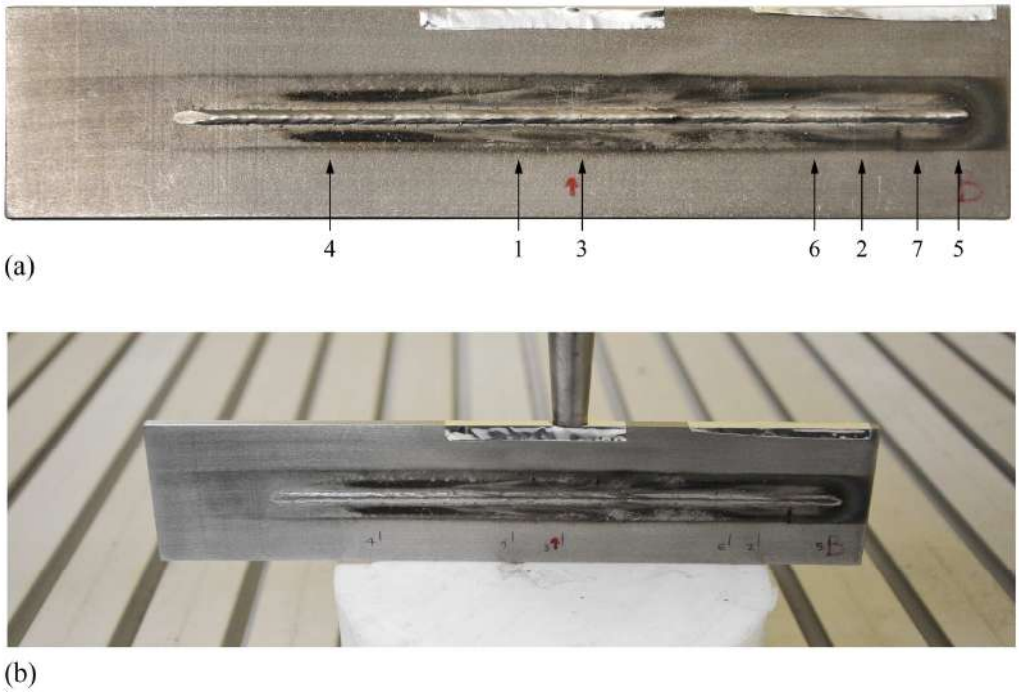

Figure 8.11. (a) Visible picture of the welded Inconel 718 sample, with numbers from one to seven showing the positions where the sonotrode has been placed in order to identify defects by performing frequency sweeps, and (b) experimental setup: the specimen stands on the Teflon base and the sonotrode fixes it vertically, with an Al film placed in between as mechanical coupling material.

Clear indications of the presence of defects have been found in positions 2 and 3 during the frequency sweeps: Figure 8.12 plots the recorded temperature as a function of the ultrasound frequency for these positions, where it can be checked that 22.9 (a) and 22.5 kHz (b) excite most efficiently the existing defects in such positions, respectively.

As may be noted, a second ultrasound frequency has also been found to excite the defects efficiently in both positions (34.3 (a) and 24.2 kHz (b) for positions 2 and 3, respectively), but, logically, only the ultrasound frequency that produces the highest surface temperature rise in each case has been considered for the later experiments in the lock-in regime. With respect to the right border of the specimen (corresponding to the start of the welding bead), positions 2 and 3 are located at 31 and 87 mm, respectively.

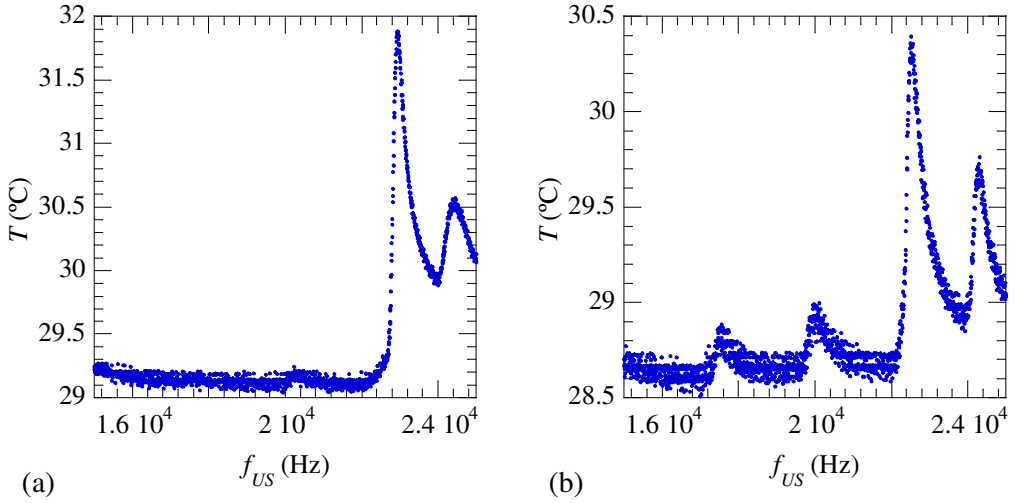

Figure 8.12. Frequency sweeps performed using the welded Inconel 718 specimen, with the sonotrode located in positions (a) 2 and (b) 3, pointing out that the ultrasound frequencies that excite the defects most accurately are 22.9 and 22.5 kHz, respectively.

Focusing on position 2, in Figure 8.13 (a) we show a thermogram corresponding to the ultrasound frequency where the presence of two defects is evidenced (22.9 kHz) (top), along with a thermogram at another ultrasound frequency at which the defects are not activated (bottom). The locations of the defects are marked with ellipses and Figure 8.13 (b) and (c) show different side views of the same thermograms.

Position x = 0 along x-axis coincides with the location of the sonotrode on top of the specimen and position y = 0 along y-axis has been chosen so that it represents the centre of the welding bead. In this way, it can be observed that the main defect is centred with respect to the sonotrode, whereas the second and smaller defect is located at x = -3.5 mm with respect to the centre of position 2. Along the ordinate, both defects are in line with y = 1.2 mm, which in the visible picture of the specimen corresponds to the upper toe of the welding bead.

As for position 3, a single defect has been identified, which generates an even smaller surface temperature distribution than that shown in Figure 8.13.

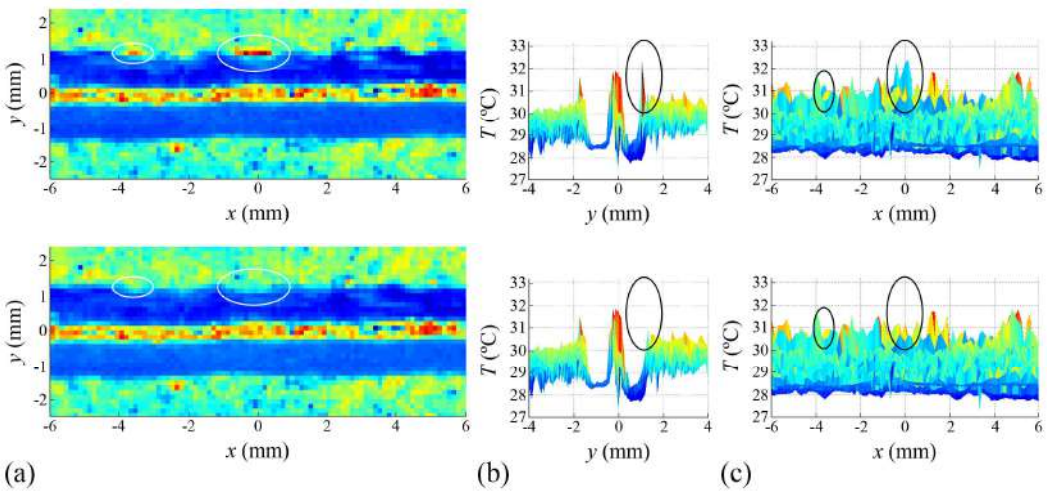

Figure 8.13. (a) Surface thermograms at f_{US} = 22.9 kHz evidencing the presence of two defects in position 2 (top) and at another ultrasound frequency where the defects are not activated (bottom). (b) and (c) are different side views of the same thermograms. The location of the defects is marked with ellipses.

Since the specimen is not coated with high emissivity paint and due to a high reflectance of the sample surface, the features of the welding bead can be seen in the thermograms shown, as well as other irregularities on the measuring surface such as weld spatter. For this reason, for the reconstruction of the three defects found (two defects in position 2 and a defect in position 3), surface temperature data taken in lock-in vibrothermography experiments have been cropped so that only information around the defects can enter the inversion algorithm. In each case, the coordinates have been repositioned so that position (0, 0) refers to the centre of the observed signals.

As an example, Figure 8.14 shows the Ln(|*T*|) (top) and Ψ (bottom) surface thermograms corresponding to the main defect in position 2, obtained at $f_{lock\text{-}in}$ = 0.1 (a), 0.2 (b) and 0.4 Hz (c), exciting the sample with an ultrasound frequency f_{US} = 22.9 kHz.

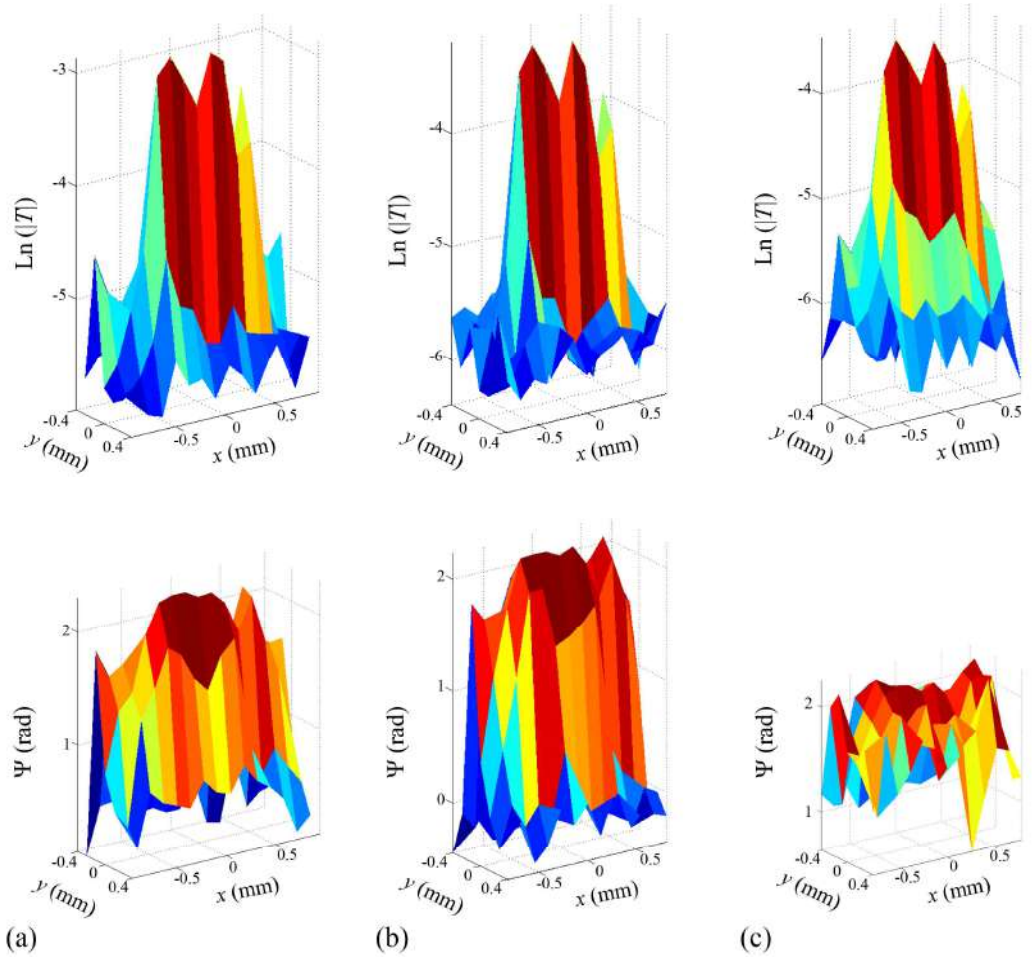

Figure 8.14. Ln(|*T*|) (top) and Ψ (bottom) thermograms taken in vibrothermography experiments applying low US power and exciting the sample at f_{US} = 22.9 kHz, corresponding to the main defect found in position 2 of the welded Inconel 718 sample, at $f_{lock\text{-}in}$ = 0.1 (a), 0.2 (b) and 0.4 Hz (c).

Surface temperature data obtained at $f_{lock\text{-}in}$ = 0.1, 0.2, 0.4 and 0.8 Hz have been inverted in order to reconstruct the three defects found, since no signals have been detected at 0.05 Hz and data taken at modulation frequencies higher than 0.8 Hz are affected by such a high noise level that provide no exploitable information, even increasing the number of images analysed in the lock-in process.

It is worth mentioning that, for the inversions, the initial values of the regularization parameters corresponding to Tikhonov, Total Variation and L_1 given in equations (5.24),

(5.25) and (5.26) have been multiplied by 10, in order to increase the regularization degree due to the poor signal-to-noise ratio in surface temperature data.

In Figure 8.15 we show the reconstructions corresponding to the (a) main and (b) second defects found in position 2, and (c) the defect found in position 3.

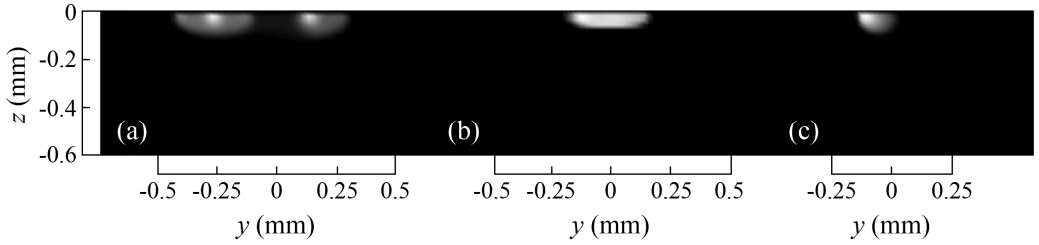

Figure 8.15. Grey level representation of the normalized heat source distribution in inversions from experimental data corresponding to the (a) main and (b) second defects found in position 2, and (c) the defect found in position 3, retrieved by combining data taken in lock-in vibrothermography experiments at $f_{lock\text{-}in}$ = 0.1, 0.2, 0.4 and 0.8 Hz and exciting the welded Inconel 718 sample at f_{US} = 22.9 and 22.5 kHz for positions 2 and 3, respectively, and using low US power. Inverted by implementing the optimum protocol.

As may be checked, all the defects found are surface breaking and very short, the maximum depths being 100 and 50 μm for the main and second heat sources in position 2, respectively, and even less than 50 μm for the defect in position 3.

The reconstruction of the main defect in position 2 indicates that the length of the defect is about 800 μm. Within this defect, two main heat sources can be identified, which are in good agreement with the two temperature peaks observed in the surface thermograms. The second defect in position 2 has a length of about 300 μm and the defect found in position 3 looks more like a point-like heat source.

Liquids penetrants testing has been performed in order to identify surface breaking defects. The results are shown in Figure 8.16. The test has produced two indications: a rather visible one in position 7 (at 17 cm with respect to the right border of the especimen) and a fainter one pointing out a very small defect volume and coinciding with the main defect detected by vibrothermography in position 2.

The reconstructions of the second defect found in position 2 and that found in position 3 indicate that these defects are even smaller than the main defect in position 2, which could be consistent with the absence of any liquids trace.

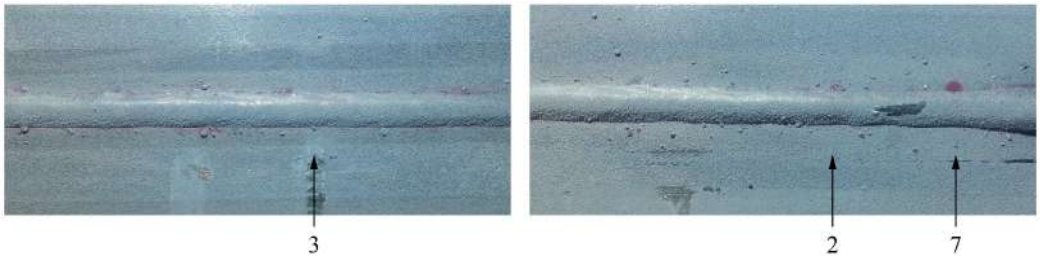

Figure 8.16. Result of the liquids penetrants testing performed in the welded Inconel 718 specimen, showing two indications: a rather visible one in position 7 (at 17 cm with respect to the right border of the especimen) and a fainter one coinciding with the main defect detected by vibrothermography in position 2 (at 31 cm).

On the contrary, the stronger indication by penetrants testing in position 7 did not give any signal in the vibrothermography testing. Two reasons could be responsible for this. On the one hand, the larger liquid exuded volume might point out to an open defect, in which case rubbing friction barely takes place. Another possibility is that the ultrasound frequency that activates that defect is outside our frequency range.

9 Conclusions and future work

The most important conclusions that can be drawn from the work presented in this thesis are summarized below.

Concerning the direct problem and data acquisition in lock-in vibrothermography experiments:

- The direct problem in this thesis, consisting in the calculation of the surface temperature distribution generated by a buried modulated heat source distribution, has been solved and its solution has been analysed by performing simulations. Heat sources of different geometries are very hard to distinguish when their particular features correspond to the lower (buried) contour of the geometry, which evidences the ill-posed nature of the problem and leads to the determination of using multi-frequency data in order to gather as much information as possible.
- The direct problem has been experimentally verified and three methods to tackle the contribution of the transient temperature rise of the sample to the measured surface temperature have been proposed, which provide surface temperature data in good agreement with the predictions of the theory.
- The frequency dependence of the experimental equipment has been measured.
- The optimum data acquisition procedure has been defined: using low US power (25-40 W) so as to preserve the non-destructive nature of the technique and acquire surface temperature data in steady state, taking advantage of the key feature of the lock-in process by analysing a large number of images at all modulation frequencies and removing the phase shifts introduced by the equipment to whole surface phase thermograms.

As for the inverse problem and the inversion algorithm:

- The inverse problem in this thesis, consisting in retrieving the heat source distribution giving rise to a certain surface temperature distribution, has been tackled

and analysed by means of SVD for the proposal of appropriate regularization methods.

- A robust inversion algorithm based on least squares minimization stabilized with penalty terms corresponding to Tikhonov, Total Variation and L_1 functionals has been implemented, which is able to recover heat source distributions from vibrothermography data.
- A complete analysis of the inversion algorithm has been carried out using synthetic data corresponding to square/rectangular heat sources representing homogeneous vertical kissing cracks:
    - The optimum inversion protocol has been defined by analysing the effects of the Total Variation functional model and data normalization on the retrieved normalized heat source distribution: the isotropic TV model and raw data should be used in order to obtain best reconstructions.
    - A quality factor of the reconstructions and an accurate reconstruction criterion have been defined, providing quantitative information about the quality of the retrieved normalized heat source distribution. According to it, we are able to retrieve a square heat source of side L down to depths of $3.6L$ and $5L$ for data affected by 5% and 0.5% uniform noise, respectively.
    - The convergence property of the inversion algorithm has been demonstrated by verifying the effect of the noise level on the reconstructions. In addition, the effect of noise distribution has been checked, which indicates that data acquisition should be carried out by analysing the same number of images for all modulation frequencies or even increasing the number of images at high modulation frequencies.
    - The minimization stopping criterion has been validated by making use of the retrieved set of intensities: at the discrepancy term minimal iteration, the intensities are fitted in an optimum way.
    - The use of multi-frequency data and the design of experiments have been verified: combining surface temperature data at multiple modulation frequencies gives more accurate reconstructions in comparison to inverting data at any single modulation frequency, and entering data at doubling modulation frequencies is determinant for the accurate recovery of deep heat sources. Furthermore, the good choice for all values concerning the regularization parameters corresponding to Tikhonov, Total Variation and L_1 stabilization procedures has been checked.

  - The spatial resolution of the inversion algorithm has been determined for two equal square heat sources as a function of depth.
  - Different cases concerning the geometrical parameters of the heat sources for which the shadowing effect arises in reconstructions have been identified.

- The ability of the inversion algorithm to retrieve heat sources of other geometries from synthetic data, namely, semicircular and triangular heat sources, has been analysed:
  - Smooth contours are easily recovered because of the rounded shapes that TV_{Isot} delivers by default.
  - Narrow or sharp corners are very hard to reproduce and a shallow depth ($|d| \leq 0.1$ mm) along with a low noise level ($\delta \leq 5\%$) are necessary for their accurate reconstruction.
  - The robustness of the inversion algorithm against noise has been checked considering the depths at which the particular features of the geometries are accurately retrieved: increasing the noise level in the data does not significantly harm the recovery of the particular shapes, with the exception of pointy ends.
- Real situations have been approached by retrieving open heat sources representing surface breaking homogeneous vertical open cracks of different geometries from synthetic data. The inversion algorithm is able to recover the thickness and depth of the strips very accurately and the shadowing effect is the main limitation for the reconstruction of the deeper central part of the strips.
- Lastly, both kissing and open inhomogeneous heat sources have been retrieved from synthetic data, proving that the inversion algorithm is capable of reproducing certain flux dependences. In kissing heat sources, width-dependent fluxes can be accurately retrieved at shallow positions. In open heat sources, width- or angle- dependent fluxes are very well recovered, even at deep positions, as long as the strips are thin in relation to the height of the heat sources, and depth-dependent fluxes can also be reproduced. Large radial flux gradients represent a limitation of the method.

In relation to the experimental verification of the implemented inversion algorithm:

- The results of inversions from synthetic data have been verified by with data obtained in lock-in vibrothermography experiments using samples with calibrated heat sources and following the optimum data acquisition procedure:

  - The optimum inversion protocol gives best results in inversions from experimental data, with similar reconstruction qualities for square heat sources to those obtained from synthetic data.
  - The limiting distances obtained from synthetic data for the spatial resolution of two equal square heat sources as a function of depth are in good agreement with the results from experimental data.
  - Heat sources of arbitrary orientation and shape have been considered in the experiments in order to prove that any geometry can be accurately retrieved.
  - Increasing the ultrasound power has shown to help the inversion algorithm defining the contour of the geometries.
  - The use of different materials has been proposed so as to produce an inhomogeneous heat flux generation within open heat sources in the experiments. The results prove that the inversion algorithm is capable of retrieving flux differences.

- The use of the inversion algorithm has been extended for the characterization of the cracks encountered in experiments using a real welded Inconel 718 specimen. The results are in good qualitative agreement with the results of liquids penetrants testing.

These conclusions lay the grounds for future research.

Interests first focus on the reduction of the shadowing effect in the retrieved areas as well as on the optimization of the recovery of certain heat flux variations. In order to tackle the shadowing effect, two options may be considered. First, other experimental designs could be studied so as to favour the recovery of the shadowed heat sources. Another solution could be to implement a procedure that chops the highest values of the retrieved normalized heat source distribution so that, over iterations, they equalise the values obtained for the shadowed positions.

The next step is the characterization of inclined instead of vertical heat sources, i.e., contained in a plane that is not perpendicular with respect to the sample surface, with the ultimate goal of characterizing non-planar heat sources, where a 3D search region needs to be considered for the inversion. For open inclined or non-planar heat sources, where the heat generated at a certain band needs to cross the air gap corresponding to the area where the crack faces do not contact in order to reach de sample surface, the modelling of a thermal resistance is of major importance, which may be tackled by using discontinuous finite elements.

Lastly, an aspect in vibrothermography experiments that is worth addressing in future research is the measurement of the absolute heat flux produced at the heat source. In experiments with real cracks, the knowledge of the relation between vibration strain and heat flux at the crack would allow for the determination of the minimum vibration strain so as to produce a detectable heat generation, which is a key point for vibrothermography to become a fully accepted technique for non-destructive evaluation.

Resumen

Esta tesis recoge el trabajo desarrollado con el fin de potenciar el uso de la vibrotermografía para la caracterización de grietas verticales sumergidas, ya que es una técnica de evaluación no destructiva (NDE) aun en desarrollo. La investigación llevada a cabo durante esta tesis contribuye a la sistematización y normalización de la vibrotermografía como técnica NDE y supone un avance de cara a la cuantificación de los defectos, lo que, a su vez, supone una contribución significativa a la información que esta técnica puede ofrecer a sectores industriales estratégicos como el aeronáutico o la máquina herramienta.

En la termografía con excitación ultrasónica o vibrotermografía, la muestra o pieza objeto de estudio se excita mediante ultrasonidos. En los defectos, parte de esta energía mecánica se disipa en forma de calor como consecuencia del rozamiento entre las caras del defecto y, si se trata de grietas, por deformación plástica del material que las rodea. La energía térmica generada en los defectos se difunde en el material, produciendo un aumento de temperatura en la superficie de la muestra que puede medirse mediante una cámara infrarroja. Así, en el caso de los metales, donde la atenuación de los ultrasonidos en el material es pequeña, los defectos se convierten en una fuente de calor en un entorno frío, lo que hace que la técnica sea selectiva con los mismos, ya que sólo los defectos producen señal vibrotermográfica.

La vibrotermografía compite con las clásicas técnicas de evaluación no destructiva que tienen como objeto la detección de defectos ligeramente sumergidos o abiertos a la superficie, como los líquidos penetrantes, partículas magnéticas o corrientes inducidas. La técnica de líquidos penetrantes requiere que el material no sea poroso y que los defectos lleguen a la superficie y, para aplicar los métodos de partículas magnéticas o corrientes inducidas, el material debe ser ferromagnético o conductor eléctrico, respectivamente. Sin embargo, no hay restricción en cuanto al material para la aplicación de la vibrotermografía, a excepción de que no sea frágil.

La vibrotermografía también compite con otros métodos termográficos, ya que además de mediante excitación mecánica, la muestra se puede excitar por medios electromagnéticos u ópticos. Las mayores limitaciones de la excitación electromagnética son la evaluación de piezas de gran tamaño y su restricción a materiales conductores eléctricos y, en relación a la excitación óptica, la vibrotermografía permite la detección de defectos más profundos. Además, para la detección de defectos verticales (perpendiculares a la superficie de medida) como los abordados en esta tesis, es necesario escanear un haz de luz focalizado sobre la superficie del material, lo que supone una importante inversión de tiempo.

La vibrotermografía puede implementarse en dos regímenes de excitación diferentes: lock-in (modulada) y burst (pulsada). En la vibrotermografía burst, se aplica un pulso de amplitud constante y se registra la evolución de la temperatura superficial de la muestra durante y después de la excitación, siendo su mayor ventaja la rapidez de los ensayos. En la vibrotermografía lock-in, sin embargo, los ultrasonidos se modulan en amplitud, provocando una deposición de calor periódica en el defecto que da lugar a la generación de ondas térmicas que, a su vez, se propagan de acuerdo a las propiedades térmicas del material y se detectan en la superficie. La magnitud que se evalúa en el régimen modulado es la componente oscilatoria de la temperatura superficial de la muestra en cada píxel, que se promedia durante un cierto número de períodos de modulación para obtener las imágenes de amplitud y fase de la oscilación de la temperatura superficial.

A pesar de que la adquisición de datos en el régimen modulado es más larga que en el régimen pulsado por tener que evaluar muchos períodos para cada frecuencia de modulación, la gran ventaja del régimen lock-in es su eficiente capacidad de filtrado del ruido aleatorio, permitiendo extraer señales embebidas en un nivel de ruido varios órdenes de magnitud mayor, siempre y cuando las señales sean periódicas. La reducción del nivel de ruido, a su vez, permite disminuir la potencia de los ultrasonidos en los ensayos, lo cual es favorable para minimizar el riesgo de alterar la superficie de los defectos y, en consecuencia, la generación de calor en los mismos, preservar la naturaleza no destructiva de la técnica y así aumentar su reproducibilidad y su fiabilidad. Por estos motivos, se ha elegido el régimen lock-in para la realización de esta tesis.

El fin último de la detección de defectos es su caracterización, es decir, la determinación de los parámetros geométricos de los defectos como su tamaño, forma y la profundidad a la que están sumergidos. El problema directo es la relación “causa-efecto”, es decir, el cálculo de la distribución de temperatura superficial generada por una grieta, mientras que el problema inverso consiste en recuperar la causa (la geometría de la grieta), a partir de la distribución de temperatura superficial. Sin embargo, la información físicamente accesible

a partir de datos de vibrotermografía es la distribución de fuentes de calor responsable de esa distribución de temperatura superficial, más que la geometría de la grieta en sí. La región que contiene las fuentes de calor y la geometría de la grieta coinciden en el caso de grietas cerradas, donde el calor es generado en la totalidad de la superficie de la grieta, mientras que, en el caso de grietas abiertas, la generación de calor se da solo en una región determinada de la grieta. Además, en grietas abiertas, es probable que el calor se genere de manea inhomogénea dentro de la región considerada.

La naturaleza difusiva de la propagación del calor y el hecho de que la temperatura solo pueda obtenerse en la superficie de la muestra y no en el propio lugar de generación del calor (sumergido bajo la superficie), provocan que el problema de reconstruir la geometría de la distribución de fuentes de calor sea un problema mal puesto en el sentido de Hadamard, ya que su solución es fuertemente dependiente de pequeños errores en los datos y la inversión es inestable. En este tipo de problemas, la minimización por mínimos cuadrados no converge. Sin embargo, la inestabilidad del problema inverso se puede paliar mediante técnicas de regularización.

Esta tesis se centra en la caracterización de grietas verticales mediante vibrotermografía lock-in, principalmente cerradas, que suponen un reto para la gran mayoría de las técnicas END. Así pues, el primer objetivo es la *implementación de un algoritmo de inversión basado en minimización por mínimos cuadrados estabilizados, para la reconstrucción de fuentes de calor verticales sumergidas a partir de datos de vibrotermografía*. También se lleva a cabo un análisis del algoritmo de inversión usando datos sintéticos, con el fin de optimizar el algoritmo para expandir su aplicación a la caracterización del mayor rango de geometrías de fuentes de calor posible y aumentar la calidad de las reconstrucciones, aportando información cuantitativa sobre las fuentes de calor.

La verificación experimental del algoritmo de inversión es un paso obligado para demostrar el potencial del mismo para reconstruir fuentes de calor. El segundo objetivo de esta tesis, entones, es el de *verificar los resultados obtenidos usando datos sintéticos con datos experimentales obtenidos en ensayos de vibrotermografía lock-in, utilizando muestras con fuentes de calor calibradas y también muestras reales con grietas internas*.

Para la consecución de los objetivos, el primer paso es el planteamiento y resolución del problema directo, es decir, el cálculo de la distribución de temperatura superficial generada por fuentes de calor moduladas. La solución del problema directo se ha analizado llevando a cabo simulaciones, en las cuales se estudia la influencia de alterar los parámetros geométricos de una fuente de calor homogénea de geometría cuadrada en la distribución de

temperatura superficial. También se han considerado otras geometrías con el objetivo de explorar la capacidad de la vibrotermografía para distinguir entre distribuciones de temperatura superficial generadas por distintas geometrías. La dificultad de distinguir entre las diferentes geometrías cuando las características distintivas de las mismas se encuentran en la parte inferior (sumergida) de las fuentes de calor, evidencia el carácter de problema mal planteado, que además empeora con la profundidad a la que están sumergidas las fuentes. El uso de datos obtenidos a múltiples frecuencias de modulación permite aumentar la información sobre las fuentes de calor. Por tanto, el diseño experimental seleccionado consta de 9 frecuencias de modulación, cubriendo un rango de 0.05 a 12.8 Hz.

Las predicciones de las simulaciones del problema directo se han verificado llevando a cabo experimentos de vibrotermografía con muestras que contienen fuentes de calor verticales calibradas. Se han observado diferencias entre las predicciones del modelo teórico y los resultados experimentales cuando la muestra se excita con una potencia de ultrasonidos "alta" (250-300 W), especialmente a frecuencias de modulación bajas. Se ha demostrado que estas discrepancias se deben a la contribución de la subida de temperatura de la muestra a la distribución de temperatura superficial medida, al tomar datos en régimen transitorio.

Tras la propuesta de tres métodos para la eliminación del transitorio de la temperatura superficial medida, se ha optado por el que permite una mayor reducción de la potencia de los ultrasonidos, realizando así los ensayos con una potencia de ultrasonidos "baja" (25-40 W). Para compensar la disminución de la relación señal-ruido que ello conlleva, se ha hecho uso de la capacidad de filtrado de la técnica lock-in analizando un mayor número de imágenes, en concreto 32.000 imágenes, para cada frecuencia de modulación. De esta manera, se ha llegado a la definición del procedimiento óptimo de adquisición de datos en los ensayos de vibrotermografía. Además, se ha medido la dependencia en frecuencia del equipo experimental, con el fin de corregir los errores introducidos en los termogramas de fase sistemáticamente.

En cuanto al problema inverso, éste ha sido abordado y su carácter mal planteado ha sido analizado mediante descomposición en valores singulares, con el fin de seleccionar métodos de regularización apropiados. La investigación en este sentido ha resultado en la implementación de un algoritmo de inversión robusto, basado en minimización por mínimos cuadrados estabilizados mediante términos de penalización basados en los funcionales de Tikhonov, Total Variation y L_1, capaz de reconstruir distribuciones de fuentes de calor partiendo de datos de vibrotermografía. El planteamiento adoptado implica el ajuste de los datos al resultado de un modelo semi-analítico que describe la propagación

de las ondas térmicas generadas en los defectos. En este sentido, el tratamiento del problema es puramente térmico, dejando de lado los mecanismos de generación de calor en los defectos.

A partir del profundo análisis del algoritmo de inversión realizado usando datos sintéticos generados para fuentes de calor que representan grietas homogéneas de geometría cuadrada/rectangular, en el que se analizan los efectos en las reconstrucciones de aspectos tanto en relación al propio algoritmo como a los datos que se introducen, se ha llegado a su optimización, es decir, a la determinación del protocolo de inversión para la obtención de resultados óptimos. Con el objetivo de cuantificar la similitud entre la distribución de fuentes de calor reconstruida y la real, se ha definido un factor de calidad y un criterio de "reconstrucción precisa". Conforme a este criterio, el algoritmo de inversión es capaz de reconstruir fuentes de calor cuadradas de lado L hasta profundidades de $3.6L$ y $5L$, con datos afectados por un 5% y un 0.5% de ruido uniforme, respectivamente, demostrando así la propiedad de convergencia del algoritmo, ya que la solución obtenida tiende a la solución exacta a medida que el nivel de ruido en los datos disminuye.

Otros aspectos importantes han sido también verificados, como el criterio de parada del proceso iterativo de minimización, los valores seleccionados de los parámetros de regularización correspondientes a los funcionales de Tikhonov, Total Variation y L_1, el diseño del experimento o el uso de datos multi-frecuencia para lograr una óptima reconstrucción. Además, se ha determinado la resolución espacial del algoritmo de inversión en función de la profundidad de dos fuentes de calor y, por último, se han identificado los casos en los que ensombrecimiento, es decir, la reconstrucción difusa de ciertas zonas de las fuentes de calor, afecta a las reconstrucciones.

En cuanto a la caracterización de fuentes de calor que representan grietas homogéneas cerradas de otras geometrías, el algoritmo de inversión reproduce las formas redondeadas fácilmente, mientras que las formas puntiagudas son muy difíciles de reconstruir, requiriendo profundidades muy pequeñas, además de niveles de ruido bajos. Excepto en este último caso, el algoritmo es robusto frente al aumento del nivel de ruido de cara a la recuperación de las particularidades de las diferentes geometrías.

Con el objeto de abordar situaciones que surgen a menudo en experimentos con grietas reales abiertas a la superficie, se han considerado fuentes de calor abiertas representadas por bandas de diferentes geometrías. El algoritmo de inversión, en este caso, reconstruye adecuadamente los extremos superficiales de las bandas donde la producción de calor tiene lugar, siendo el ensombrecimiento, es decir, la reconstrucción poco definida de las áreas

centrales y más profundas de las bandas, la mayor limitación para la reproducción de la totalidad de las geometrías.

Para una mayor aproximación a situaciones reales, se han reconstruido flujos de calor inhomogéneos, tanto en fuentes de calor cerradas como abiertas, de manera cualitativa. A pesar de que la reconstrucción de gradientes de flujo es todo un reto para un problema inverso mal planteado, el algoritmo de inversión ha demostrado ser capaz de reconstruir de manera precisa ciertas variaciones de flujo. En concreto, en fuentes de calor cerradas, se reconstruyen de manera precisa las variaciones de flujo cercanas a la superficie que se dan a lo largo de la anchura de la geometría y, en fuentes de calor abiertas, aquellas que se dan a lo largo de la anchura incluso a profundidades mayores, así como las variaciones de flujo que tengan lugar a lo largo de la profundidad de la fuente de calor.

Finalmente, los resultados obtenidos en inversiones de datos sintéticos se han verificado con datos experimentales obtenidos en ensayos de vibrotermografía, realizados siguiendo el procedimiento óptimo de adquisición de datos. Se ha comprobado que el protocolo óptimo de inversión permite obtener las mejores reconstrucciones también partiendo de datos experimentales y, para demostrar que se puede reconstruir cualquier geometría haciendo uso del algoritmo de inversión implementado, se han considerado geometrías diferentes a las analizadas con datos sintéticos, como rectángulos inclinados o formas arbitrarias. Además, se ha demostrado que el aumento de la potencia de ultrasonidos a altas frecuencias (dentro de la potencia "baja" establecida) permite una mayor definición del contorno de las geometrías en las reconstrucciones. Para la producción inhomogénea de calor en los experimentos de vibrotermografía se ha propuesto el uso de diferentes materiales en las fuentes de calor calibradas. Al igual que en inversiones de datos sintéticos, el algoritmo de inversión ha reproducido las diferencias de flujo de calor generados en las distintas zonas, para fuentes de calor abiertas de geometría semicircular y triangular.

Finalmente y como objetivo último, se ha aplicado el algoritmo de inversión para caracterizar grietas reales en una muestra soldada de Inconel 718. Los resultados están en buena correlación cualitativa con los resultados del ensayo de líquidos penetrantes realizado posteriormente.

El trabajo realizado a lo largo de esta tesis sirve de base para líneas futuras de investigación relacionadas con el algoritmo de inversión. El interés más inmediato está en la reducción del ensombrecimiento, muy presente en la reconstrucción de ciertas geometrías y también entre dos fuentes de calor reconstruidas en una misma inversión, así como en la

optimización de la reconstrucción de cualquier tipo de flujo de calor inhomogéneo. El siguiente paso es la caracterización de grietas oblicuas en lugar de verticales, con el fin último de poder caracterizar grietas no planas, caso en el cual el algoritmo de inversión necesitaría considerar una zona de búsqueda tridimensional. Finalmente, un avance importante es la determinación absoluta del flujo de calor generado en las grietas, ya que supone un conocimiento determinante para la aceptación total de la vibrotermografía como técnica NDE.

List of publications

Research activity for this thesis has resulted in the following publications:

- Mendioroz A, Castelo A, Celorrio R and Salazar A 2013 Characterization of vertical buried defects using lock-in vibrothermography: I. Direct problem *Meas. Sci. Technol.* **24** 065601 (11 pp)

- Mendioroz A, Castelo A, Celorrio R and Salazar A 2014 Characterization and spatial resolution of cracks using lock-in vibrothermography *NDT&E Int.* **66** 8-15

- Mendioroz A, Castelo A, Celorrio R and Salazar A 2015 Defect characterization from lock-in vibrothermography data *International Journal of Thermophysics* **36** 1208-1216

- Castelo A, Mendioroz A, Celorrio R and Salazar A 2017 Optimizing the inversion protocol to determine the geometry of vertical cracks from lock-in vibrothermography *J. Nondestr. Eval.* **36** 3 (12 pp)

- Castelo A, Mendioroz A, Celorrio R, Salazar A, López de Uralde P, Gorosmendi I and Gorostegui-Colinas E 2017 Characterizing open and non-uniform vertical heat sources: towards the identification of real vertical cracks in vibrothermography experiments *Proc. SPIE* **10214** Thermosense XXXIX 102140L (12 pp)

In addition, the work has been presented in the conferences below:

- Mendioroz A, Castelo A, Salazar A and Celorrio R, *Defect reconstruction from lock-in vibrothermography*, 17th International Conference on Photoacoustic and Photothermal Phenomena, Suzhou (China), 2013, **Invited**

- Mendioroz A, Castelo A, Celorrio R and Salazar A, *Vertical cracks characterization and resolution from lock-in vibrothermography*, Quantitative Infrared Thermography (QIRT 2014), Bordeaux (France), 2014, Oral

- Castelo A, Mendioroz A, Celorrio R and Salazar A, *Characterization of vertical cracks using lock-in vibrothermography*, 18th International Conference on Photoacoustic and Photothermal Phenomena, Novi Sad (Serbia), 2015, Oral

- Castelo A, Mendioroz A, Celorrio R and Salazar A, *Optimization of Total Variation regularization to improve the accuracy of the characterization of vertical cracks by lock-in vibrothermography*, 13th Quantitative Infrared Thermography (QIRT 2016), Gdansk (Poland), 2016, Oral

- Mendioroz A, Castelo A, Cifuentes A, Celorrio R and Salazar A, *Improving the inversion procedure to characterize vertical cracks using IR thermography*, Fourth Mediterranean International Workshop on Photoacoustic and Photothermal Phenomena, Erice, Sicily (Italy), 2016, **Invited**

- Mendioroz A, Castelo A, Celorrio R, Salazar A, López de Uralde P, Gorosmendi I and Gorostegui-Colinas E, *Characterizing open and non-uniform vertical heat sources: towards the identification of real vertical cracks in vibrothermography experiments*, Thermosense: Thermal Infrared Applications XXXIX, Anaheim (USA), 2017, Oral

- Castelo A, Mendioroz A, Celorrio R and Salazar A, *Characterization of open distribution of heat sources in lock-in vibrothermography experiments*, accepted paper in 19th International Conference on Photoacoustic and Photothermal Phenomena, Bilbao (Spain), 2017, Oral

References

[1] Henneke E G and Jones T S 1979 Detection of Damage in Composite Materials by UT *Nondestructive Evaluation and Flaw Criticality for Composite Materials* by Amer. Society for Testing and Materials STP **696** 83-95

[2] Henneke E G, Reifsnider K L and Stinchcomb W W 1979 Thermography - An NDI Method for Damage Detection *J. Met.* **31** 11-15

[3] Renshaw J, Chen J C, Holland S D and Thompson R B 2011 The sources of heat generation in vibrothermography *NDT&E Int* **44** 736-739

[4] Pye J and Adams R D 1981 Heat emission from damaged composite materials and its use in nondestructive testing *J. Phys. D* **14** 927-941

[5] Pye J and Adams R D 1981 Detection of damage in fibre reinforced plastics using thermal fields generated during resonant vibration *NDT Int.* **14** 111-118

[6] Mignogna B, Green R E, Duke J C, Henneke E G and Reifsnider K L 1981 Thermographic investigation of high-power ultrasonic heating in materials *Ultrasonics* **19** 159-163

[7] Rantala J, Wu D and Busse G 1995 Amplitude-modulated lock-in vibrothermography for NDE of polymers and composites *Res. Nondestr. Eval.* **7** 215-228

[8] Favro L D, Han X, Ouyang Z, Sun G, Sui H and Thomas R L 2000 Infrared imaging of defects heated by a sonic pulse *Rev. Sci. Instr.* **71** 2418-2421

[9] Favro L D, Han X, Ouyang Z, Sun G and Thomas R L 2001 Sonic IR imaging of cracks and delaminations *Analytical Sciences* **17** 451-453

[10] Mian A, Han X, Islam S and Newaz G 2004 Fatigue damage detection in graphite/epoxy composites using sonic infrared imaging technique *Comp. Sci. Tech.* **64** 657-666

[11] Barden T J, Almond D P, Pickering S G, Morbidini M and Cawley P 2007 Detection of impact damage in CFRP composites by thermosonics *Nondestr. Test. Eval.* **22** 71-82

[12] Han X, Favro L D and Thomas R L 2011 Sonic IR imaging of delaminations and disbonds in composites *J. Phys D: Appl. Phys.* **44** 034013 (5 pp)

[13] Dillenz A, Zweschper T, Riegert G and Busse G 2003 Progress in phase angle thermography *Rev. Sci. Instr.* **74** 417-419

[14] Fernandes H, Ibarra-Castanedo C, Zhang H and Maldague X 2015 Thermographic nondestructive evaluation of carbon fiber reinforced polymer plates after tensile testing *J. Nondestr. Eval.* **34:35** 1-10

[15] Bai G, Lamboul B and Roche J-M 2016 Investigation of multiple cracking in glass/epoxy 2D woven composites by vibrothermography *QIRT J.* **13** 35-49

[16] Salerno A, Dillenz A, Wu D, Rantala J and Busse G 1998 Progress in ultrasound excited thermography *Proceedings of the 4th Conference on Quantitative Infrared Thermography* 154-160

[17] Morbidini M, Cawley P, Barden T, Almond D and Duffour P 2006 Prediction of the thermosonic signal from fatigue cracks in metals using vibration damping measurements *J. Appl. Phys.* **100** 104905 (13 pp)

[18] Holland S D, Uhl C, Ouyang Z, Bantel T, Li M, Meeker W Q, Lively J, Brasche L and Eisenmann D 2011 Quantifying the vibrothermographic effect *NDT&E Int.* **44** 775-782

[19] Montanini R, Freni F and Rossi G L 2012 Quantitative evaluation of hidden defects in cast iron components using ultrasound activated lock-in vibrothermography *Rev. Sci. Instr.* **83** 094902 (8 pp)

[20] Guo X and Vavilov V 2013 Crack detection in aluminum parts by using ultrasound excited infrared thermography *Infr. Phys. Tech.* **61** 149-156

[21] Choi M, Park J H and Kim W T 2008 Detection of delamination defect inside timber by sonic IR *Proc. SPIE* **6939** Thermosense XXX 1F 1-4

[22] Piau J-M, Bendada A, Maldague X and Legoux J-G 2008 Nondestructive testing of open microscopic cracks in plasma-sprayed-coatings using ultrasound excited thermography *Nondestr. Test. Eval.* **23** 109-120

[23] Zweschper T, Dillenz A and Busse G 2000 Ultrasound lock-in thermography – a NDT method for the inspection of aerospace structures *Proceedings of the 5th Conference on Quantitative Infrared Thermography* 212-217

[24] Balageas D, Maldague X, Burleigh D, Vavilov VP, Oswald-Tranta B, Roche J-M, Pradere C and Carlomagno G M 2016 Thermal (IR) and Other NDT Techniques for Improved Material Inspection *J. Nondestr. Eval.* **35** 18 (17 pp)

[25] Polimeno U, Almond D P, Weekes B and Chen E W J 2014 A compact thermosonic inspection system for the inspection of composites *Composites: Part B* **59** 67-73

[26] DiMambro J, Ashbaugh D M, Nelson C L and Spencer F W 2007 Sonic Infrared (IR) Imaging and Fluorescent Penetrant Inspection Probability of Detection (POD) Comparison *Rev. Prog. Quant. Nondestr. Eval.* **26A** 463-470

[27] Burke M W and Miller W O 2004 Status of vibroIR at Lawrence Livermore National Laboratory *Proc. SPIE* **5405** Thermosense XXVI 313-321

[28] Sakagami T and Kubo S 1999 Development of a new crack identification method based on singular current field using differential thermography *Proc. SPIE* **3700** Thermosense XXI 269-376

[29] Riegert G, Zweschper T and Busse G 2004 Lock-in thermography with Eddy current excitation *QIRT J.* **1** 21-31

[30] Lemistre M B and Balageas D L 2003 A Hybrid electromagnetic acousto-ultrasonic method for SHM of carbon/epoxy structures *SHM* **2** 153-160

[31] Oswald-Tranta B 2004 Thermoinductive investigations of magnetic materials for surface cracks *QIRT J.* **1** 33-46

[32] Tsopelas N and Siakavellas N J 2006 Electromagnetic-thermal NDT in thin conducting plates *NDT&E Int.* **39** 391-399

[33] Kostson E, Weekes B, Almond D P, Wilson J and Tian G Y 2011 Crack detection using pulsed eddy current stimulated thermography *Rev. Progr. Quant. Nondestruct. Eval.* **30** 415-422

[34] Almond D P and Lau S K 1994 Defect sizing by transient thermography I: an analytical treatment *J. Phys. D: Appl. Phys.* **27** 1063-1069

[35] Maldague X and Marinetti S 1996 Pulse phase infrared thermography *J. Appl. Phys* **79** 2694

[36] Shepard S M, Lhota J R, Rubadeux B A, Wang D and Ahmed T 2003 Reconstruction and enhancement of active thermographic image sequence *Opt. Eng.* **42** 1337-1342

[37] Roche J M, Leroy F-H and Balageas D 2014 Images of TSR coefficients: a simple way for rapid and efficient detection of defects *Mater. Eval.* **72** 73-82

[38] Datong W and Busse G 1998 Lock-in thermography for nondestructive evaluation of materials *Rev. Gén. Therm.* **37** 693-703

[39] Zenzinger G, Bamberg J, Satzger W and Carl V 2007 Thermographic crack detection by Eddy current excitation *Nondestr. Test. Eval.* **22** 101-111

[40] Maldague X 2001 Theory and practice of infrared technology for nondestructive testing *Wiley series in microwave and optical engineering*, New York, John Wiley & Sons

[41] Breitenstein O, Warta W and Langenkamp M 2003 Lock-in Thermography: Basics and use for Evaluating Electronic Devices and Materials, Series in Advanced Microelectronics, Berlin Heidelberg, Springer-Verlag

[42] Almond D P and Patel P M 1996 Photothermal Science and Techniques, London, Chapman & Hall

[43] Weekes B, Cawley P, Almond D P and Li T 2010 The effect of crack opening on thermosonics and laser spot thermography *AIP Conf. Proc.* **1211** 490-497

[44] Pilla M, Klein M, Maldague X and Salerno A 2002 New Absolute Contrast for Pulsed Thermography *Proc. QIRT* 53-58

[45] Shepard S M 2001 Advances in Pulsed Thermography *Proc. SPIE* **4360** Thermosense XXVIII 511-515

[46] Wu D and Busse G 1998 Lock-in thermography for nondestructive evaluation of materials *Rev. Gén. Thermique* **37** 693-703

[47] Osiander R and Spicer J W M 1998 Time-resolved infrared radiometry with step heating - A review *Rev. Gén. de Thermique* **37** 680-692

[48] Kaiplavil S and Mandelis A 2011 Highly depth-resolved chirped pulse photothermal radar for bone diagnostics *Rev. Sci. Instrum.* **82** 074906 (9 pp)

[49] Wang Y Q, Kuo P K, Favro L D and Thomas R L 1990 Photoacoustic and Photothermal Phenomena II *Springer Series in Optical Science* **62** 24-6

[50] Krapez J-C, Gruss C, Hüttner R, Lepoutre F and Legrandjacques L 2001 La caméra photothermique (flying spot camera) I Principe, modélisation, application à la detéction de fissures *Instr. Més. Metrol.* **1** 9-39

[51] Krapez J-C, Lepoutre F, Hüttner R, Gruss C, Legrandjacques L, Piriou M, Gros J, Gente D, Hermosilla-Lara S, Joubert P and Placko D 2001 La caméra photothermique (flying spot camera) II Applications industrielles, perspectives d'amélioration par un nouveau traitement d'image *Instr. Més. Metrol.* **1** 41-67

[52] Schlichting J, Ziegler M, Dey A, Maierhofer Ch and Kreutzbruck M 2011 Efficient data evaluation for thermographic crack detection *QIRT Journal* **8** 119-123

[53] Burrows S E, Dixon S, Pickering S G, Li T and Almond D P 2011 Thermographic detection of surface breaking defects using a scanning laser source *NDT&E Int.* **44** 589-96

[54] Li T, Almond D P and Rees D A S 2011 Crack imaging by scanning laser-line thermography and laser-spot thermography *Meas. Sci. Technol.* **22** 035701 (14 pp)

[55] Li T, Almond D P and Rees D A S 2011 Crack imaging by scanning pulsed laser spot thermography *NDT&E Int.* **44** 216-25

[56] Schlichting J, Maierhofer C and Kreutzbruck M 2012 Crack sizing by laser excited thermography *NDT&E Int.* **45** 133-40

[57] Streza M, Fedala Y, Roger J P, Tessier G and Boue C 2013 Heat transfer modelling for surface crack depth evaluation *Meas. Sci. Technol.* **24** 045602

[58] Pech-May N W, Oleaga A, Mendioroz A, Omella A J, Celorrio R and Salazar A 2014 Vertical cracks characterization using lock-in thermography: I infinite cracks *Meas. Sci. Technol.* **25** 115601 (10 pp)

[59] Celorrio R, Omella A J, Pech-May N W, Oleaga A, Medioroz A and Salazar A 2014 Vertical cracks characterization using lock-in thermography: II finite cracks *Meas. Sci. Technol.* **25** 115602 (9 pp)

[60] Pech-May N W, Oleaga A, Mendioroz A and Salazar A 2016 Fast Characterization of the Width of Vertical Cracks Using Pulsed Laser Spot Infrared Thermography *J. Nondestr. Eval.* **22** (10 pp)

[61] Holland S 2007 First measurement from a new broadband vibrothermography measurement system *Rev. Quant. Nondestr. Eval.* **26** 478-483

[62] Gleiter A, Spiessberger C and Busse G 2007 Improved ultrasound activated thermography using frequency analysis *QIRT J.* **4** 155-164

[63] Morbidini M and Cawley P 2009 Detectability of cracks using sonic IR *J. Appl. Phys.* **105** 093530 (9 pp)

[64] Zweschper T, Riegert G, Dillenz A and Busse G 2003 Frequency modulated elastic wave thermography *Proc. SPIE* **5073** Thermosense XXV 386-391

[65] Song Y and Han X 2012 Further study of coupling materials on aluminum sample using sonic IR *Rev. Prog. Quantit. Nondestr. Eval. AIP Conf. Proc.* **1430** 546-551

[66] Zweschper T, Riegert G, Dillenz A and Busse G 2004 Ultrasound excited thermography - advances due to frequency modulated elastic waves *Proceedings of the 7th Conference on Quantitative IR Thermography* **H8** 1-6

[67] Han X, Li W and Zeng Z 2002 Acoustic chaos and sonic infrared imaging *Appl. Phys. Lett.* **81** 3188-3190

[68] Plum R and Ummenhofer T 2008 Ultrasound excited thermography of load bearing members used in constructional steelwork *Proceedings of the 9th Conference on Quantitative IR Thermography* (7 pp)

[69] Holland S D, Renshaw J and Roberts R 2007 Measurement of dynamic full-field internal stresses through surface laser Doppler vibrometry *Appl. Phys. Lett.* **91** 134101 (3 pp)

[70] Renshaw J, Holland S D, Thompson R B and Anderegg J 2011 Vibration induced tribological damage to fracture surfaces via vibrothermography *Int. J. Fatigue* **33** 849-857

[71] Homma C, Rothenfusser M, Baumann J and Shannon R 2006 Study of the heat generation mechanisms in acoustic thermography *AIP Conf. Proc.* **820** 566-573

[72] Han X and Islam M S 2010 Progress on developing acoustic infrared imaging NDE: studying motions in crack faces *Proc. SPIE* **7647** 1-6

[73] Lu J, Han X, Newaz G, Favro L D and Thomas R L 2007 Study of the effect of crack closure in sonic infrared imaging *Nondestr. Test. Eval.* **22** 127-135

[74] Renshaw J, Holland S D and Thomson R B 2008 Measurement of crack opening stresses and crack closure stress profiles from heat generation in vibrating cracks *Appl. Phys. Lett.* **93** 081914 (3 pp)

[75] Bovsunovsky A P 2004 The mechanisms of energy dissipation in the non-propagating fatigue cracks in metallic materials *Eng. Fract. Mech.* **71** 2271-2281

[76] Rizi A S, Hedayatrasa S, Maldague X and Vukhanh T 2013 FEM modeling of ultrasonic vibrothermography of a damaged plate and qualitative study of heating mechanisms *Infr. Phys. Technol.* **61** 101-110

[77] Hosten B, Biateau C, Bacon C, Pradere C, Batsale J-C and Meziane A 2012 Sonothermography in composite materials: Finite Element modeling and experimental validation *NDT&E Int.* **51** 120-126

[78] Mabrouki F, Thomas M, Genest M and Fahr A 2009 Frictional heating model for efficient use of vibrothermography *NDT&E Int.* **42** 345-352

[79] Mabrouki F, Thomas M, Genest M and Fahr A 2010 Numerical modeling of vibrothermography based on plastic deformation *NDT&E Int.* **43** 476-483

[80] Holland S D, Uhl C and Renshaw J 2008 Toward a viable strategy for estimating vibrothermographic probability of detection *Rev. Prog. Quant.: Nondestr. Eval.* **27** 491-497

[81] Renshaw J, Holland S D and Barnard D J 2009 Viscous material-filled synthetic defects for vibrothermography *NDT&E Int.* **42** 753-756

[82] Plum R and Ummenhofer T 2009 Ultrasound excited thermography of thick walled steel load bearing members *QIRT J.* **6** 79-100

[83] Rothenfusser M and Homma C 2005 Acoustic thermography: vibrational modes of cracks and the mechanism of heat generation *AIP Conf. Proc.* **760** 624-631

[84] Plum R and Ummenhofer T 2011 Structural-thermal finite element simulation of vibrothermography applied to cracked steel plates *QIRT J.* **8** 201-220

[85] Han X, Zeng Z, Li W, Islam M S, Lu J, Loggins V, Yitamben E, Favro L D, Newaz G and Thomas R L 2004 Acoustic chaos for enhanced detectability of cracks by sonic infrared imaging *J. Appl. Phys.* **95** 3792-3797

[86] Han X, Loggins V and Zeng Z 2004 Mechanical model for the generation of acoustic chaos in sonic infrared imaging *Appl. Phys. Lett.* **85** 1332-1334

[87] Han X, Islam M S, Newaz G, Favro L D and Thomas R L 2005 Finite-element modeling of acoustic chaos to sonic infrared imaging *J. Appl. Phys.* **98** 014907 (4 pp)

[88] Han X, Islam M S, Newaz G, Favro L D and Thomas R L 2006 Finite element modeling of the heating of cracks during sonic infrared imaging *J. Appl. Phys.* **99** 074905 (7 pp)

[89] Han X and Song Y 2013 Study of the effect of engagement force of ultrasound transducer on crack detectability in sonic IR imaging, *AIP Conf. Proc*. **1511** 532-538

[90] Feng F-Z, Zhang C-S, Min Q-X and Wang P-F 2015 Effect of engagement force on vibration characteristics in sonic IR imaging *Ultrasonics* **56** 473-476

[91] Song Y and Han X 2012 Further study of coupling materials on aluminium sample using sonic IR *AIP Conf. Proc*. **1430** 546-551

[92] Song Y and Han X 2015 FEA study of non-linear effect of coupling media to sonic infrared imaging *AIP Conf. Proc*. **650** 1774-1781

[93] Solodov I Y and Korshak B A 2002 Instability, chaos and "memory" in acoustic-wave-crack interaction *Phys. Rev. Lett.* **88** 014303 (3 pp)

[94] Solodov I Y and Krohn, Busse G 2002 CAN: an example of nonclassical acoustic nonlinearity in solids *Ultrasonics* **40** 621-625

[95] Solodov I Y 1998 Ultrasonics of non-linear contacts: propagation, reflection and NDE-applications *Ultrasonics* **36** 383-390

[96] Solodov I, Wackerl J, Pfleiderer K and Busse G 2004 Nonlinear self-modulation and subharmonic acoustic spectroscopy for damage detection and location *Appl. Phys. Lett.* **87** 5386-5388

[97] Solodov I 2015 Highly-sensitive defect-selective imaging and NDT via resonant nonlinearity of defects *Phys. Proc.* **70** 411-414

[98] Solodov I, Bai J and Busse G 2013 Resonant ultrasound spectroscopy of defects: Case study of flat-bottomed holes J. Appl. Phys. **113** 223512 (7 pp)

[99] Solodov I, Bai J, Bekgulyan S and Busse G 2011 A local defect resonance to enhance acoustic wave-defect interaction in in nondestructive evaluation *Appl. Phys. Lett.* **99** 211911 (3 pp)

[100] Solodov I and Busse G 2013 Resonance ultrasonic thermography: High efficient contact and air-coupled remote modes *App. Phys. Lett.* **102** 161905 (3 pp)

[101] Derusova D A, Vavilov V P and Druzhinin N V 2016 Evaluating impact damage in graphite epoxy composite by using low-power UT *Proc. SPIE* **9861** Thermosense XXXVIII 98610F (7 pp)

[102] Rahammer M, Solodov I, Bisle W, Scherling D and Kreutzbruck M 2016 Phased matched guided wave excitation for ultrasonic thermography *Proceedings of the 13th Conference on Quantitative Infrared Thermography* 663-669

[103] Zalameda J, Winfree W P and Yost W T 2008 Air coupled acoustic thermography inspection technique *AIP Conf. Proc.* **975** 467-474

[104] Sathish S, Welter J T, Jata K V, Schehl N and Boehnlein T 2012 Development of nondestructive non-contact acousto-thermal evaluation technique for damage detection in materials *Rev. Sci. Instr.* **83** 095103 (10 pp)

[105] Adebahr W, Solodov I, Rahammer M, Gulnizkij N and Kreutzbruck M 2016 Local defect resonance for sensitive non-destructive testing *AIP Conf. Proc.* **1706** 050005 (9 pp)

[106] Barden T J, Almond D P, Morbidini M, Duffour P and Cawley 2004 A quantitative investigation of thermosonics *Proceedings of the 7th Conference on Quantitative Infrared Thermography* **H.12** 1-6

[107] Morbidini M and Cawley P 2009 A calibration procedure for sonic infrared nondestructive evaluation *J. Appl. Phys.* **106** 023504 (9 pp)

[108] Vaddi J S, Holland S D and Kessler M R 2016 Absorptive viscoelastic coatings for full field vibration coverage measurement in vibrothermography *NDT&E Int.* **82** 56-61

[109] Li M, Holland S D and Meeker W Q 2010 Statistical methods for automatic crack detection based on vibrothermography sequence-of-images data *Appl. Stochastic Models Bus. Ind.* **26** 481-495

[110] Holland S D 2011 Thermographic signal reconstruction for vibrothermography *Inf. Phys. Tech.* **54** 503-511

[111] Zeng Z, Zhou J, Tao N, Feng L, Zhang C and Han X 2012 Support vector machines based defect recognition in SonicIR using 2D heat diffusion features *NDT&E Int.* **47** 116-123

[112] Mayton D, Spencer F and Alvarez C 2005 Characterizing the effects of sonic IR variables on turbine disk inspection using a design of experiment approach *Rev. Prog. Quant. Nondestr. Eval.* **56** 78-91

[113] Gao C, Meeker W Q and Mayton D 2014 Detecting cracks in aircraft engine fan blades using vibrothermography nondestructive evaluation *Reliab. Eng. Syst. Saf.* **131** 229-235

[114] Guo X 2015 An analytical model and parametric analysis of ultrasound excited infrared thermography *QIRT J.* **12** 137-148

[115] Holland S D, Koester L, Vaddi J, Lesthaeghe T, Meeker W Q and Schiefelbein B 2016 VibroSim: a hybrid computational/empirical model of vibrothermography nondestructive evaluation *AIP Conf. Proc.* **1709** 100008 (7 pp)

[116] Salazar A, Mendioroz A, Apiñaniz E, Oleaga A, Venegas P and Sáez-Ocáriz I 2010 Characterization of delaminations by lock-in vibrothermography *J. Phys.: Conf. Series* **214** 012079 (4 pp)

[117] Zhao S X, Han X, Favro L D, Newaz G and Thomas R L 2012 Composite delamination depth profiling in sonic-IR imaging *Rev. Prog. Quantit. Nondestr. Eval.* **1430** 533-539

[118] Shepard S M, Lhota J R, Rubadeux B A, Wang D and Ahmed T 2003 Reconstruction and enhancement of active thermographic image sequences *Opt. Eng*. **42** 1337-1342

[119] Mendioroz A, Apiñaniz E, Salazar A, Venegas P and Sáez-Ocáriz I 2009 Quantitative study of buried heat sources by lock-in vibrothermography: an approach to crack characterization *J. Phys. D: Appl. Phys.* **42** 055502 (8 pp)

[120] Ouyang Z, Favro L D, Thomas R L and Han X 2002 Theoretical modeling of thermosonic imaging of cracks *AIP Conf. Proc.* **21** 577-581

[121] Holland S D and Renshaw J 2010 Physics-based image enhancement for infrared thermography *NDT&E Int.* **43** 440-445

[122] Vaddi J S and Holland S D 2014 Identification of heat source distribution in vibrothermography *AIP. Conf. Proc.* **1581** 1639-1643

[123] Mendioroz A, Celorrio A and Salazar A 2015 Characterization of rectangular vertical cracks using burst vibrothermography *Rev. Sci. Instr.* **86** 064903 (8 pp)

[124] Mendioroz A, Celorrio R, Cifuentes A, Zaton L and Salazar A 2016 Sizing vertical cracks using burst vibrothermography *NDT&E Int.* **84** 36-46

[125] Glorieux C, Li Voti R, Thoen J, Bertolotti M and Sibilia C 1999 Photothermal depth profiling: analysis of reconstruction errors *Inverse Problems* **15** (5) 1149-1163

[126] Li Voti R, Sibilia C and Bertolotti M 2005 Photothermal depth profiling by thermal wave backscattering and genetic algorithms *Int. J. Thermophys.* **26** 1833-1848

[127] Chen Z-J and Zhang S-Y 2010 Thermal Depth Profiling Reconstruction by Multilayer Thermal Quadrupole Modeling and Particle Swarm Optimization *Chin. Phys. Lett.* **27** 02652 (4 pp)

[128] Özisik M N and Orlande H R B 2000 Inverse Heat Transfer: Fundamentals and Applications, New York, Taylor & Francis

[129] Engl H W, Hanke M and Neubauer A 2000 Regularization of Inverse Problems, Dordrecht, Kluwer Academic

[130] Carslaw H S and Jaeger J C 1959 Conduction of heat in solids, Oxford, Oxford University Press

[131] Moore E H 1920 On the reciprocal of the general algebraic matrix *Bulletin of the American Mathematical Society* **26** 394-395

[132] Penrose R 1955 A generalized inverse for matrices *Mathematical Proceedings of the Cambridge Philosophical Society* **51** 406-413

[133] Wahba G 1980 Ill-posed problems: numerical and statistical methods for mildly, moderately and severely ill-posed problems with noisy data *Technical Report* no. 595 (Madison, University of Wisconsin)

[134] Hadamard J 1923 Lectures on Cauchy's Problem in Linear Differential Equations, Hew Haven, Yale University Press

[135] Bers L, John F and Schechter M 1964 Partial Differential Equations, New York, Wiley

[136] Tikhonov A N and Arsenin V Y 1977 Solutions of Ill-Posed Problems, Halsted Press, New York

[137] Hansen P C 1992 Analysis of discrete ill-posed problems by means of the L-curve *SIAM Rev.* **34** 561-580

[138] Depriester M, Hus P, Delenclos S and Hadj Sahraoui A **2005** New methodology for thermal parameter measurements in solids using photothermal radiometry *Rev. Sci. Instrum.* **76** 074902-1-6

[139] Balderas-López J A and Mandelis A **2003** Self-normalization photothermal technique for accurate thermal diffusivity measurements in thin metal layers *Rev. Sci. Instrum.* **74** (12) 5219-25

[140] Jensen C, Chirtoc M, Horny N, Antoniow J S, Pron H and Ban H 2013 Thermal conductivity profile determination in proton-irradiated ZrC by spatial and frequency scanning thermal wave methods. *J Appl. Phys.* **114** 133509-1-9

[141] Vogel C R 2002 Computational Methods for Inverse Problems, Philadelphia, SIAM

[142] Brune C, Sawatzky A and Burger M 2011 Primal and Dual Bregman Methods with Application to Optical Nanoscopy *Int. J. Comput. Vis.* **92** 211-229

[143] Esedoglu S and Osher S J 2004 Decomposition of images by the anisotropic Rudin-Osher-Fatemi model. *Commun. Pure Appl. Math.* **57** 1609-1626

[144] Tibshirami R 1996 Regression Shrinkage and Selection via the Lasso *Journal of the Royal Statistical Society. Series B (Methodological)* **58** (1) 267-288

Appendix

A.1 Spatial resolution of the inversion algorithm

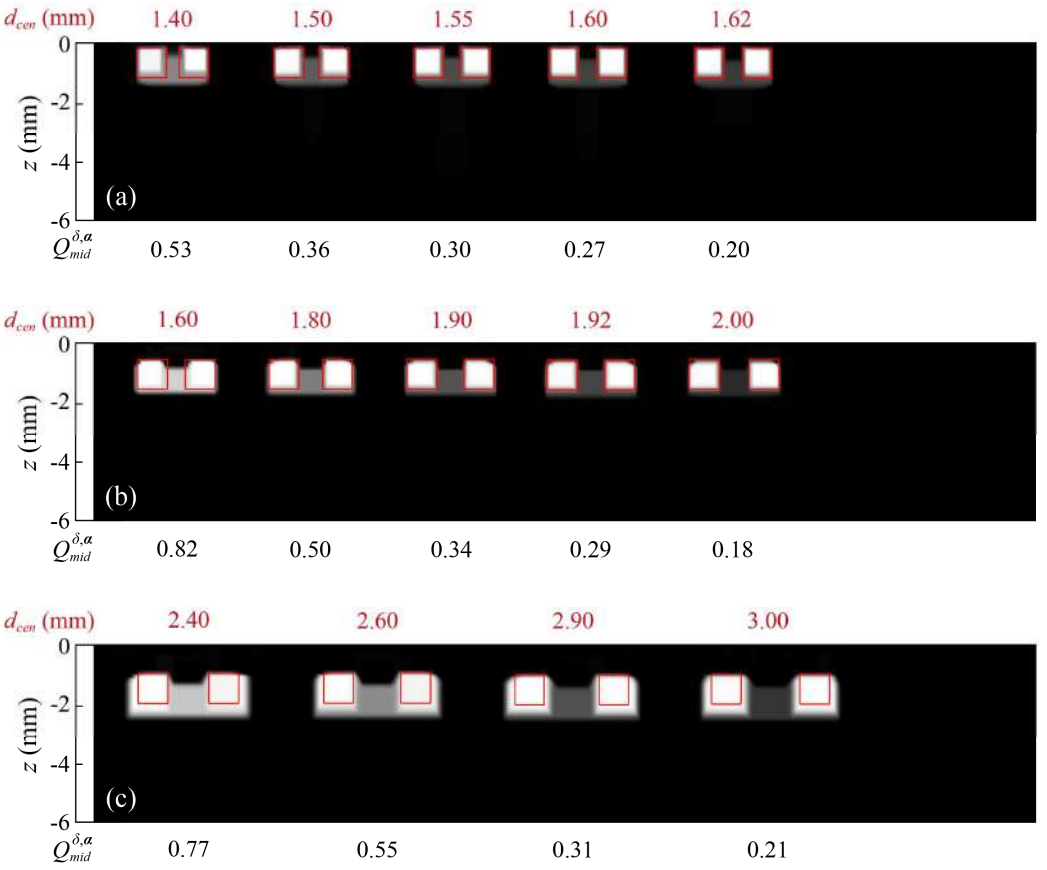

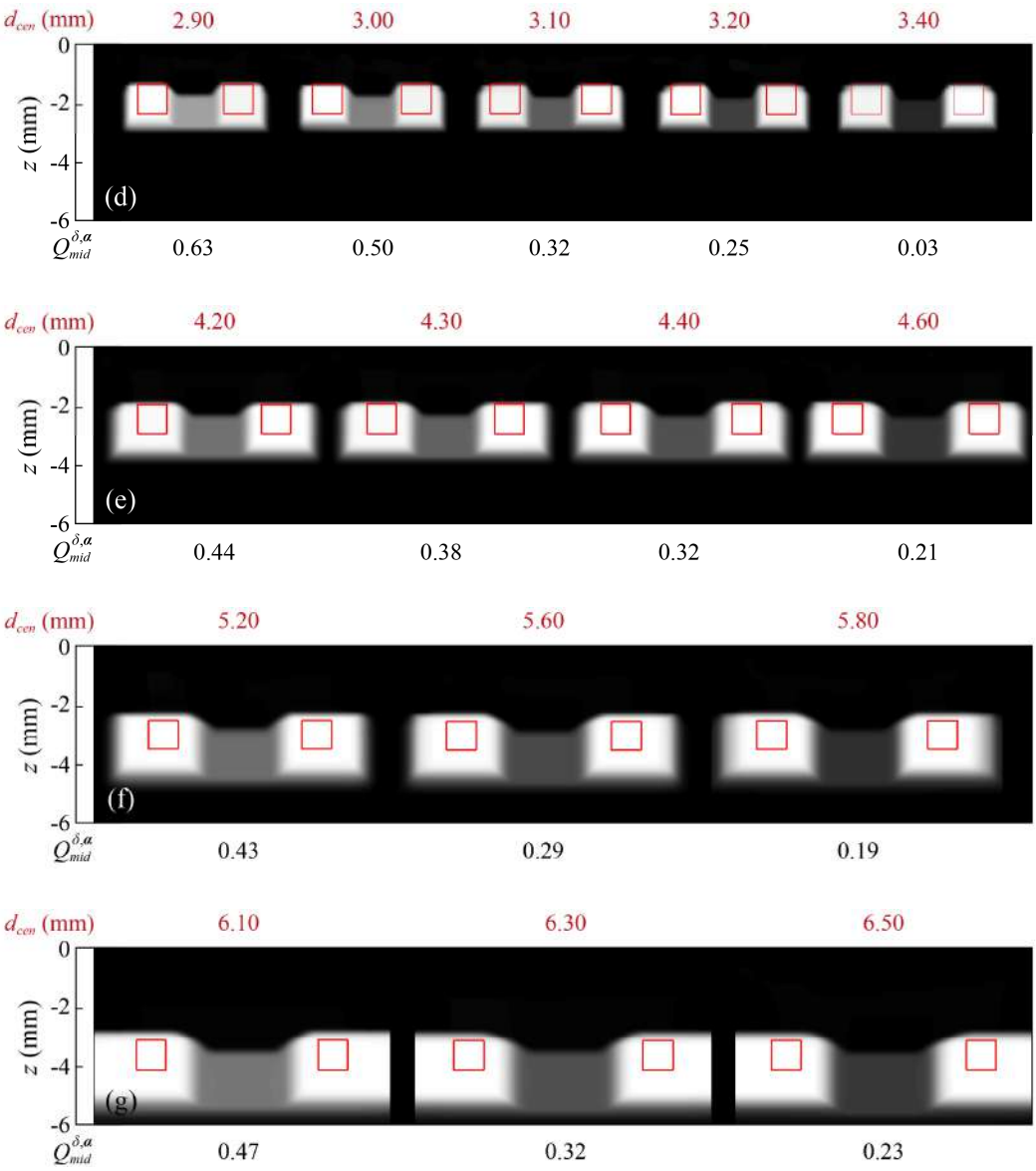

Figure A.1. Reconstructions of two squares of dimensions $w_1 = h_1 = w_2 = h_2 = 1$ mm as a function of d_{cen} (separation distance between centres), in inversions stabilized with TV_{Anisot} and entering normalized amplitudes. The contours of the real heat sources are depicted in red and the values of both d_{cen} and the normalized heat source distribution in the mid-point between the two maxima, $Q_{mid}^{\delta,\alpha}$, are displayed on top of and under each reconstruction, respectively. The depths of the heat sources are: $|d| = 0.2$ (a), 0.6 (b), 1.2 (c), 1.6 (d), 2.0 (e), 2.6 (f) and 3.2 mm (g).

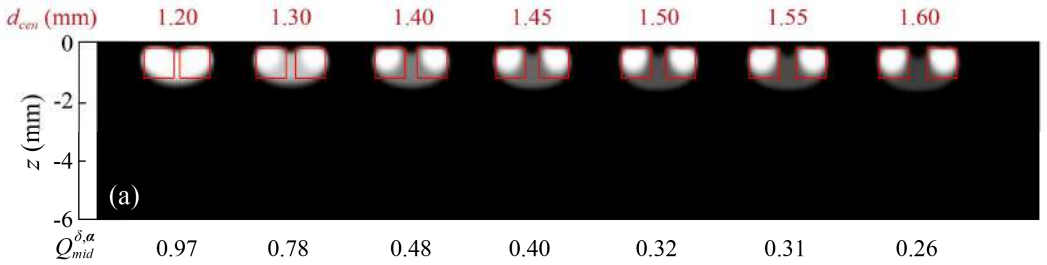
d_{cen} (mm) 1.20 1.30 1.40 1.45 1.50 1.55 1.60
z (mm)
0
-2
-4
-6
(a)
$Q_{mid}^{\delta,\alpha}$ 0.97 0.78 0.48 0.40 0.32 0.31 0.26

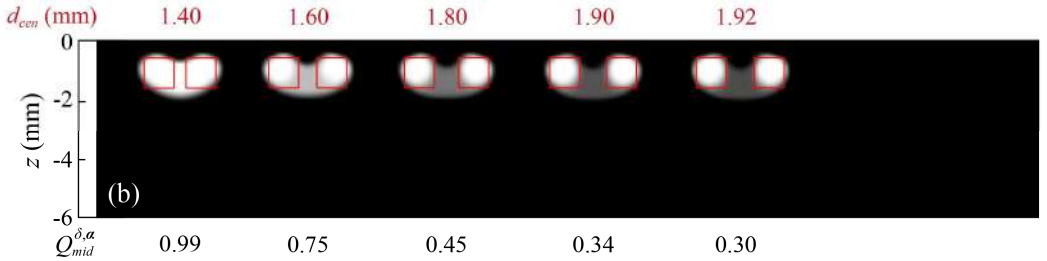
d_{cen} (mm) 1.40 1.60 1.80 1.90 1.92
z (mm)
0
-2
-4
-6
(b)
$Q_{mid}^{\delta,\alpha}$ 0.99 0.75 0.45 0.34 0.30

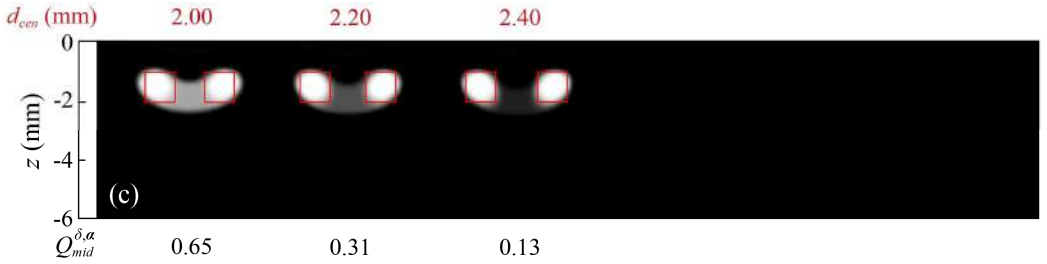
d_{cen} (mm) 2.00 2.20 2.40
z (mm)
0
-2
-4
-6
(c)
$Q_{mid}^{\delta,\alpha}$ 0.65 0.31 0.13

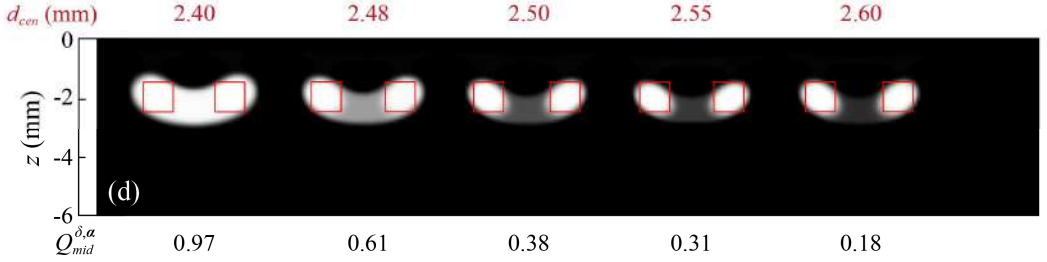
d_{cen} (mm) 2.40 2.48 2.50 2.55 2.60
z (mm)
0
-2
-4
-6
(d)
$Q_{mid}^{\delta,\alpha}$ 0.97 0.61 0.38 0.31 0.18

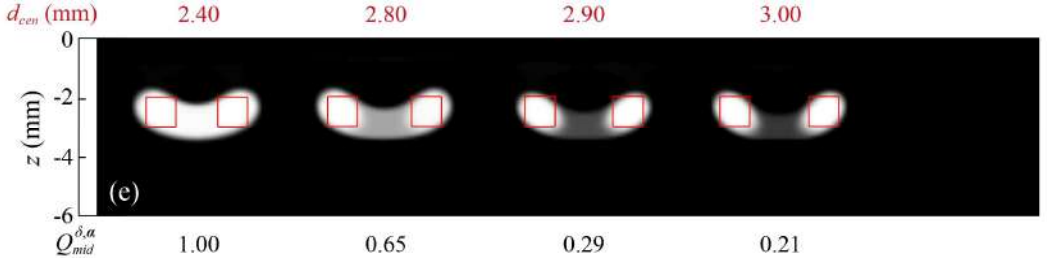
d_{cen} (mm) 2.40 2.80 2.90 3.00
z (mm)
0
-2
-4
-6
(e)
$Q_{mid}^{\delta,\alpha}$ 1.00 0.65 0.29 0.21

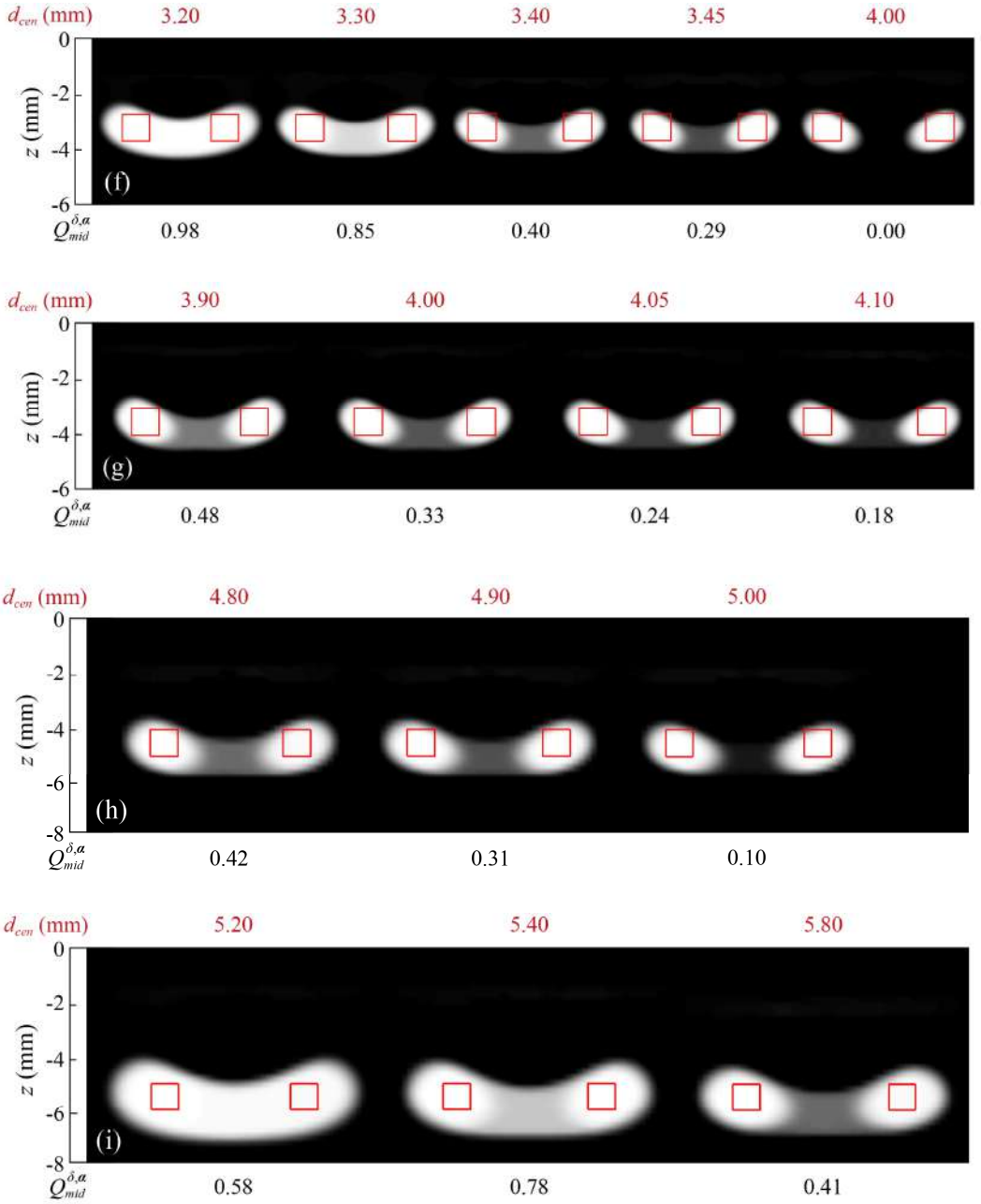
d_{cen} (mm)
3.20
3.30
3.40
3.45
4.00
z (mm)
0
-2
-4
-6
(f)
$Q_{mid}^{\delta,\alpha}$
0.98
0.85
0.40
0.29
0.00
d_{cen} (mm)
3.90
4.00
4.05
4.10
z (mm)
0
-2
-4
-6
(g)
$Q_{mid}^{\delta,\alpha}$
0.48
0.33
0.24
0.18
d_{cen} (mm)
4.80
4.90
5.00
z (mm)
0
-2
-4
-6
-8
(h)
$Q_{mid}^{\delta,\alpha}$
0.42
0.31
0.10
d_{cen} (mm)
5.20
5.40
5.80
z (mm)
0
-2
-4
-6
-8
(i)
$Q_{mid}^{\delta,\alpha}$
0.58
0.78
0.41

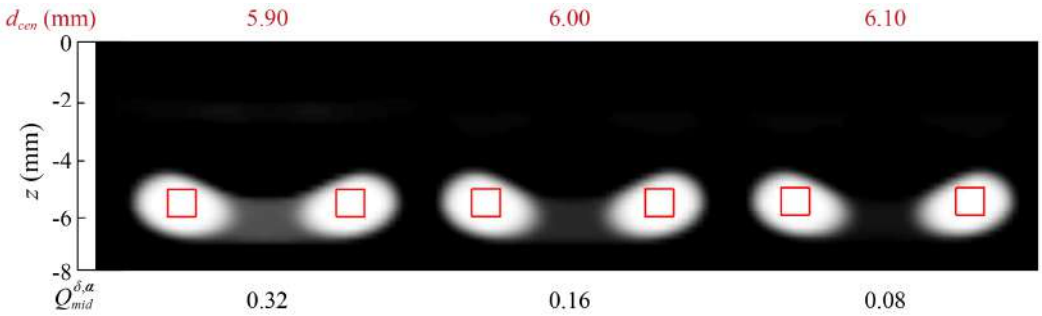

Figure A.2. Reconstructions of two squares of dimensions $w_1 = h_1 = w_2 = h_2 = 1$ mm as a function of d_{cen} (separation distance between centres), in inversions stabilized with TV_{Isot} and entering raw amplitudes. The contours of the real heat sources are depicted in red and the values of both d_{cen} and the normalized heat source distribution in the mid-point between the two maxima, $Q_{mid}^{\delta,\alpha}$, are displayed on top of and under each reconstruction, respectively. The depths of the heat sources are: $|d|$ = 0.2 (a), 0.6 (b), 1.2 (c), 1.6 (d), 2.0 (e), 2.6 (f), 3.2 (g), 4.0 (h) and 5.0 mm (i).

A.2 Micrographs of the calibrated heat sources

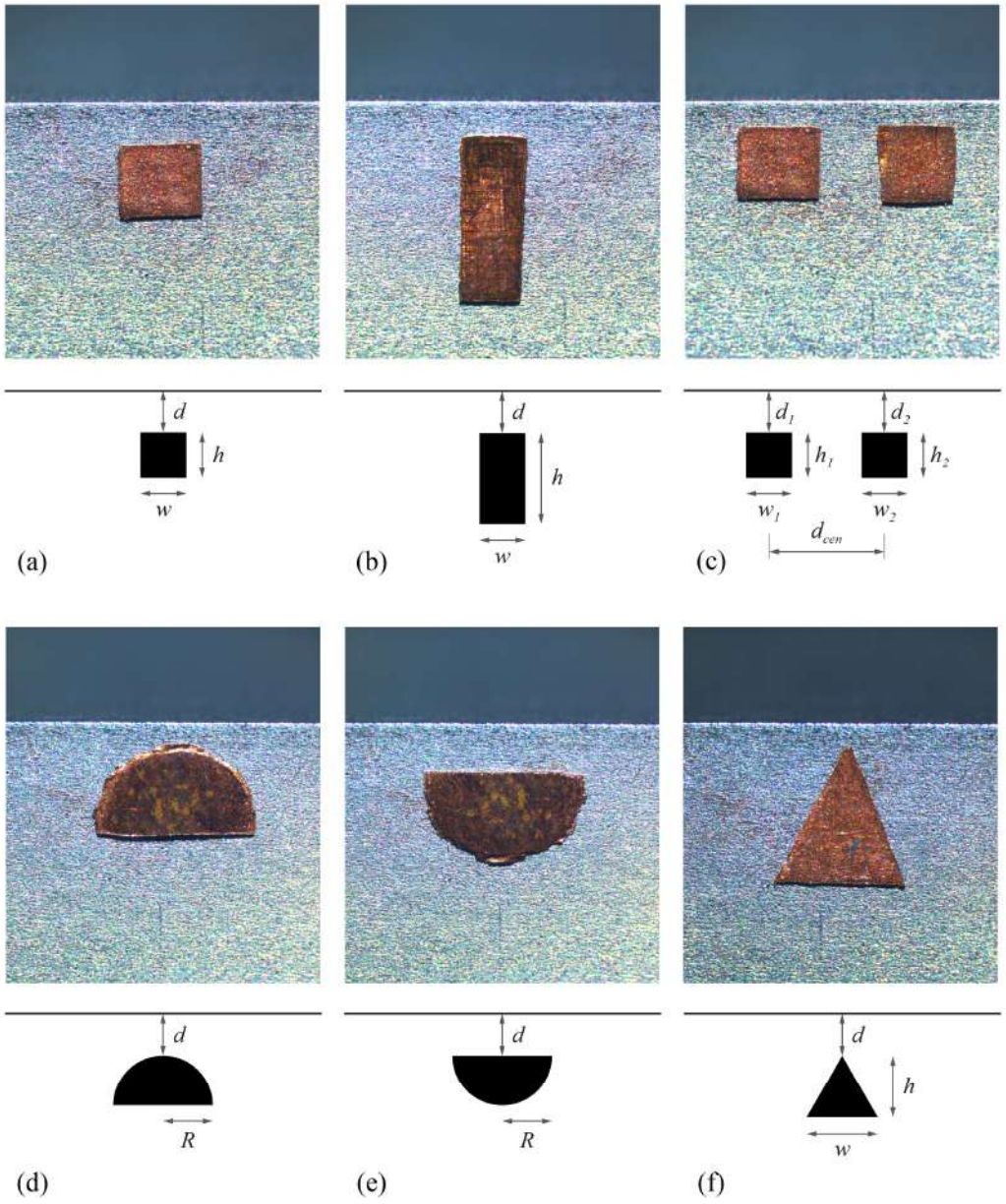

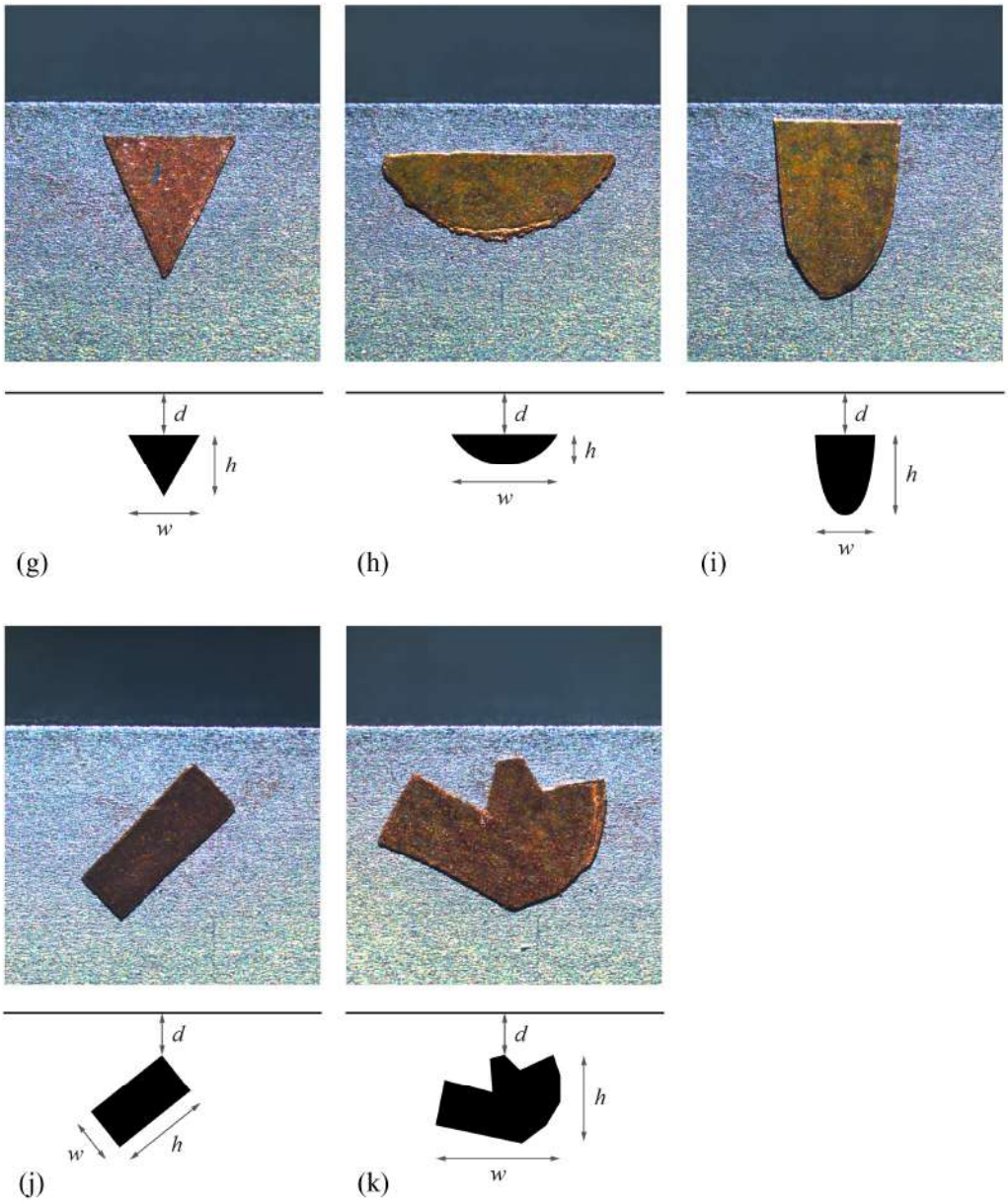

Figure A.3. Micrographs and diagrams of the Cu foils used in vibrothermography experiments using samples containing calibrated heat sources, representing homogeneous kissing vertical cracks of different geometries: (a) square, (b) rectangle, (c) two squares, (d) *sUp*, (e) *sDown*, (f) *tUp*, (g) *tDown*, (h) shallow and elongated half-penny, (i) deep and narrow half-penny, (j) rectangle inclined 45º and (k) arbitrary shape.

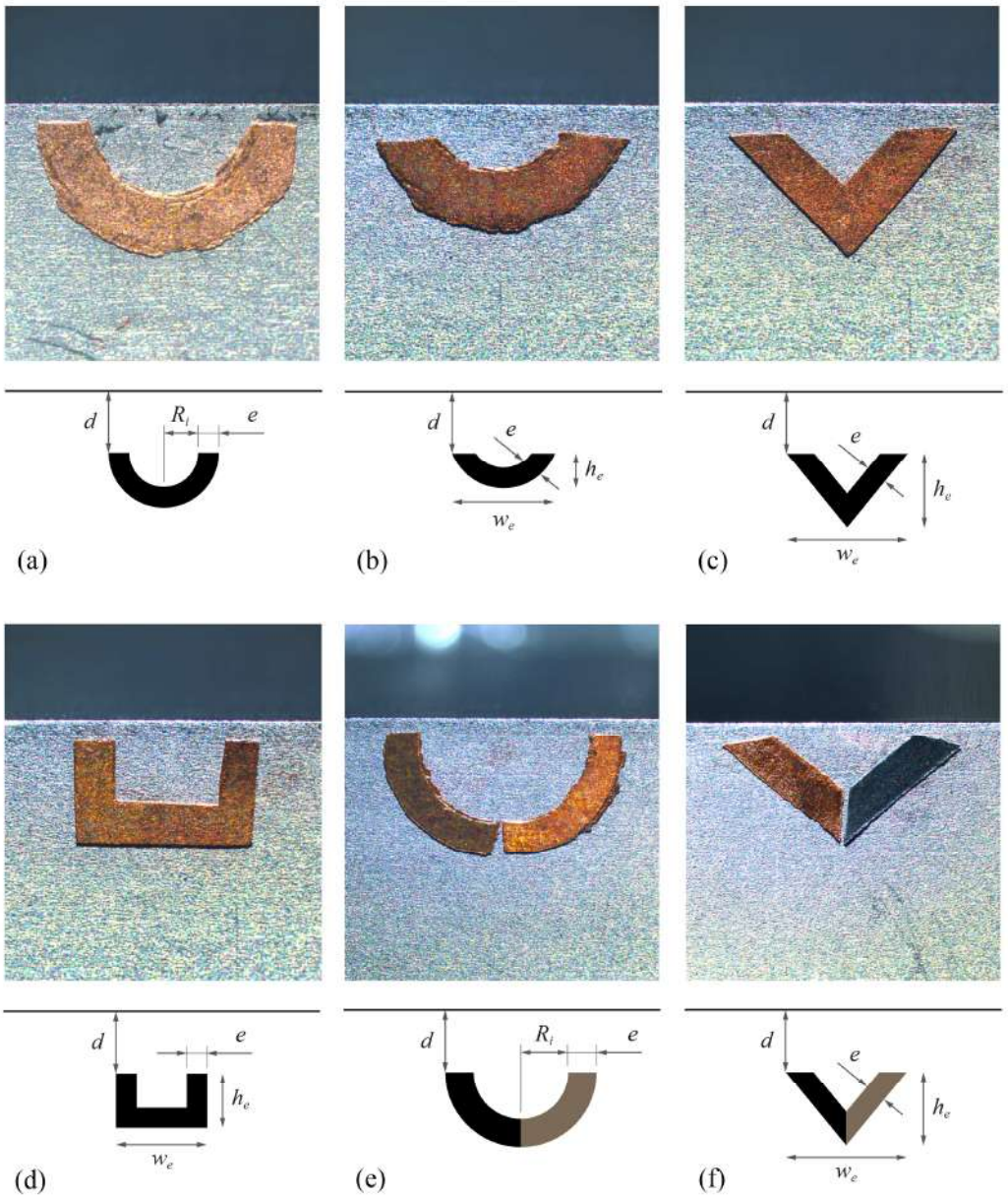

Figure A.4. Micrographs and diagrams of the geometries considered in vibrothermography experiments using samples containing calibrated heat sources, representing both homogeneous and inhomogeneous vertical open cracks of different geometries: (a) semicircle, (b) half-penny, (c) triangle, (d) rectangle, (e) semicircle with left and right halves corresponding to 38 μm annealed and hard Cu foils and (f) triangle with left right halves corresponding to 25 μm Cu and stainless steel foils. All the homogeneous heat sources correspond to 38 μm Cu strips.